Spiral Defect Chaos and the Skew-Varicose Instability in Generalizations of the Swift–Hohenberg Equation

Jinendrika Anushi Weliwita

Submitted in accordance with the requirements for the degree of Doctor of Philosophy

The University of Leeds
School of Mathematics

November, 2011

The candidate confirms that the work submitted is her own and that appropriate credit has been given where reference has been made to the work of others. This copy has been supplied on the understanding that it is copyright material and that no quotation from the thesis may be published without proper acknowledgement.

©2011 The University of Leeds and Jinendrika Anushi Weliwita

Acknowledgments

First and the foremost I wish to acknowledge is Alastair Rucklidge who gave the opportunity to me for doctoral studies. Apart from being my principal supervisor he was a strength, an inspiration, a critique and a dearly friend to me. My co-supervisor Steve Tobias brought unique perspectives to my research, enriching it greatly. I would thankfully remember his encouragement and enthusiasm. My appreciation also goes to Ian Melbourne for his valuable suggestions. I am also grateful for some helpful conversations with Edgar Knobloch, Stephen Morris and Paul Matthews.

There is nothing like the parents' love. While I was tirelessly tied up with the thesis, they held me close to their hearts, watching my wellbeing from their far away home. Words cant express how much I owe to Sanjeeva Witharana, who stayed by my side in the most needed times. I am forever indebted to my parents and Sanjeeva for their understanding, endless patience and encouragement when it was most required- it is to them that this thesis is dedicated.

Many thanks also to my colleagues and friends, especially Beverley and Rowan for being wonderful.

Lastly I would like to express my gratitude for financial support provided by the School of Mathematics at University of Leeds.

Famous French mathematician Joseph Fourier said “the profound study of nature is the most fertile source of mathematical discoveries”. I studied naturally occurring patterns and their formations. I hope this Doctoral thesis did the justice to all who stood by me during this courageous endeavour.

Abstract

Mean flows are known to play an important role in the dynamics of the Spiral Defect Chaos state and in the existence of the skew-varicose instability in Rayleigh–Bénard Convection. SDC only happens in large domains, so computations involving the full three-dimensional PDEs for convection are very time-consuming. We therefore explore the phenomena of Spiral Defect Chaos and the skew-varicose instability in Generalized Swift–Hohenberg (GSH) models that include the effects of long-range mean flows. Our analysis is aimed at linking the two phenomena.

We apply analytical and numerical methods to study the linear stability of stripe patterns in two generalizations of the two-dimensional Swift–Hohenberg equation that include coupling to a mean flow. A projection operator is included in our models to allow exact stripe solutions. In the generalized models, stripes become unstable to the skew-varicose, oscillatory skew-varicose and cross-roll instabilities, in addition to the usual Eckhaus and zigzag instabilities. We analytically derive stability boundaries for the skew-varicose instability in various cases, including several asymptotic limits. Close to the onset of pattern formation, the skew varicose instability has the same dependence on wavenumber as the Eckhaus instability provided the coupling to the mean flow is greater than a critical value. We use numerical techniques to determine eigenvalues and hence stability boundaries of other instabilities. We extend our analysis to both stress-free and no-slip boundary conditions and we note a cross-over from the behaviour characteristic of no-slip to that of stress-free boundaries as the coupling to the mean flow increases or as the Prandtl number decreases. The region of stable stripes is completely eliminated by the cross-roll instability for large coupling to the mean flow or small Prandtl number.

We characterize the nonlinear evolution of the modes that are responsible for the skew-varicose instability in order to understand whether the bifurcation from stable stripes at the skew-varicose instability is supercritical or subcritical. The systems of ODEs, which are derived from the PDEs by selecting 3 relevant modes and truncating, show that the skew-varicose instability is supercritical whereas for an extension with 5 relevant modes shows the skew-varicose instability is subcritical.

We solve the PDEs of one GSH model in spatially-extended domains for very long times, much longer than previous efforts in the literature. We are able to investigate the influence of domain size and other parameters much more systematically, and to develop a criterion for when the spiral defect chaos state could be expected to persist in the long time limit. The importance of the mean flow can be adjusted via the Prandtl number or parameter that accounts for the fluid boundary conditions on the horizontal surfaces in a convecting layer and hence we establish a relation between these parameters that preserves the same pattern. We further analyze the onset of chaotic state, and its dependence on the Prandtl number and the domain size.

An outstanding issue in the understanding of SDC is that it exists at parameter values where simple straight roll convection is also stable, and the region of co-existence increases as the domain size increases. The results of our numerical simulations are coupled with the analysis of the skew-varicose instability of the straight-roll pattern in the Generalized Swift–Hohenberg equation, allowing us to identify the role that skew-varicose events in local patches of stripes play in maintaining Spiral Defect Chaos.

Contents

List of Figures

List of Publications

Published

- J. A. Weliwita, A. M. Rucklidge, and S. M. Tobias; Skew-varicose instability in two-dimensional generalized Swift–Hohenberg equations, *Phys. Rev. E*, 84 036201 (2011).

(*The Chapters 2 and 3 are formed on the basis of the publication.*)

List of Abbreviations

RBC	Rayleigh–Bénard Convection
SHE	Swift–Hohenberg Equation
GSH	Generalized Swift–Hohenberg Equation
SVI	Skew-Varicose Instability
SV	Skew-Varicose
CR	Cross-Roll
ZZ	Zigzag
OSV	Oscillatory Skew-Varicose
PDE	Partial Differential Equation
ODE	Ordinary Differential Equation
SDC	Spiral Defect Chaos
DC	Defect Chaos

Chapter 1

Introduction

1.1 Pattern formation

The Universe, from the grandest to the smallest scales, mostly consists of non equilibrium systems that possess an extraordinarily rich and visually fascinating variety of spatiotemporal structures, patterns. An example of grand pattern formation, spiral galaxies, is shown in figure 1.1(a). Descending from galaxies to the natural world, one can experience how the formation of patterns has become a common theme in nature; patterns in cloud streets, animal coatings such as dappling on giraffes and stripes in zebras, patterns in the ocean, patterns of hurricanes, snowflakes patterns and cracks in mud. One terrestrial example of natural pattern formation, ripples found in sand dunes, is shown in figure 1.1(b).

Pattern formation has, mostly since the 1960s, attracted experimentalists and theoreticians and become a large, growing and increasingly important part of modern physical science, one relevant to everyday phenomena. The common phenomenon of these pattern forming non-equilibrium systems is the change from a spatially uniform state to a patterned state. Some of the patterns and dynamics that are observed in natural non-equilibrium systems have been explored using representative non-equilibrium systems in the laboratory. Of these non-equilibrium systems, Rayleigh–Bénard Convection (RBC) [12, 13], in


(a) (b)

Figure 1.1: *Nature of patterns: (a) Galactic spirals: Why galaxies evolve to form spiral, is an important open question in current astrophysical research [1]. (b) Pattern formation in wind-swept sand at the Sand Dunes in Mui Ne, Vietnam. The photo was taken by Ali Watters [2]. The wind lifts sand grains into the air, transferring translational and rotational energy to sand grains, which eventually fall back to earth and dissipate their energy into heat by friction as they roll and rub against other sand grains.*

which a fluid is driven out of equilibrium by a destabilizing temperature gradient, has been studied extensively. The Taylor–Couette [14] fluid dynamics experiment and the Faraday wave experiment [15], which are driven out of equilibrium by a velocity gradient and an applied forcing respectively, are also particularly well studied paradigms of pattern formation.

The work reported in this thesis is based on Rayleigh-Bénard Convection and we use the next section to elaborate upon the details of RBC.

1.2 Rayleigh–Bénard Convection

Convection is one of the major modes of heat transfer and mass transfer that occurs in a large scale in atmospheres, oceans, planetary mantles, and interestingly the outermost 30% of the sun is driven by convective motion [6, 16]. Convective motion in experiments

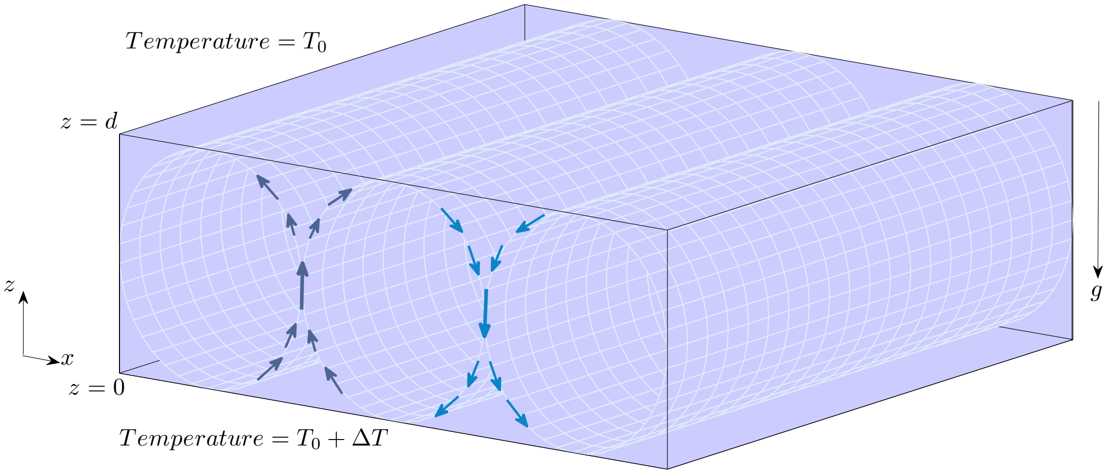

Figure 1.2: *Schematic diagram for the convective flow in the Rayleigh-Bénard Convection of a fluid layer between two horizontal plates. When the temperature difference ΔT is sufficiently large, the warm less-dense fluid near the bottom plate starts to rise and the cold more-dense fluid near the top plate spontaneously starts to fall. This eventually forms structures known as convection rolls. The characteristic roll size is about the same as the depth d. The gravitational acceleration is denoted by g. Arrows indicate the flow of hot rising and cold descending fluid.*

was reported initially by Bénard, in 1900 [12] and investigated further by Lord Rayleigh in 1916 [13]. The phenomenon of thermal convection under an adverse temperature gradient is therefore known as the Rayleigh–Bénard Convection (RBC) in their honour.

In RBC, a fluid layer of depth d is held in a vertical temperature gradient $\Delta T/d$ that determines whether or not the fluid is in thermodynamic equilibrium. When this temperature gradient exceeds a critical value, the buoyancy forces overcome the dissipation and the fluid layer undergoes a transition from a uniform conducting state to a convecting state of lower symmetry. The roll pattern occurring across the fluid layer was described as the linear instability of the conducting state by Rayleigh [13]. This phenomenon is illustrated in figure 1.2.

The temperature difference, ΔT is characterized by the dimensionless Rayleigh number,

Ra, a measure of the external temperature difference applied to the system, defined as $Ra = \alpha g d^3 \Delta T/\kappa\nu$. In the expression, α is the volumetric thermal expansion coefficient, g is the gravitational acceleration, κ is the thermal diffusivity, and ν is the kinematic viscosity. Also the vertical thermal diffusion time is d^2/κ and the vertical viscous relaxation time d^2/ν.

Rayleigh–Bénard Convection is described by the well-known non-dimensionalized Boussinesq equations; under the Boussinesq approximation fluid properties do not vary over the imposed temperature interval, except for the density in the buoyancy term. The dimensionless equations for the temperature perturbation $\theta(\mathbf{x}, z, t)$, the pressure $P(\mathbf{x}, z, t)$ and the velocity field $\mathbf{u}(\mathbf{x}, z, t)$, where $\mathbf{x} = (x, y)$ denotes the horizontal coordinates are [6, 17, 18]:

$$\left.\begin{aligned} \frac{1}{Pr}\left(\frac{\partial \mathbf{u}}{\partial t} + \mathbf{u}\cdot\nabla\mathbf{u}\right) &= -\nabla P + \nabla^2\mathbf{u} + \theta\hat{\mathbf{e}}_{\mathbf{z}} \\ \frac{\partial \theta}{\partial t} + \mathbf{u}\cdot\nabla\theta &= \nabla^2\theta + Ra\hat{\mathbf{e}}_{\mathbf{z}}\cdot\mathbf{u} \\ \nabla\cdot\mathbf{u} &= 0. \end{aligned}\right\} \tag{1.1}$$

The resulting temperature gradient is thus parallel to the vertical unit vector $\hat{\mathbf{e}}_{\mathbf{z}}$ and parallel to gravity $-g\hat{\mathbf{e}}_{\mathbf{z}}$ and temperature T is given by $T = 1-z+\theta$. The Prandtl number, Pr, is a dimensionless number; the ratio of kinematic viscosity to thermal diffusivity.

Boundary conditions must be added with these equations. No-slip boundary conditions yield: $\mathbf{u} = \theta = 0$ at top and bottom boundaries. Rayleigh [13] assumed stress-free boundary conditions at top and bottom, hence: $\theta = u_z = \partial_z u_x = \partial_z u_y = 0$.

This set of equations is the starting point of most theoretical work, which has been in three stages: the linear stability analysis of the conducting solution; the roll solution and its stability to small perturbations; and the description of spatial temporal modulations in terms of amplitude equations.

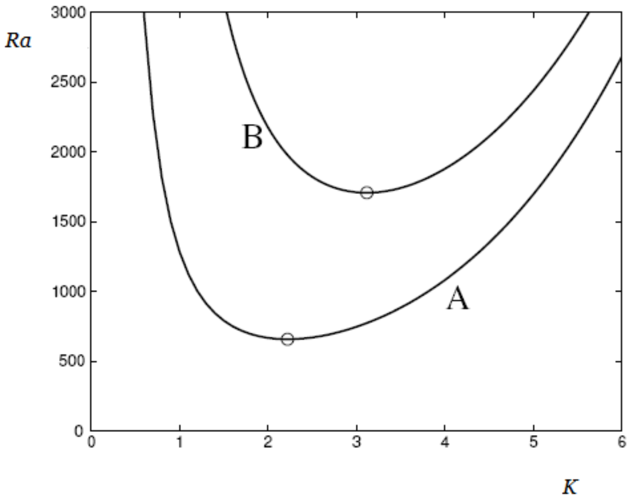

Figure 1.3: *Instability of the uniform conducting state to growth of convecting solution with wavenumber K. Marginal stability curves for stress-free (A) and no-slip (B) velocity boundary conditions and isothermal plates [3].*

1.2.1 Straight-Roll Patterns

When the amplitude of convection is small, the terms $\mathbf{u} \cdot \nabla \mathbf{u}$ and $\mathbf{u} \cdot \nabla \theta$ can be neglected, the equations (5.3) become linear and homogeneous. The linear stability of the conducting state is obtained by solving equations for Fourier normal modes in the form $e^{(i\mathbf{K} \cdot \mathbf{x})}$, which yields the marginal stability condition, (here $K = |\mathbf{K}|$)

$$Ra = \frac{(K^2 + \pi^2)^3}{K^2},$$

in the case of stress-free boundaries. Neutral stability curves for stress-free and no-slip boundaries (obtained by Pellew & Southwell in 1940 [3]) are illustrated in figure 1.3. The heat conduction state $\mathbf{u} = 0$ becomes unstable and convection is commenced for a layer with no lateral boundaries [17], if the Rayleigh number exceeds the critical value $R_c = 1708$ (for no-slip boundaries) or $R_c = 27\pi^4/4 \approx 657.5$ (for stress-free boundaries), independent

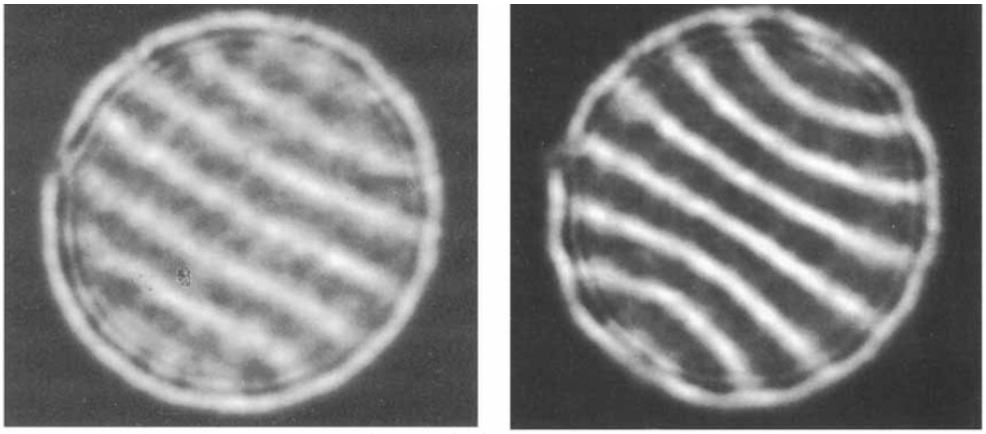

Figure 1.4: *Examples of shadowgraph images of the patterns, at onset when the system started to convect, seen in Argon layer in a circular convective cell with aspect ratio (radius-to-height ratio),* 7.66*. On the left: a straight-roll pattern at* $Ra = 1793.4$*. On the right: at* $Ra = 1913$*, the rolls bend in order to end perpendicular to the sidewalls. The rolls in the centre are squeezed, while those near the sidewall are widened [4].*

of the fluid under consideration [19]. In Boussinesq convection the primary bifurcation turns out to be supercritical and the system builds up a well defined steady straight roll pattern just above threshold.

Steady straight rolls are made of a single pair of wave vectors $\pm K\hat{\mathbf{x}}$ where $\hat{\mathbf{x}}$ is a unit vector in the horizontal plane. The periodic straight-roll solutions can be described by their horizontal roll wavelength $\lambda = 2\pi/K$, where the critical wavenumbers are $K_c = 3.117$ and $K_c = \pi/\sqrt{2} \approx 2.22$ for no-slip and stress-free boundary conditions respectively. Figure 1.4 shows how straight rolls develop in the interior of a convection cell in the experiments carried out by Croquette in 1989 [4]. They increased the temperature across an Argon layer (at $Ra = 1793$) and the first convective pattern, shown in left plot, is a straight defect-free roll pattern. They examined that the roll diameter is close to the thickness of the Argon layer, indicating that the pattern has the expected critical wavenumber. When Ra is slightly increased to 1913, a permanent deformation has built up to make rolls squeezed at the centre and expanded near the boundary, as shown in right plot. They have explored many complex time dependent patterns for further higher Ra.

It has been shown by Schluter *et al.* in 1965 [17], for values of Ra sufficiently close to the critical value, that the only stable solution in an infinite horizontal layer corresponds to convection in the form of periodic rolls.

1.2.2 Secondary Instabilities

If the Rayleigh number is increased from R_c, the straight parallel-roll pattern could become unstable to various instabilities. Combinations of these instabilities could replace rolls by more complex spatio-temporal structures. In the Boussinesq approximation, pattern selection is completely determined by the values of Ra, Pr and K, the wavenumber of the pattern. The theoretical analysis of pattern-forming instabilities are quite extensively discussed in the literature [20, 21]. Above but close to onset, the predictions of the linear and weakly nonlinear theory [17] for the stability of convection rolls with varying wavenumber were reproduced in a number of experiments [5, 22]. A particularly detailed study was carried out by Hu *et al.* in 1993 [23]. Developments concerning the stability of the rolls against various secondary instabilities have been mainly carried out by Busse and coworkers [6, 24, 25, 26]. Using perturbation theory, they considered the stability of rolls with respect to arbitrary disturbances of infinitesimal amplitude [27]. They extended the analysis to the case of higher Rayleigh numbers by employing the Galerkin method [24]. From 1978 to 1989, they calculated the region in (K, Pr, Ra) parameter space in which rolls are stable (known now as the Busse Balloon [6, 28]). The Busse Balloon was found to agree well with experiments for large Pr (for example water) [5], and reasonably well for gases with lower Pr [4, 8]. However an important question of which of the stable states will be selected by the physical system is yet largely unanswered. Figure 1.5 shows the Busse Balloon in (Pr, K, Ra) space: for lower Pr, there is a smaller stability region for stationary

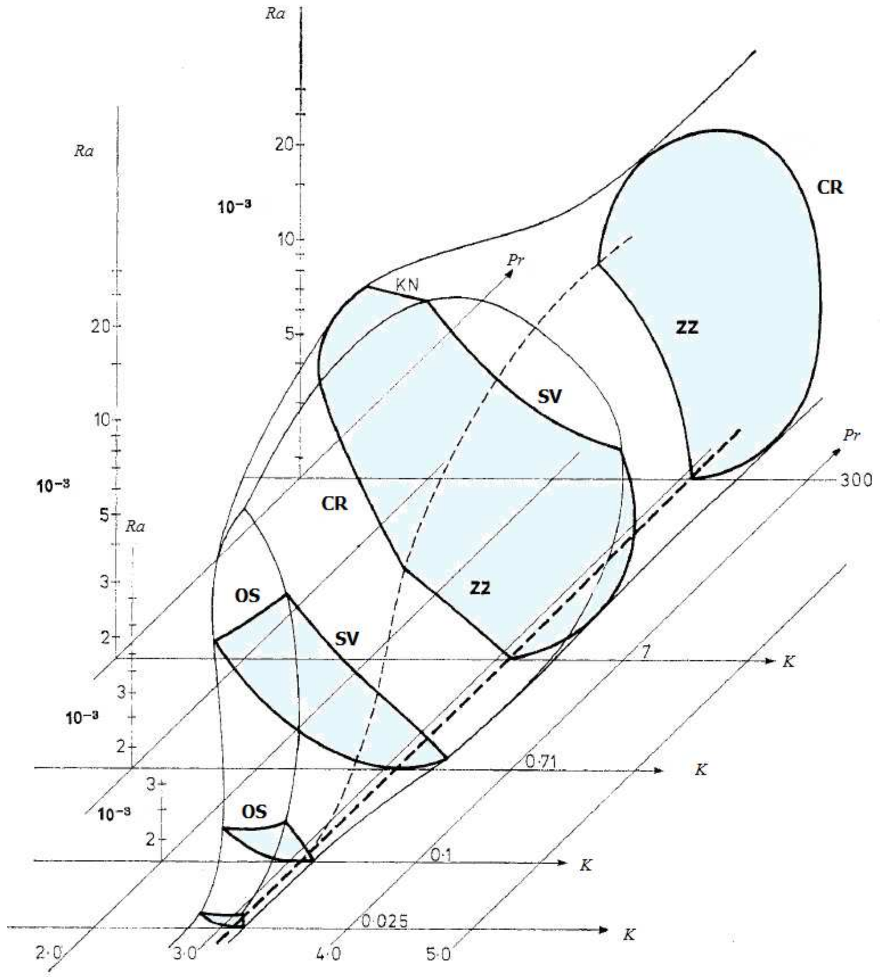

Figure 1.5: *Busse Balloon: stability region of convection rolls evolves in the three-dimensional* $Ra - Pr - K$ *space. Stability diagrams show the range of* Ra *and* K *for* $Pr = 0.1, 0.71, 7$ *and* 300 *where the roll state is stable (light blue region). The thick curves represent computed stability boundaries for the oscillatory (OS), the skew-varicose (SV), the cross-roll (CR), the knot (KN), and the zigzag (ZZ) instabilities. The other curves represent approximate interpolations [5, 6].*

convection and a larger domain of dynamic behaviour. The stable states are limited at the low-wavenumber side by the Eckhaus and the cross-roll instabilities and at the high-wavenumber side by the skew-varicose instability. The secondary modes for the Eckhaus and zigzag instabilities [5, 29], do not depend on the fact that the pattern is generated by the RB mechanism but on the symmetries of the rolls whereas for short wavelength cross-roll (rolls form perpendicular to the existing roll pattern) and long wavelength skew-varicose instability they are much more specific to convection, and are strongly depended on the value of Pr. We next describe the seminal results in the analysis of the Eckhaus, zigzag, cross-roll, oscillatory and skew-varicose instabilities in RBC.

Eckhaus and zigzag Instabilities

Various modulations to the roll patterns lead to instabilities that depend on initial wavenumber of the roll pattern and this is what sets the instability boundaries as indicated in Busse Balloon.

The simplest secondary long-wavelength instability is the Eckhaus instability [30], the well known modulation of the wavenumber of the pattern. In convection, rolls adjust wavenumber by destroying or creating rolls due to the Eckhaus instability. The Eckhaus instability occurs if the roll wavelength is too long or too short and eventually adjusts with a more favourable wavelength. If a roll pattern is at some Ra and wavenumber $K_0 < K_c$ or $K_0 > K_c$ in the Eckhaus unstable region (in the Busse Balloon) the evolution of the Eckhaus instability leads to the addition or subtraction of rolls and the increase or decrease the wavenumber. Figure 1.6 illustrates the experimental results of convecting liquid crystal layer showing how the initially periodic pattern develops a long-wavelength modulation if the initial condition is located in the Eckhaus unstable region [7].

The zigzag instability [5, 29], a long-wavelength instability, creates wavy distortions of the rolls to reduce the wavelength when it is too large. The zigzag modulation is of the form $e^{iq_0x}e^{\pm is_yy}$, where $q_0 = K - 1$ and $s_y \ll q_0$.

Therefore zigzag instability initiates a bending process of rolls and breaks the translation invariance of the pattern along the roll axis. Figure 1.7 exhibits the experimental

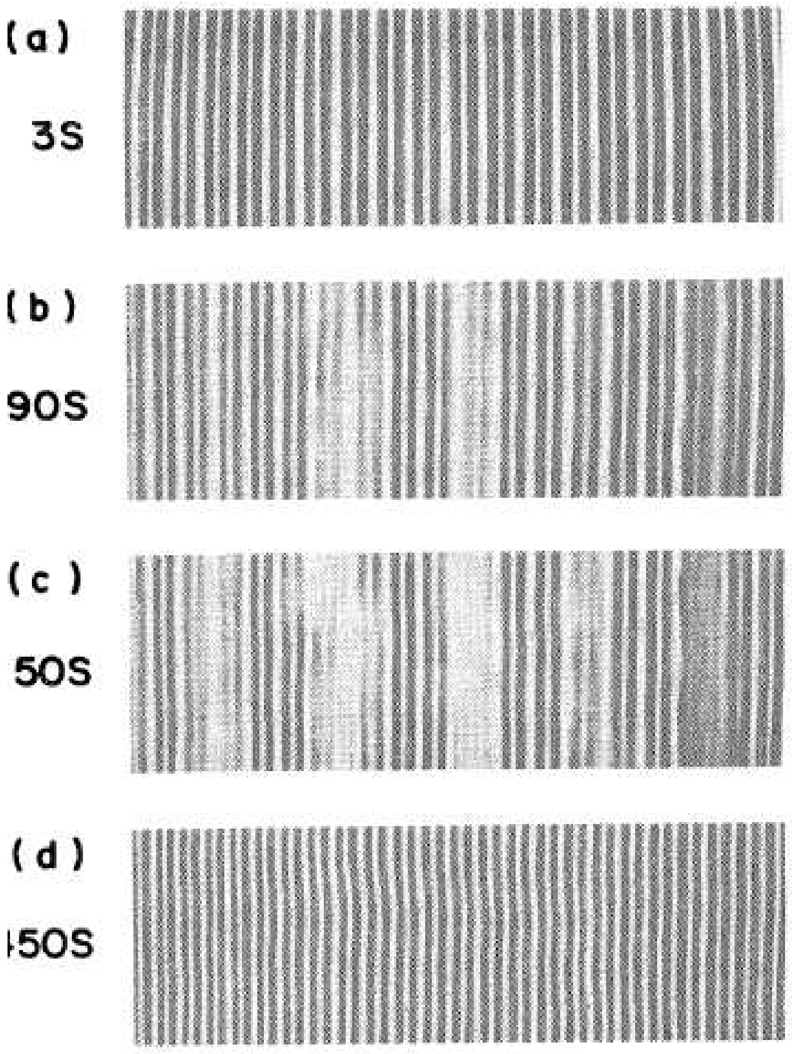

Figure 1.6: *Four subsequent stages in the development of the Eckhaus instability from a spatially periodic pattern for* $\epsilon = 0.052$*. New roll pairs nucleate in the regions of weak optical contrast, leading to a higher wavenumber. In the initial pattern, the dimensionless wavenumber,* $(K_0 - K_c)/K_c$ *is* 0.194 *[7].*

results of convecting silicone oil layer showing how the initially periodic pattern can develop into zigzagging if the the initial condition is located in the zigzag unstable region [5]. The

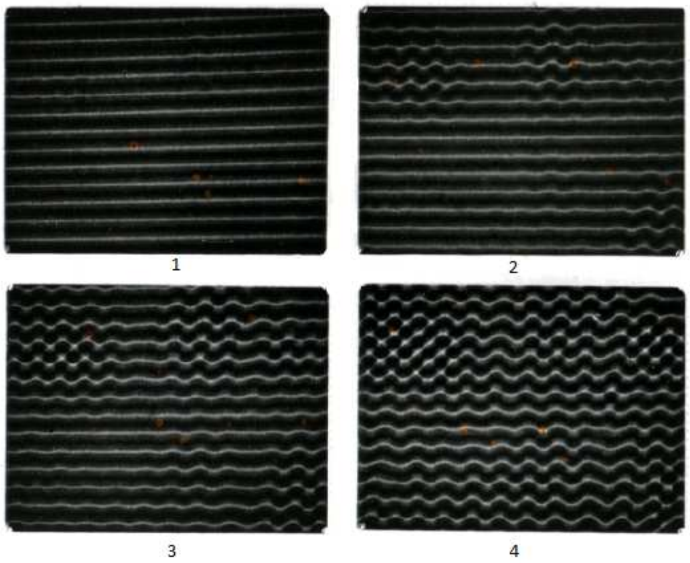

Figure 1.7: *Four subsequent stages in the development of the zigzag instability from a spatially periodic pattern with wavenumber $K = 2\pi/2.8$ for $Ra = 3600$, showing bending process of straight rolls into a wavy roll pattern, leading to a higher wavenumber. The initial pattern is shown in planform (1) and the time interval between planforms, (1)-(4), are $9\,mins$, $10\,mins$ and $26\,mins$ respectively [5].*

zigzag instability plays a minor role for small Pr but for large Pr, the zigzag instability forms a larger portion of the boundary to stable rolls in Busse Balloon.

The Eckhaus and the zigzag instabilities can be dealt within the framework of the amplitude-equation formalism, which retains the behaviour of convection close to the onset; amplitude equations describe the slow spatiotemporal evolution of the most unstable mode. The Eckhaus instability is subcritical, so the Eckhaus unstable rolls do not saturate in the bifurcated state and thus the pattern breaks down, creating defects that alter the wavelength of the pattern until it gets into the stable region. On the other hand, the zigzag instability is supercritical, stabilizing the pattern.

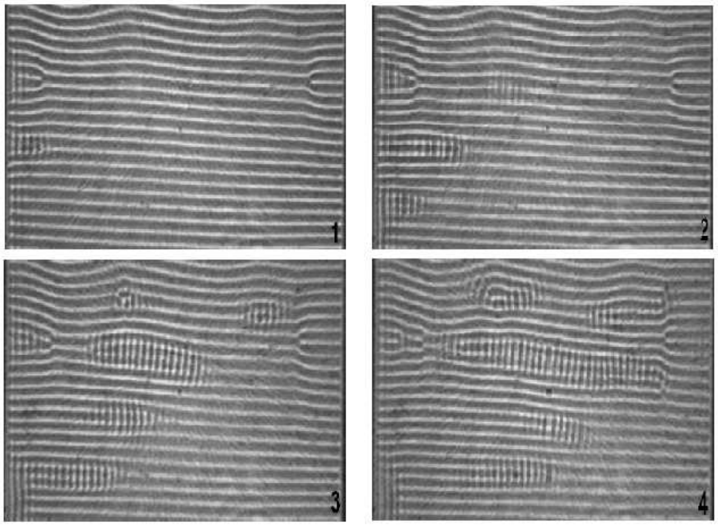

Figure 1.8: *Four subsequent stages in the development of the cross-roll instability at* $\epsilon = 0.2$ *(*ϵ*, the reduced Rayleigh number, is given by* $\epsilon = (R - R_c)/R_c$*)* $Pr = 1.1$*. Pictures are spaced* $23\,sec$ *apart [8].*

Cross-roll and oscillatory Instabilities

The cross-roll instability, being a short-wavelength instability, makes rolls perpendicular to the given rolls, changing convection with large wavenumber to a pattern with more favourable wavenumber and hence makes radical changes to the original convection pattern. The cross-roll instability of rolls have been investigated in the earlier experiments by Busse & Whitehead (1971) [5] and experimental evidence shows the occurrence of this instability at all Prandtl numbers [31]. Unlike, the Eckhaus and the zigzag instabilities, the wavelength of the cross rolls is independent of the wavelength of the original rolls in a way that as the cross rolls grow, the original ones decay and finally disappear. Figure 1.8 illustrates the experimental results showing the development of cross rolls in the bulk of the original rolls [8].

The oscillatory instability, a short wavelength and a transverse instability, has been observed in experiments with a layer of mercury by Rossby in 1969 [32] and the transverse structure on each roll is observed to propagate along the length of the roll due to this instability. Therefore, from the phenomenological point of view the oscillatory instability of rolls resembles a wave propagating along a rope [24].

Skew-Varicose Instability

The skew-varicose instability is an important predominant instability at Prandtl numbers of the order of unity or smaller and it tends to distort the roll pattern; the skew-varicose mechanism causes a periodic thickening and thinning of the rolls and the resulting bulges are tilted towards the roll axis, so the patterns exhibit a skewed appearance. As the unstable modes grow, pinches are formed that cause the elimination of a roll and associated counter roll from the pattern [33] causing a shift towards larger wavelengths [6]. The tendency of the instability mechanism is to eliminate large wavenumber rolls in favour of small wavenumber rolls. A good example describing the evolution of skew-varicose instability is shown in figure 1.9. The instability starts with wavy distortion (shown in planform 1) of the originally uniform roll pattern. These disturbances grow to form cells in the form of short rolls with large wavelength and then evolve into defects which travel along the roll axis to the boundaries, destroying one or two roll pairs; in complex pattens these defects are known to play a crucial role in determining the dynamics and the structure of the pattern. Thus the skew-varicose instability does not correspond to a transition to a qualitatively new kind of convection pattern, but instead transforms one pattern into another one with a stable wavenumber. This decrease of the wavenumber of convection caused by the skew-varicose instability is more pronounced at lower Prandtl numbers [25].

The skew-varicose instability disappears both for large and very small Prandtl numbers

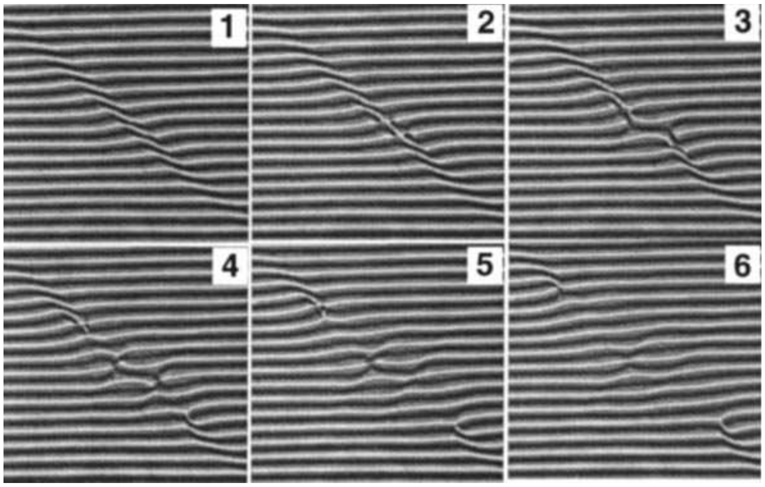

Figure 1.9: *Time evolution of the skew-varicose instability at* $\epsilon = 2.26$ *(*ϵ*, the reduced Rayleigh number, is given by* $\epsilon = (R - R_c)/R_c$*))* $Pr = 1.07$ *[about* $(183t_v)$ *after* ϵ *was increased from* 2.23*]. Pictures are spaced* $0.54t_v$ *apart* [8] *(*t_v *is the vertical diffusion time). Evolution from the pattern of convection rolls which are distorted by the skew-varicose instability is to a state with a few defects.*

and therefore is thought to originate from the combined effect of the momentum and heat advection terms in the basic equations [25]. Clever & Busse in 1978 and 1979 performed a detailed comparison of the theoretical description with experimental observation of the skew-varicose instability for moderate Prandtl numbers [25, 33]. For free-free boundaries, Zippelius & Siggia [34] and Busse & Bolton [26, 35] found that the parallel roll state is unstable against the skew-varicose instability immediately above onset if $Pr < 0.543$.

The theoretical analysis proceeded by obtaining two-dimensional steady solutions, which correspond to the convection rolls and imposing perturbations of arbitrary three-dimensional form on the steady solution. In the stability analysis these infinitesimal disturbances required the introduction of two additional wavenumber parameters along and perpendicular to roll axis [36]. The skew-varicose instability is characterized by a finite ratio between wavenumbers along and perpendicular to the roll axis. The critical Rayleigh number for the onset of the skew-varicose instability corresponds to disturbances for which both these wavenumbers tend to zero. The SVI has been difficult to capture due to the lack of consistent scaling for these disturbances and system parameters. Also that its growth rate, which is relatively low in the neighbourhood of this critical Ra, increases only quadratically, as the Ra exceeds the critical value [37]. Owing to these difficulties, a new technique is needed to capture whole of the SVI. In this thesis we attempt to address this question by developing a method to investigate the SVI using a reduced model of convection (for models of convection see section 1.3).

It is believed that the SVI plays a role in the formation of complex patterns such as Spiral Defect Chaos (see section 1.3.1), which occurs in low Pr convection. However, because the understanding of the SVI is not yet forthcoming, the question about this relation remain unanswered. In next section we describe some complex patterns that are exhibited by RBC and depend on the Prandtl number.

1.2.3 Complex Patterns: Spiral Defect Chaos

When the Rayleigh number is increased, convection rolls may become disordered and exhibit complex patterns. The characterization of these complex time-dependent patterns remains a challenge in the experimental investigation of pattern dynamics. As a result of the substantial progress in experiments of RBC, Morris *et al.* in 1993 [38] discovered the novel state, Spiral Defect Chaos (SDC), in large-aspect ratio systems. This SDC pattern is irregular in time and space, but it maintains a relatively simple structure in the vertical direction. The SDC state is characterized by rotating spirals, dislocations, disclinations and patches of rolls. The experiments of Ahlers in 1998 [39] have provided evidence that SDC is an intrinsic state of RBC for fluids with $Pr \approx 1$ and it has been observed using several pure gases with Prandtl numbers near one, including SF_6 [40, 41],

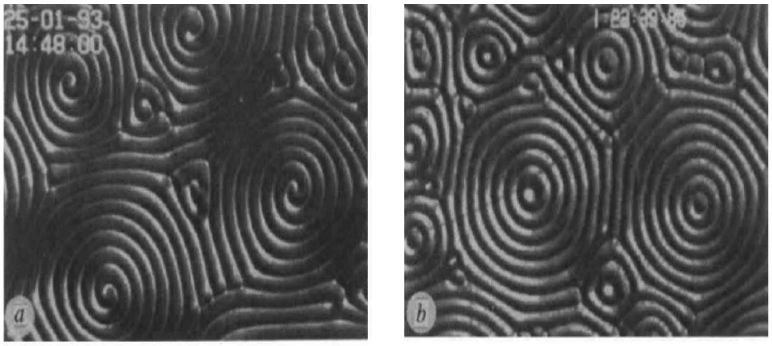

Figure 1.10: *Examples of shadowgraph images of the patterns seen in a fraction of the cell near the center of Rayleigh–Bénard convection in SF_6 near its gas-liquid critical point [9]. Spirals and Targets depend on the Prandtl number, Pr. (a) Spirals with $Pr = 3.3$, $Ra = 6217.12$ (b) Targets with $Pr = 6.6$, $Ra = 6200.04$. The horizontal size of each frame is $\approx 4.5mm$.*

N_2 [42] and Ar [41], gas mixtures [41], which have smaller Prandtl numbers than pure gases, and in liquid ^{4}He [43]where Pr is smaller than unity. Assenheimer and Steinberg in 1993 [9] found that SDC evolved into a state of target chaos when the Prandtl number is raised. The observation of SDC in large aspect ratio systems and in simulations with periodic boundary conditions [44] supports the conclusion that SDC is a generic state for low Pr and large aspect ratio convection which is not related to the detailed boundary conditions [45]. However, no conclusion has been made as to which of the many dynamic phenomena that occur at low Prandtl numbers [20] is responsible for the formation of spiral defect chaos.

Some examples of possible complex patterns, spirals and targets that can occur in RBC are shown in figure 1.10, which is taken from the work of by Assenheimer and Steinberg [9, 40]. In experiments using compressed SF_6 gas, they reported a continuous transition from SDC to target chaos when the Prandtl number was increased above approximately 4 by tuning the temperature and pressure near the critical point of the gas. The experimental results were described on the basis of full hydrodynamic equations for convection [11, 44, 45, 46]. Decker *et al.* [44] were able to reproduce SDC by a Galerkin truncation of standard three-dimensional Boussinesq equations. These numerical dynamics resembled the results of experiments [47].

SDC has attracted much theoretical attention because it was a completely unexpected state within the framework of straight-roll instabilities. Interestingly, the SDC state exists in a parameter regime for an infinitely extended system, where parallel straight rolls are stable [36]. Straight rolls only develop for initial conditions that are very close to the rolls whilst for most other initial conditions SDC is seen [48]. Inspired by this behaviour, several investigations have been performed to identify the onset of SDC. Liu and Ahlers in 1996 [41] originated investigations that were concerned with the onset of SDC. The influence of cell geometry on the onset of SDC is found to be weak; Hu *et al.* [49] used a circular box and Cakmur *et al.* [48] used a square box with same aspect ratio and their onset value of SDC was the same. However, the onset of SDC decreases as the domain gets larger and Li *et al.* in 1998 [50] predicted (without any justification) that this onset approaches to zero for as the domain size becomes large.

A quantitative understanding of SDC has not been achieved so far. However, several attempts have taken place in characterizing this state and the following facts have been considered: statistics of spiral and defect populations [51], the distributions of local roll properties such as the wavenumber [52], the mechanisms for the generation of chaos from spatial disorder [53]; the wavenumber selection mechanism for spirals [10, 54, 55]; and the conditions under which spiral defect chaos transitions to other states. Ecke *et al.* in 1995 [51] experimentally determined the time dependence with the number of spirals of the SDC state and their results suggested that at any instant, the probability distribution of spirals is fit by a Poisson distribution. Hu *et al.* [49] computed local wavenumbers and curvatures in experimental pictures and proposed order parameters to describe transitions in spatiotemporal chaos in Rayleigh–Bénard Convection. In order to characterize the statistical structure of SDC, Morris *et al.* [45] analyzed series of shadowgraph images of SDC and constructed the three dimensional structure-factor (the modulus squared of the Fourier transform of the space-time shadowgraph data). Egolf *et al.* [52] found the characteristic feature of SDC that the average wavenumbers, as determined by local measurements in physical space, are in the middle of the stability region for rolls; the distribution of local wavenumber includes the skew-varicose and the CR instabilities; this indicates that the Busse Balloon applies locally in disordered SDC patterns [52]. In SDC, to identify spirals and to measure their characteristics, Riecke *et al.* [10] analysed SDC based on direct numerical simulations of the Boussinesq equations employing a pseudospectral code, and they suggested an approach that allows the extraction of the spiral tip, the size of the spiral as measured using the spiral arm length and the winding number. They evaluated spiral features of SDC state and their dependence on Ra and Pr. Figure 1.11 illustrates some of their results: figure 1.11(a) (defect state) and 1.11(b) (SDC) show snapshots of the temperature field in the mid plane of the convection cell for $Pr = 1.5$ with reduced Rayleigh numbers $\epsilon = 0.7$ and 1 respectively; the reduced Rayleigh number $\epsilon = (R - R_c)/R_c$ with $R_c = 1708$. Their results suggest that at $Pr = 1.5$, $\epsilon = 0.7$ is close to the onset of spiral defect chaos. Figure 1.11(c) shows the dependence of the mean number (average of mean of black and white components) of closed contours on ϵ for three different Prandtl numbers. The number of closed contours increases with increasing ϵ and decreasing Pr. This has been found to be consistent with the fact that the driving force of spiral defect chaos is a large-scale flow, which is driven by the curvature of the convection rolls.

Many fundamental aspects of patterns and their instabilities have been addressed precisely over the past three decades in the context of Rayleigh–Bénard Convection [47].

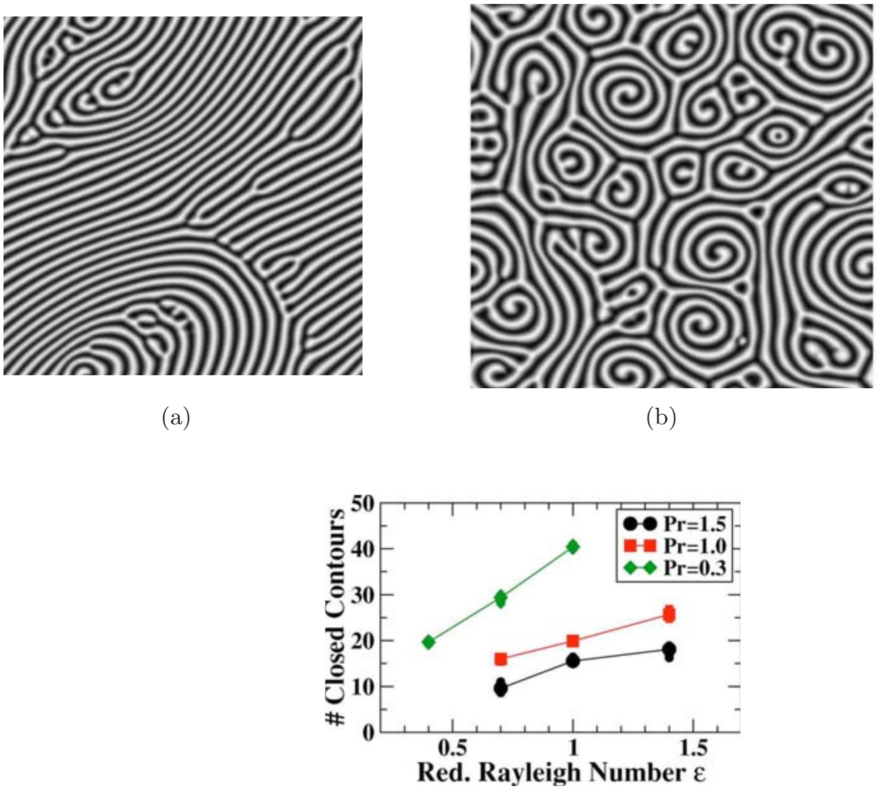

(a) (b)

(c)

Figure 1.11: *Results based on direct numerical simulations of the Boussinesq equations: (a) Snapshot of a typical convection pattern for* $Pr = 1.5$ *and* $\epsilon = 0.7$*. (b) Snapshot of SDC state at* $\epsilon = 1$ *for* $Pr = 1.5$*. The system size is* $L = 64.9$*. The spiral defect chaos planform is characterized by a disordered collection of spirals rotating in both directions and co-existing with dynamical defects such as grain boundaries and dislocations. Dark regions correspond to cold sinking fluid, light regions to hot rising fluid. (c) Mean number of closed contours (mean of white and black components of closed contours that enclose up and down flow regions) as a function of* ϵ *for different values of* Pr *[10].*

However, there is still little theoretical understanding of why the SDC state develops and its dynamic behaviour; the important questions such as which of the stable states will be selected by the physical system? What is the onset of chaotic state, such as spiral defect chaos? are still open.

1.2.4 Mean flow field

In convection, a mean flow is induced by distortions of the convective rolls [56]. Mean flow is the name given to the component of the velocity field with a non-zero horizontal mean over the depth of the system; it is generated by the differences of the structure of the convection rolls such as curvature, amplitude and wavenumber, and the mean flow in turn affects the roll structure [57]. The presence of a mean flow is an important phenomenon in low Prandtl number convection [58] and its magnitude is approximately inversely proportional to the Prandtl number [59]. Siggia and Zippelius in 1981 [60] found a particularly important theoretical result, which motivated much of the work during 1990s, that for a fluid of $Pr = 1$, roll curvature induces slowly varying long-range pressure gradients that drive a mean flow that affects with the roll curvature. Manneville in 1983 [56] described how mean flow is induced by distortions of the convective rolls. Indeed, it was shown experimentally by Daviaud & Pocheau [61] that suppression of the mean flow dramatically reduces the roll curvature. Studies of mean flow are not straightforward in experiments, mainly because mean flow is difficult to measure in an experimental setup and therefore the direct numerical simulations are particularly valuable for the study of mean flow.

Mean flows are known to play an important role in the dynamics of spiral defect chaos: Assenheimer *et al.* established using experimental observations in Rayleigh–Bénard Convection that Spiral Defect Chaos occurs most readily at low Prandtl numbers [9, 40]. Mean flows are stronger at low Prandtl numbers [58, 60], suggesting that SDC is an effect of the mean flow [45]. In the absence of the mean flow, SDC is found numerically to collapse to a stationary pattern of rolls with angular bends, again suggesting that Spiral Defect Chaos is an effect of the mean flow [38]. Cross in 1996 [54] found by numerical simulations that the mean flow is localised where curvature is high in SDC pattern such as the cores of spirals and also in patterns with defects. Although the mean flow is weak it

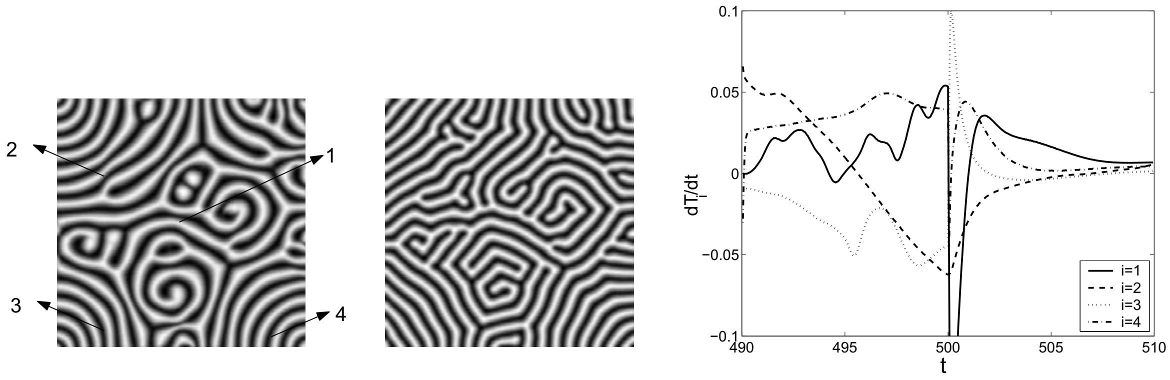

(a) (b)

Figure 1.12: *(a) An example of spiral defect chaos observed in a numerical simulation of Boussinesq equations. The mid-plane temperature field is plotted. For parameters* $\epsilon = 1$ *and* $Pr = 1$ *in a square cell with aspect ratio 20. Dark regions correspond to cold sinking fluid, light regions to hot rising fluid. Left-SDC state at time* $t = 500$*. The labels* $1-4$ *are discussed in (b). Right-At time* $t = 510$ *after the quenching has been introduced at* $t = 500$ *(this quenching has done by constructing a modified velocity field that does not have any mean flow). When mean flow is quenched, spiral defect chaos collapses to a stationary pattern of textures of stripes with angular bends. (b) The rate of change of the temperature field with time for the four locations of left planform of (a). Before the quenching,* $t < 500$*, the derivative fluctuates and differs from zero. After quenching,* $t > 500$*, it approaches zero that the pattern is approaching stationarity [11].*

can have a significant effect upon the dynamics and stability boundaries of the flow field. The effect of mean-drift flows depress the onset of the skewed-varicose (SV) instability [49].

Chiam *et al.* in 2003 [11] described direct numerical simulation of Rayleigh–Bénard Convection, showing that spiral defect chaos is indeed a consequence of the presence of mean flow. They verified that in the absence of a mean flow, spiral defect chaotic states are replaced by states whose statistical properties differ from those of spiral defect chaos. Figure 1.12 illustrates their results, observed in numerical simulation of RBC for parameters $\epsilon = 1$ and $Pr = 1$. Figure 1.12(a) shows when the mean flow is quenched, the SDC state (left) is replaced by a state in which rolls are straightened out, and have developed angular bends (right). Figure 1.12(b) shows the time series before and after mean flow is quenched, the rate of change of temperature at several locations, suggesting that a stationary pattern is being approached with loss of mean flow.

1.3 Models of convection

In this section we introduce specific models that have been developed to understand convection. The three-dimensional hydrodynamic equations are too complicated to analyze conveniently. Therefore several 2-dimensional phenomenological models have been introduced; these lead to the correct amplitude equations near threshold and can be solved in the nonlinear regime. The derivation of these models relies on the fact that vertical spatial variations of the patterns remain quite smooth even when these patterns show complex space and time dependence, and so projections of the three-dimensional hydrodynamic description onto the two-dimensional horizontal plane provides a reliable description of the fluid's behaviour.

The Swift–Hohenberg Equation (SHE) [62] was obtained by a semi-rigorous elimination of the vertical dependence through a Galerkin expansion of the thermo-hydrodynamic fields in the stress-free case. It describes the evolution of a real scalar field $\psi(x, y, t)$ that mimics the convection [62, 63]:

$$\partial_t \psi = \epsilon\psi - (1 + \nabla^2)^2\psi - \psi^3, \tag{1.2}$$

where ϵ is the driving parameter and the bifurcation to stripe pattern (rolls in convection correspond to stripes in the SHE) occurs with critical wavenumber unity. The nonlinear term ψ^3 is used as an approximation of a nonlocal integral term. However, different nonlinearities have been incorporated in the SHE and none of them can be derived rigorously, but some are better at reproducing the Busse Balloon than others. The SHE has a Lyapunov function and the persistent dynamic, periodic or chaotic is not possible. Also the stability diagram is qualitatively different from the Busse Balloon and, in particularly the skew-varicose instability is absent. Therefore the SHE fails to model medium to low Prandtl number convection even qualitatively and so generalizations have been developed to remove these imperfections [56, 64].

The importance of the mean flow in reduced models of convection was discovered by Siggia and Zippelius [60] in their study of the amplitude equation for free-slip convection. Following the analysis of importance of long-wavelength vertical vorticity or mean drift effects by Siggia and Zippelius [56, 57, 60], coupling to mean flow was incorporated in a generalization of SHE. Manneville in 1983 [56] and Greenside and Cross in 1985 [64] added the mean flow phenomenologically by replacing $\partial_t\psi$ by $\partial_t\psi+(\mathbf{U}\cdot\nabla)\psi$ with $\mathbf{U}=\left(\frac{\partial\zeta}{\partial y},-\frac{\partial\zeta}{\partial x}\right)$, where ζ is a stream function for the mean flow $\mathbf{U}$. The generalizations differ in how the mean vertical vorticity $\omega=-\nabla^2\zeta$ is generated.

Manneville's [56] model includes the mean flow for the case of stress-free boundary conditions, and introduces a second PDE that describes the evolution of the stream-function for the large scale mean flow $\mathbf{U}$:

$$\left.\begin{aligned}\partial_t\psi+(\mathbf{U}\cdot\nabla)\psi &= \epsilon\psi-(1+\nabla^2)^2\psi-g_1\psi^3-g_3\psi|\nabla\psi|^2\\ (\partial_t-Pr\nabla^2)\nabla^2\zeta &= g_m\left[\nabla(\nabla^2\psi)\times\nabla\psi\right]\cdot\widehat{\mathbf{z}},\end{aligned}\right\}\tag{1.3}$$

where g_m is the coupling constant to the mean flow. g_1 and g_3 are parameters controlling the strength of the nonlinearities and the term $-Pr\nabla^2$ serves to reduce the importance of higher-wavenumber modes in the vorticity field.

To extend the model for the no-slip boundary convection he suggested a modified second PDE;

$$\left(\partial_t-Pr(\nabla^2+\tilde{c})\right)\nabla^2\zeta=g_m\mathcal{F}\left[\nabla(\nabla^2\psi)\times\nabla\psi\right]\cdot\widehat{\mathbf{z}},$$

where $\tilde{c}$, which is negative, is used to switch between stress free and no-slip boundary conditions. In the absence of forcing, ζ tends to a constant whereas $\nabla^2\zeta$ becomes a constant otherwise. Bestehorn *et al.* in 1990 [65] suggested that the selection $g_1 = g_3 = 1$ gives a better description of fluid nonlinearities and in 1993 [66] they solved this model numerically and showed that the mean flow accounts for the deformation of straight convection rolls to spirals. Li, Xi and Gunton in 1996 [67] studied the dynamic properties of spirals using this model.

Greenside & Cross in 1985 [64] suggested two models where the time derivatives of the vorticity field do not enter:

$$\left.\begin{aligned} \partial_t\psi + (\mathbf{U}\cdot\nabla)\psi &= \epsilon\psi - (1+\nabla^2)^2\psi - a\psi^3 - b\psi|\nabla\psi|^2 + c\psi^2\nabla^2\psi \\ \nabla^2\zeta &= g\mathcal{F}\left[\nabla(\nabla^2\psi)\times\nabla\psi\right]\cdot\widehat{\mathbf{z}} \end{aligned}\right\} \tag{1.4}$$

and [68]

$$\left.\begin{aligned} \partial_t\psi + (\mathbf{U}\cdot\nabla)\psi &= \epsilon\psi - (1+\nabla^2)^2\psi + d\nabla^2\psi|\nabla\psi|^2 \\ \nabla^2\zeta &= g\mathcal{F}\left[\nabla(\nabla^2\psi)\times\nabla\psi\right]\cdot\widehat{\mathbf{z}}. \end{aligned}\right\} \tag{1.5}$$

Here g is a coupling constant and a, b, c, d are constants that control the nonlinearities. The filtering operator, $\mathcal{F}$ is an artificial Gaussian filter included in order to remove the short-wavelengths from the mean flow vorticity and it was first included in two dimensional models by Greenside & Cross [64]. They performed stability analysis of stripes for both models, using $a = 1$, $b = c = 0$ in the first model and $d = 3$ in the second and suggested the second model with $d = 3$ as an optimal choice among other models, as the stability diagram of this closely approximates the Busse Balloon; They found that the skew-varicose instability is encountered for $g \neq 0$.

Xi *et al.* in 1993 [69] described an important insight into the mechanism of spiral-defect chaos (SDC) using the model:

$$\left.\begin{aligned} \partial_t\psi + (\mathbf{U}\cdot\nabla)\psi &= \epsilon\psi - (1+\nabla^2)^2\psi - \psi^3 - g_2\psi^2 \\ (\partial_t - Pr(\nabla^2 - c^2))\nabla^2\zeta &= g_m\mathcal{F}\left[\nabla(\nabla^2\psi)\times\nabla\psi\right]\cdot\widehat{\mathbf{z}}. \end{aligned}\right\} \tag{1.6}$$

In this model, $g_2 = 0$ allows the Boussinesq symmetry $\psi \to -\psi$. However, since the higher-order derivative terms are omitted, the Busse Balloon is in general not described correctly by this model [70].

Due to coupling to the mean flow, these GSH models do not have a Lyapunov function, which opens the possibility for complex spatio-temporal behaviour. These models of Rayleigh–Bénard convection have been used in the study of different spatiotemporal chaotic states that produce in convection. In this work we consider two representative models, which are referred in the following work as the generalized Swift–Hohenberg (GSH) models: the first model contains PDEs (1.6), with $g_2 = 0$ and the second model contains PDEs (1.4), with with constants $a = 1$ and $b = c = 0$. In order to avoid the complexity, we include only the cubic nonlinearity. We choose these two models to represent two different behaviours to the dynamics of the vorticity field: one model has time derivative of the vorticity field and a parameter that controls the boundary conditions whereas they do not enter in the other model.

1.3.1 Spiral Defect Chaos

The hypothesis of the importance of the mean flow field to SDC led investigations to explore the dynamics of SDC in these generalized Swift–Hohenberg model equations. Xi *et al.* in 1993 [71] claimed that spirals are obtained with the quadratic nonlinearities, but Bestehorn *et al.* in 1994 [72] showed it is not the quadratic nonlinearity that leads to the formation of spirals. Instead, it is the nonvariational terms, such as terms describing mean flow effects, that are responsible for the formation of spirals.

SDC was found numerically in solutions of the several generalized Swift–Hohenberg models in the early 1990's [69, 73]. When the coupling to the mean flow is large, Spiral Defect Chaos is observed [50, 74, 75]. Xi *et al.* in 1993 [69] showed that the large aspect ratio and low Pr also play a crucial role in the spontaneous formation of SDC state.

Thus the generalizations of the SHE to include mean flows have become pivotal in understanding SDC. Numerical solutions of GSH models not only reproduce SDC but also resemble experimental results reasonably well [69], reproducing some qualitative features of Spiral Defect Chaos. However, Schmitz *et al.* in 2002 [76] claimed that the SDC state may not persist in long time dynamics and hence the direct comparison between the models and convection may not be appropriate.

1.3.2 Parameter Selection

It is not possible to achieve a quantitative match with the Boussinesq equations and experiments by adjusting the model parameters in (1.3)-(1.6). In this section we discuss qualitatively appropriate choices of parameter values for model (1.6) taking only cubic nonlinearity, $-\psi^3$ (with $g_2 = 0$). For the standard description of the Boussinesq equations only two non-dimensionalized control parameters are available; Ra and Pr. The value of Pr varies widely for different experimental fluids, from $\mathcal{O}(10^{-2})$ for liquid metals to values close to one for gases and for liquid Helium, and to $2 < Pr < 12$ for water, and into the thousands for silicone oil [77]. For pure gases away from the critical point, the value of the Prandtl number is $Pr \approx 1$; for SF_6 [40, 41], N_2 [42] and Ar [41] and CO_2, the Prandtl number is in the range $0.85 < Pr < 0.98$ [49]. However, compressed gases have the advantage that it is possible to tune the Prandtl number in several ways, for example, by changing layer heights. Therefore the experimentally accessible range is $0.17 < Pr < 115$.

Assenheimer and Steinberg [9, 40] conducted experiments near the critical point of SF_6, and were able to cover the Prandtl number range $2 < Pr < 115$. In another experiment, Liu *et al.* [41] used gas mixtures such as $He-SF_6$, $He-CO_2$, and $Ne-Ar$, that cover the range $0.3 < Pr < 0.8$. Smaller values of Pr can be achieved by mixing two gases, one with a large and the other with a small atomic or molecular weight [78]. A readily available example is a mixture of H_2 and Xe where the Prandtl number 0.16 can be reached.

The stress parameter is supposed to mimic the role of the reduced Rayleigh number, $\epsilon = (R - R_c)/R_c$. The models involve two more parameters: g_m, the strength of the coupling to the mean flow and c, a parameter related to the choice of boundary conditions on the bottom and top plates of a three-dimensional convection system. In the derivation by Manneville [56], c emerges as part of the expansion and averaging procedures used when starting from the Boussinesq equations. This model was first derived for the stress free condition, where it was found that $c = 0$. For no-slip boundary condition, the precise numerical value of c depends upon the approximation process as well as the manner in which the averaging is done in the vertical direction [79]. However a precise estimation for values of parameters c and g_m has not been performed in literature; and different values have been used by different authors: $c^2 = 2$ [69, 74, 76] or 10 [80]. Usually, g_m is taken to be 50. However, Decker & Pesch [44] claim that the strength of the coupling to mean flow in these models is overestimated by a factor of about 4 and they suggested (without providing any derivation) that the value of g_m can be calculated from results in Manneville and Piquemal in 1983 [81].

The estimation of parameter values in models that link with the experiments and results of hydrodynamics equations is not straightforward since the approximations applied in deriving the GSH from hydrodynamics equations are not systematic. However, based on the fact that the amplitude equations for the GSH and the full hydrodynamics equations are the same at leading order near onset, several attempts have been made to establish relations between convection parameters and parameter values in the GSH model. For example, the GSH model 1 (model (1.6) with $g_2 = 0$), is:

$$\left.\begin{aligned} \tau_0[\partial_t'\psi' + (\mathbf{U}'\cdot\nabla')\psi'] &= \epsilon'\psi' - (\xi_0/2K_c)^2(K_c+\nabla'^2)^2\psi' - g_1'\psi'^3 \\ (\partial_t' - Pr'(\nabla'^2 - c'^2))\nabla'^2\zeta' &= g_m'\mathcal{F}\left[\nabla'(\nabla'^2\psi')\times\nabla'\psi'\right]\cdot\widehat{\mathbf{z}}. \end{aligned}\right\}. \tag{1.7}$$

where K_c is the critical wavenumber at onset, g_1' is the parameter that controls the cubic nonlinearity, and the other parameters model the properties of the system. Cross [82] and Zippelius and Siggia [34] in their derivation of the amplitude equations from the Boussinesq equations, have stated expressions for the parameters τ_0, ξ_0 and g_1' in terms of Pr for both stress-free and rigid boundary convection. Xi *et al.* [83] used these expressions to approximate parameter values for the experiments on CO_2 by Bodenschatz in 1991 [84]. However, they have not given clear evidence for the choice of values for g_m' and c'. They introduced appropriate scalings, including $g_m \rightarrow (4\tau_0^2K_c^2g_m'/g_1'\xi_0^2)$, $Pr \rightarrow (4\tau_0/\xi_0^2)Pr'$, $\epsilon \rightarrow (4/K_c^2\xi_0^2)\epsilon'$ and $c^2 \rightarrow c'^2/K_c^2$, to derive the dimensionless form:

$$\left.\begin{aligned} \partial_t\psi + (\mathbf{U}\cdot\nabla)\psi &= \epsilon\psi - (1+\nabla^2)^2\psi - \psi^3 \\ (\partial_t - Pr(\nabla^2 - c^2))\nabla^2\zeta &= g_m\mathcal{F}\left[\nabla(\nabla^2\psi)\times\nabla\psi\right]\cdot\widehat{\mathbf{z}}, \end{aligned}\right\}. \tag{1.8}$$

and calculated corresponding parameter values for g_m, Pr and c. However there derivations were for non-Boussinesq approximations: they included the quadratic nonlinearity, $-g_2\psi^2$. Hence, in the situation of SDC, their calculation of parameter values is not suitable for the Boussinesq fluids. Li, Xi and Gunton in 1997 [85] attempted to describe the parameter relation for SDC state with Boussinesq approximations. They used the expressions for τ_0, ξ_0 and ${g_1}'$ defined by Cross [82]. In order to calculate g_m' and c', they supplemented the solutions, presented by Cross [82]. The values of these parameters are found to be dependent on the boundary conditions,

for stress-free boundary conditions : $g'_m = 6$, $c' = 0$, $\xi_0^2 = 8/3\pi^2$, $\tau_0 = 2\frac{1+\frac{1}{Pr'}}{3\pi^2}$;

for no-slip boundary conditions: $g'_m = 24.77$, $c'^2 = \pi^2$, $\xi_0^2 = 0.148$, $\tau_0 = \frac{1+0.5117\frac{1}{Pr'}}{19.65}$.

Hence $c^2 = 2$ for scaled model with no-slip boundary conditions. In order to get g_m from g'_m, the value of g'_1, the coefficient of the cubic nonlinearity, should be suitably chosen using the work presented by Cross [82] and Li, Xi and Gunton [85] claimed it as $g_m = 50$.

1.3.3 Advantages and criticisms of GSH models

Recent advances in parallel computers and data storage have allowed the direct numerical simulations that allow for the efficient integration of the Boussinesq equations with realistic boundary conditions in large domains, although the computational cost remains very high [86]. The GSH models are computationally much less expensive to integrate than the Boussinesq equations and hence have the advantage of allowing large scale numerical simulations that help to understand features of SDC. Although GSH models can not be derived systematically from the Boussinesq equations, they capture much of the experimentally observed physical behaviour and have been useful when qualitative, and not quantitative, comparisons between theory and experiment are needed quickly.

However, there are several limitations to Swift–Hohenberg modelling, primarily, the models describe the spatiotemporal behaviour of a field in two dimensions, whereas convection is a three-dimensional phenomenon. Moreover, the generalizations of Swift–Hohenberg equation produce spiral defect chaos only as a transient for some system parameter values, whereas in experiments, spiral defect chaos is known to persist for much longer times [76] and this could be because the small-scale features of the depth averaged vorticity at the cores of the spirals are not precisely captured by these Swift–Hohenberg models [47].

In addition, in many GSH models, the stability balloon is dissimilar to the correct one. However, Greenside and Cross argued that their model (1.5) with $d = 3$ and $g = 10$, corresponding roughly to $Pr = 0.7$ in convection [20], resembles very closely the fluid stability diagram, the Busse Balloon. However, this model neglects the intrinsic dynamics of the vorticity field and as a result, the oscillatory instability is absent. The filtering operator in their models effectively eliminates the more serious unphysical short-wavelength cross-roll instability that could render a large region of rolls to be unstable.

1.4 Thesis Outline

In this chapter we discussed some of the investigations that have been performed on the Rayleigh–Bénard Convection, focussing on the skew-varicose instability and the Spiral Defect Chaos state. We also discussed the models of convection, generalizations of Swift–Hohenberg equation and their connection to the original fluid equations. In the chapters that follow, two of the generalizations of Swift–Hohenberg equations [56, 64, 69, 87] including the effect of mean flow are investigated. The skew-varicose instability and its relation to the parameter regimes, in which the system exhibits Spiral Defect Chaos will be the main concerns of this thesis.

In Chapter 2, we perform a linear stability analysis of the two sets of model equations in order to investigate the long wave-length instabilities (including the SVI) and how they depend on the parameters in the models. The novelty we apply here is the use of a projection operator, which acts as a filter in Fourier space and allows an exact stripe solution with wavenumber close to the critical wavenumber. We then carry out a linear stability analysis of the stripe solution and investigate the growth rate of perturbations corresponding to Eckhaus, zigzag, the skew-varicose, oscillatory and cross-roll instabilities including the effect of two different boundary conditions, stress-free and no-slip, establishing the agreement of stability calculations of the SVI with PDE solutions of models. We also establish a relation between two models of interest.

The analytical expressions obtained for the Jacobian matrices are quite complex, not allowing explicit expressions for the eigenvalues for all cases. Hence in chapter 3, we use numerical continuation in order to derive the complete stability diagram for the models. The stability boundaries are computed for a range of system parameters and are presented graphically.

In chapter 4, we perform a truncation of the model PDEs onto three or five modes, chosen to focus on the nonlinear development of the SVI, and carry out a bifurcation analysis of the resulting ODEs using center manifold reduction and numerical path following. We choose a set of parameters involved in the GSH models and present bifurcation diagrams for the transition of the stripes to the skew-varicose phenomena. We establish our results. We also focus on establishing results with direct simulations of the PDEs. The dynamics of Spiral Defect Chaos is exceedingly complex and it is known to exist in the region where rolls are stable. One ambitious goal of chapter 5 is to gain a better understanding of the dynamics of Spiral Defect Chaos, addressing questions associated with it such as its connection with the SVI, the onset of SDC and its dependence with system parameters, whether the SDC state is a transient in the model equations, and a statistical evaluation of local roll properties such as the wavenumber.

Finally, in Chapter 6, we present conclusions to the results from all the chapters and propose some suggestions for future work.

Chapter 2

Generalizations of the two dimensional Swift–Hohenberg Equation: long-wavelength instabilities

2.1 Introduction

In this chapter, we study two generalized Swift–Hohenberg models that include a coupling to the mean flow [56, 64, 69, 87]. We perform a linear stability analysis to investigate long wave-length instabilities and how they depend on the parameters in the models. In particular, we consider different behaviours of the skew-varicose instability (SVI), for which we derive stability boundaries. We further extend our analysis to study the SVI behaviour for different boundary conditions.

The Swift–Hohenberg equation, as a model of convection near onset, has a major drawback as a model of low-viscosity convection: mean flows are excluded. The importance of the large scale mean flow on the stability of convection rolls was first investigated by Siggia and Zippelius [60]. Mean flows are also known to play an important role in the dynamics of spiral defect chaos [11]. Motivated by the strong impact of mean flows on spiral defect chaos, we study two related generalizations of the SHE, which have been developed to include the effects of mean flows [69, 87].

Including mean flows in these models allows an interesting long-wavelength instability, the skew-varicose instability (SVI) [6], which resembles the Eckhaus instability but the most unstable modes are those at an angle to the original roll axes. In the SVI, rolls bend and become irregular in order to decrease their effective wavenumber, and often dislocation pairs form [20]. Indeed, chaotic spiral patterns have been observed during the transition from the conducting state to rolls. The onset of SDC and defect chaos has therefore been tentatively associated with the occurrence of the SVI [47, 88, 89]. It is this connection that motivates this detailed investigation into the SVI in this chapter .

An additional problem that occurs in the analysis of the SVI is that there is no consistent relative scaling of lengths parallel and perpendicular to the roll axes, owing to the singular nature of the slow length scale expansion of the stability problem, as detailed below.

Although the model equations of interest have been well studied, a complete analysis of the SVI in the models is not available. One difficulty in the analysis comes from the contribution of terms proportional to $k^2l^2/(k^2+l^2)$, where (k,l) is the small wavevector of the perturbations associated with the SVI. Terms like this are responsible for the absence of a consistent asymptotic scaling in the limit of small amplitude and small k and l [90]. This difficulty is resolved in this chapter.

The remaining part of this chapter is organized as follows: in section 2.2, we present the two generalizations of the Swift–Hohenberg equation, both of which incorporate the effect of a mean flow. We discuss two operators: $\mathcal{P}_\alpha$ is a projection operator included in the model to allow exact stripe solutions, and $\mathcal{F}_\gamma$ is a filtering operator that suppresses the cross-roll instability. $\mathcal{F}_\gamma$ is present in an original formulation of the models [64]; $\mathcal{P}_\alpha$ was suggested by Ian Melbourne [91]. We find a stable stripe solution in section 2.3 and in section 2.4, we present a detailed analysis of the linear stability of that stripe solution.

The structure of the maximum eigenvalue for instability for small k and l is also presented.

In section 2.5, we analyze the zigzag and Eckhaus long-wavelength instabilities. Section 2.6 shows how the SVI in no-slip boundary conditions can be located by means of the stability analysis. The work is extended to the asymptotic behaviour of the SVI boundary. In section 2.7 and 2.8 we consider stress-free boundary conditions for which the skew-varicose and the oscillatory skew-varicose instabilities co-exist. We illustrate the agreement between linear stability calculations of the SVI with solving the PDEs numerically in section 2.9. Our results are discussed in last section.

2.2 Description of Models

In this section, we set out the two models we will investigate, and discuss basic properties of the models. We start with the standard two-dimensional Swift–Hohenberg equation [62],

$$\frac{\partial \psi}{\partial t} = \left[\mu - (1+\nabla^2)^2\right]\psi - \psi^3, \tag{2.1}$$

where the real field $\psi(x, y, t)$ is a scalar function of t and the horizontal spatial coordinates and represents the pattern-forming field, for example, the vertical component of the velocity in the horizontal mid-plane of the convection cell. $\mu \in \Re$ is the driving parameter (in convection, μ represents the temperature difference between the top and the bottom layer), taking the value zero at the onset of pattern formation. The SHE is generalized by adding a term that models the coupling to the vertical vorticity. In both models, we introduce a $(\mathbf{U} \cdot \nabla)\,\psi$ term to the left-hand side of (2.1), where $\mathbf{U}(x, y, t)$ is a mean flow driven by pattern distortion. This mean flow is calculated from a stream function $\zeta(x, y, t)$:

$$\mathbf{U} = \left(\frac{\partial \zeta}{\partial y}, -\frac{\partial \zeta}{\partial x}\right).$$

Vertical vorticity $\omega(x, y, t) = -\nabla^2\zeta$. The way that vorticity is generated by nonlinear forcing from ψ differs in the two models.

2.2.1 Model 1

In the first model [69], the vertical vorticity $\omega(x, y, t)$ has its own independent dynamics:

$$\frac{\partial\psi}{\partial t} + (\mathbf{U}\cdot\nabla)\,\psi = \left[\mu - (1+\nabla^2)^2\right]\psi - \mathcal{P}_\alpha\left(\psi^3\right), \tag{2.2}$$

$$\left[\frac{\partial}{\partial t} - Pr(\nabla^2 - c^2)\right]\omega = -g_m\mathcal{F}_\gamma\left[\nabla(\nabla^2\psi)\times\nabla\psi\right]\cdot\widehat{\mathbf{z}}, \tag{2.3}$$

where Pr, c and g_m are parameters. The Prandtl number Pr (the ratio between kinematic viscosity and thermal diffusivity) is effectively a viscosity parameter for the mean flow, which plays a much greater role in low Prandtl number convection. Indeed, in the limit of large Pr, the vertical vorticity is hardly excited and the dynamics of ψ becomes purely relaxational [5, 20, 76], reducing model 1 back to the SHE. The coefficient g_m is a coupling parameter that controls the strength of the mean flow effects relative to the ordinary Swift–Hohenberg nonlinear term $-\psi^3$. The parameter c models the effect of top and bottom boundary conditions on the vertical vorticity, with $c \neq 0$ corresponding to more realistic no-slip boundary conditions. In this case, ω decays to zero in the absence of nonlinear forcing. The choice $c = 0$ corresponds to mathematically simpler stress-free boundary conditions. In this case ω = constant is an allowed solution of the linearised vorticity equation. The operators $\mathcal{P}_\alpha$ and $\mathcal{F}_\gamma$ are explained in more detail in section 2.2.3.

2.2.2 Model 2

The second model [56, 64, 87] has the vertical vorticity slaved to the nonlinear driving term:

$$\frac{\partial \psi}{\partial t} + (\mathbf{U} \cdot \nabla)\, \psi = \left[\mu - (1 + \nabla^2)^2\right] \psi - \mathcal{P}_\alpha \left(\psi^3\right), \tag{2.4}$$

$$\omega = -g\mathcal{F}_\gamma \left[\nabla(\nabla^2\psi) \times \nabla\psi\right] \cdot \widehat{\mathbf{z}}, \tag{2.5}$$

so the vertical vorticity responds instantly to the nonlinear driving. The parameter g is a non negative coupling parameter that controls the relative strength of mean flow effects compared to the ordinary nonlinearity. Large g corresponds to small Pr in model 1.

2.2.3 Basic properties of the models

The major novelty in this work is the introduction of the projection operator $\mathcal{P}_\alpha$ in both models to project amplitudes to a desired wavelength α. This projection acts as a filtering in Fourier space and is defined as

$$\mathcal{P}_\alpha(e^{i\mathbf{K}\cdot\mathbf{x}}) = \begin{cases} e^{i\mathbf{K}\cdot\mathbf{x}} & \text{if } |\mathbf{K}| \leq \alpha; \\ 0 & \text{if } |\mathbf{K}| > \alpha. \end{cases}$$

By setting $\alpha = 2.5$, we allow stripes with a single Fourier mode with wavenumber close to one to be exact solutions of the PDEs (2.2–2.3) and (2.4–2.5) [91]. We show in section (2.3), the consequences of the application of this projection operator to our models and the derivation of the stripe solution and the effect of α in selecting the wavenumber.

The other operator we use in both models is a filtering, $\mathcal{F}_\gamma$. This filtering operator eases the analysis by reducing the short-wavelength modulations of the mean flow [64]. Hence it ensures that the SVI is not pre-empted by other instabilities; in Fourier space, the operator is defined by

$$\mathcal{F}_\gamma(e^{i\mathbf{K}\cdot\mathbf{x}}) = e^{-\gamma^2|\mathbf{K}|^2} e^{i\mathbf{K}\cdot\mathbf{x}}.$$

Throughout this work, we set $\gamma = 2.5$, coincidentally same as α, in order to reduce short-wavelength instabilities effectively. This selection of γ does not disturb long-wavelength instabilities. The effect of this filtering on short-wavelength instabilities, particularly the cross-roll instability, is discussed in Chapter 3.

The two models can be related to each other close to onset, regardless of the projection and filtering. By scaling $\mu = \mathcal{O}\left(\epsilon^2\right)$ with $\epsilon \ll 1$, introducing a slow time scale $\partial/\partial t \to \epsilon^2 \partial/\partial t$, and assuming that the wavenumbers that are excited in the vorticity variable ω are of order $\mathcal{O}(\epsilon)$, the largest term on the left-hand side of the vorticity equation (2.3) in model 1 is $Pr\, c^2 \omega$. Thus model 1 reduces to model 2 in this limit, with the relation

$$g = g_m/(Pr\, c^2). \tag{2.6}$$

These models are not restricted to be variational as in the SHE and they are rotationally invariant. Mean flows are much stronger when the Prandtl number is small, following from (2.6); indeed for large Pr, the effect of nonlinear term in vorticity equation in model 1 is small and hence the effect of mean flows is small, reducing to the SHE.

2.3 Solution to the linearized equations

For model 1, linearisation yields:

$$\frac{\partial \psi}{\partial t} = \left[\mu - (1 + \nabla^2)^2\right] \psi \quad \text{and} \quad \frac{\partial \omega}{\partial t} = Pr\left(\nabla^2 - c^2\right) \omega \ ;$$

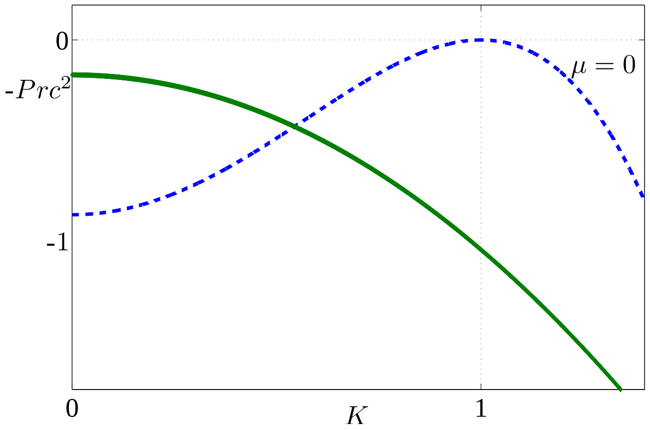

Figure 2.1: *Growth rates as functions of wavenumber* $K = |\mathbf{K}|$*. Blue curve:* σ_1 *for* $\mu = 0$*, which peaks at* $K = K_{critical} = 1$*. Green curve:* σ_2*, which takes the value* $-Pr\, c^2$ *at* $K = 0$ *and decreases as* K *increases.*

only the first equation is relevant to model 2. Normal mode solutions to these linear equations are given by $\psi = F_1 e^{\sigma_1 t + i\mathbf{K}\cdot\mathbf{x}}$ and $\omega = F_2 e^{\sigma_2 t + i\mathbf{K}\cdot\mathbf{x}}$, where σ_1 and σ_2 are growth rates, $\mathbf{K}$ is a wavevector, and F_1 and F_2 are constants. Substituting these into the linearized equations gives the dispersion relations, $\sigma_1 = \mu - \left(1 - K^2\right)^2$ and $\sigma_2 = -Pr\left(K^2 + c^2\right)$. These are shown in Figure 2.1 for $\mu = 0$, when the trivial solution is marginally stable. The most unstable wavenumber is $K_{critical} = 1$, and for $\mu > 0$, a band of wavenumbers close to $K = 1$ is linearly unstable, signalling the onset of pattern formation. The vorticity ω (in model 1) is always linearly damped, unless $c = 0$.

We define $q = K - K_{critical}$ and thus the trivial solution loses stability for any q at $\mu_{Existence}$, where

$$\mu_{Existence} = (1 - (1+q)^2)^2.$$

Note that as $q \to 0$, $\mu_{Existence} \sim 4q^2$.

In this chapter, we are interested in the stability of the nonlinear equilibrium stripe solution of the PDEs. We note that with the projection $P_{2.5}$

$$\psi_0 = \sqrt{\beta}\left(e^{i(1+q)x} + e^{-i(1+q)x}\right) \quad \text{and} \quad \omega_0 = 0 \quad \text{with} \quad \beta = \frac{\mu - (1-(1+q)^2)^2}{3}, \tag{2.7}$$

is an ***exact stripe solution*** of both models. This can be shown by substituting the expressions for ψ_0 and ω_0 into the PDEs (2.2) & (2.4). Models (1) and (2) with combination (2.7) results in:

$$\begin{aligned}0 = \mu\sqrt{\beta}\left(e^{i(1+q)x} + e^{-i(1+q)x}\right) - (1+\nabla^2)^2\left(\sqrt{\beta}\left(e^{i(1+q)x} \;\; + e^{-i(1+q)x}\right)\right)\\ -\mathcal{P}_\alpha\left[\left(\sqrt{\beta}\left(e^{i(1+q)x} + e^{-i(1+q)x}\right)\right)^3\right].\end{aligned} \tag{2.8}$$

The nonlinear term in the vorticity equation is zero. Next, we note that in this equation (2.8)

$$(1+\nabla^2)^2 e^{\pm i(1+q)x} = (1-(1+q)^2)^2 e^{\pm i(1+q)x}, \tag{2.9}$$

and

$$\begin{aligned}P_\alpha\left[\left(\sqrt{\beta}\left(e^{i(1+q)x} + e^{-i(1+q)x}\right)\right)^3\right] = P_\alpha\Big[3\beta\sqrt{\beta}\times\left(e^{i(1+q)x} + e^{-i(1+q)x}\right) + \beta\sqrt{\beta}\times\Big(e^{3i(1+q)x}\\ +e^{-3i(1+q)x}\Big)\Big].\end{aligned}$$

In order to retain the $e^{\pm i(1+q)x}$ terms and discard the $e^{\pm 3i(1+q)x}$ terms, we require $|3(1+q)| > \alpha$ and $|(1+q)| < \alpha$ with $\alpha = 2.5$ (for example). These inequalities result in $-0.167 < q < 1.5$, and for these values of q,

$$\mathcal{P}_{2.5}\left[\left(\sqrt{\beta}\left(e^{i(1+q)x} + e^{-i(1+q)x}\right)\right)^3\right] = 3\beta\sqrt{\beta}\times\left(e^{i(1+q)x} + e^{-i(1+q)x}\right), \tag{2.10}$$

provided that q is between -0.167 and 1.5.

Therefore, combining equations (2.9) and (2.10) with (2.8) and considering the components of $e^{\pm i(1+q)x}$, we find that with $\beta = \frac{\mu-(1-(1+q)^2)^2}{3}$, the two model PDEs are satisfied exactly, and so (ψ_0, ω_0) is an exact stripe solution with wavenumber close to unity. In the limit of small q, we have $\beta = (\mu - 4q^2)/3$, so stripe solutions exist when $\mu > 4q^2$.

The advantage of using the projection $\mathcal{P}_\alpha$ is that it allows this exact stripe solution with wavenumber close to unity of the PDEs [91]. The alternative would be to consider the limit of small μ and β. However, by obtaining an exact solution, which matches the asymptotic result we would obtain without the projection, we do not have to be concerned with the relative sizes of these parameters compared to other small parameters that will be introduced below.

2.4 Linear stability Analysis

The linear stability theory for stripes in the SHE is well known [90]: stripes with wavenumber $1+q$ (with $|q| \ll 1$) exist provided $\mu > 4q^2$, and they are stable with respect to the Eckhaus and zigzag instabilities provided $\mu > 12q^2$ and $q > 0$. Once mean flows are included, there is the additional SVI, and the zigzag instability needs to be modified at finite Prandtl number by the presence of mean-flow modes with non-zero vertical vorticity [34, 35]. The Eckhaus instability is unchanged. We consider the stability of stripe solutions with respect to long-wavelength perturbations, deriving three (model 1) or two (model 2) linear ODEs for the perturbation amplitudes, and so determine the parameter regions in which the stripe configuration is stable, as well as the boundary of the SVI.

2.4.1 Linearisation

We proceed by considering perturbations to the basic stripe solution. We suppose that the vorticity perturbation contains wavevectors (k, l) and $(-k, -l)$, where k is along the stripes and l is perpendicular to stripes. These interact with the wavevectors $(1+q,0)$ and $(-1-q,0)$ in the stripe solution to give four new wavevectors, $(1+q+k,l)$ and $(-1-q+k,l)$ and their conjugates. Having chosen particular modes, the perturbed solution can be written as ψ and ω, where

$$\psi = \psi_0 + \psi^{'} \quad \text{with} \quad \psi^{'} = A(t)e^{i(1+q+k,l)\cdot\mathbf{x}} + B(t)e^{i(-1-q+k,l)\cdot\mathbf{x}} + \bar{A}(t)e^{-i(1+q+k,l)\cdot\mathbf{x}} + \bar{B}(t)e^{i(1+q-k,-l)\cdot\mathbf{x}}, \tag{2.11}$$

$$\omega = \omega_0 + \omega^{'} \quad \text{with} \quad \omega_0 = 0 \quad \text{and} \quad \omega^{'} = C(t)e^{i(k,l)\cdot\mathbf{x}} + \bar{C}(t)e^{i(-k,-l)\cdot\mathbf{x}}, \tag{2.12}$$

provided A, B, $C \ll 1$.

We can calculate the stream function ζ from $\omega(x,y,t) = -\nabla^2\zeta$ by inverting the Laplacian, and hence obtain the mean flow:

$$\mathbf{U} = \frac{i}{k^2+l^2}\left(C(t)e^{i(k,l)\cdot\mathbf{x}} - \bar{C}(t)e^{-i(k,l)\cdot\mathbf{x}}\right)(l,-k)\ .$$

We first substitute the expressions above into the equations (2.2) & (2.4) in both models and linearize (assuming that A, B and C are small and therefore neglecting quadratic terms). Examining only the coefficients of $e^{i(1+q+k,l)\cdot\mathbf{x}}$ and $e^{i(-1-q+k,l)\cdot\mathbf{x}}$ we get on the LHS:

$$\frac{\partial[\psi' + \psi_0]}{\partial t} \quad : \quad \dot{A}(t)e^{i(1+q+k,l)\cdot\mathbf{x}} + \dot{B}(t)e^{i(-1-q+k,l)\cdot\mathbf{x}},$$

$$(\mathbf{U}\cdot\nabla)\left[\psi' + \psi_0\right] : \frac{iC(t)}{k^2+l^2}(l,-k)e^{i(k,l)\cdot\mathbf{x}}\cdot\left(i\sqrt{\beta}(1+q),0\right)(e^{i(1+q,0)\cdot\mathbf{x}} - e^{-i(1+q,0)\cdot\mathbf{x}}),$$

and on the RHS:

$$\left[\mu - (1+\nabla^2)^2\right]\left[\psi' + \psi_0\right] : [\mu - (1-(1+q+k)^2 - l^2)^2]\times(A(t)e^{i(1+q+k,l)\cdot\mathbf{x}} + B(t)e^{i(-1-q+k,l)\cdot\mathbf{x}}),$$

$$
\begin{aligned}
-\mathcal{P}_{2.5}[\psi' + \psi_0]^3 : \mathcal{P}_{2.5}[-3\beta(e^{i(1+q,0)\cdot\mathbf{x}} + e^{-i(1+q,0)\cdot\mathbf{x}})^2 \times (A(t)e^{i(1+q+k,l)\cdot\mathbf{x}} + B(t)e^{i(-1-q+k,l)\cdot\mathbf{x}})],\\
: \beta[-6A(t) - 3B(t)]e^{i(1+q+k,l)\cdot\mathbf{x}} + [-6B(t) - 3A(t)]e^{i(-1-q+k,l)\cdot\mathbf{x}}.
\end{aligned}
$$

We simplify this further and consider both sides separately for the components of $e^{i(1+q+k,l)\cdot\mathbf{x}}$ and $e^{i(-1-q+k,l)\cdot\mathbf{x}}$ would result in two linear ODEs for A and B:

$$
\dot{A} = \left(\mu - \left[1 - \left((1+q+k)^2 + l^2\right)\right]^2 - 6\beta\right) A - 3\beta B + \frac{l(1+q)\sqrt{\beta}}{k^2+l^2} C, \tag{2.13}
$$

$$
\dot{B} = \left(\mu - \left[1 - \left((-1-q+k)^2 + l^2\right)\right]^2 - 6\beta\right) B - 3\beta A - \frac{l(1+q)\sqrt{\beta}}{k^2+l^2} C\,. \tag{2.14}
$$

The term $k^2 + l^2$ that appears in the denominator of the governing equations for $\dot{A}$ and $\dot{B}$ arises from inverting the Laplacian when calculating ζ, and hence $\mathbf{U}$, in the linearisation of the $(\mathbf{U}\cdot\nabla)\,\psi$ term. This makes the analysis difficult in long wavelength limit.

We next substitute the expressions for ψ, ω and $\mathbf{U}$ into the vorticity equations of the models. Substituting into equation (2.3) and retaining only the coefficients of $e^{i(k,l)\cdot\mathbf{x}}$ on the LHS yields:

$$
\frac{\partial\omega'}{\partial t} - Pr(\nabla^2 - c^2)\omega' \quad = \quad [\dot{C(t)} - Pr\left(-(k^2+l^2) - c^2\right)C(t)]e^{i(k,l)\cdot\mathbf{x}},
$$

and on the RHS:

$$
\begin{aligned}
-g_m\mathcal{F}_\gamma\left[\nabla(\nabla^2[\psi'+\psi_0]) \times \nabla[\psi'+\psi_0]\right]\cdot\widehat{\mathbf{z}} = -g_m\mathcal{F}_\gamma\{i\sqrt{\beta}(1+q)^3(-e^{i(1+q,0)\cdot\mathbf{x}} + e^{-i(1+q,0)\cdot\mathbf{x}}),\\
-Al((1+q+k)^2+l^2)ie^{i(1+q+k,l)\cdot\mathbf{x}} - Bl((-1-q+k)^2+l^2)ie^{-i(-1-q+k,l)\cdot\mathbf{x}}\}\\
\times\{i\sqrt{\beta}(1+q)(e^{i(1+q,0)\cdot\mathbf{x}} - e^{-i(1+q,0)\cdot\mathbf{x}}), Alie^{i(1+q+k,l)\cdot\mathbf{x}} + Blie^{-i(-1-q+k,l)\cdot\mathbf{x}}\}\cdot\widehat{\mathbf{z}},
\end{aligned}
$$

which remains same with the replacement g_m by g, for the nonlinear term in the vorticity equation of the model 2.

In Fourier space, the effect of the filtering, $\mathcal{F}_\gamma$, is to reduce the amplitude of a Fourier component; for the function $e^{i(k,l)\cdot\mathbf{x}}$, $\mathcal{F}_\gamma$ reduces the amplitude by the multiplicative factor $e^{-\gamma^2(k^2+l^2)}$. Therefore we get,

$$\begin{aligned}\dot{C} = -Pr\left(k^2+l^2+c^2\right)C + \mathcal{F}_\gamma g_m l(1+q)\sqrt{\beta}\Big(\Big[-(1+q-k)^2 - l^2 + (1+q)^2\Big]B \\ + \Big[(1+q+k)^2 + l^2 - (1+q)^2\Big]A\Big),\end{aligned} \tag{2.15}$$

with $\mathcal{F}_\gamma$ taken to be equal to $e^{-\gamma^2(k^2+l^2)}$. The equation for C differs between the two models and in the model 2, with no intrinsic dynamics for ω, there is an algebraic relation between C, A and B:

$$C = \mathcal{F}_\gamma g l(1+q)\sqrt{\beta}\left(((1+q+k)^2 + l^2 - (1+q)^2)A + (-(1+q-k)^2 - l^2 + (1+q)^2)B\right). \tag{2.16}$$

Equations (2.13–2.15) for model 1 can be succinctly expressed as:

$$\begin{pmatrix}\dot{A}\\ \dot{B}\\ \dot{C}\end{pmatrix} = \begin{bmatrix} M_1 & M_2 & M_3\\ M_2 & M_4 & -M_3\\ g_m M_5 & g_m M_6 & M_7\end{bmatrix}\begin{pmatrix}A\\ B\\ C\end{pmatrix} = J_1\begin{pmatrix}A\\ B\\ C\end{pmatrix}. \tag{2.17}$$

Equations (2.13–2.14) and (2.16) for model 2 yield:

$$\begin{pmatrix}\dot{A}\\ \dot{B}\end{pmatrix} = \begin{bmatrix} M_1 + gM_3M_5 & M_2 + gM_3M_6\\ M_2 - gM_3M_5 & M_4 - gM_3M_6\end{bmatrix}\begin{pmatrix}A\\ B\end{pmatrix} = J_2\begin{pmatrix}A\\ B\end{pmatrix}. \tag{2.18}$$

Here, we use the abbreviations:

$$
\begin{aligned}
M_1 &= \mu - [1 - ((1+q+k)^2 + l^2)]^2 - 6\beta, \\
M_2 &= -3\beta, \\
M_3 &= l(1+q)\sqrt{\beta}/(k^2+l^2), \\
M_4 &= \mu - [1 - ((-1-q+k)^2 + l^2)]^2 - 6\beta, \\
M_5 &= -e^{-\gamma^2(k^2+l^2)} l(1+q)\sqrt{\beta}[2k(1+q) + k^2 + l^2], \\
M_6 &= -e^{-\gamma^2(k^2+l^2)} l(1+q)\sqrt{\beta}[2k(1+q) - k^2 - l^2], \\
M_7 &= -Pr(k^2 + l^2 + c^2).
\end{aligned}
$$

Following this procedure we derive two Jacobians for both models and hence reduce the problem to an eigenvalue problem. We note that in the limit $(k,l) \to (0,0)$, we have $M_7 \approx -Pr\, c^2$, so it is not surprising (looking at the bottom line of the 3×3 matrix for model 1) that long-wavelength instabilities in model 1 will depend on the Prandtl number only on the combination $g_m/(Pr\, c^2)$.

2.4.2 Approximations to the eigenvalues in the limit of small k and l

The characteristic polynomials (and hence the eigenvalues, traces and determinants) of each of these Jacobian matrices are even in k and l. Bifurcations occur when the real part of an eigenvalue crosses through zero. The stripe solution is stable only if all eigenvalues are negative for all (k,l), so we are interested in extreme values of the eigenvalues as functions of k and l. The product of eigenvalues is the determinant and hence a zero extreme value of the eigenvalue corresponds to a zero extreme value of the determinant. Consequently, we use the determinants of J_1 and J_2 to assist our analysis of instabilities.

The determinant of J_1, $Det(J_1)$, is:

$$\frac{1}{k^2+l^2}\left\{\left(P_1^{(1)}k^4+P_2^{(1)}k^2l^2+P_3^{(1)}l^4\right)+\left(Q_1^{(1)}k^6+\cdots+Q_4^{(1)}l^6\right)+\left(R_1^{(1)}k^8+\cdots+R_5^{(1)}l^8\right)\right.$$
$$\left.+\left(S_1^{(1)}k^{10}+\cdots+S_6^{(1)}l^{10}\right)-Pr(k^2+l^2)^6\right\},$$

where all coefficients $P_i^{(1)}$ etc., are functions of μ, q, Pr, g_m, c and the filtering $e^{-\gamma^2(k^2+l^2)}$.

The determinant of J_2, $Det(J_2)$, is:

$$\frac{1}{k^2+l^2}\left\{\left(P_1^{(2)}k^4+P_2^{(2)}k^2l^2+P_3^{(2)}l^4\right)+\left(Q_1^{(2)}k^6+Q_2^{(2)}k^4l^2+Q_3^{(2)}k^2l^4+Q_4^{(2)}l^6\right)+\left(R_1^{(2)}k^8\right.\right.$$
$$\left.\left.+\cdots+R_5^{(2)}l^8\right)\right\},$$

where all coefficients $P_i^{(2)}$ etc. are functions of μ, q, g and the filtering $e^{-\gamma^2(k^2+l^2)}$. The traces of the two Jacobians can be written as

$$Tr(J_1)=-6\beta-Pr\,c^2+\left(4-Pr-12(1+q)^2\right)k^2+\left(4-Pr-4(1+q)^2\right)l^2-2\left(k^2+l^2\right)^2$$

and

$$Tr(J_2)=-6\beta+\left(4-12(1+q)^2\right)k^2+\left(4-4(1+q)^2-2\beta g(1+q)^2e^{-\gamma^2(k^2+l^2)}\right)l^2-2\left(k^2+l^2\right)^2,$$

where we recall the relationship in (2.7) between β and μ.

Note that at this point, no approximations or truncations have been made in the linear stability problem of the stripe solution, by virtue of having an exact solution. Our task is now to calculate the most unstable eigenvalues in the limit of small k and l; this is made more challenging by the presence of k^2+l^2 in the denominators of the determinants above.

We note that explicit expressions for eigenvalues of J_1 are not, in general, analytically attainable (though the eigenvalues can be calculated numerically). The Jacobian J_2 is easiest to tackle first. Eigenvalues of a 2×2 Jacobian can be obtained by, $\frac{1}{2}\left(Tr \pm \sqrt{Tr^2 - 4Det}\right)$. At this point we are interested on long-wavelength limit, $(k,l) \to (0,0)$. In this limit, for the matrix J_2, the trace is $Tr(J_2) = -6\beta$ and the determinant is zero, so, for small (k,l), one eigenvalue will be $-6\beta + \mathcal{O}(k^2+l^2)$, which is bounded away from zero for a finite-amplitude stripe. The other eigenvalue will be close to zero, approximately $Det(J_2)/Tr(J_2)$. Similarly, in the limit $(k,l) \to (0,0)$, $Det(J_1) = 0$, so J_1 will have an eigenvalue close to zero for small (k,l). Since bifurcations occur when an eigenvalue is equal to zero, this can be detected in both cases by considering only the determinants of the two matrices. Hopf bifurcations (see section (2.7)) require additional consideration. We will expand $Det(J_1)$ and $Det(J_2)$ in powers of k and l, including the filtering $e^{-\gamma^2(k^2+l^2)}$ in the expansion. This yields expressions of the form,

$$\begin{aligned} &Det(J_{1,2}) = \\ &\frac{\left(A_{1,2}k^4 + B_{1,2}k^2l^2 + C_{1,2}l^4\right) + \left(D_{1,2}k^6 + E_{1,2}k^4l^2 + F_{1,2}k^2l^4 + G_{1,2}l^6\right) + \mathcal{O}((k^2+l^2)^4)}{k^2+l^2}, \end{aligned} \tag{2.19}$$

where in model 2, the coefficients are:

$$\begin{aligned} A_2 &= 12\beta(3(1+q)^2 - 1) - 16q^2(1+q)^2(2+q)^2, \\ B_2 &= -24\beta(1 - 2(1+q)^2) - 16q^2(1+q)^2(2+q)^2 + 4(1+q)^2\beta\left(3\beta - 4q(1+q)^2(2+q)\right)g, \\ C_2 &= 12\beta\left(\beta g(1+q)^2 - q(2+q)\right), \\ D_2 &= 6\beta + 4 + 4(1+q)^2\left((1+q)^2 + 2\right), \\ E_2 &= g\left[4\gamma^2(1+q)^2\beta\left(4(1+q)^4 - 3\beta - 4(1+q)^2\right) - 4\beta(1+q)^2\left((1+q)^2+1\right)\right] + 12 + 8(1+q)^2 \\ &\quad + 18\beta - 4(1+q)^4, \end{aligned} \tag{2.20}$$

and in model 1, the coefficients are:

$$\begin{aligned}
A_1 &= -Pr\, c^2 A_2, \\
B_1 &= -Pr\, c^2 B_2, \\
C_1 &= -Pr\, c^2 C_2, \\
D_1 &= -Pr\, c^2 D_2 - Pr A_2, \\
E_1 &= -Pr\, c^2 E_2 + \beta(-48 - 84q^2 - 168q) + 32q^2(q+1)^2(q+2)^2.
\end{aligned} \tag{2.21}$$

We will hence refer to the determinants of two matrices in the general form with no subscripts:

$$Det(J) = \frac{\left[\left(Ak^4 + Bk^2l^2 + Cl^4\right) + \left(Dk^6 + Ek^4l^2 + Fk^2l^4 + Gl^6\right) + \mathcal{O}((k^2+l^2)^4)\right]}{k^2+l^2}, \tag{2.22}$$

where $A - G$ are chosen from the sets (2.20) and (2.21) according to the model of interest. Following the derivation of the expression (2.22) to the determinant, we next express long-wavelength instabilities in terms of $A - E$ and hence using the parameters involved in relevant model. The values of F and G are not needed subsequently. Stripes are stable if all eigenvalues are less than zero, corresponding to $Det(J_1) < 0$ and $Det(J_2) > 0$. To simplify the presentation, we focus on $Det(J_1)$ since the sign of $Det(J_1)$ coincides with the sign of the most unstable eigenvalue.

2.5 Eckhaus and zigzag instabilities

Bifurcation points correspond to parameter values for which an eigenvalue has zero real part. We first investigate how the determinants depend on k and l, and then use this information to explore how the bifurcation lines of these instabilities depend on the other parameters μ, q and either g or g_m, Pr and c.

We first examine the well known Eckhaus instability. We recall that the Eckhaus instability arises for perturbations with $l = 0$ and therefore (2.22) yields $Det(J) = Ak^2 + Dk^4 + \dots$ and for small k, this is positive when $A > 0$. Thus for model 1, instability corresponds to $A_1 > 0$ and for model 2, instability corresponds to $A_2 < 0$.

Accordingly, in both cases, the Eckhaus instability, which is independent of the mean flow, occurs when $A = 0$:

$$\mu_{Eck} = \frac{q^2(7q^4 + 42q^3 + 90q^2 + 80q + 24)}{(3q^2 + 6q + 2)}.$$

Note that the Eckhaus instability is not dependent on g and c and hence it remains the same with no-slip and stress-free boundary conditions. In the limit of $q \to 0$, $\mu_{Eck} \to 12q^2$ and hence $\mu_{Eck} \to 3\mu_{Existence}$.

When $A > 0$, the maximum of Det occurs at finite k, which is given by $\frac{\partial Det(J)}{\partial k^2} = 0$ when $l = 0$. Therefore the maximum occurs at

$$k = -A/2D + \mathcal{O}(A^2). \tag{2.23}$$

Figure 2.2(a) depicts how the contours of the maximum eigenvalue depend on (k, l) when stripes are Eckhaus unstable. It illustrates an example for parameter values, $\mu = 0.1$, $q = 0.091$ and $g = 0$. Due to the symmetry we consider only the first quadrant of (k, l) space. We also show in figure 2.2(b), the behaviour of the Det in the (k, l) plane. The coefficients $A - G$ in the Det are calculated using the same parameter values as above.

We next consider the zigzag instability, which corresponds to perturbations with $k = 0$. Therefore (2.22) yields $Det(J) = Cl^2 + Gl^4 + \dots$, which is positive for small l when $C > 0$. Thus for model 1, instability corresponds to $C_1 > 0$ and for model 2, instability corresponds

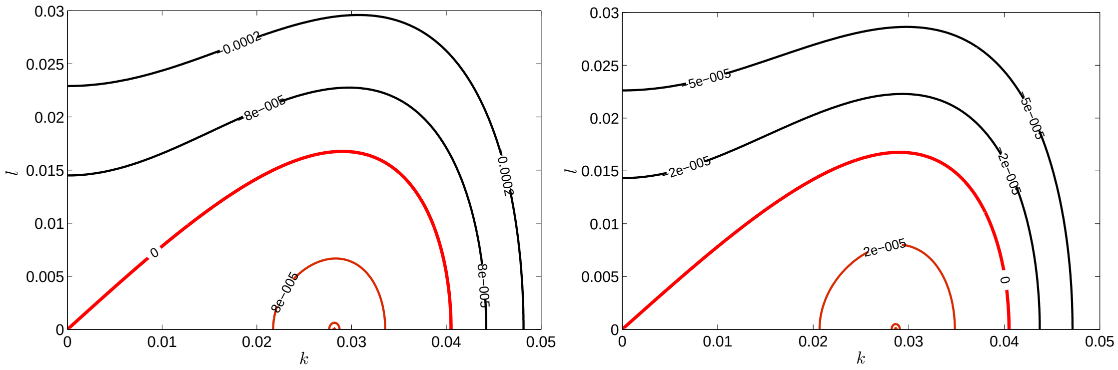

(a)

(b)

Figure 2.2: *(a) Contours of largest eigenvalue for the parameters $\mu = 0.1$, $q = 0.91$ and $g = 0$. (b) Contours of the determinant, of which the coefficients $A - G$ are calculated using the expressions with the same parameters as in (a). For these parameter values, $A = 0.06332 > 0$ and stripes are unstable to the Eckhaus instability. In both cases, the zero contour, which is denoted as a thick red line extends from $k = 0$ to $k = 0.0405$. The maximum growth rate occurs at $k = 0.0286$ and satisfies the equation (2.23). Negative values of growth rates are indicated by black contours while zero and positive values of growth rate are in red.*

to $C_2 < 0$. Accordingly, the zigzag instability in both models occurs when $C = 0$:

$$\mu_{zigzag} = \mu_{Existence} - \frac{3q(2+q)}{g(1+q)^2}, \tag{2.24}$$

where for model 1 we have identified $g = g_m/Pr\, c^2$.

When $C > 0$, the maximum of Det occurs at a finite l, which is given by $\frac{\partial Det(J)}{\partial l^2} = 0$ when $k = 0$. Therefore the maximum occurs at

$$l = -C/2G + \mathcal{O}(C^2). \tag{2.25}$$

The zigzag instability however does not exist for stress-free boundary conditions. If we substitute $g = g_m/Pr\, c^2$ into equation (2.24), $c = 0$ results in $\mu_{zigzag} = \mu_{Existence}$.

Figure 2.3(a) depicts how contours of the maximum eigenvalue depend on (k, l) for

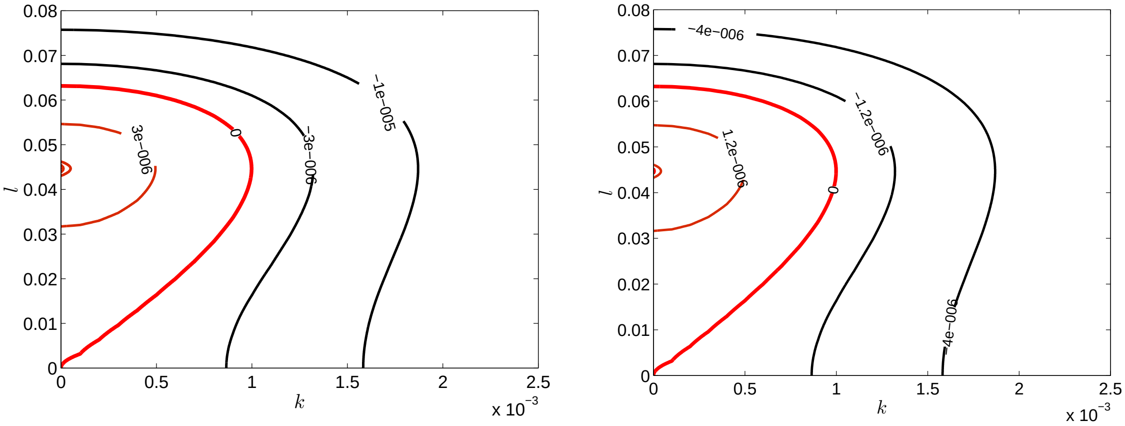

(a) (b)

Figure 2.3: *(a) Contours of largest eigenvalue for the parameters $\mu = 0.1$, $q = -0.001$ and $g = 0$. (b) Contours of the determinant, of which the coefficients $A - G$ are calculated using the expressions with the same parameters as in (a). For these parameter values, $C = 0.0016 > 0$ and stripes are unstable to the zigzag instability. In both cases, the zero contour, which is denoted as a thick red line extends from $l = 0$ to $l = 0.06325$. The maximum growth rate occurs at $l = 0.0447$ and it is in a complete agreement with equation (2.24). Negative values of growth rates are indicated by black contours while zero and positive values of growth rate are in red.*

$\mu = 0.1$, $q = -0.001$ and $g = 0$ at which stripes are zigzag unstable. Due to the symmetry we consider only the first quadrant of (k, l) space. We also show in figure 2.3(b), the behaviour of the Det in the (k, l) plane.

Unlike the Eckhaus instability, the zigzag instability is affected by the strength of the mean flow. Vorticity and mean flows act as a stabilizing influence on the zigzag instability, which is suppressed for larger values of g, resulting in a larger region of stable stripes for $q < 0$ in the (μ, q) stability diagram. Figure 2.4 shows how the zigzag instability boundary behaves for different values of g. Note that for sufficiently large g, it no longer forms the lower stability boundary except for very small μ.

The zigzag and Eckhaus instabilities cross in parameter space when $g\,(= g_m/Pr\,c^2)$ and q are related by

$$g = \frac{3(3(1+q)^2 - 1)}{4q(1+q)^4(2+q)},$$

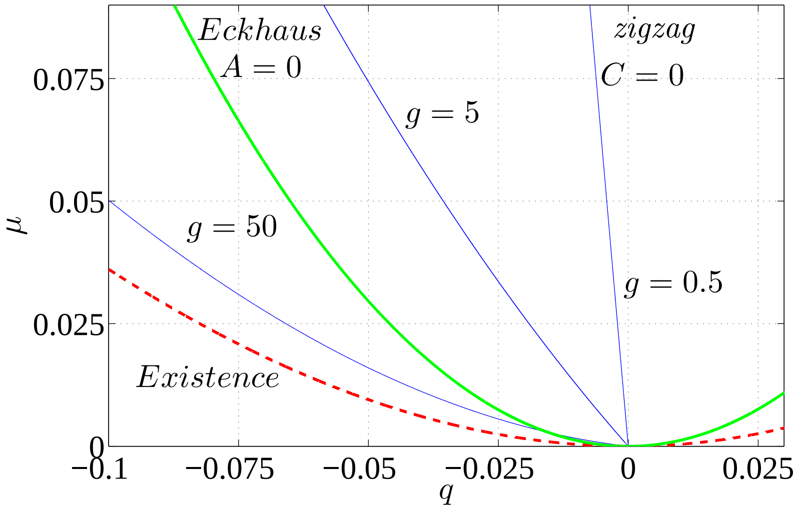

Figure 2.4: *Location of the Eckhaus and zigzag stability boundaries in the* (q, μ) *plane* $(q < 0)$*, for* $g = 0.5, 5$ *and* 50*. The Eckhaus boundary derived from* $A = 0$*, is denoted in green. The red curve is the existence boundary. The zigzag boundary (blue) crosses the Eckhaus boundary at* $q \approx -0.015$ *when* $g = 50$*. The behaviour for small* q *is approximately* $\mu = -6q/g$*. Stripes are stable to the right of the Eckhaus and zigzag boundaries.*

where $q < 0$. Furthermore, when $g \to 0$, we recover the standard result for the SHE without mean flow, and when $g \to \infty$, we have $\mu_{zigzag} \to \mu_{Existence}$. For small μ and q, we can show from the equation (2.24) that μ_{zigzag} is approximately $-6q/g$ for $g > 0$, so the zigzag stability boundary emerges from $(q, \mu) = (0, 0)$ in a straight line of slope $-6/g$, as can be seen in figure 2.4.

2.6 The skew-varicose instability in no-slip boundary conditions

The skew-varicose instability is driven by the inclusion of mean flow, the strength of which is determined by either g in model 1 or by g_m, Pr and c in model 2. It is associated with modes for which the maximum positive growth rate occurs when $k \neq 0$ and $l \neq 0$, and

$0 < k, l \ll 1$.

Two conditions are required to characterize the SVI: the determinant should be zero and should have maximum or minimum value (for model 1 and model 2 respectively) for $k \neq 0$ and $l \neq 0$. We first express these conditions for the SVI in terms of the coefficients $A - G$ of the expression (2.22), the power series expansion of the determinants of J_1 and J_2, which we denote simply by Det. We then express these conditions in terms of the parameters μ, q and either g or g_m, c and Pr, in order to locate the SVI boundary in the (μ, q) plane.

2.6.1 Different manifestations of the skew-varicose instability

There are two different manifestations of the skew-varicose instability. We first illustrate the contour behaviour of numerically calculated maximum eigenvalue in order to highlight the two cases. In the first case (case I), the instability emerges from $k = l = 0$, as illustrated in figure 2.5(a). This behaviour takes place only if stripes are stable to the Eckhaus instability.

The other possibility (Case II) for the skew-varicose instability is that it can accompany the Eckhaus instability and hence the instability emerges from a finite k and $l = 0$. The contour behaviour of the maximum eigenvalue for case II is denoted in figure 2.5(b).

We now derive the conditions for different cases of the SVI using the $Det(J)$. In the case I, the determinant is negative for (k, l) close to the axes, corresponding to $A < 0$ and $C < 0$. We suppose in the first instance that we can write the leading order terms in the determinant as $Det = \frac{Ak^4+Bk^2l^2+Cl^4+\mathcal{O}\big((k^2+l^2)^3\big)}{k^2+l^2}$. We impose $Det = 0$, along with $\partial Det/\partial k = 0$ and $\partial Det/\partial l = 0$. These three conditions consequently give the following

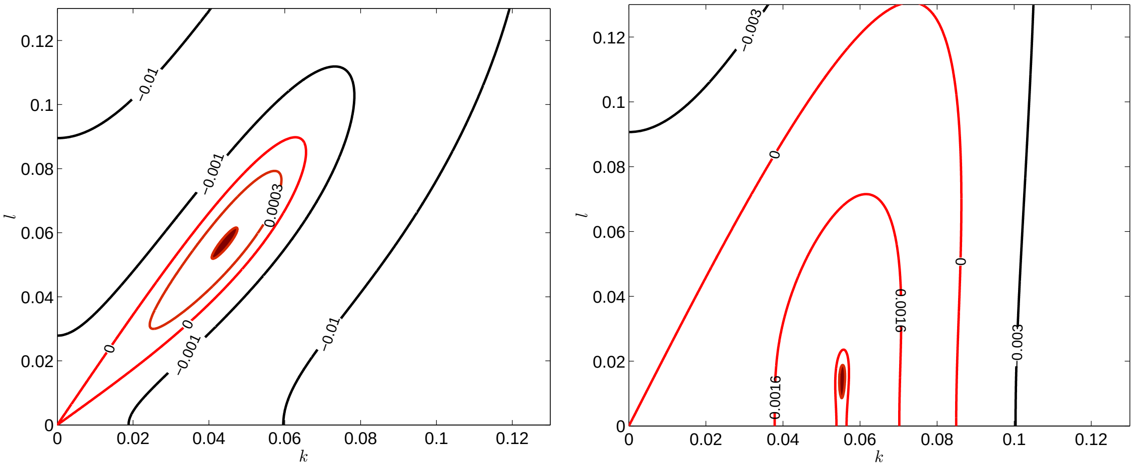

(a) (b)

Figure 2.5: *Contour behaviour of the maximum eigenvalue in the (k, l) plane for parameter values, $Pr = 1$, $c^2 = 2$. (a) Case I of the SVI for $q = 0.053$, $g = 50$ and $\mu = 0.07$: maximum eigenvalue emerges from $(k, l) = (0, 0)$ but occurs with $k \neq 0$ and $l \neq 0$. (b) Case II of the SVI for $q = 0.082$, $g = 1$ and $\mu = 0.07$: maximum eigenvalue emerges from a finite k on $l = 0$ but occurs with $k \neq 0$ and $l \neq 0$. A negative value of the maximum eigenvalue is indicated by black contours while zero and positive values of the maximum eigenvalues are in red.*

equations

$$Ak^4 + Bk^2l^2 + Cl^4 = 0, \tag{2.26}$$

$$Ak^4 + 2Ak^2l^2 + (B - C)l^4 = 0, \tag{2.27}$$

$$(B - A)k^4 + 2Ck^2l^2 + Cl^4 = 0. \tag{2.28}$$

Solving the equations (2.26) & (2.27) result in $\frac{k^2}{l^2} = \frac{B-2C}{B-2A}$, which can combine with (2.28) to give

$$(B^2 - 4AC)(A - B + C) = 0. \tag{2.29}$$

In order for k^2/l^2 to be positive, we need $B > max(2A, 2C)$, which excludes $B = A + C$

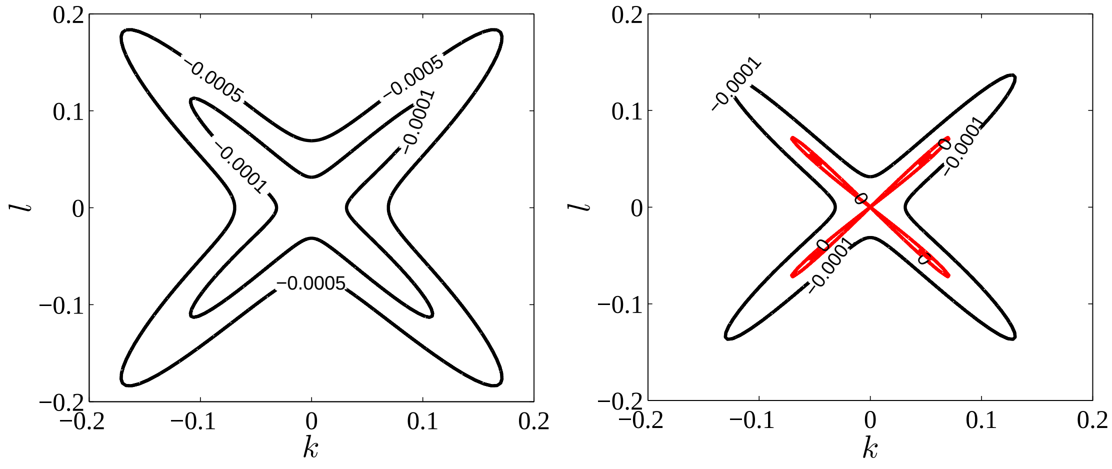

(a) (b)

Figure 2.6: *Case I of the SVI: behaviour of the Det in the* (k, l) *plane for* $A = -0.1$ *and* $C = -0.1$ *(*$A < 0$ *and* $C < 0$ *makes stripes Eckhaus and zigzag stable). The other coefficients are* $D = -1$, $E = 2$, $F = -1$ *and* $G = -1$. *(a)* $B = 0.195$, *giving stable stripes (*$B^2 < 4AC$*). (b)* $B = 0.205$, *giving stripes that are unstable to the SVI (*$B^2 > 4AC$*). The positive maximum of the determinant emerges from* $(k, l) = (0, 0)$ *but occurs with* $k \neq 0$ *and* $l \neq 0$. *A negative value of the determinant is indicated by black contours while zero and positive values of the determinant are in red.*

in (2.29), leaving $B = \pm\sqrt{4AC}$. On the other hand, equations (2.26) & (2.28) result in $\frac{k^2l^2}{k^4+l^4} = \frac{-B}{2(A+C)}$, which can combine with the condition $C < 0$ to give $B > 0$. Therefore we exclude the solution $B = -\sqrt{4AC}$ of (2.29). Finally with the solution $B = \sqrt{4AC}$ of (2.29), we can simplify $\frac{k^2}{l^2} = \frac{\sqrt{4AC}-2C}{\sqrt{4AC}-2A}$ as $\frac{k^2}{l^2} = \frac{1}{(-A)}\sqrt{CA}$.

We conclude that

$$B^2 - 4AC > 0,\ A < 0,\ C < 0 \text{ and } B > 0 \,\text{with}\, \frac{k^2}{l^2} = \frac{1}{(-A)}\sqrt{CA} \tag{2.30}$$

is the condition for the SVI. However, the truncation of *Det* above is degenerate: the conditions are satisfied along a line in the (k, l) plane, rather than at a point. This degeneracy is resolved by restoring the higher order terms, as illustrated in figure 2.6.

In the case II, $A > 0$ and $C < 0$: for $l = 0$ and $D < 0$, *Det* is positive for a range

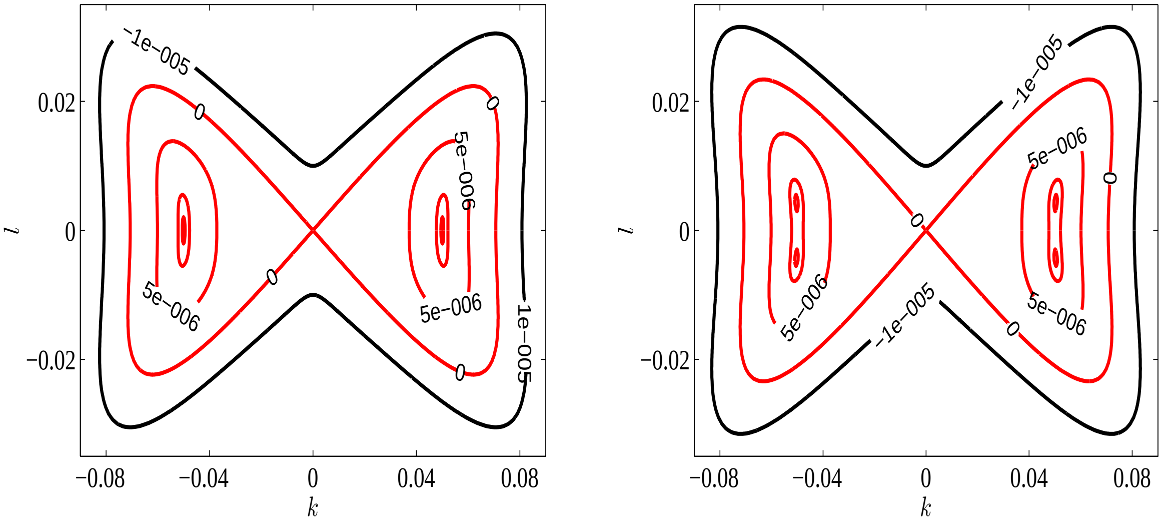

(a)

(b)

Figure 2.7: *Case II of the SVI: behaviour of the Det in the* (k, l) *plane for* $A = 0.005$ *and* $C = -0.1$ *(*$A > 0$ *and* $C < 0$ *makes stripes Eckhaus unstable but stable to zigzags). The other coefficients are* $D = -1$, $E = 2$, $F = -1$ *and* $G = -1$. *(a)* $B = -0.003$, *giving SV stable and Eckhaus unstable stripes* $\left(B < \frac{D+E}{2D}A\right)$; *the maximum occurs with* $l = 0$. *(b)* $B = -0.001$, *giving stripes that are unstable to both SV and Eckhaus instabilities* $\left(B > \frac{D+E}{2D}A\right)$; *the maximum moves off axis, and* $(k_{max}, 0)$ *is now a saddle. A negative value of the determinant is indicated by black contours while zero and positive values of the Determinant are in red.*

of k and attains its maximum on the $l = 0$ axis at a finite $k = k_{max}$. In the (k, l) plane, $(k_{max}, 0)$ can either be a maximum or a saddle, as illustrated in figure 2.4. We define the SVI (case II) to be the point at which $(k_{max}, 0)$ changes from a maximum to a saddle; at this point the maximum eigenvalue moves off the k axis.

Unlike in the previous case, the growth rate at the SVI is positive, since stripes are already Eckhaus unstable. Therefore the SVI occurs when there is a degenerate maximum at $l = 0$ and $k = k_{max}$, about to become saddle. In this case, we consider the *Det* with leading order terms as indicated in (2.22).

The conditions $\frac{\partial Det}{\partial k^2} = 0$ and $\frac{\partial Det}{\partial l^2} = 0$ at the point $(k, l) = (k_{max}, 0)$ yield the parameter values at which this variant of the skew-varicose instability occurs. These two

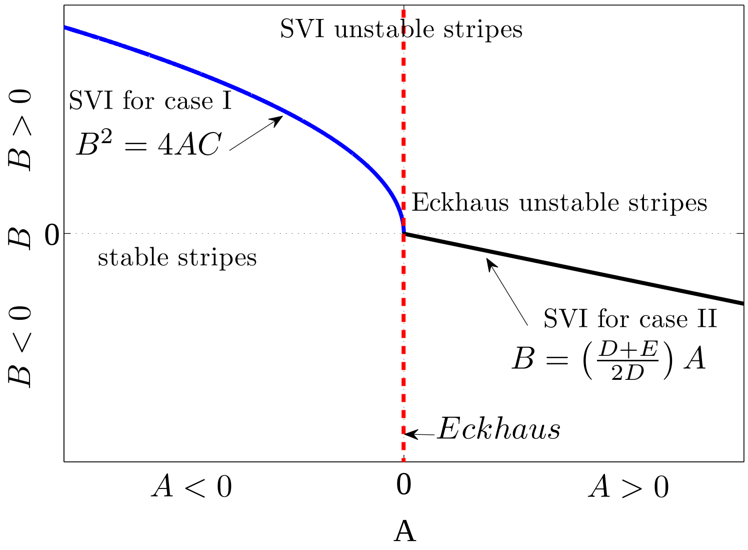

Figure 2.8: *Schematic diagram of the conditions for the Eckhaus and SV instabilities in cases I and II in (A, B) plane. The Eckhaus instability occurs when $A = 0$ (red line). The blue curve shows the SV stability boundary: $B^2 = 4AC$ in case I ($A < 0$), and $B = \left(\frac{D+E}{2D} A\right)$ in case II ($A > 0$). At the intersection of the two stability boundaries, $(A, B) = (0, 0)$.*

conditions together with $l = 0$, consequently give the following equations

$$A + 2Dk^2 + ... = 0,$$

$$(B - A) + (E - D)k^2 + ... = 0$$

at $k = k_{max}$.

The first equation implies $k_{max}^2 = -\frac{A}{2D} + \mathcal{O}(A^2)$, which we combine with the second equation to give $(B - A) + (E - D)\left(-\frac{A}{2D}\right) = 0$ at $k = k_{max}$. Hence in the limit of small A, we conclude the condition for case II of the SVI is

$$B = \left(\frac{D+E}{2D}\right) A + \mathcal{O}(A^2),\ A > 0 \,\text{and}\, D < 0,\ \text{with}\ k^2 = \frac{-A}{2D} + \mathcal{O}(A^2)\,\text{and}\ l = 0\,. \tag{2.31}$$

Contours of *Det* on either side of this boundary are illustrated in figure 2.7. Moreover, the conditions (2.30) and (2.31) are summarized in the schematic diagram in figure 2.8, which also indicates the regions affected by the SVI and Eckhaus instability. Interestingly, the Eckhaus instability and SVI coincide at the point $(A, B) = (0, 0)$. This separates the two different cases, I and II above and is discussed in detail in next section.

2.6.2 The boundary of the skew-varicose instability

We continue by expressing how the conditions (2.30) and (2.31) possibly relate to the bifurcation lines in the (μ, q) plane. A feature of the SVI is that it makes stripes unstable only for $q > 0$ and, for any given value of μ, g must be large enough for the SVI to preempt the Eckhaus instability. The crossing point between the Eckhaus and skew-varicose instabilities is found by $(A, B) = (0, 0)$, where A and B are taken from equation sets (2.3) or (2.20) accordingly in model 2 and model 1. For a given value of q it occurs for some g, say g_{Eck}, which is given by

$$g_{Eck} = \frac{3}{8}\left[\frac{3(1+q)^2 - 1}{(1+q)^6}\right]. \tag{2.32}$$

The condition $A = 0$ could be used to express g_{Eck} as a function of μ if desired. In the limit $\mu \to 0$ and $q \to 0$, g_{Eck} leads to 0.75, which we call $g_{critical}$. The expression for g_{Eck} and the value $g_{critical} = 0.75$ is the same in models 1 and 2 provided we use the relation $g = g_m/(Pr\, c^2)$. The Eckhaus instability precedes the SVI for some range of μ only if $g < g_{critical}$. We have found that the SVI boundary for $g > g_{critical}$ approaches the origin as $\mu = 12q^2$, as does the Eckhaus curve, whilst SVI approaches as $\mu = nq^2$, with $4 < n < 12$ when $g < g_{critical}$. A detailed presentation of this asymptotic result will be discussed in section 2.6.3. The distinction between $g > g_{critical}$ and $g < g_{critical}$ is illustrated in the schematic diagram 2.9. Interestingly, for a fixed q, $g \to 0$ implies $\mu_{SV} \to \mu_{Existence}$. Therefore when $g \to 0$, the SVI boundary coincides with the existence curve of stable stripes for small μ.

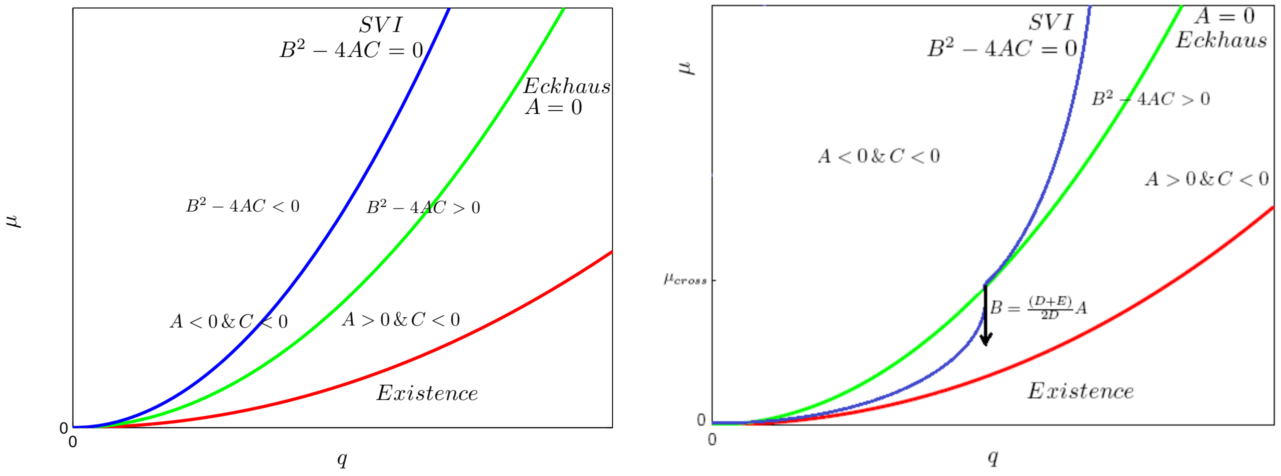

Figure 2.9: *Schematic diagrams of the SVI boundary. (a) $g > g_{critical}$: the region of stable stripes is bounded by the blue (SVI) curve, which approaches the origin as $\mu = 12q^2$, as does the green (Eckhaus) curve. (b) $g < g_{critical}$: $0 < \mu < \mu_{cross}$: the region of stable stripes is bounded by the green (Eckhaus) curve and blue (SVI) curve is approximately a parabola $\mu = nq^2$, with $4 < n < 12$ for small q. $\mu > \mu_{cross}$: the region of stable stripes is bounded by the blue (SVI) curve.*

We then illustrate some examples of bifurcation lines in the (μ, q) plane. In order to derive bifurcation lines we have used a branch-following package, MATCONT [92]. We discuss in detail about the package MATCONT and the conditions that we use in derivation of bifurcation lines in chapter 3. An example of the calculation for model 2 is given in figure 2.10, which was computed working directly with numerically determined eigenvalues and computing $\frac{\partial}{\partial k^2}$ and $\frac{\partial}{\partial l^2}$ numerically. In case I, the SVI boundaries derived using condition (2.30) coincide with the numerical computation. However, in case II, condition (2.31) agrees with the numerical computation only when A is close to zero, as would be expected. The transition from case I to case II occurs at $(\mu, q) = (0.1367, 0.2387)$ for $g = 0.5$: for smaller μ, the stability region of stripes is bounded on the right by the Eckhaus instability, while for larger μ, the Eckhaus instability is pre-empted by the SVI. For $g = 5$, the SVI pre-empts the Eckhaus instability for all μ.

The Eckhaus and SVI boundaries are often very close, so we present our result in an

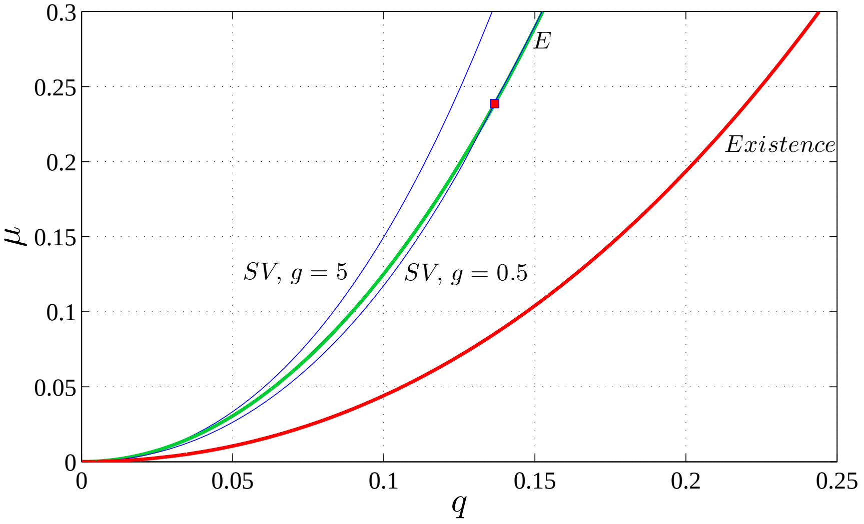

Figure 2.10: *Numerical computation (in model 2) of the SV stability boundary in the* (μ, q) *plane. For* $g = 5$*, the SVI pre-empts the Eckhaus instability for all* μ *and hence the region of stable stripes is bounded by the skew-varicose instability curve. However, for* $g = 0.5$*, the region of stripe stability is bounded by the skew-varicose instability curve only when* $\mu > 0.2387$*. The crossing point,* $(0.1367, 0.2387)$*, of the two boundaries is denoted as a red square. For* $0 < \mu < 0.2387$*, the Eckhaus precedes the SV curve, which reaches the origin as a parabola* $\mu = 9.33q^2$*. The green curve denoted by E is for the Eckhaus boundary whereas the red curve is the boundary of existence of stripes.*

alternative way in figure 2.11. Figures 2.11(a) and 2.11(b) present the SVI boundaries for $g = 5$ and $g = 0.5$ in the $(\mu/\mu_{Existence}\ , \log(q))$ plane. This is a better way of illustrating the regions of stable stripes (shaded regions) and the behaviour of the Eckhaus and SVI boundaries as $q \to 0$. Moreover, it shows how the coordinate axes A and B from (14) can be defined near the SVI–Eckhaus crossing point.

2.6.3 Asymptotic analysis of the SVI boundary

In this section we focus on the asymptotic behaviour of the SVI boundary, which we derived using the two conditions: condition (2.30) for $g > g_{critical}$ and the condition (2.31) for $g < g_{critical}$. We first express these conditions in terms of the parameters in models 1 or 2 and consider their limiting behaviour.

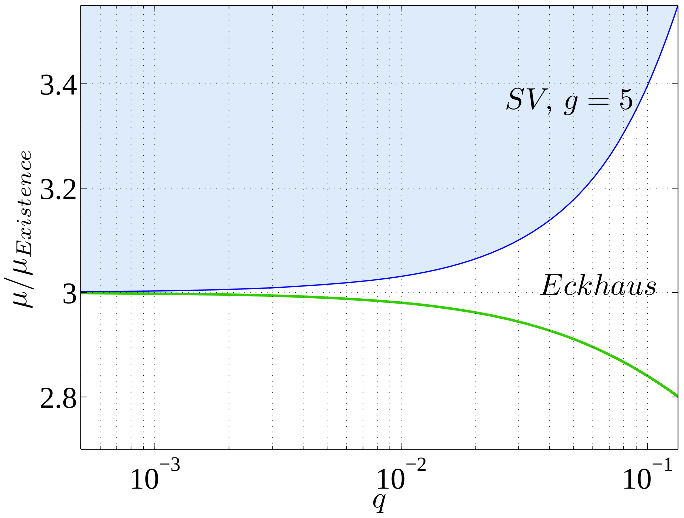

(a)

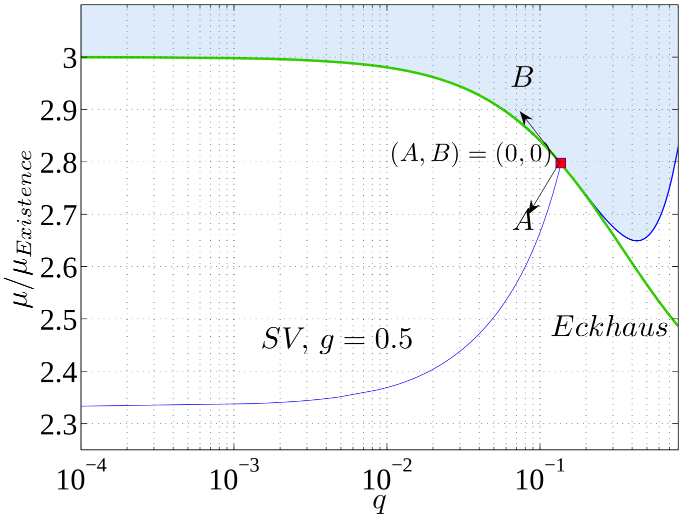

(b)

Figure 2.11: *Numerical computation (in model 2) of the SVI boundary as a function of $\mu/\mu_{Existence}$ and $\log(q)$. $\mu_{Existence} = (1-(1+q)^2)^2$. The Eckhaus boundary, $A = 0$, is denoted by a green curve and the shaded region corresponds to stable stripes. (a) $g = 5 > g_{critical}$. Here, $\mu_{SV}/\mu_{Existence} \to 3$ as $q \to 0$. The SVI precedes the Eckhaus for all q values. (b) $g = 0.5 < g_{critical}$. Here, $\mu_{SV}/\mu_{Existence} \to 2.3333$ as $q \to 0$, which in turn becomes $\mu_{SV} \to 9.3333q^2$ as $q \to 0$. The point of intersection of the SVI boundary with the Eckhaus boundary is denoted by $(A,B) = (0,0)$. A schematic illustration of the A and B axes at the crossing point is also shown (see figure 2.8).*

Case 1: $g > g_{critical}$

Here we consider the case when $g > g_{critical}$, where the SVI boundary pre-empts the Eckhaus instability boundary. We use the condition $B^2 - 4AC = 0$ and for model 2, it is expressed as

$$F_1 g^2 + F_2 g + F_3 = 0, \tag{2.33}$$

where the F_i's are functions of μ and q. In the limit of very small μ and q,

$$F_1 \approx \frac{1}{9}(1024q^6 - 512\mu q^4 + 64\mu^2 q^2 - 16\mu^3 q + \mu^4), \tag{2.34a}$$

$$F_2 \approx \frac{1}{3}(-1536q^5 + 512\mu q^3 - 32\mu^2 q - 4\mu^3), \tag{2.34b}$$

$$F_3 \approx (576q^4 - 96\mu q^2 + 4\mu^2). \tag{2.34c}$$

To proceed, we consider the behaviour of the boundary at the highest order as $\mu \sim q^\alpha$, where $\alpha = 1$ or 2. Depending on α, we select the smallest orders of F_1, F_2 and F_3. We demonstrate this in figure 2.12.

For smallish $g \geq g_{critical}$, as $\mu \to 0$, $\mu \sim q^2$ as shown in figure 2.11(a) and hence the functions in equation (2.34) can be taken as $F_1 \sim q^6$, $F_2 \sim q^5$ and $F_3 \sim q^4$ as illustrated in figure 2.12. Therefore we have $F_1 g^2 + F_2 g + F_3 \sim q^4\left(q^2 g^2 + qg + 1\right)$. If $q \ll 1/g$, we set $F_3 = 0$. This results in $144 - 24(\frac{\mu}{q^2}) + (\frac{\mu}{q^2})^2 = 0$, which gives

$$\mu = 12q^2.$$

This can be improved by including F_2 and hence $F_2 g + F_3 = 0$ and we can select relevant terms of lowest orders of F_2 and F_3 as shown in figure 2.12. In this case we

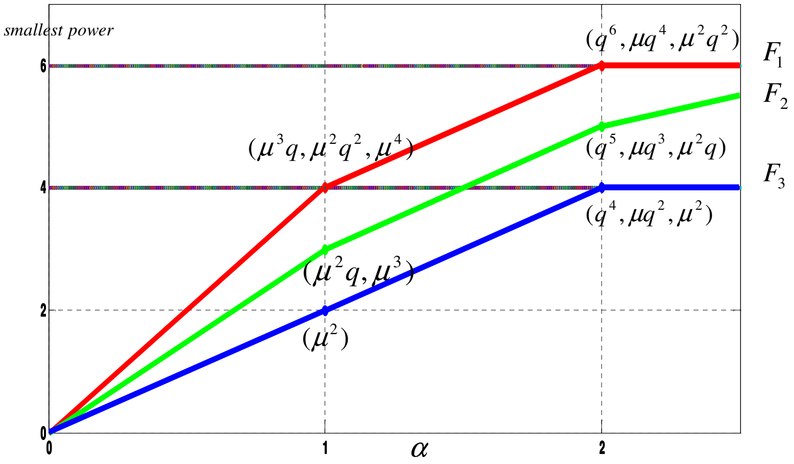

Figure 2.12: *The smallest order of $\mu\ q^{\alpha}$ for F_1, F_2 and F_3 is shown with respect to α.*

obtain,

$$\begin{aligned}\frac{q}{3}\left[384+128\left(\frac{\mu}{q^2}\right)-8\left(\frac{\mu}{q^2}\right)^2\right]g+\left[144-24\left(\frac{\mu}{q^2}\right)+\left(\frac{\mu}{q^2}\right)^2\right]&=0\\ \Rightarrow (3-8qg)\left(\frac{\mu}{q^2}\right)^2-8\,(9-16qg)\left(\frac{\mu}{q^2}\right)+48\,(9-8qg)&=0\\ \Rightarrow \left(\frac{\mu}{q^2}-4\frac{(9-8qg)}{(3-8qg)}\right)\left(\frac{\mu}{q^2}-12\right)&=0.\end{aligned}$$

We conclude that

$$\mu_{SV}=12q^2\left(\frac{9-8qg}{9-24qg}\right),\ (g>g_{critical}\,,q\ll 1/g) \tag{2.35}$$

and hence $\mu \to 12q^2$ when $q \to 0$. Therefore when $g > g_{critical}$, the SVI boundary for small μ has the same curvature as the Eckhaus boundary. Note that figure 2.11(a) shows how the SVI boundary for $g = 5$ coincides with the Eckhaus boundary as $q \to 0$.

The limit of very large g is also of interest, as it corresponds to stress-free boundary conditions (see section 2.7 below). In this limit, we expect the SVI boundary (as shown

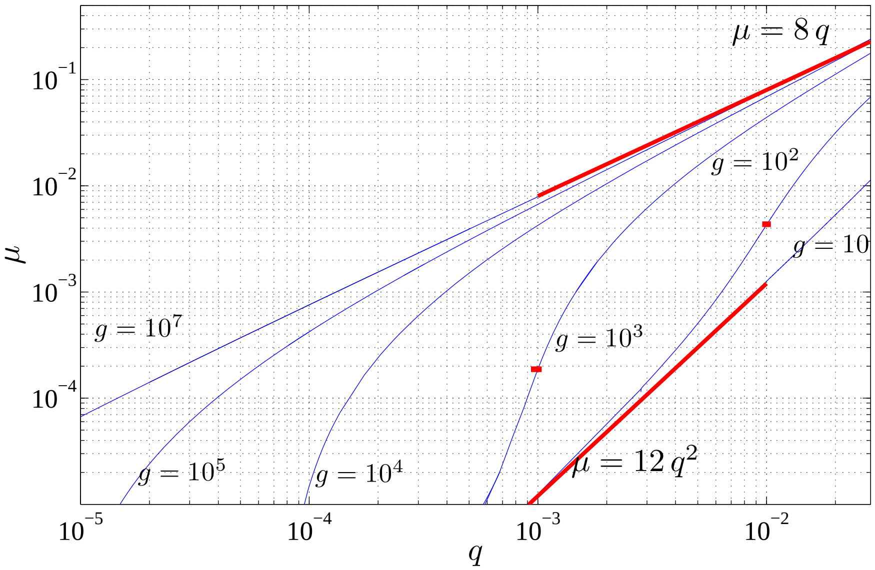

Figure 2.13: *Numerical computation of the SVI boundary on a logarithmic scale for $g = 10^i$ for $i = 1, 2, 3, 4, 5$ and 7. The transition from $\mu \sim q$ to $\mu \sim q^2$ occurs when $g \propto 1/q$ (inflection points, denoted in red points, are almost exactly at $q = \frac{1}{g}$). In the limit of small q, the SVI curve is tangent to $\mu = 12q^2$, whereas in the limit of large g, the SVI curve goes as $\mu \sim 8q$ as μ increases. Both asymptotes, $\mu \sim 8q$ and $\mu \sim 12q^2$ are denoted by red lines.*

in figure 3.5 in chapter 3) should have $\mu \sim q$ [93]. From equation (2.34) with $\mu \sim q$, we have $F_1 \sim q^4$, $F_2 \sim q^3$ and $F_3 \sim q^2$ as shown in figure 2.12. Therefore we have $F_1 g^2 + F_2 g + F_3 \sim q^2 \left(q^2 g^2 + qg + 1\right)$. If $qg \ll 1$, we set $F_3 = 0$ and recover $\mu = 12q^2$.

If $qg \gg 1$, we set $F_1 = 0$. This results in, $64 - 16\left(\frac{\mu}{q}\right) + \left(\frac{\mu}{q}\right)^2 = 0$, which gives

$$\mu \sim 8q.$$

Again, this can be improved by setting $F_1 g + F_2 = 0$, and we obtain

$$\mu_{SV} = 8q\left(\frac{2qg + 3}{2qg - 3}\right), \; (g > g_{critical}\,, q \gg 1/g). \tag{2.36}$$

Finally, we note that the transition between $\mu \sim 12q^2$ and $\mu \sim 8q$ will occur when qg is of order unity, so $q_{transition} \sim \frac{1}{g}$. Figure 2.13 illustrates the behaviour of the SVI boundary for selected values of g with $g > g_{critical}$ and the transition agrees with $q \sim \frac{1}{g}$.

All these explicit results are for model 2. When $g > g_{critical}$, the expressions for conditions given in (2.30) are the same for model 1 with the relation $g = g_m/Pr\, c^2$. Therefore, equations (2.35) and (2.36) are the same for model 1.

In the skew-varicose mechanism for $g > g_{critical}$, the maximum of Det is attained for perturbations of a mode, say (k_{max}, l_{max}), as $k_{max} \to 0$ and $l_{max} \to 0$. As shown in equation (2.30), $\frac{{k_{max}}^2}{{l_{max}}^2} = \sqrt{\frac{C}{A}}$. The expressions for A and C are taken from equation sets (2.20) or (2.21) accordingly for the model 2 or model 1.

For $g > g_{critical}\, , q \ll 1/g$, $\mu = 12q^2$ at the asymptotic limit of the SVI and we get,

$$\left(\frac{k_{max}}{l_{max}}\right) = (2 - (27/2 + 8/3g)q + (46/3g + 639/8)q^2 - (15045/32 + 521/6g)q^3 + \mathcal{O}(q^4))^{1/4}$$

which results in

$$\left(\frac{k_{max}}{l_{max}}\right) = \mathcal{O}(1).$$

For $g > g_{critical}\, , q \gg 1/g$, $\mu = 8q$ at the asymptotic limit of the SVI and we get,

$$\left(\frac{k_{max}}{l_{max}}\right) = \mathcal{O}(q^{1/4}).$$

Case 2: $g < g_{critical}$

We now consider the case $g < g_{critical}$, for which the SVI boundary lies in the Eckhaus band for small μ. We do not have an exact criterion for the SVI in this case, though equation (2.31) is an approximate criterion. However, for small μ, we expect μ_{SV} to depend approximately linearly on g. We know from equation (2.35) that for $g = g_{critical}$,

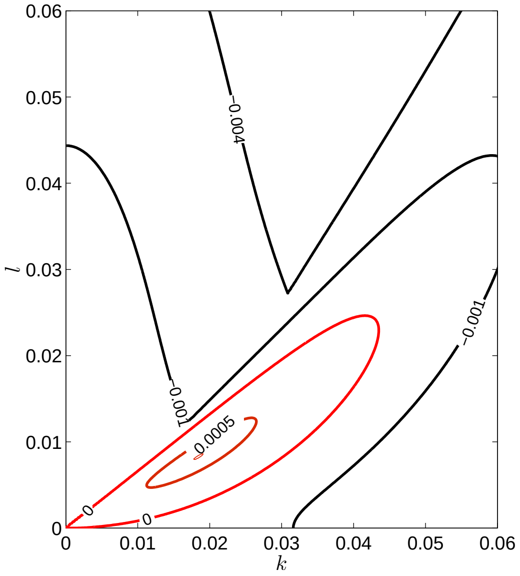

Figure 2.14: *Contours of largest eigenvalue for the parameter values* $\mu = 0.02$*,* $q = 0.0036$*,* $g_m = 10$*,* $Pr = 1$ *and* $c = 0$*. For these parameter values stripes are unstable to the SVI. The zero and positive real growth rates are denoted as red lines and the negative real values of growth rates are indicated by black contours. The maximum real eigenvalue emerges from* $(k, l) = (0, 0)$ *but occurs with* $k \neq 0$ *and* $l \neq 0$

$\mu_{SV} \rightarrow 12q^2$ as $q \rightarrow 0$ and from conditions in equation (2.31) in the limit $g \rightarrow 0$, we have $\mu_{SV} \rightarrow 4q^2$ as $q \rightarrow 0$. A linear interpolation between these yields

$$\mu_{SV} \approx 4\left(\frac{2}{g_{critical}}g + 1\right)q^2, \; (g < g_{critical}\, , q \ll 1). \tag{2.37}$$

This relation is shown numerically using MATCONT [92] (see section 3.2) to be a very good approximation; $\mu_{SV}/\mu_{Existence}$ behaves linearly with g with a gradient 8/3. In addition, the numerical simulation illustrated in figure 2.11, shows at $g = 0.5$, $\mu/\mu_{Existence} \rightarrow 2.333$ as $q \rightarrow 0$ which agrees well with equation (2.37). The conditions for the SVI and its asymptotic behaviour can be expressed for model 1 with the relation $g = g_m/(Pr\, c^2)$. The case where $c = 0$ is considered in the next section.

2.7 SVI in stress-free boundary conditions

We now consider the case that models convection with stress-free boundary condition. In model 1, c is the parameter that accounts for the boundary conditions at the top and bottom, and stress-free boundary conditions corresponds to $c = 0$. Using the relation $g = g_m/Pr\, c^2$ to connect the two models, taking the limit $g \to \infty$ corresponds to stress-free boundary condition in model 2.

When $c = 0$, an example for the behaviour of the maximum eigenvalue for the SVI is shown in figure 2.14. The instability emerges from $k = l = 0$ and extends to $k \neq 0$ and $l \neq 0$. The conditions for the SVI in stress-free boundary conditions are the same as in equation (2.30), corresponding to case I above with no-slip boundary conditions. Hence for any coupling constant g_m, the SVI boundary always pre-empts the Eckhaus boundary in the (μ, q) plane, and it takes the form,

$$\mu = 8q + 24q^2 + 20q^3 + 5q^4 + \mathcal{O}(q^5)$$

and in the limit of small q, $\mu \sim 8q$, approximating $g \to \infty$ in model 2. A remarkable property of the SVI in model 1 with stress-free boundary conditions is that the stability boundary is independent of Pr and g_m.

2.8 Oscillatory SVI in stress-free boundary conditions

Another instability of interest in the stress-free case is the oscillatory skew-varicose (OSV) instability, which consists of a long-wavelength transverse oscillation of the stripes that propagates along their axis [26]. For OSV modes, the associated eigenvalues are complex. This instability does not occur in model 2 because $Tr(J_2) < 0$ for small k and l and so

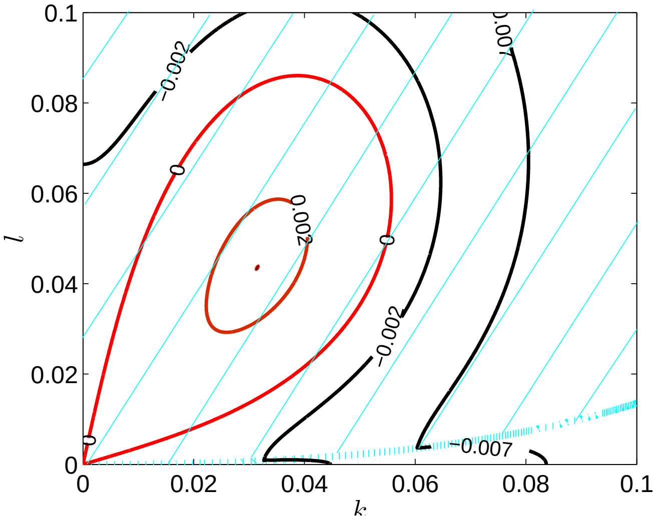

Figure 2.15: *Contours of largest eigenvalue for the parameter values $\mu = 0.02$, $q = -0.025$, $g_m = 10$, $Pr = 1$ and $c = 0$. For these parameter values stripes are unstable to the OSV instability. Hatched region indicates where the maximum eigenvalue has a non zero imaginary part. The zero real growth rate is denoted as a thick red line and the negative real values of growth rates are indicated by black contours. The complex eigenvalue that emerges from $(k, l) = (0, 0)$ occurs with $k \neq 0$ and $l \neq 0$*

complex eigenvalues are not possible. In model 1, the OSV instability does not appear for $c^2 = 2$, no-slip boundary conditions. In contrast for $c = 0$, the regions in the (k, l) plane with positive growth rate and non-zero frequency emerge from $(k, l) = (0, 0)$ in a way that resembles the contours for the SVI, as shown in figure 2.15.

We derive the asymptotic behaviour of the OSV instability boundary as follows. At the point of instability, the eigenvalues of J_1 are purely imaginary. We take the real eigenvalue as λ_1 and purely imaginary eigenvalues as $\pm i\omega$ and so the characteristic equation of J_1 can be written as,

$$(\lambda - \lambda_1)(\lambda^2 + \omega^2) = 0$$

$$\Rightarrow \lambda^3 - \lambda_1\lambda^2 + \omega^2\lambda - \lambda_1\omega^2 = 0.$$

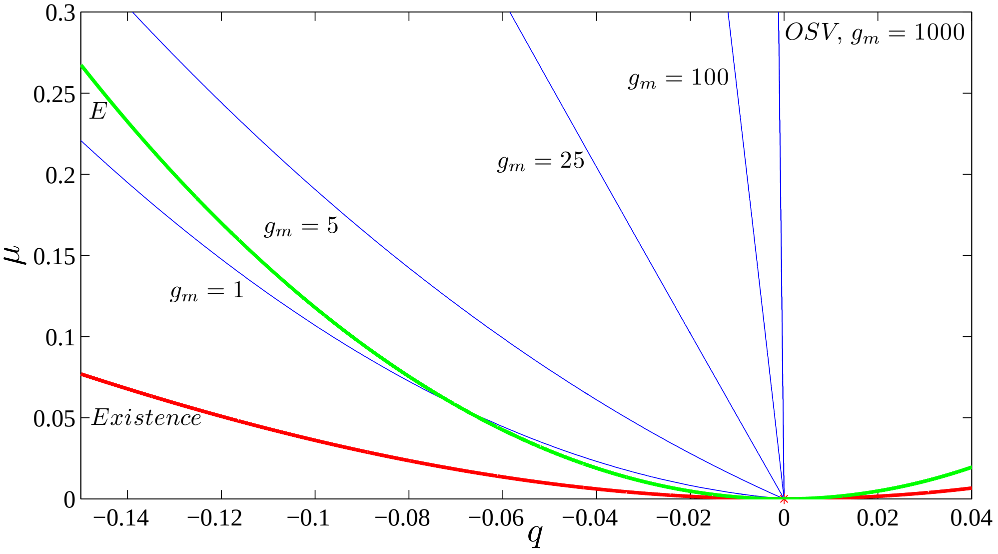

Figure 2.16: *The location of the OSV instability boundary for model 1 for* $c = 0$ *(stress-free boundary conditions),* $Pr = 1$ *and* $g_m = 1000, 100, 25, 5$ *and* 1*. Stripes are OSV unstable to the left of the OSV boundary. For small* μ*, the boundary is asymptotic to* $\mu = \left(\frac{-3+\sqrt{5}}{3}\right) q g_m$*. The Eckhaus boundary is denoted in green and the existence curve is in red.*

Therefore we can write the characteristic equation of J_1 as

$$\lambda^3 + A\lambda^2 + B\lambda + C = 0,$$

where

$$A = -\lambda_1, B = \omega^2 \,\text{and}\, C = \lambda_1 \omega^2.$$

This gives two conditions, $C - AB = 0$ and $B > 0$ for J_1 to have pure imaginary eigenvalues. The coefficients A, B and C are functions of g_m, Pr, q, μ, k and l. We will set $Pr = 1$ to illustrate this calculation. For small k and l, the condition $C - AB = 0$ gives,

$$G_1 \left(\frac{g_m q}{\mu}\right)^2 + G_2 \left(\frac{g_m q}{\mu}\right) + G_3 = 0, \tag{2.38}$$

after maximizing $C - AB$ over (k, l). The G_i's are functions of μ and q. In the limit of very small μ and q, we find,

$$G_1 \approx \frac{1024}{9} + \mathcal{O}\left(\frac{q^2}{\mu}\right) \ , \tag{2.39a}$$

$$G_2 \approx 512 + \mathcal{O}\left(\frac{q^2}{\mu}\right) \ , \tag{2.39b}$$

$$G_3 \approx 256 + \mathcal{O}\left(\frac{q^2}{\mu}\right), \tag{2.39c}$$

where we have dropped terms that can be shown to be smaller than those retained.

We note at this point that equations (2.38) and (2.39) with $(q^2/\mu) \ll 1$ give

$$\frac{1024}{9}\left(\frac{g_m q}{\mu}\right)^2 + 512\left(\frac{g_m q}{\mu}\right) + 256 = 0,$$

which implies

$$\mu = \left(\frac{-3+\sqrt{5}}{3}\right) q g_m. \tag{2.40}$$

The OSV instability boundary has a linear relationship between q and μ for small μ, and it bounds the region of stable wavenumbers for negative q, (figure 2.16). Stripes are stable to the right of the boundary. In this asymptotic limit, the point of maximum growth rate in the (k, l) plane can be found at the point of maximum of $C - AB$; this point satisfies

$$l/k = \sqrt{5}.$$

We now derive the expression for B on $l = \sqrt{5}k$ with the relation (2.40). We obtain, $B = Hk^2 + \mathcal{O}(k^4)$, where $H \approx 10\left(\frac{-3+\sqrt{5}}{3}\right)\left(\frac{1}{3}g_m + 2\right) q + \mathcal{O}(q^2)$. Therefore, for small k and in the limit of small q, we establish the condition $B > 0$.

Figure 2.16 shows the behaviour of the OSV instability boundary in model 1 with

$c = 0$, for $Pr = 1$ and different values of the coupling constant g_m.

2.9 Agreement of results of direct simulations of the models and stability calculations

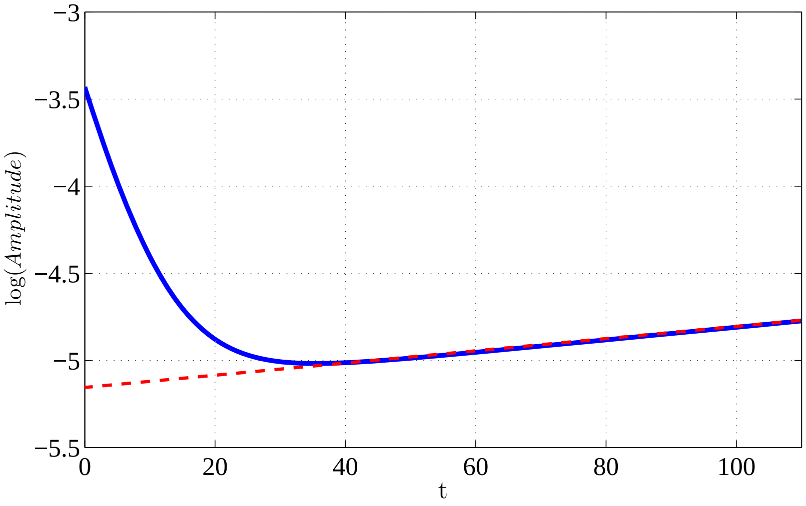

Figure 2.17: *Logarithmic plot of the amplitude of the growth rate of the perturbed mode with respect to time. Here the perturbed mode is* $(1.1 + k, l)$ *with* $k = l = 0.05$. *Parameter values are* $\mu = 0.1$ *and* $g = 0.75$. *Secondary growth rate, which is calculated by a linear fitting, of the perturbed mode is* 0.00360926 *whereas the stability calculations for the corresponding mode gives* 0.00360933

In this section we show by an example that the quantitative results of stability calculations have been in remarkable agreement with studies of the full equations and is our justification for stability analysis above.

In order to compare with the stability calculations that were performed for the SVI, we find the solutions to the nonlinear system of PDEs (2.2-2.3 & 2.4-2.5). These original models are solved numerically using a spectral method and exponential time differencing of fourth order, ETDRK4. We discuss the numerical scheme in detail in chapter 5.

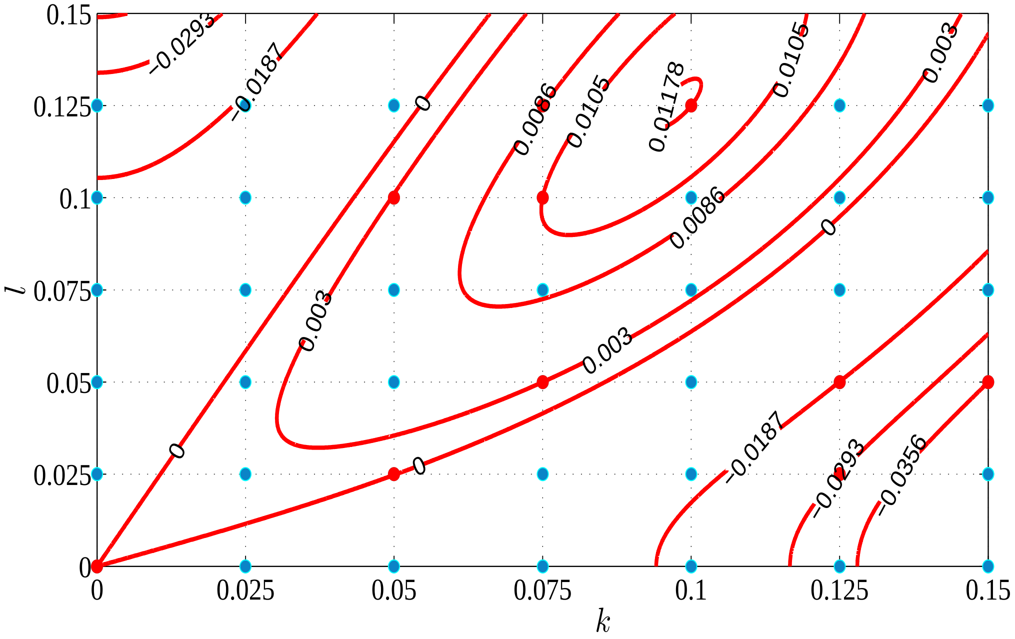

Figure 2.18: *Comparison of the stability calculations with the numerical solution of model 2. We use a (k, l) grid with grid spacing $(\Delta k, \Delta l) = (0.025, 0.025)$. The parameter values are $\mu = 0.1$, $q = 0.075$ and $g = 25$. We calculate the growth rates numerically on the grid points indicated on the grid (k,l) in red and blue. Contours are derived using the Jacobian in a finer grid. The contours indicated are the ones that pass through the points marked in red. For instance, for $(k, l) = (0.05, 0.025)$, numerical solution gives the growth rate as zero and the zero contour, which calculated using the Jacobian, over plot the point showing the agreement of* 99.97%.

To investigate the stability of parallel stripes, we begin with finding non-linear solutions of the PDEs starting from an initial condition $\psi = 0.01\sin((1+q)x)$ and $\omega = 0$ and time stepping until the amplitude of $\sin((1+q)x)$ saturates. We then add perturbations to the stripe solution, $10^{-6}\sin((1+q+k)x, ly)$ varying k and l over the grid and time step for a further length of time. We then look for exponential growth or decay of the perturbation. The secondary growth rate was calculated by fitting a straight line to the data as indicated in figure 2.17. Note that we choose the initial amplitude of the perturbation and the time interval over which the calculation was done to ensure that the amplitude of the perturbation remains in the linear regime.

This calculation of the eigenvalues depends on the perturbed mode, which again depends on the choice of k and l. This is determined by the size of the domain and in order to investigate details of stability for small (k, l), we need a large domain size, which is time consuming. Therefore the numerical simulation is not guaranteed to capture the instability boundaries, but can only find sufficient conditions for instabilities.

On the other hand, we can use the Jacobian to calculate the maximum eigenvalue for a range of values of k and l; it allows to investigate details of stability in the limit of small (k, l), and hence to derive the SV boundary precisely. Therefore the calculations using the Jacobian are exceedingly useful to consider eigenvalue behaviour for any set of parameters and importantly, in calculating instability boundaries.

For this illustration, the PDE calculations were carried out in a square domain of size $L = 2\pi \times 40$ with 512 Fourier modes for periodic boundary conditions. This fixes a lattice in (k, l) space with lattice spacing $2\pi/L = 0.025$. On this grid, at each point, we calculated the growth rates. This is illustrated in figure 2.17 and the results of the two methods appeared to be identical. The blue and red points in the figure correspond to grid points, which we use to compare growth rates. Contours of growth rates, computed from the Jacobian on a much finer grid, are also shown. The contour levels correspond to the PDE growth rates at the red points, and contours go exactly through these points, with about 0.03% error. The reason for this agreement is because the conditions we used in the stability calculations are kept in PDE simulations; we apply the projection and filtering operations in numerical simulations.

Calculating the eigenvalues directly from the Jacobian can be done for arbitrary k and l and therefore we have overcome the difficulty of numerical calculation; eigenvalues depend on k and l and is restricted by the largest domain we can simulate.

2.10 Concluding remarks

In this work we considered the consequences of including the mean-flow on the generalized Swift–Hohenberg models. We analyzed two models: in the first model vorticity has its own independent dynamics [69]. In the second, vorticity is directly slaved to the order parameter [64]. In most circumstances, the stability theory for the two models is exactly the same, when the relation $g = g_m/(Pr\ c^2)$ is made. Even with $c = 0$, the behaviour of model 1 is reproduced by model 2 in the limit $g \to \infty$. Two boundary conditions were considered in this work: stress-free ($c = 0$) and no-slip ($c^2 = 2$).

In order to explore long-wavelength instabilities, we carried out a complete linear stability analysis of stripes. We expressed the relevant determinants as power series in k^2 and l^2, where (k, l) is the perturbation wavevector. We were able to derive explicit expressions for the largest growth rates in most cases. This has led to an improved understanding of the instabilities of stripes. Unlike in previous work [90, 93, 94], we have not had to make assumptions on the relation between k, l and the amplitude of the basic stripe solution. This approach has been made possible through the use of the projection operator, P_α, which allows the exact stripe solution to be written down easily [91].

With this linear stability analysis of the stripe solution, we investigated the growth rate of perturbations corresponding to the Eckhaus, zigzag, skew-varicose and the oscillatory skew-varicose instabilities. The Eckhaus instability does not depend on the mean flow. However, the zigzag instability depends on the mean flow and higher mean flow suppresses the zigzag instability. The skew-varicose instability has two different behaviours: if stripes are stable to the Eckhaus instability, in the limit of $\mu = 0$, the SVI scales as $\mu \sim 12q^2$, provided $g > 0.75$. The most unstable wavevector satisfies $k^2/l^2 = \mathcal{O}(1)$. For $g < 0.75$, the SVI boundary crosses the Eckhaus curve, and in the limit of $\mu = 0$, it goes as $\mu \sim aq^2$

with $4 < a < 12$. In model 1, the critical g_m is $0.75 Pr\, c^2$. In the large g limit (that is, for very low Pr, or for stress-free boundary conditions), there is a transition of the SVI boundary from $\mu = 12q^2$ to $\mu = 8q$ at a wavenumber satisfying $q \propto 1/g$.

An additional instability, the oscillatory skew-varicose (OSV) instability, is encountered for stress-free boundary conditions in model 1. The OSV instability boundary is approximately $\mu = \left(\frac{-3+\sqrt{5}}{3}\right) q g_m$, for small μ. For higher mean flow, region of stripes that is unstable to the OSV instability is increased.

The projection operator P_α, which is equivalent to a truncation to selected wavenumbers, made this analysis straightforward. The most significant benefit is the complete understanding of the skew-varicose instability in our models. Numerical simulations of these projected models for small μ, have the same solutions as the unprojected PDE and this is our justification for using these projected models in stability analysis for small μ. It would be of interest to find out whether a similar projection could be used to overcome the difficulty of analysis of the Navier-Stokes equations.

In order to appreciate fully the method, we compare the results of the SVI growth rates derived using stability calculations with those from numerical solutions of the PDEs. We found a very good agreement (of 99.974%) between the two.

In the next chapter, we extend the asymptotic results in this chapter using MATCONT to explore fully the long wavelength instabilities of stripes. In addition, we discuss short-wavelength instabilities and how these depend on the coupling to the mean flow.

Chapter 3

Generalizations of the two dimensional Swift–Hohenberg Equation: effect of system parameters on the region of stable stripes

3.1 Introduction

In this chapter, our main objective is to use numerical methods to derive the region of stable stripes of the models: Model 1 (2.2-2.3) and Model 2 (2.4-2.5). The numerical analysis in this chapter provides further reassurance that the stability results of long-wavelength instabilities, derived in chapter 2, are correct. For the two different manifestations of skew-varicose instability (case I and case II) we presented illustrative examples using numerical results in chapter 2. Here we mainly focus on the stability region of SVI for case I. However, we consider case I and II later in this chapter, where we discuss the influence of the mean flow on the stability region. The short-wavelength instabilities, despite the $\mathcal{F}_\gamma$ filtering, are found to limit the region of stable stripes and we numerically analyze the types of short wavelength instabilities. We further extend our numerical derivations to identify the dependence of the mean flow to all instabilities that exist in the models.

In order to compute the stability boundaries, we use the continuation package MATCONT [92]. First we recall the governing Jacobians J_1 in (2.17) and J_2 in (2.18) in Chapter

2 and calculate the maximum eigenvalue (or the real part if the eigenvalue is complex), σ_{max}, numerically. The eigenvalue σ_{max} behaves differently for the different instabilities (Eckhaus, zigzag, skew-varicose, cross-roll, oscillatory skew-varicose, oscillatory cross-roll), and we determine numerically how it depends on k and l in order to compute the derivatives that govern the criteria for each instability. Given an appropriate initial parameter value, MATCONT can calculate the curves in parameter space on which these criteria are satisfied.

The numerical results obtained with MATCONT are presented for different boundary conditions: no-slip ($c = \sqrt{2}$), stress free ($c = 0$) and for the case with small $c > 0$. We first present the stability diagrams in (μ, q) plane for illustrative parameter values. The parameter value of the coupling strength on the meanflow is chosen to be larger than the critical value that we discussed in chapter 2, so that the SV boundary always preempts the Eckhaus boundary. Second, we discuss the impact of the coupling strength on the meanflow, Prandtl number and the filtering coefficient, γ, on modifying the region of stable stripes.

The chapter is structured as follows. We start by describing how the short-wavelength instabilities appear in our models in section 3.2. Our numerical method is discussed in section 3.3, where we discuss the behaviour of σ_{max} for each instability. Then we present numerically computed stability diagrams for both no-slip and stress-free boundary conditions in section 3.4. We illustrate the growth rates of perturbations at selected points in the stability diagram in the same section. Section 3.5 shows the influence of the mean flow on the region of stable stripes. In section 3.5, we discuss the influence of the Pr on the region of stable stripes and present numerical results that show the relation $g = g_m/Pr\, c^2$ in section 3.6. Section 3.7 presents the numerical results to show how the filtering coefficient γ of the filtering operator $\mathcal{F}_\gamma$, which is used to reduce short-wavelength instabilities, affects the cross- roll instability boundary and hence the region of stable stripes. Further numerical exploration of a curious behaviour of the growth rates is included in section 3.8. This chapter closes with some concluding remarks in section 3.9.

3.2 Short-wavelength instabilities

In this section we illustrate two types of short-wavelength instabilities present in our models: the Cross-Roll (CR) instability and Oscillatory Instability (OI). These short-wave instabilities are produced when a mode with k and l that are not small, is associated with a positive growth rate.

3.2.1 The Cross-roll instability.

The cross-roll (CR) instability is so-called because the fastest growing disturbances appear to take the form of stripes perpendicular to the basic steady stripe pattern: these disturbances have non-zero k and l in the limit $\mu \to 0$ [5]. In contrast to the oscillatory instability discussed below, the most unstable eigenvalue at the CR instability is real.

We use numerical results in section 3.5 below to show that the CR instability only forms a boundary of the region of stability of stripes if g is large. The filtering $\mathcal{F}_\gamma$, discussed in section 2.2.3 in Chapter 2, was introduced to suppress the CR instability in favour of the SVI, so the location of the CR instability boundary depends on γ, while the SVI is not influenced by γ for small enough μ and q. Since the CR instability sets in with non-zero k and l, even for small μ and q, asymptotic analysis of the type carried out above in chapter 2 cannot be done.

3.2.2 The oscillatory instability

When the parameter c is increased from zero (which models stress-free boundary conditions), the OSV instability disappears and is replaced by the so-called oscillatory instability (OI). This has the nature of an oscillatory cross-roll instability, setting in with non zero k and l. The boundary of this oscillatory instability emerges from $\beta = 0$, the existence curve. However, this instability is prominent only for $Pr\, c^2 \ll 1$; for higher values of $Pr\, c^2$, the instability moves to larger negative q. The behaviour of the oscillatory instability boundary and the effect of the mean flow are illustrated in section 3.4.3.

3.3 Numerical Technique: MATCONT

In this section we outline the method used in tracing the bifurcation lines. We use MATCONT, which is a continuation package for the interactive numerical study of dynamical systems. [92]. MATCONT works in the MATLAB environment and it provides the means for continuing equilibria and periodic orbits of systems of ordinary differential equations (ODEs), and their bifurcations. We first need to identify the type of solutions of the branch to be computed and to set up the equations file which helps to trace the solution. Then the continuation can be initialized with a known initial solution or at a bifurcation point.

We begin by setting up equations file in MATCONT to derive algebraic bifurcation lines. We first calculate the maximum eigenvalue, σ_{max}, numerically. This eigenvalue is a function of k and l, and each instability corresponds to different conditions on σ_{max} and its derivatives with respect to k and l, as detailed below. These conditions are then programmed into files in MATCONT in terms of the parameters of the models.

Eckhaus instability

Stripes are unstable to the Eckhaus instability if σ_{max} is positive for $l = 0$ and $k = k_{max} > 0$. The Eckhaus stability boundary occurs when $k_{max} \to 0$, in which case $\frac{\partial^2 \sigma_{max}}{\partial k^2} = 0$ at $(k, l) = (0, 0)$. An example of the maximum eigenvalue behaviour due to the Eckhaus instability is shown in figure 2.2 in Chapter 2.

Zigzag instability

Stripes are unstable to the zigzag instability if σ_{max} is positive for $k = 0$ and $l = l_{max} > 0$. The zigzag stability boundary occurs when $l_{max} \to 0$, in which case $\frac{\partial^2 \sigma_{max}}{\partial l^2} = 0$ at $(k, l) = (0, 0)$. An example of the maximum eigenvalue behaviour due to the zigzag instability is shown in figure 2.3 in chapter 2)

Skew-varicose instability

There are two cases of the SVI, as discussed in chapter 2. First, if the SVI precedes the Eckhaus instability, we consider σ_{max} as a function of k and l with $k = \epsilon \cos(\theta)$ and $l = \epsilon \sin(\theta)$. Stripes are unstable to the SVI, if σ_{max} is positive for some θ in the limit of $\epsilon = 0$. The SV stability boundary occurs when $\epsilon \to 0$, in which case $\sigma_{max} = 0$ and $\frac{\partial \sigma_{max}}{\partial \theta} = 0$. An example of the maximum eigenvalue behaviour for this case of the skew-varicose instability is shown in figure 2.5(a) in chapter 2.

Second, if the SVI follows the Eckhaus instability, σ_{max} (which is then located on $l = 0$ and $k = k_{max}$ owing to the Eckhaus instability), moves off the k axis. Therefore the SV stability boundary occurs when $l_{max} \to 0$, in which case $\frac{\partial \sigma_{max}}{\partial k^2} = 0$ and $\frac{\partial \sigma_{max}}{\partial l^2} = 0$ at $(k, l) = (k_{max}, 0)$. An example of the maximum eigenvalue behaviour for this case of the skew-varicose instability is shown in figure 2.5(b) in chapter 2.

Cross-roll instability

In the case of CR instability, $\sigma_{max} = 0$ occurs at non-zero (k, l) and when $\sigma_{max} > 0$, the contours of $\sigma_{max} = 0$ do not reach $(k, l) = (0, 0)$. Hence the three conditions are $\frac{\partial \sigma_{max}}{\partial k} = 0$, $\frac{\partial \sigma_{max}}{\partial l} = 0$ and $\sigma_{max} = 0$ at $k = k_{max} \neq 0$ and $l = l_{max} \neq 0$. An example of the maximum eigenvalue behaviour for the CR instability is shown in figure 3.4(a).

Oscillatory skew-varicose instability

The oscillatory skew-varicose instability occurs for stress-free boundary conditions. In this case, we check whether the eigenvalue is complex and consider σ_{max} to be the real part of the eigenvalue and use the same conditions stated in the first case of the skew-varicose instability. An example of the maximum eigenvalue behaviour for the OSV instability is shown in figure 2.15 in chapter 2.

Oscillatory instability

The CR instability can be oscillatory for boundary conditions, where c is positive but not too large. In this case, we check that the extreme of the maximum eigenvalue is complex and we consider σ_{max} to be the real part of the eigenvalue. We then use the same conditions stated above for cross-roll instability. An example of the maximum eigenvalue behaviour for the OI is shown in figure 3.10(a). Note that the contours of zero real part of the eigenvalue do not reach $(k, l) = (0, 0)$.

The remainder of the chapter illustrates the bifurcation diagrams, which we derived using these conditions in MATCONT, for different parameter values.

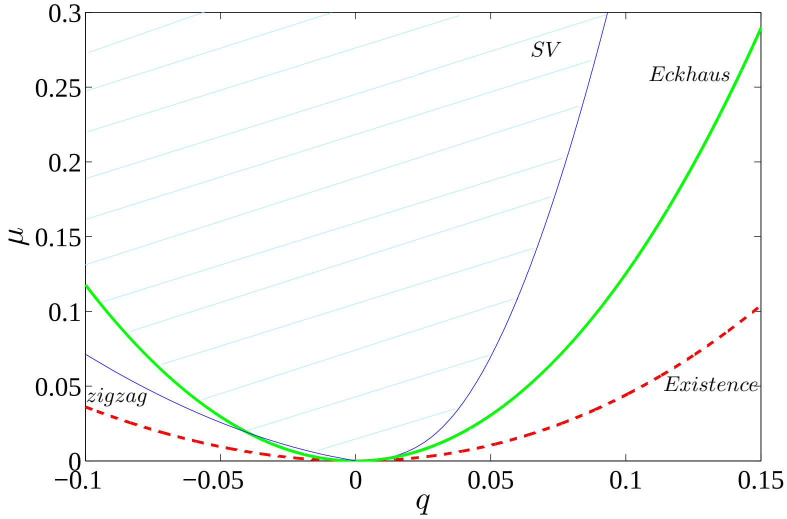

Figure 3.1: *Stability diagram in the neighbourhood of $\mu = 0$ for model 1 with $c^2 = 2$ (no-slip boundary conditions), $Pr = 1$, $g_m = 50$ and $\gamma = 2.5$. Stable stripes are in the region hatched in blue, bounded by zigzag instability and then Eckhaus instability from below and by the SVI boundary from above.*

3.4 Stability Diagrams

In this section, we illustrate our numerical results of model 1, with $Pr = 1$. We choose two illustrative parameter values: $g_m = 50$ and $g_m = 1000$, and three different boundary conditions: no-slip ($c^2 = 2$), stress-free ($c = 0$) and smallish $c > 0$.

3.4.1 No-slip boundary conditions: $c = \sqrt{2}$

Figure 3.1 shows the stability diagram for model 1 with parameter value $c^2 = 2$ (corresponding to no-slip boundary conditions), $Pr = 1$, $g_m = 50$ and $\gamma = 2.5$. The region of stable stripes is bounded by the SVI from above and the Eckhaus instability from below. The zigzag instability boundary for this value of g_m lies below the left Eckhaus boundary except for very small μ and q (as in figure 2). The CR instability does not occur in this range of parameters.

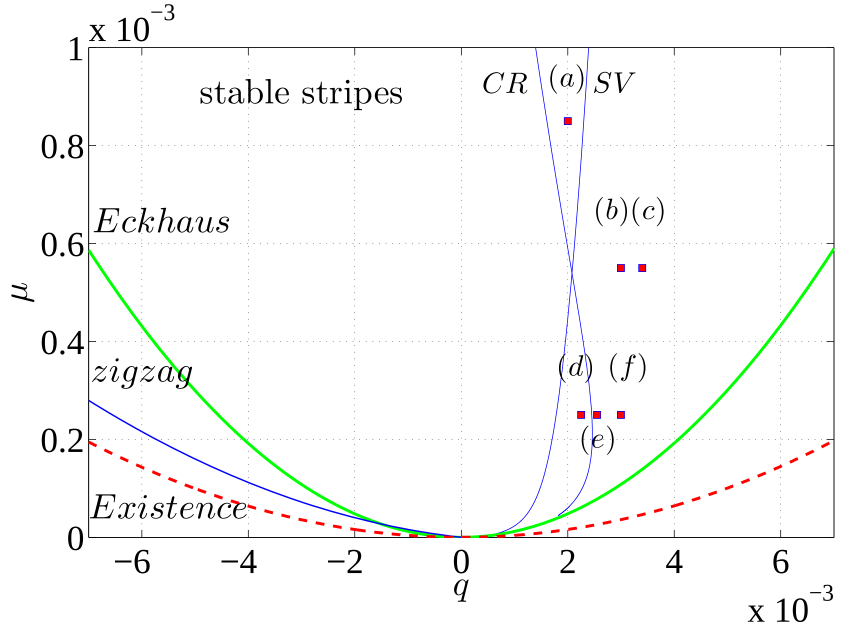

Figure 3.2: *Stability diagram in the neighbourhood of $\mu = 0$ for model 1 with $c^2 = 2$ (no-slip boundary conditions), $Pr = 1$, $g_m = 1000$ and $\gamma = 2.5$. Stable stripes are in the region indicated, bounded by the SV and CR instabilities from above, and by the zigzag and Eckhaus instabilities from below. Growth rates as a function of k and l at the points indicated by (a)–(f) are given in figure 3.4.*

Figures 3.2 and 3.3 show the stability diagram for model 1 with parameters $c^2 = 2$ (no-slip), $Pr = 1$, $g_m = 1000$ and $\gamma = 2.5$. Close to $\mu = 0$ (figure 3.2), a neighbourhood of $q = 0$ is in the stable regime and the zigzag and the SV instabilities bound the region of stable stripes. For $\mu > 5 \times 10^{-4}$, the region of stable stripes is bounded by the CR instability from above and by the Eckhaus instability from below. For this value of g_m, the CR instability boundary crosses the SVI boundary, and the zigzag instability boundary is linear for small μ. For the same parameter values, the stability diagram for a larger range of q and μ is shown in figure 3.3. The region of stable stripes is bounded by the Eckhaus instability from below and the CR instability from above. The zigzag instability boundary lies close to the existence curve and is of less interest for this value of g_m.

Figure 3.4 shows the eigenvalue behaviour at selected points in the (q, μ) space from

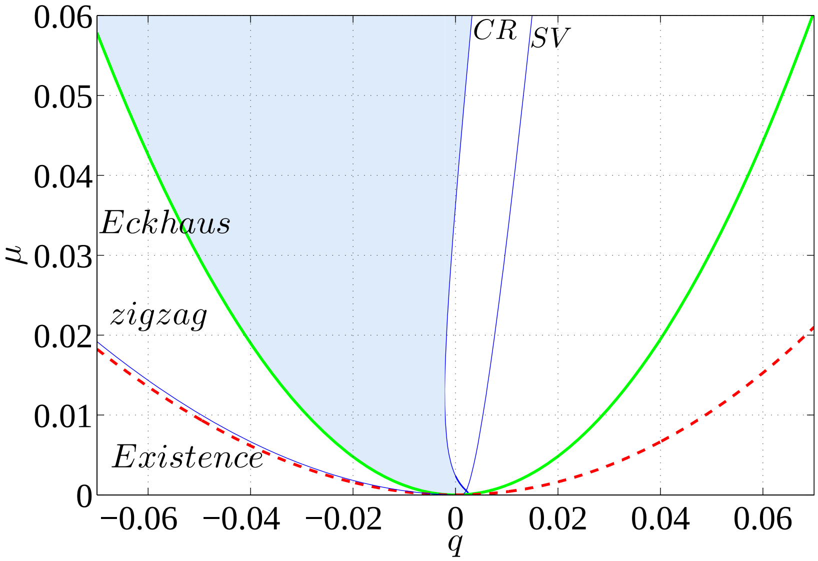

Figure 3.3: *Stability diagram with parameters as in figure 3.2 covering a larger range of q and μ. Stripes are stable in the shaded region, bounded by the Eckhaus, CR and a small part is due to SVI. Stable stripes exist at $q = 0$ for range of μ close to zero.*

figure 3.2, as a function of (k, l), showing how stripes can be unstable to one or both of the SV and CR instabilities. We note that the CR instability occurs for reasonably large values of $k \approx 0.04$ and $l \approx 0.2$ (3.4(a)). In contrast, for the SVI, contours of positive growth rate emerge from $(k, l) = (0, 0)$ (3.4(d)). When both instabilities exist, two separate peaks of growth rates appear (3.4(b) & 3.4(e)). For larger q, these contours can join to form one large contour (3.4(c) & 3.4(f)).

We have computed the stability diagrams for model 2 with $g = 500$ and $g = 25$, and these are qualitatively the same as figures 3.1 and 3.2, consistent with the relation $g = g_m/Pr\, c^2$.

3.4.2 Stress-free boundary conditions: $c = 0$

Figures 3.5 and 3.7 similarly show the instability boundaries for model 1, with parameters $c = 0$ (corresponding to stress-free boundary conditions), $Pr = 1$, $\gamma = 2.5$ and $g_m = 1000$

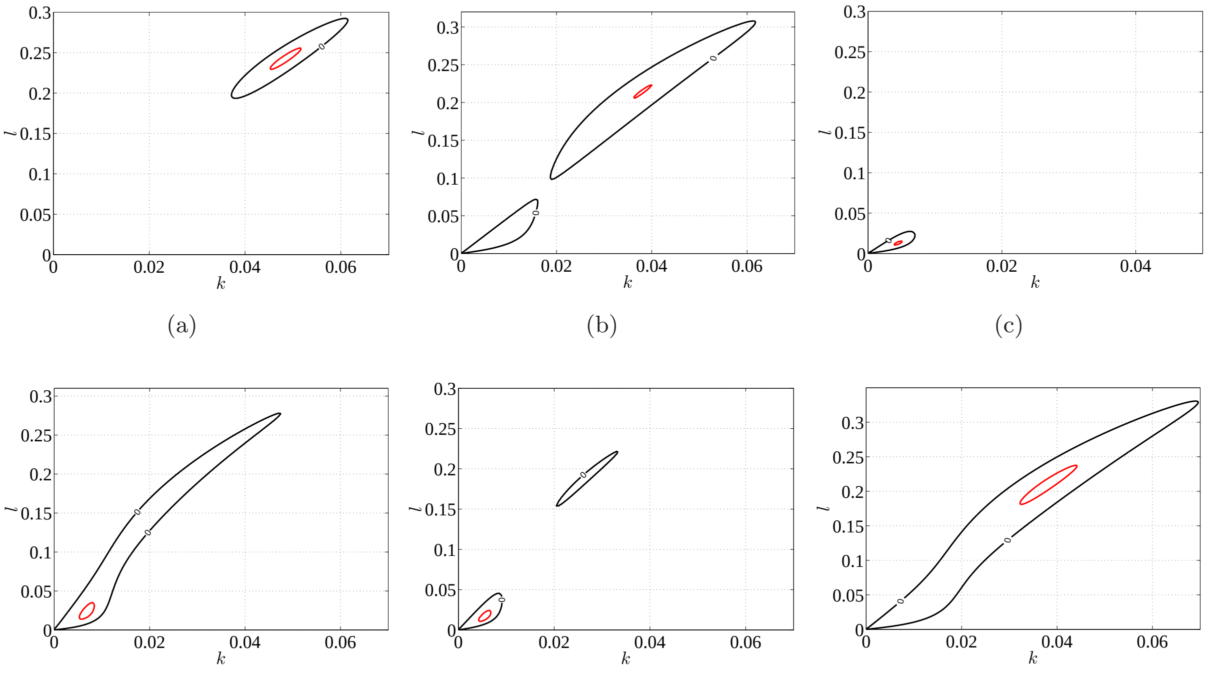

(a) (b) (c)

(d) (e) (f)

Figure 3.4: *Growth rates of perturbations at selected* (μ, q) *indicated by (a)–(f) in figure* 3.2. *(a)* $\mu = 8.5 \times 10^{-4}$, $q = 0.002$*; stripes are CR unstable, but growth rates for* k *and* l *close enough to zero are negative. (b)* $\mu = 5.5 \times 10^{-4}$, $q = 0.003$*; stripes are CR and SV unstable. Growth rates for* k *and* l *close enough to zero become positive due to the SVI and there are two distinct zero contours. (c)* $\mu = 5.5 \times 10^{-4}$, $q = 0.0034$*; stripes are CR and skew-varicose unstable. One large zero contour encloses both the SV and CR instabilities. (d)* $\mu = 2.5 \times 10^{-4}$, $q = 0.00225$*; stripes are skew-varicose unstable, and growth rates for* k *and* l *close enough to zero are positive for a range of polar angles. (e)* $\mu = 2.5 \times 10^{-4}$, $q = 0.0025$*; same as case (b), but the maximum occurs in the SV region. (f)* $\mu = 2.5 \times 10^{-4}$, $q = 0.003$*; same as case (c), but again the maximum occurs in the SV region. The zero contour is denoted in black (outer) and contours of positive growth rate are denoted in red.*

and $g_m = 50$. The results agree qualitatively with earlier calculations by Bernoff [93], who found a similar linear relation between μ and q for the SV and OSV instabilities in convection with stress-free boundary conditions; he did not consider the CR instability.

Disregarding the CR instability, stripes would be stable between the OSV instability and SVI boundaries. However, as seen in figure 3.5, the SVI is always preempted by the CR instability; these boundaries appear to be parallel for larger μ. For $\mu < 0.32$, there are

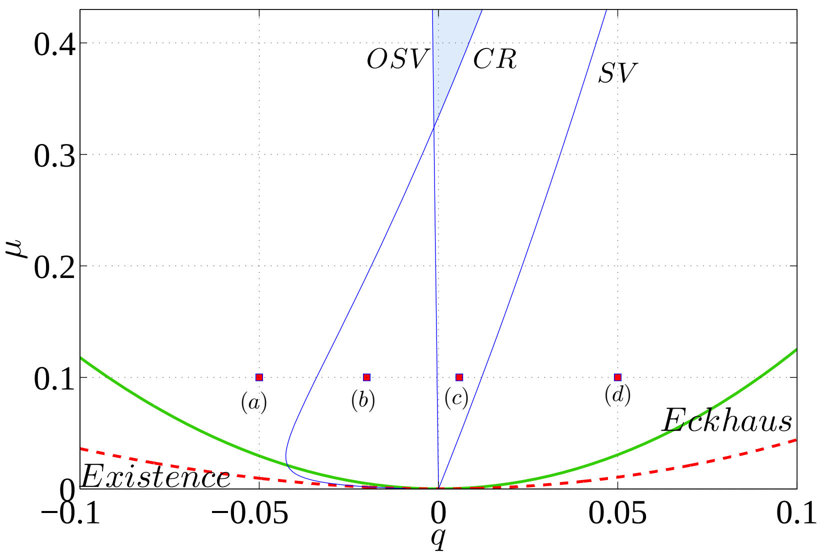

Figure 3.5: *Stability diagram for model 1 with* $c = 0$ *(stress-free boundary conditions),* $Pr = 1$*,* $g_m = 1000$ *and* $\gamma = 2.5$*. Stripes are skew-varicose unstable to the right of the SVI boundary, OSV unstable to the left of the OSV boundary and CR unstable to the right of the CR boundary. Stable stripes exist for* $\mu > 0.32$*; the region of stable stripes is shaded, and is bounded by the OSV instability boundary on the left and the CR boundary on the right. Growth rates as a function of* k *and* l *at the points indicated by (a)–(d) are given in figure 15.*

no stable stripes. For higher μ, the stable region is bounded by the CR instability from above and by the OSV instability from below.

Figure 3.6 shows the change of structure of the eigenvalues when moving from left to right in the stability diagram shown in figure 3.5. At $\mu = 0.1$, we selected four different wavenumbers: $q = -0.05$, where stripes are OSV unstable (3.6(a)), $q = -0.02$, where stripes are CR and OSV unstable (3.6(b)), $q = 0.0058$, where stripes are CR unstable but OSV stable and $q = 0.05$ (3.6(c)), where stripes are CR and skew-varicose unstable, though the distinction between these two instabilities has become blurred (3.6(d)).

Figure 3.7 presents instability boundaries for stress-free boundary conditions with $Pr = 1$, $g_m = 50$ and $\gamma = 2.5$. This provides an illustration of the change of the CR instability

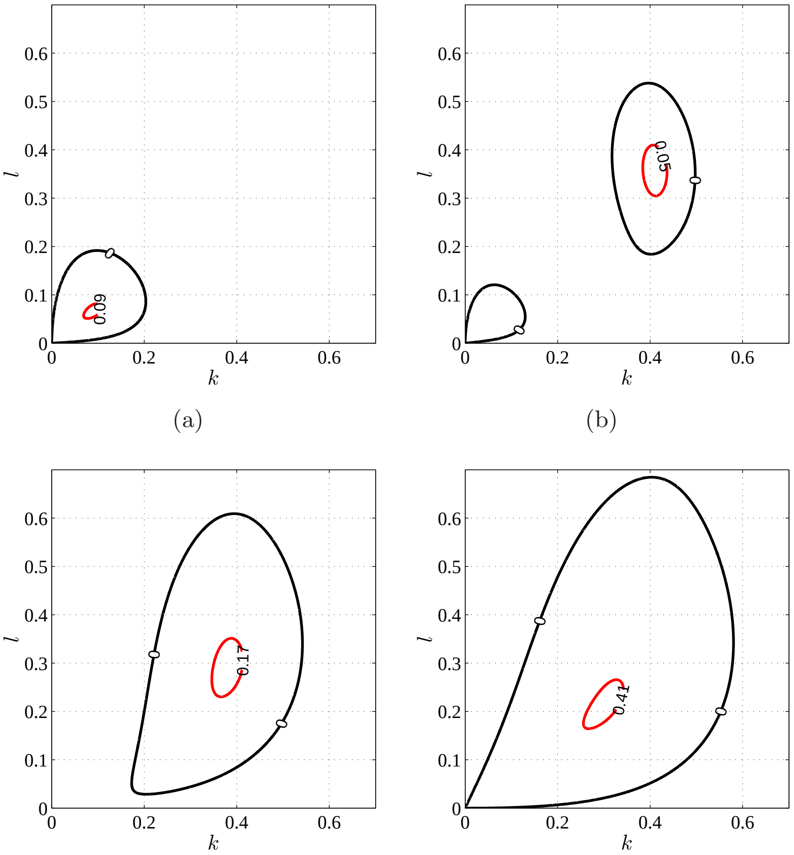

(a) (b)

(c) (d)

Figure 3.6: *Growth rates of perturbations at selected* (μ, q) *indicated in figure 3.5, all with* $\mu = 0.1$. *(a)* $q = -0.05$*, where stripes are OSV unstable. (b)* $q = -0.02$*, where stripes are CR and OSV unstable. (c)* $q = 0.0058$*, where stripes are CR unstable but OSV stable. (d)* $q = 0.05$*, where stripes are CR and skew-varicose unstable, though the distinction between these two instabilities has become blurred. The zero contour of the real part of the eigenvalue is denoted in black and contours of positive growth rate are in red. The eigenvalues in the OSV case are complex.*

boundary with g_m. For $g_m = 50$, the CR instability boundary crosses the SVI boundary and the effect of the CR instability is reduced.

3.4.3 Nearly stress-free boundary conditions: $c > 0$

The parameter c, approximates the no-slip boundary conditions in convection when $c = \sqrt{2}$ and stress-free boundary condition in convection when $c = 0$. It is interesting to determine

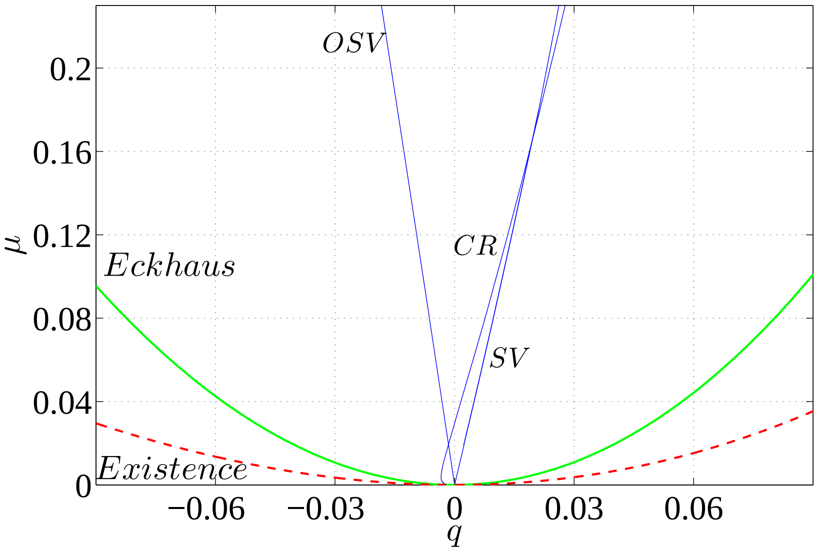

Figure 3.7: *Stability diagram for model 1 with $c = 0$ (stress-free boundary conditions), $Pr = 1$, $g_m = 50$ and $\gamma = 2.5$. Stable stripes exist for $\mu > 0.02$; the region of stable stripes is bounded by the OSV boundary on the left and the CR boundary and then the SV on the right.*

how the stability diagram changes when c is increased from 0. Therefore, in this section, we introduce the stability diagram for small c.

Figure 3.8 shows the stability diagram for model 1 with parameter values $c = 0.1$, $Pr = 1$, $g_m = 50$ and $\gamma = 2.5$. The region of stable stripes is bounded by the CR instability from above and the oscillatory instability from below. Stripes are unstable to the left of the OI boundary and to the right of the CR boundary. The CR instability preempts the SVI for lower values of μ. Thus, when the parameter value c is slightly increased from zero, the OSV instability seems to turn in to the oscillatory instability.

Figure 3.9 shows the stability diagram for model 1 with parameter values $c = 0.1$, $Pr = 1$, $g_m = 1000$ and $\gamma = 2.5$. The stability diagram is qualitatively the same as that in figure 3.5 ($c = 0$, with the other parameters the same). The main difference is that the OSV boundary is replaced by the oscillatory instability boundary. As seen in figure 3.9, the SVI is always preempted by the CR instability; these boundaries appear to be parallel

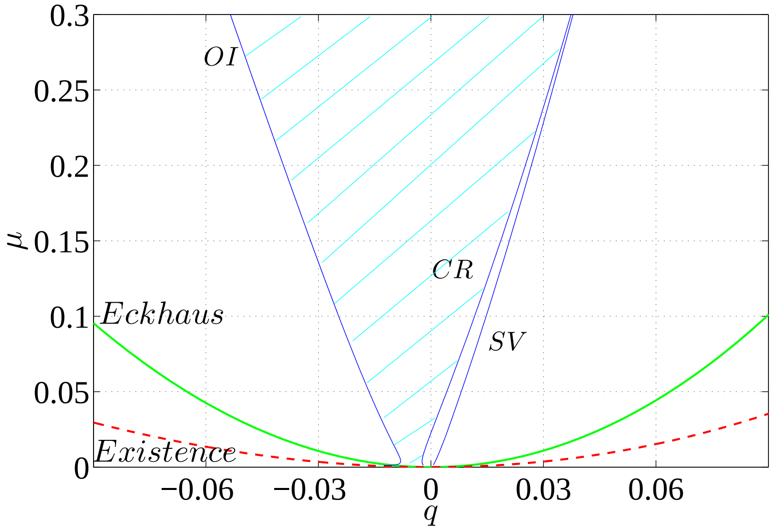

Figure 3.8: *Stability diagram for model 1 with $c = 0.1$, $Pr = 1$, $g_m = 50$ and $\gamma = 2.5$. The OI boundary extends from the existence boundary and hence it crosses the Eckhaus boundary when $q = -0.01$. The CR instability boundary preempts the SV boundary when $\mu < 0.35$. The region of stable stripes, which is hatched in blue, is bounded by the Eckhaus instability and then OI boundary on the left and the CR boundary on the right.*

for larger μ. For $\mu < 0.28$, there are no stable stripes. For higher μ, the stable region is bounded by the CR instability from above and by the OI from below. Figure 3.10 shows the change of the structure of the eigenvalues at selected points in the (q, μ) space from figure 3.9; at the wavenumber $q = -0.01$, we select $\mu = 0.3$, where stripes are unstable to the OI and $\mu = 0.2$, where stripes are unstable to the OI and CR instability. We note that the CR instability, as before, occurs for reasonably large values of k and l. The eigenvalues for OI are complex and the contours of positive growth rate emerge from smaller (but non-zero) k and l (figure 3.10(a)). When both instabilities exist, two separate peaks of growth rates appear (figure 3.10(b)).

We have computed the stability diagrams for model 2 with $g = 5000$ and $g = 10^5$, in order to keep the consistency with the relation $g = g_m/Pr\, c^2$ for the boundary condition $c = 0.1$ and the parameter values $Pr = 1$, $g_m = 50$ and $g_m = 1000$. However, the oscillatory instability is absent in model 2, owing to the $Tr(J_2) < 0$ prevents complex

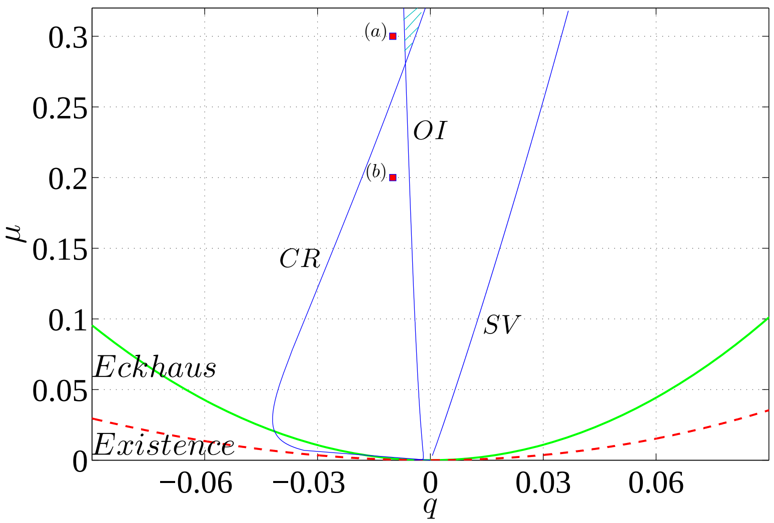

Figure 3.9: *Stability diagram for model 1 with $c = 0.1$, $Pr = 1$, $g_m = 1000$ and $\gamma = 2.5$. Stripes are skew-varicose unstable to the right of the SVI boundary, OI unstable to the left of the OI boundary and CR unstable to the right of the CR boundary. Stable stripes exist for $\mu > 0.28$; the region of stable stripes is hatched, and is bounded by the OI instability boundary on the left and the CR boundary on the right. Growth rates as a function of k and l at the points indicated by (a) and (d) are given in figure 3.10*

eigenvalues. In contrast, the SVI and CR instabilities have the same qualitative behaviour and since the OI is absent, stripes are stable over a wide range in (q, μ).

We now examine in more detail how the CR and OI boundaries depend on c. We illustrate the numerical results using two parameter values, $g_m = 50$ and $g_m = 1000$. It is evident in figure 3.11 that the cross-roll instability, for $c = 0.01$ and $c = 0.2$ depends strongly on g_m but only weakly on c. Small values of g_m reduce the effect of the CR instability so the location of the CR instability boundary moves to higher q. Comparing the CR instability boundaries in figure 3.11 with stress-free boundary conditions (figures 3.5 and 3.7), we can conclude that the CR instability has a qualitatively similar behaviour for a range of c, which we have found to be $0 \leq c < 1$.

On the other hand, the OI depends crucially on both g_m and the choice of the boundary condition value c. For the case $c = 0.01$, as depicted in figure 3.11(a), the OI boundary

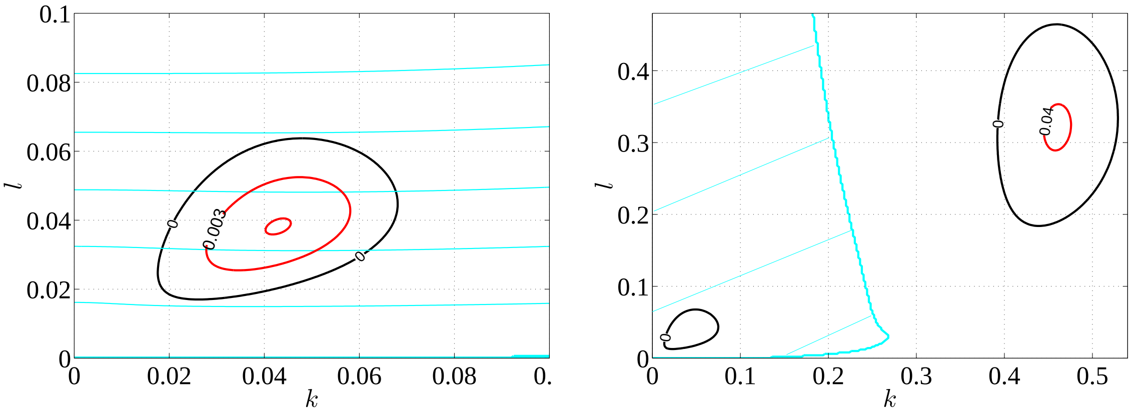

(a) (b)

Figure 3.10: *Growth rates of perturbations at selected* (μ, q) *indicated in figure 3.9, all with* $q = -0.01$. *(a)* $\mu = 0.3$, *where stripes are OI unstable. (b)* $\mu = 0.2$, *where stripes are CR and OI unstable. The zero contour of the real part of the eigenvalue is denoted in black and contours of positive growth rate are in red. The eigenvalues in the OI case are complex; blue thick contour denotes the zero imaginary part of the eigenvalue and the hatched region is where the eigenvalue complex.*

is qualitatively same as the OSV boundary for the stress-free boundary conditions (figure 3.5). In this case the OI boundary, for both values of g_m, extends linearly from $(\mu, q) = (0, 0)$. However, for larger c, the OI boundary moves to smaller wavenumber, starting on the existence curve $\beta = 0$. This identifies the starting point of the OI boundary to be a point where a Hopf bifurcation occurs. We find that for any value of g_m, the OI disappears when c is increased above about 0.6. As with the CR instability, small g_m reduces the effect of the OI instability.

3.5 The role of mean-flows

In this section we study the effect of the mean flow, presenting the stability diagrams in a different manner to emphasis the dependence on g. For a fixed μ, we show how the coupling to the mean flow affects the region of stable stripes. This choice of presentation

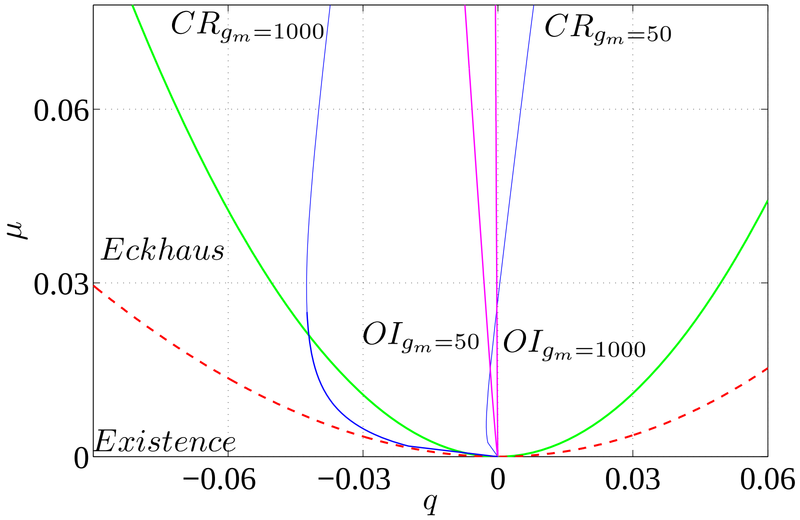

(a)

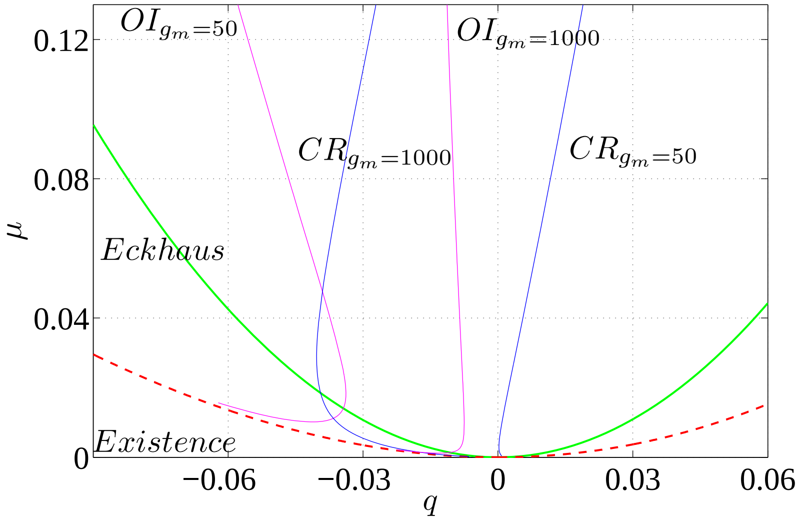

(b)

Figure 3.11: *Effect of* c *and* g_m *on the CR and OI boundaries. Stability diagram for model 1 with* $Pr = 1$, $\gamma = 2.5$ *and two different parameter values,* $g_m = 50$ *and* 1000. *(a)* $c = 0.01$. *The OI boundary seems to be linear and it extends from* $(\mu, q) = (0, 0)$ *(b)* $c = 0.2$. *The OI boundary appears with Hopf bifurcation close to the existence boundary and this bifurcation is very sensitive to the value of* g_m. *In both cases, small* g_m *suppresses the CR boundary to the right and the OI boundary to the left. CR boundary is denoted in blue and the OI boundary is in pink.*

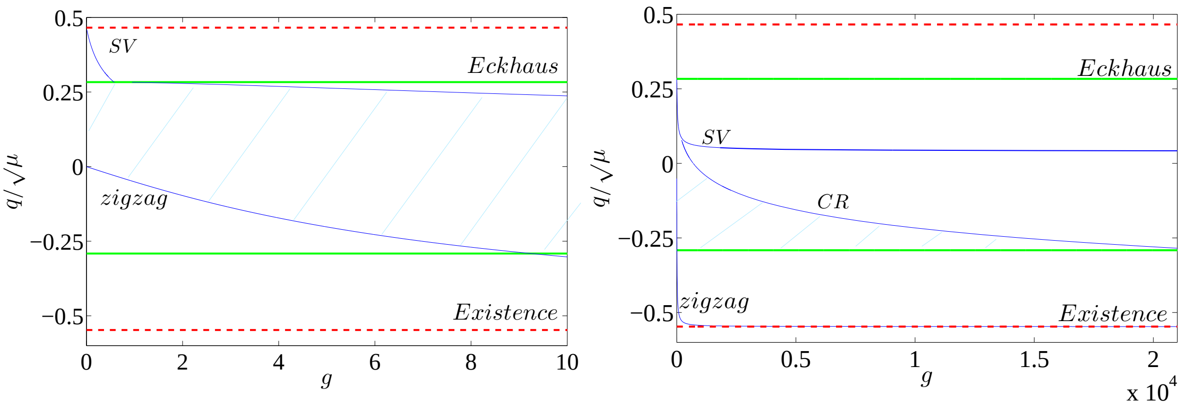

(a) (b)

Figure 3.12: *Stability diagrams in $(g, q/\sqrt{\mu})$ plane for model 2 with $\mu = 0.1$ and $\gamma = 2.5$. (a) For small g: the region of stable stripes is mainly bounded by zigzag and SV instabilities. (b) For large g, the region of stable stripes is bounded by the Eckhaus (thick green) and CR instabilities. These instability boundaries cross around $g = 2 \times 10^4$, eliminating the region of stable stripes. The region of stable stripes is hatched.*

provides useful information for numerical simulations of the PDEs in large domains.

3.5.1 No-slip boundary conditions

Figure 3.12 represents the region of stable stripes for model 2 in the $(g, q/\sqrt{\mu})$ plane for $\mu = 0.1$. We choose $q/\sqrt{\mu}$ as the coordinate for ease of comparison between different values of μ and with this choice, parabolas in the (q, μ) plane become a single value of $q\sqrt{\mu}$. Figure 3.16(a) shows the stability diagram for small g, where the region of stable stripes is bounded from above by the Eckhaus instability for $g < 0.574$ and by the SVI for $g > 0.574$, and by the zigzag instability from below. Figure 3.12(b) shows how for large g, the region of stable stripes is bounded by the CR instability from above and by the Eckhaus instability from below. There are no stable stripes for $g \gtrsim 2 \times 10^4$. Figure 3.13 shows the location of the CR instability for $\mu = 0.01, 0.001$ and 0.0001. The upper bound on g, beyond which there are no stable stripes, initially decreases with μ and then increases. The behaviour of model 1 with $c^2 = 2$, $Pr = 1$ is qualitatively the same.

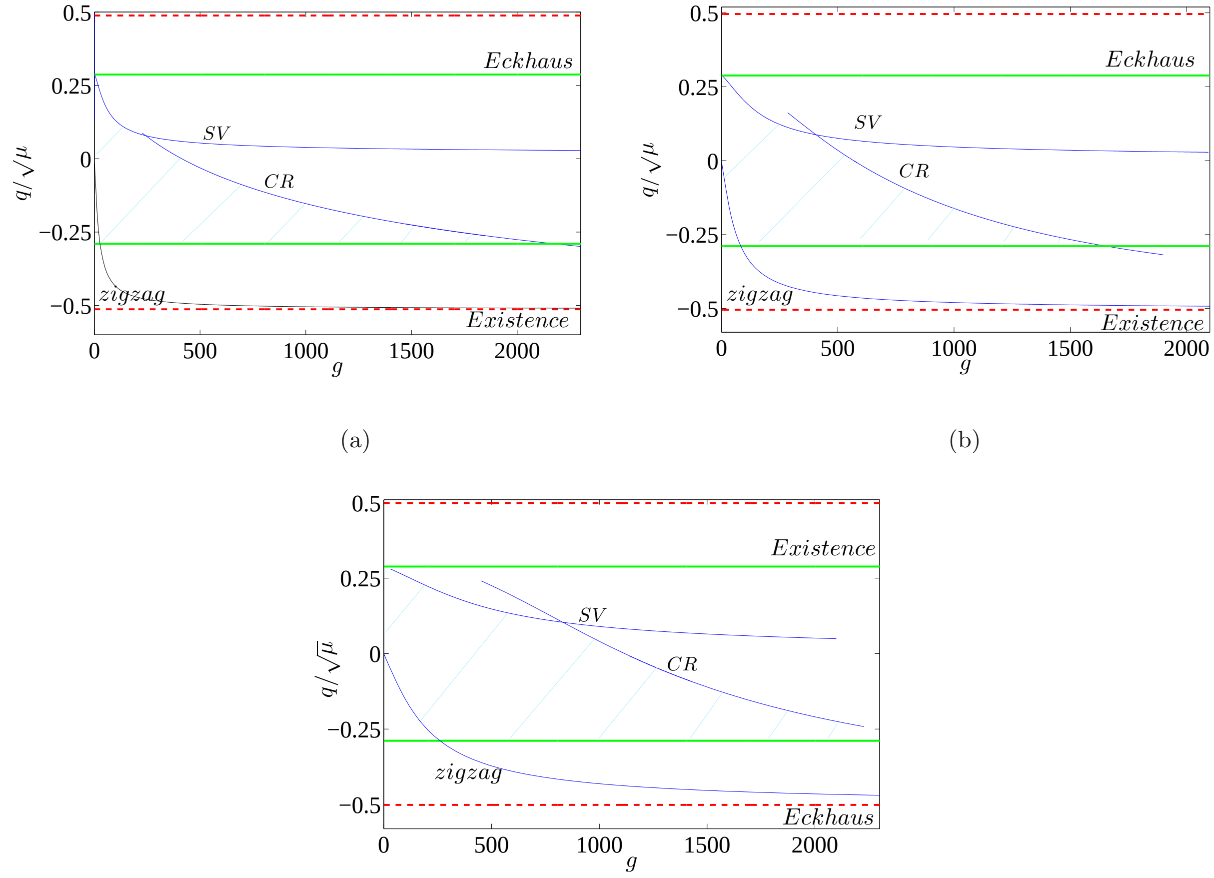

(a) (b)

(c)

Figure 3.13: *Stability diagrams in* $(g, q/\sqrt{\mu})$ *plane for model 2 with* $\gamma = 2.5$. *(a)* $\mu = 0.01$, *(b)* $\mu = 0.001$ *and (c)* $\mu = 0.0001$. *In all three cases CR instability reduces the region of stable stripes which is hatched.*

3.5.2 Stress-free boundary conditions

Figure 3.14 presents stability diagrams for model 1 with $c = 0$ (stress-free boundary conditions), for $\mu = 0.1$ and $\mu = 0.01$. The SV and the OSV instabilities bound the region of stable rolls from above and below and the CR instability makes the upper bound on g_m. Stable stripes exist only for small g_m and the upper bound on g_m is further reduced with μ.

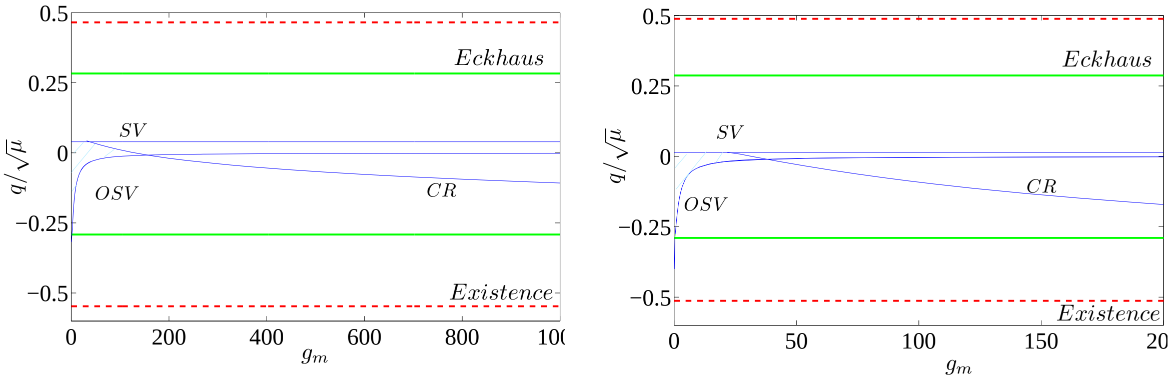

(a) (b)

Figure 3.14: *Stability diagrams in $(g_m, q/\sqrt{\mu})$ plane with $c = 0$ (stress-free boundary conditions), $Pr = 1$ and $\gamma = 2.5$. (a) $\mu = 0.1$ and for large g_m: stable stripes are completely eliminated when $g_m \gtrsim 130$. (b) $\mu = 0.01$ and for small g_m. In all three cases, the region of stable stripes (hatched) is mainly bounded by the OSV, SV and CR instabilities, and the CR instability makes the upper bound in g_m and reduces the region of stable stripes with μ.*

3.6 The effect of Prantl number, Pr

In this section we study the effect of varying Pr, presenting the stability diagrams in the $(1/Pr, q/\sqrt{\mu})$ plane. We choose $q/\sqrt{\mu}$ as the coordinate for ease of comparison between different values of μ. For a fixed μ, we show how Pr affects the region of stable stripes. This choice of coordinates supports to show the relation $g = (\frac{g_m}{c^2})\frac{1}{Pr}$.

3.6.1 No-slip boundary conditions

Figure 3.15 represents the region of stable stripes for model 1 in the $(1/Pr, q/\sqrt{\mu})$ plane for $\mu = 0.1$ and $\mu = 0.001$ with $c^2 = 2$ and $g_m = 50$. Figure 3.15(a) shows when $\mu = 0.1$ the region of stable stripes is eliminated when $1/Pr \gtrsim 800$. The upper bound on $1/Pr$ beyond which there are no stable stripes initially decreases with μ and then increases. This stability diagram is similar to the figure 3.12(b) with $g = 25\frac{1}{Pr} = g_m/(Pr\, c^2)$; figure 3.12(b) shows that the region of stable stripes is eliminated when $g \gtrsim 2 \times 10^4$.

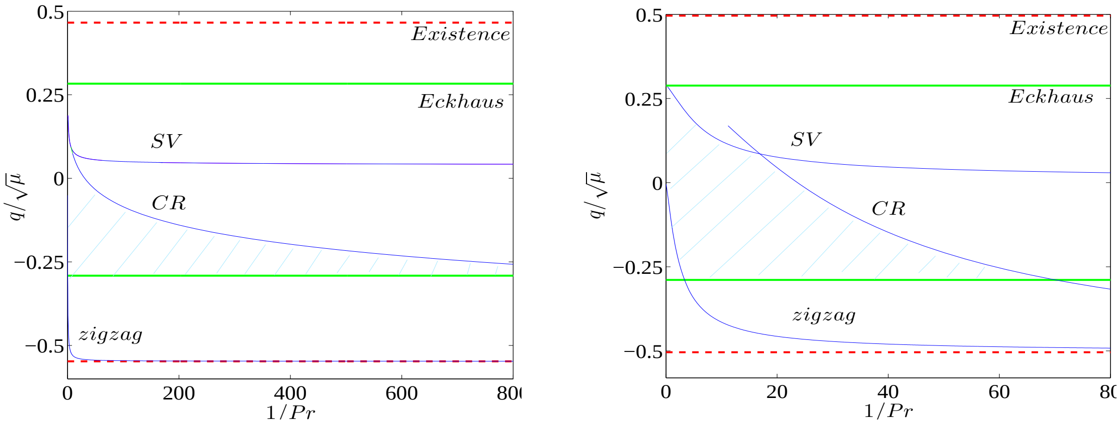

(a) (b)

Figure 3.15: *Stability diagrams in* $(1/Pr, q/\sqrt{\mu})$ *plane for model 1 with* $g_m = 50$, $c^2 = 2$ *and* $\gamma = 2.5$. *(a)* $\mu = 0.1$ *(b)* $\mu = 0.001$. *For small* Pr, *the region of stable stripes is bounded by the Eckhaus (thick green) and CR instabilities. These instability boundaries cross around* $1/Pr \approx 800$ *in (a) and* $1/Pr \approx 65$ *in (b), eliminating the region of stable stripes. The region of stable stripes is hatched. The stability diagrams (a) and (b) are similar to 3.12(b) and 3.13(b) respectively with* $\frac{1}{Pr} = \frac{g}{25}$.

Figure 3.15(a) shows the region of stable stripes and how it is bounded by the CR instability from above and by the Eckhaus instability from below for $\mu = 0.001$. The region of stable stripes is completely eliminated when $1/Pr \gtrsim 65$. This stability diagram is similar to the figure 3.13(b) if we consider $g = 25/Pr = g_m/(Pr\, c^2)$.

3.6.2 Stress-free boundary conditions

Figure 3.16 presents stability diagrams for model 1 with $c = 0$ (stress-free boundary conditions), for $\mu = 0.1$. Stable stripes exist only for large Pr; the SV and the OSV instabilities bound the region of stable rolls from above and below and the CR instability makes the upper bound on $1/Pr$ (upper bound is at $1/Pr \approx 2.6$). The stability diagram is similar to figure 3.14(b) with $\frac{1}{Pr} = \frac{g_m}{50}$. This is due to the fact that for $c = 0$ the ratio, g_m/Pr is preserved by the instabilities.

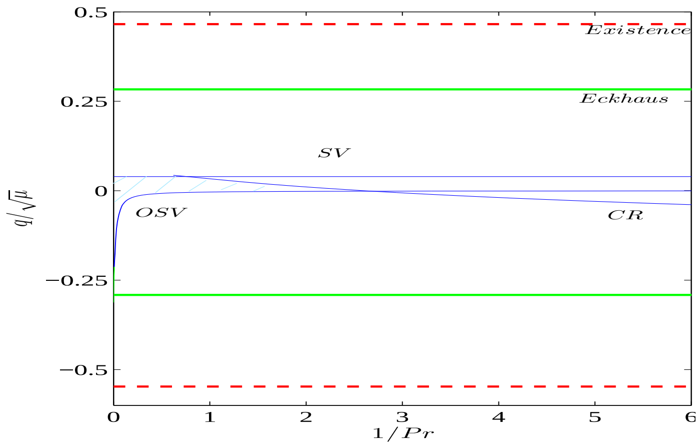

(a)

Figure 3.16: *Stability diagrams in* $(1/Pr, q/\sqrt{\mu})$ *plane with* $c = 0$ *(stress-free boundary conditions),* $g_m = 50$ *and* $\gamma = 2.5$*.* $\mu = 0.1$ *and for small* Pr*: stable stripes are completely eliminated when* $1/Pr \gtrsim 2.6$*. The region of stable stripes (hatched) is mainly bounded by the OSV, SV and CR instabilities, and the CR instability makes the upper bound in* $1/Pr$*. The stability diagram is similar to 3.14(b) with* $\frac{1}{Pr} = \frac{g_m}{50}$*.*

3.7 The effect of filtering coefficient, γ

The filtering operator, $\mathcal{F}_\gamma$, is used to reduce the short-wavelength modulations of the mean flow and we use it to suppress the cross-roll instability. So far we have illustrated results for $\gamma = 2.5$. We now discuss how this filtering coefficient γ affects the cross-roll instability and hence the region of stable stripes. Figure 3.17 illustrates the stability diagrams of model 2 in $(g, q/\sqrt{\mu})$ for $\mu = 0.1$ and $\gamma = 1.5, 2.5$ and 3.5. As shown in the figure, different choices of γ change the cross- roll instability. Figure 3.17(a) shows the stability diagram for no-slip boundary conditions. The CR instability makes the upper bound in g to the region of stable stripes and the upper bound increases for larger γ. When $\gamma = 3.5$, cross-roll instability boundary extends parallel to the SVI boundary for large g and the region of stable stripes is not eliminated for any g. When $\gamma = 0$, the region of stable stripes further decreases retaining a small region of stable stripes for smaller g. Figure 3.17(b) shows the

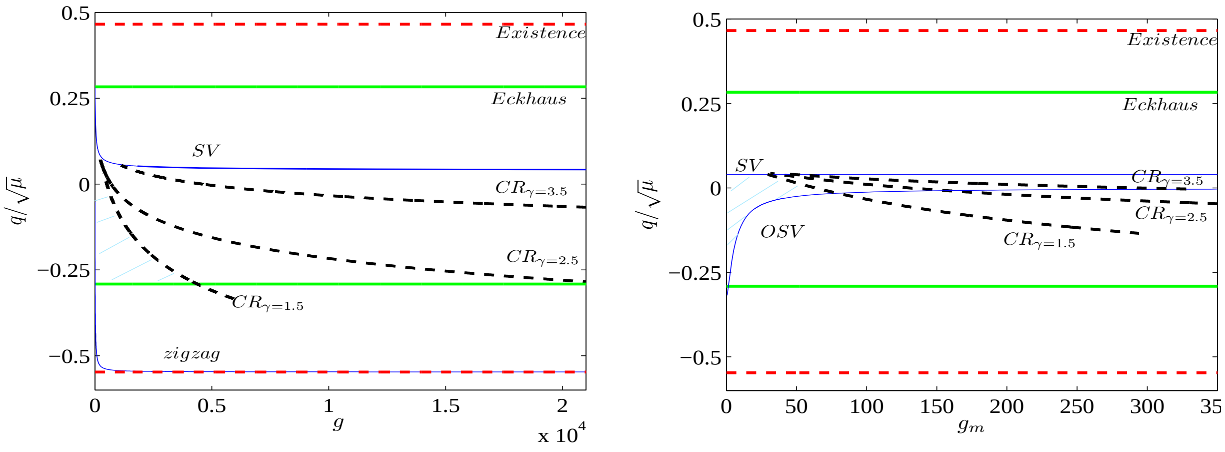

(a)

(b)

Figure 3.17: *Effect of the filtering coefficient* γ *for cross roll instability. Stability diagrams in* $(g, q/\sqrt{\mu})$ *plane for model 2 with* $\mu = 0.1$ *and for* $\gamma = 1.5$, 2.5 *and* 3.5*. (a) No-slip boundary conditions* ($c^2 = 2$)*. The region of stable stripes is mainly bounded by Eckhaus and cross-roll instabilities. These instability boundaries cross around* $g \approx 4.3 \times 10^3$, $g \approx 2 \times 10^4$ *and* $\gamma = 1.5$, 2.5 *and* 3.5 *respectively and no crossing for* $\gamma = 3.5$*, giving larger regions of stable stripes for higher* γ*. (b) Stress-free boundary conditions* ($c = 0$)*. CR instability makes the upper bound in* g *to the region of stable stripes and the upper bound increases for larger* γ*. The region of stable stripes for* $\gamma = 1.5$ *is hatched.*

stability diagram for stress-free boundary conditions. The CR instability makes the upper bound in g to the region of stable stripes. This upper bound increases for larger γ and the effect of γ is not significant as that for no-slip boundary conditions.

3.8 Curious behaviour of growth rates

We report here an observation of the curious behaviour of the growth rates of some modes, which, to the best of our knowledge, has not been previously observed earlier in any model of the Swift–Hohenberg equation.

In previous sections, we considered the growth rate behaviour for (k, l) close to zero.

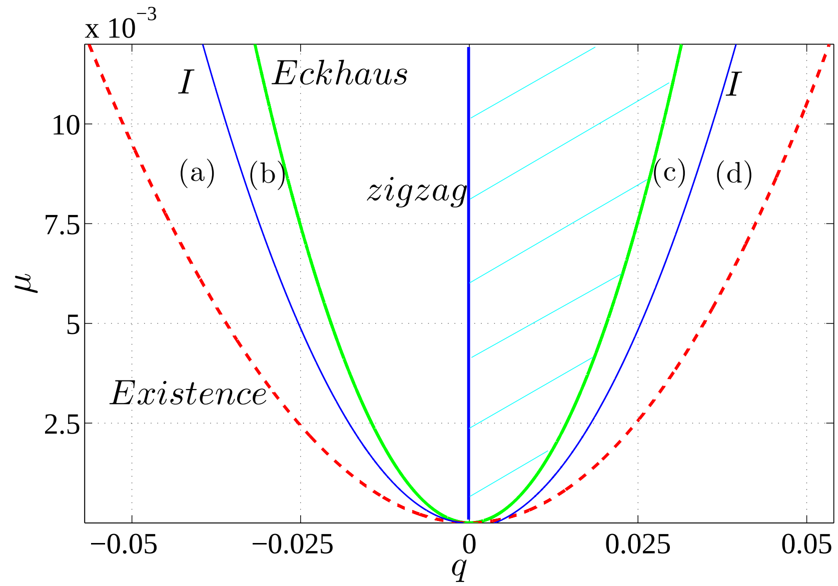

Figure 3.18: *Stability diagram for Swift–Hohenberg equation(models 1 and 2 with* $g = 0$*) (2.1). The* I *instability boundary generates positive growth rates for some large* k *and* l *and this instability occurs in regions (a) and (d). is due to the curious behaviour of growth rates, which is shown in figure 3.19. The region of stable stripes, which is hatched in blue, is not affected by the* I *instability. Growth rates as a function of* k *and* l *in the regions indicated by (a)–(d) are given in figure 3.19*

However, when a larger range of k and l is considered, we noticed additional instabilities in the regime where stripes are already unstable. These instabilities occur even in the SHE and so are not related to presence of the mean-flow. They have not been studied before, though they are of less interest since they do not bound the region of stable stripes. We consider them briefly here.

Figure 3.18 shows the stability diagram of model 2 with $g = 0$, which is same as the ordinary Swift–Hohenberg equation. The parabolic boundary indicated by I shows the instability associated with this curious behaviour; it occurs between the Existence and the Eckhaus boundaries.

Contours of the growth rates of perturbations for selected parameter values in regions indicated by (a)–(d) in figure 3.18 are shown in figure 3.19. As shown in figure 3.19(a),

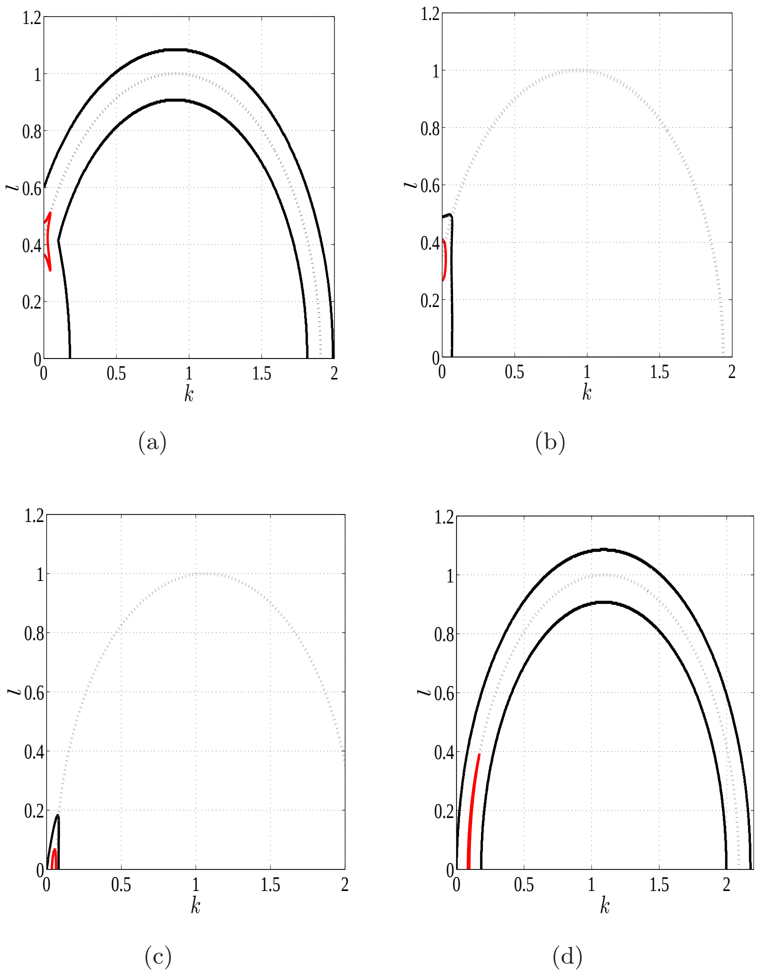

(a) (b)

(c) (d)

Figure 3.19: *Growth rates of perturbations as a function of* (k, l) *for the Swift–Hohenberg equation (2.1), with* ψ^3 *replaced by* $P_\alpha(\psi^3)$*. Figures (a) and (b) correspond to points in the left Eckhaus band,* $q < 0$*, whereas (c) and (d) correspond to points in the right Eckhaus band,* $q > 0$*. (a) Stripes are zigzag and Eckhaus unstable, and additional unstable modes lie approximately in a annulus of unit radius centred at* $(k, l) = (1 + q, 0)$*. (b) Stripes are zigzag and Eckhaus unstable. (c) Stripes are Eckhaus unstable. (d) Stripes are Eckhaus unstable and in addition, an annulus of unit radius centred at* $(k, l) = (1+q, 0)$ *has positive real eigenvalues. Thick black: zero contour. Red: positive contour. Dotted line: circle of unit radius centred at* $(k, l) = (1 + q, 0)$*.*

for a fixed small μ, when q is increased from the left existence boundary ($q < 0$), modes approximately in an annulus of unit radius centered at $(k, l) = (1 + q, 0)$ have positive real eigenvalues in addition to unstable modes for small k and l, corresponding to the Eckhaus and zigzag instabilities. This annulus disappears for larger q (in region (b)) leaving only the Eckhaus and zigzag unstable modes close to $(k, l) = (0, 0)$, as is shown in figure 3.19(b). This process is in part reversed for $q > 0$ going towards the right existence boundary. First are Eckhaus unstable only, close to the Eckhaus boundary (in region (c)) but for large enough q (in region (d)), the annulus of unstable modes reappears. The behaviour of growth rates in the right Eckhaus band is illustrated in figure 3.19(c) and 3.19(d).

We use the solutions of PDEs to check whether this curious behaviour is due to our projection and hence the stability calculations. Interestingly the comparison of the eigenvalues of the Jacobians with the growth rates of relevant modes, which is taken by the calculations of PDEs, confirms that this curious behaviour is not a result of using the projection operator P_α in the Swift–Hohenberg equation so that it does occur in the full equations.

3.9 Concluding remarks

In this chapter we have used the continuation package MATCONT in order to calculate bifurcation lines corresponding to instabilities that appear due to the mean flow. We outlined the numerical method and conditions on eigenvalues for each instability. We confirmed the analytical results in chapter 2 by numerical computations of the eigenvalues of the stability matrices and these eigenvalues also allowed us to explore short-wavelength instabilities: cross-roll and the oscillatory instabilities. We extended our study to three values of c, which controls the boundary conditions: $c = \sqrt{2}$, $c = 0$ and $c = 0.1$. The selection of the value $c = 0.1$ leads us to understand the transition between the stress-free to no-slip boundary conditions. We presented contours in perturbation space to illustrate the eigenvalue behaviour of each instability and combined instabilities.

The interesting oscillatory instability (OI) occurs for small values of c and it arises from a Hopf bifurcation at $\beta = 0$ in model 1. For this reason, the OI does not appear for very large g in model 2 in which Hopf bifurcations are excluded. The cross-roll instability, despite the filtering operator, seems to eliminate a range of stable stripes for $c < 1$ and large g_m. Therefore the region of stability of stripes is eliminated for small μ and large enough g_m when $c < 1$.

We illustrated stability diagram in order to understand the effect of the mean flow on the region of stable stripes, using which we highlighted again that a large value of the coupling constant to the mean flow significantly affect the region of stable stripes. We also presented the stability diagrams to show the effect of Pr on the region of stable stripes and we established again that the relation $g = g_m/Pr\, c^2$ is preserved. Even for the stress-free boundary conditions ($c = 0$), the ratio g_m/Pr is preserved by the parameter values of g_m and Pr of model 1.

Finally we discussed the effect of the filtering coefficient on the cross-roll instability. The region of stable stripes improves for higher values of γ and effect of γ is significant on cross-roll instability for no-slip boundary conditions.

We now have a complete understanding of the stability diagrams for any given parameter of our models of interest. Therefore the results of this work provide useful information for the choice of parameters for different instability regimes in model 1 and model 2. This work also justifies using model 2 with large g, since this has been shown to have similar instability boundaries for the skew-varicose, cross-roll, zigzag and Eckhaus as to model 1.

We finally comment on the implications of our analysis on the direct numerical simulations of PDEs in large domains. The most striking signature of the inclusion of a mean-flow is the existence of the skew-varicose instability, which can play an important role in the formation of the spiral defect chaos or defect chaos [6, 47]. Hence the improved understanding of the stability of stripes in this work provides a foundation for numerical simulations of spiral defect chaos and defect chaos. The SDC state exists inside the Busse balloon, where convection rolls are stable [38]. We suspect that the defect chaos (DC) state also exists due to the cross-roll and skew-varicose instabilities. Thus we intend in next chapter to relate the SDC and defect chaotic states present in these GSH models to calculations carried out using Rayleigh–Bénard convection with stress-free [38] and no-slip [11] boundary conditions, using the stability boundaries computed in this chapter to improve the understanding of why SDC occurs in convection.

Chapter 4

Bifurcation analysis of the Skew-Varicose instability

4.1 Introduction

In this chapter we focus on a detailed mathematical study, combining numerical pathfollowing and bifurcation analysis, of the nonlinear development of the skew-varicose instability. The organization of the bifurcations enables us to understand the existence of different patterns. A possible approach to gain insight in the transitions from stable stripes to stripes that are unstable to the skew-varicose instability is by characterizing the nonlinear evolution of the modes that are responsible for the skew-varicose instability through a systems of ODEs. To aid this investigation, we reduce the infinite-dimensional PDEs (recall models 1 and 2, repeated in (4.2-4.4)) to a finite-dimensional set of ODEs by considering a particular set of modes of the system: ψ and ω are expanded using the selected set of modes and nonlinear differential equations for the amplitudes of the eigenfunctions are derived. These systems are investigated through numerical computations and theoretical analysis in this chapter in order to perform a bifurcation analysis for the skew-varicose instability.

Busse *et al.* in 1992 [95] suggested that a significant part of the nonlinear dynamics of the convection layer can be understood in terms of reduced systems of a few coupled amplitude equations. They derived a finite dimensional system of differential equations, the Busse system, by doing a Galerkin truncation of the original fluid equations. The ODEs are for the coefficients in a Fourier type expansion of velocity and temperature fields in Rayleigh–Bénard convection assuming stress free boundary conditions and restricting wave vectors to a grid. They have selected wavenumbers from a grid with the domain size $L = 2 \times 2\pi$, and sufficiently close to the critical wavenumber $\pi/\sqrt{2}$; wave vectors $k_i = (\frac{\pi}{2} + \frac{\pi i}{4}, \frac{\pi}{2})$ for $i = -1, 0, 1$ and derived the system:

$$\begin{aligned}
M_{-1}\dot{C}_{-1} &= (R - R_{-1})C_{-1} - C_{-1}\sum_{i=-1}^{1}\alpha_{-1i}C_i^2 - \alpha_{-14}C_0^2C_1 - q_{-1}C_0G \\
M_0\dot{C}_0 &= (R - R_0)C_0 - C_0\sum_{i=-1}^{1}\alpha_{0i}C_i^2 - \alpha_{04}C_{-1}C_0C_1 - q_0C_{-1}G - q_1C_1G \\
M_1\dot{C}_1 &= (R - R_1)C_1 - C_1\sum_{i=-1}^{1}\alpha_{1i}C_i^2 - \alpha_{14}C_0^2C_{-1} - q_4C_0G \\
\dot{G} &= -\frac{\pi^2}{16}G + \frac{3\pi^4}{16}C_{-1}C_0 + \frac{5\pi^4}{16}C_0C_1
\end{aligned} \tag{4.1}$$

where $R_i = (\pi^2 + |k_i|^2)^3/|k_i|^2$, $M_i = (1 + Pr)(\pi^2 + |k_i|^2)^2/|k_i|^2$ and other coefficients depend on R and Pr. The three variables C_i, $(i = -1, 0, 1)$, correspond to amplitudes of basic wave components whereas G is responsible for the meanflow. Although a proof is missing they considered the real system, observing the numerical results; different initial conditions indicate that the arguments of complex solutions tend to be real; real subspace is invariant. The Busse system is reminiscent of the Lorenz model [96], but considers a three dimensional instead of two dimensional fluid motion. Like the Lorenz model, the Busse system is obtained as a truncation to few modes; it also involves the introduction of a specific aspect ratio for the periodicity interval in the fluid layer and the system has $\mathbb{Z}_2 \times \mathbb{Z}_2$ symmetry. The Busse system was derived to study the spatio-temporal structure evolving from the onset of the skew-varicose instability; they observed that some characteristic spatio-temporal structures appear in numerical simulations and the way in which the transitions to chaos occur depends on the set up.

Nguyen *et al.* in 2005 [97] carried out a thorough investigation of the Busse system relevant to the study of initial and secondary instabilities of convection patterns in RBC. Their study of global bifurcation showed how homoclinic and heteroclinic bifurcations organize the bifurcation diagram in the parameter plane of Rayleigh number and Prandtl number. Also they extended the Busse system including one extra mode, $k_2 = (0, 3\pi/4)$; the reason for this selection is not given. They found that much of the bifurcation scenarios are the same in both systems [97]. We note here that this selection is not supported as regards the skew-varicose behavior, but for cross-roll instability; they have selected modes with large perturbation wave vectors and hence their analysis is only valid for short wave length instabilities such as cross-roll.

The bifurcation analysis for the Eckhaus instability was presented first by Tsiveriotis & Brown in 1989 [98]. They presented the bifurcation diagram corresponding to the Eckhaus stability curve, constructed for the one-dimensional Swift–Hohenberg equation in a finite domain. The complete bifurcation analysis for the Eckhaus instability has been carried out by Tuckerman and Barkley in 1990 [99], and they presented the bifurcation diagram from the work based on the Ginzburg–Landau equation in a finite domain with either stress free or periodic boundary conditions. Through a centre manifold reduction, they showed that all restabilizing bifurcations of the pure-mode states are subcritical, and hence that the Eckhaus instability is itself subcritical. They also confirmed the length-independent downwards shift of the Eckhaus parabola for a finite geometry.

We have carried out a truncation of model 1, retaining only a few modes and giving a system which has the same structure of the Busse system. We find that this system does not accurately describe the transitions of stable stripes to the skew-varicose stripes: the truncated system predicts that the bifurcation is supercritical, whereas our expectation from the numerical work in chapter 3 and from the results of [99] is that the bifurcation should be subcritical. However, we extend the system by incorporating more relevant modes, resulting in a larger system in which the skew-varicose bifurcation is subcritical.

We start in section 2 with a description of the derivation of the truncated systems of equations using two sets of modes (the smaller set having three complex modes, the larger having five). In next section we perform a centre manifold reduction at the skew-varicose bifurcation point in order to check the supercriticality or the subcriticality of the pitchfork bifurcation. We discuss the numerical method used to solve the truncated systems in section 4 and illustrate a case study in section 5, in which we present bifurcation diagram for the transition of the stripes to the skew-varicose phenomena. In section 6 we focus on the agreement between the PDE and the two systems of ODEs. This chapter closes with some concluding remarks in section 7.

4.2 Derivation of two systems of Ordinary Differential Equations

We begin with restating the two generalized Swift–Hohenberg models. Model 1 is:

$$\frac{\partial\psi}{\partial t} + (\mathbf{U}\cdot\nabla)\,\psi = \left[\mu - (1+\nabla^2)^2\right]\psi - \mathcal{P}_\alpha\left(\psi^3\right), \tag{4.2}$$

$$\left[\frac{\partial}{\partial t} - Pr(\nabla^2 - c^2)\right]\omega = -g_m\mathcal{F}_\gamma\left[\nabla(\nabla^2\psi)\times\nabla\psi\right]\cdot\widehat{\mathbf{z}}. \tag{4.3}$$

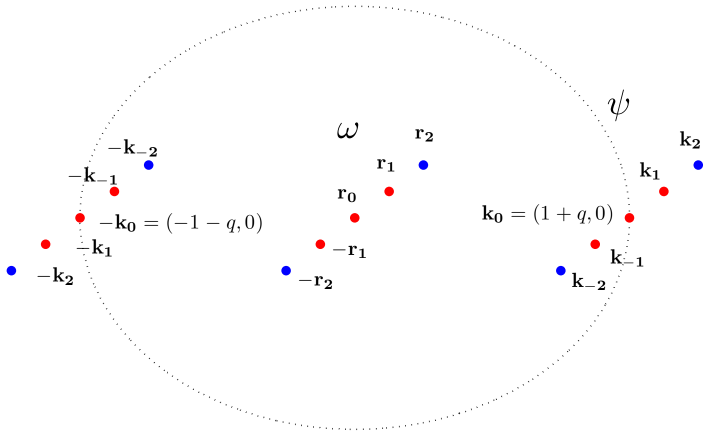

Figure 4.1: *Mode selection. 3-mode truncation: Set of modes with wave vectors* $(1+q+nk, nl)$ *for* ψ *and* (nk, nl) *for* ω *where* $n = -1, 0, 1$. *5-mode truncation: Set of modes with wave vectors* $(1+q+nk, nl)$ *for* ψ *and* (nk, nl) *for* ω *where* $n = -2, -1, 0, 1, 2$.

In model 2, the equation for ψ is same as equation (4.2) but the equation for vorticity is

$$\omega = -g\mathcal{F}_\gamma \left[\nabla(\nabla^2\psi) \times \nabla\psi\right] \cdot \widehat{\mathbf{z}}. \tag{4.4}$$

The purpose of this section is to describe how we obtain the systems of coupled ODEs from these models. In order to proceed we select a particular set of modes, $e^{i\mathbf{k_n}\cdot\mathbf{x}}$ for the field ψ and $e^{i\mathbf{r_n}\cdot\mathbf{x}}$ for the field ω, where $\mathbf{n} = (n, n)$, $\mathbf{k_n} = (1+q+nk, nl)$ and $\mathbf{r_n} = (nk, nl)$. Here n is an integer and k and l are small wave vector components along and perpendicular to stripes respectively. Having chosen the modes, we interact them with the stripe solution, which incorporates the wave vectors $\pm(1+q, 0)$, and expand ψ and ω:

$$
\begin{aligned}
\psi &= A(t)e^{i(1+q,0)\cdot\mathbf{x}} + \sum_{\mathbf{n}\neq 0} A_{\mathbf{n}}(t)e^{i\mathbf{k_n}\cdot\mathbf{x}} + \quad \text{c.c.} \\
\omega &= \sum_{\mathbf{n}\neq 0} B_{\mathbf{n}}(t)e^{i\mathbf{r_n}\cdot\mathbf{x}}
\end{aligned} \tag{4.5}
$$

provided $A(t)$, $A_{\mathbf{n}}(t)$ and $B_{\mathbf{n}}(t)$ are complex amplitudes.

The summation here could be infinite in principle. We need to truncate expression (4.5) in order to get a finite set of ODEs which involves the eigenfunctions. When this set of ODEs are small, the bifurcation analysis becomes easier. On the other hand the details of bifurcations will be more accurate with more modes.

To obtain a finite dimensional set of equations, we chose two sets of modes (one with three modes, one with five), illustrated in figure 4.1. For the 3-mode truncation we consider only the modes with wave vectors indicated in red, whereas for the 5-mode truncation, we extend this set by including the modes that are indicated in blue. In chapter 2, we have shown that the modes k_0 and $-k_0$ associate with the stripe solution and we incorporated modes $\pm k_1$ and $\pm k_{-1}$ for linear stability analysis ($\pm k_2$ and $\pm k_{-2}$ are higher order modes).

4.2.1 The 3-mode truncation

We start by deriving the truncated system by taking the modes with wave vectors $\mathbf{k_n}$ and $\mathbf{r_n}$ for $\mathbf{n} \in \{(-1,-1), (0,0), (1,1)\}$ and considering the equations corresponding to these terms. The three mode truncation amounts to

$$
\begin{aligned}
\psi &= A_0(t)e^{i(1+q,0)\cdot\mathbf{x}} + A_1(t)e^{i(1+q+k,l)\cdot\mathbf{x}} + A_{-1}(t)e^{i(1+q-k,-l)\cdot\mathbf{x}} + \bar{A}_0(t)e^{i(-1-q,0)\cdot\mathbf{x}} \\
&\quad + \bar{A}_1(t)e^{i(-1-q-k,-l)\cdot\mathbf{x}} + \bar{A}_{-1}(t)e^{i(-1-q+k,+l)\cdot\mathbf{x}}
\end{aligned} \tag{4.6}
$$

$$
\omega = B_1(t)e^{i(k,l)\cdot\mathbf{x}} + \bar{B}_1(t)e^{i(-k,-l)\cdot\mathbf{x}}. \tag{4.7}
$$

Observe that $\bar{A}_n$ is the complex conjugate of A_n, $B_0 = 0$ and the convention $B_{-1} = \bar{B}_1$ has been used. Substituting these expressions for ψ and ω into model PDEs and truncating to the modes that are used in the expansion of ψ and ω yields the coupled ODEs for the amplitudes. At this point we introduce some notations to ease the illustration.

$$\begin{aligned} r_n &= \mu - [1 - ((1+q+nk)^2 + (nl)^2)]^2, \quad \text{for} \quad n = -1, 0, 1 \\ \lambda_{\pm} &= (1+q)l((l^2+k^2) \pm 2(1+q)k) \\ \delta &= l(1+q)/(l^2+k^2), \end{aligned}$$

and

$$\begin{pmatrix} C_0 \\ C_1 \\ C_{-1} \end{pmatrix} = \begin{bmatrix} 1 & 2 & 2 \\ 2 & 1 & 2 \\ 2 & 2 & 1 \end{bmatrix} \begin{pmatrix} |A_0|^2 \\ |A_1|^2 \\ |A_{-1}|^2 \end{pmatrix}$$

We first examine each term in the equation (4.2) and consider only the coefficients of each mode, $e^{i(1+q+nk,nl)\cdot\mathbf{x}}$ for $n = -1, 0, 1$ and their complex conjugates. Since the vertical vorticity $\omega(x, y, t)$ is $-\nabla^2\zeta$, we have $\zeta = \frac{1}{k^2+l^2}\left(B_1 e^{i(k,l)\cdot\mathbf{x}} + \text{c.c.}\right)$ and so $\mathbf{U} = \frac{i}{k^2+l^2}\left(B_1 e^{i(k,l)\cdot\mathbf{x}} - \bar{B}_1(t)e^{-i(k,l)\cdot\mathbf{x}}\right)(l, -k)$. Therefore we have, after truncation,

$$(\mathbf{U}\cdot\nabla)\,\psi = -\delta(B_1 A_{-1} - \bar{B}_1 A_1)e^{i\mathbf{k_0}\cdot\mathbf{x}} - \delta(B_1 A_0)e^{i\mathbf{k_1}\cdot\mathbf{x}} + \delta(\bar{B}_1 A_0)e^{i\mathbf{k_{-1}}\cdot\mathbf{x}} + \text{c.c.},$$

and

$$\left(\mu-(1+\nabla^2)^2\right)\psi = r_0A_0e^{i\mathbf{k_0}\cdot\mathbf{x}} + r_1A_1e^{i\mathbf{k_1}\cdot\mathbf{x}} + r_{-1}A_{-1}e^{i\mathbf{k_{-1}}\cdot\mathbf{x}} + \text{c.c.},$$

$$\psi^3 = (3A_0C_0+6A_1A_{-1}\bar{A}_0)e^{i\mathbf{k_0}\cdot\mathbf{x}} + (3A_1C_1+3A_0^2\bar{A}_{-1})e^{i\mathbf{k_1}\cdot\mathbf{x}}$$

$$+ (3A_{-1}C_{-1}+3A_0^2\bar{A}_1)e^{i\mathbf{k_{-1}}\cdot\mathbf{x}} + \text{c.c.}.$$

Combining these we obtain three coupled ODEs for amplitudes A_n for $n=-1,0,1$:

$$\dot{A}_0 = (r_0-3C_0)A_0 - 6A_1A_{-1}\bar{A}_0 + \delta(B_1A_{-1}-\bar{B}_1A_1), \tag{4.8}$$

$$\dot{A}_1 = (r_1-3C_1)A_1 - 3A_0^2\bar{A}_{-1} + \delta(B_1A_0), \tag{4.9}$$

$$\dot{A}_{-1} = (r_{-1}-3C_{-1})A_{-1} - 3A_0^2\bar{A}_1 - \delta(\bar{B}_1A_0). \tag{4.10}$$

Next we examine each term in equations (4.3) and (4.4) and consider only the coefficients of each mode, $e^{i(nk,nl)\cdot\mathbf{x}} = e^{i\mathbf{r_n}\cdot\mathbf{x}}$ for $n=-1,0,1$. Note that computations yield:

$$\left[\nabla(\nabla^2\psi)\times\nabla\psi\right]\cdot\widehat{\mathbf{z}} = (\lambda_+A_1\bar{A}_0-\lambda_-\bar{A}_{-1}A_0)e^{i\mathbf{r_1}\cdot\mathbf{x}} + (\lambda_+\bar{A}_1A_0-\lambda_-A_{-1}\bar{A}_0)e^{i\mathbf{r_{-1}}\cdot\mathbf{x}}.$$

Hence the equation (4.3) follows to differential equation for B_1,

$$\dot{B}_1 = -Pr(c^2+k^2+l^2)B_1 - g_m\mathcal{F}_\gamma(\lambda_+A_1\bar{A}_0-\lambda_-\bar{A}_{-1}A_0), \tag{4.11}$$

where $\mathcal{F}_\gamma = e^{-\gamma^2(k^2+l^2)}$. Therefore the reduced system for model 1, (4.2)-(4.3), is given by the system of differential equations (4.8) - (4.11). For model 2, equation (4.4) gives an algebraic relation for B_1,

$$B_1 = -g\mathcal{F}_\gamma(\lambda_+A_1\bar{A}_0-\lambda_-\bar{A}_{-1}A_0). \tag{4.12}$$

Substituting this into the ODEs (4.8)-(4.10) results in the following system for model 2:

$$\dot{A}_0 = (r_0 - [3|A_0|^2 + (6-P)|A_1|^2 + (6-Q)|A_{-1}|^2])A_0 - SA_1A_{-1}\bar{A}_0 \tag{4.13}$$

$$\dot{A}_1 = (r_1 - [(6+P)|A_0|^2 + 6|A_1|^2 + 3|A_{-1}|^2])A_1 - (3-Q)A_0^2\bar{A}_{-1} \tag{4.14}$$

$$\dot{A}_{-1} = (r_{-1} - [(6+Q)|A_0|^2 + 3|A_1|^2 + 6|A_{-1}|^2])A_{-1} - (3-P)A_0^2\bar{A}_1, \tag{4.15}$$

where $P = g\delta\lambda_+F_\gamma$, $Q = g\delta\lambda_-F_\gamma$ and $S = 2(3 + g(l(1+q))^2F_\gamma)$.

4.2.2 The 5-mode truncation

We now derive the truncated system by putting the modes with wave vectors $\mathbf{k_n}$ and $\mathbf{r_n}$ for $\mathbf{n} \in \{(-2,-2),\ (-1,-1),\ (0,0),\ (1,1),\ (2,2)\}$ and considering the equations corresponding to these terms. Five modes truncation amounts to setting

$$\psi = \sum_{n=-2}^{2} A_n(t)e^{i(1+q+nk,nl)\cdot\mathbf{x}} + \text{c.c.},$$
$$\omega = \sum_{n=-2}^{2} B_n(t)e^{i(nk,nl)\cdot\mathbf{x}}.$$

These expressions involve all the modes that appear in the 3-mode truncation with the addition of 2 modes, as indicated in blue in figure 4.1. Therefore the resulting system includes all the terms of the systems we derived with 3-mode truncation with additional terms corresponding to the extra modes. We now examine each term in equation (4.2) and consider only the coefficients of each mode, $e^{i(1+q+nk,nl)\cdot\mathbf{x}} = e^{i\mathbf{k_n}\cdot\mathbf{x}}$ for $n = -2, -1, 0, 1, 2$.

At this point we introduce some notation:

$$
\begin{aligned}
r_n &= \mu - [1 - ((1+q+nk)^2 + (nl)^2)]^2, \quad \text{for} \quad n = -2, 2 \\
\eta_\pm &= (1+q)l(3(l^2+k^2) \pm 2(1+q)k) \\
\upsilon_\pm &= (1+q)l((l^2+k^2) \pm (1+q)k), \\
\nu_\pm &= \frac{2(1+q \pm k)}{1+q}
\end{aligned}
$$

and

$$
\begin{pmatrix} D_0 \\ D_1 \\ D_{-1} \\ D_2 \\ D_{-2} \end{pmatrix} = \begin{bmatrix} 1 & 2 & 2 & 2 & 2 \\ 2 & 1 & 2 & 2 & 2 \\ 2 & 2 & 1 & 2 & 2 \\ 2 & 2 & 2 & 1 & 2 \\ 2 & 2 & 2 & 2 & 1 \end{bmatrix} \begin{pmatrix} |A_0|^2 \\ |A_1|^2 \\ |A_{-1}|^2 \\ |A_2|^2 \\ |A_{-2}|^2 \end{pmatrix}
$$

Following the 3-mode derivation, we confine ourselves to illustrating only the additional terms that result from incorporating the two extra modes. Note the extensions in ζ : $\frac{1}{4(k^2+l^2)}\left(B_2 e^{i(2k,2l)\cdot\mathbf{x}} + \text{c.c.}\right)$ which results in $\mathbf{U} : \frac{i}{2(k^2+l^2)}\left(B_2 e^{i(2k,2l)\cdot\mathbf{x}} - \bar{B}_2(t) e^{-i(2k,2l)\cdot\mathbf{x}}\right)(l,-k)$. Hence

$$
\begin{aligned}
(\mathbf{U}\cdot\nabla)\,\psi = \frac{\delta}{2}\Big[&(\bar{B}_2 A_2 - B_2 A_{-2})e^{i\mathbf{k_0}\cdot\mathbf{x}} - (2\bar{B}_1 A_2 - B_2 A_{-1})e^{i\mathbf{k_1}\cdot\mathbf{x}} + (2B_1 A_{-2} - \bar{B}_2 A_1)e^{i\mathbf{k_{-1}}\cdot\mathbf{x}} \\
&-(A_0 B_2 + \nu_+ A_1 B_1)e^{i\mathbf{k_2}\cdot\mathbf{x}} + (A_0\bar{B}_2 + \nu_- A_{-1}\bar{B}_{-1})e^{i\mathbf{k_{-2}}\cdot\mathbf{x}}\Big].
\end{aligned}
$$

Further, the extensions of terms $\left(\mu - (1+\nabla^2)^2\right)\psi : r_2 A_2 e^{i\mathbf{k_2}\cdot\mathbf{x}} + r_{-2}A_{-2}e^{i\mathbf{k_{-2}}\cdot\mathbf{x}}$ and ψ^3, can be combined to compute ODEs for the amplitudes A_n, $(n = -2, \ldots, 2)$:

$$
\begin{aligned}
\dot{A}_0 &= (r_0 - 3D_0)A_0 - 6\left[\bar{A}_0(A_{-1}A_1 + A_2A_{-2}) + \bar{A}_{-1}A_1A_{-2} + A_{-1}\bar{A}_1A_2\right] - 3\left[A_1^2\bar{A}_2 + A_{-1}^2\bar{A}_{-2}\right] \\
&\quad + \frac{\delta}{2}\left[2(B_1A_{-1} - \bar{B}_1A_1) + (B_2A_{-2} - \bar{B}_2A_2)\right], \\
\dot{A}_1 &= (r_1 - 3D_1)A_1 - 6\left[A_0(A_{-1}\bar{A}_{-2} + A_2\bar{A}_1) + A_2(A_{-1}\bar{A}_0 + A_{-2}\bar{A}_{-1})\right] - 3A_0^2\bar{A}_{-1} \\
&\quad + \frac{\delta}{2}\left[2(B_1A_0 - \bar{B}_1A_2) + B_2A_{-1}\right], \\
A\dot{}_{-1} &= (r_{-1} - 3D_{-1})A_{-1} - 6\left[A_0(A_1\bar{A}_2 + A_{-2}\bar{A}_{-1}) + A_{-2}(A_1\bar{A}_0 + A_2\bar{A}_1)\right] - 3A_0^2\bar{A}_1 \\
&\quad - \frac{\delta}{2}\left[2(\bar{B}_1A_0 - B_1A_{-2}) + \bar{B}_2A_1\right],
\end{aligned}
$$

$$
\begin{aligned}
\dot{A}_2 &= (r_2 - 3D_2)A_2 - 6A_1(A_0\bar{A}_{-1} + A_{-1}\bar{A}_{-2}) - 3A_0^2\bar{A}_{-2} - 3A_1^2\bar{A}_0 + \frac{\delta}{2}\left[B_2A_0 + \nu_+B_1A_1\right], \\
A\dot{}_{-2} &= (r_{-2} - 3D_{-2})A_{-2} - 6A_{-1}(A_0\bar{A}_1 + A_1\bar{A}_2) - 3A_0^2\bar{A}_2 - 3A_{-1}^2\bar{A}_0 + \frac{\delta}{2}\left[\bar{B}_2A_0 + \nu_-\bar{B}_1A_{-1}\right].
\end{aligned}
\tag{4.16}
$$

Next we examine each of the term in equation (4.3) and (4.4) and consider only the coefficients of each mode, $e^{i(nk,nl)\cdot\mathbf{x}}$ for $n = 1$, 2. Note that the extension yields

$$
\begin{aligned}
\left[\nabla(\nabla^2\psi)\times\nabla\psi\right]\cdot\widehat{\mathbf{z}} &= (\eta_+\bar{A}_1A_2 - \eta_-A_{-1}\bar{A}_{-2})e^{i\mathbf{r_1}\cdot\mathbf{x}} + 8(lk(1+q)^2A_1\bar{A}_{-1} \\
&\quad + \upsilon_+A_0\bar{A}_2 - \upsilon_-A_0\bar{A}_{-2})e^{i\mathbf{r_2}\cdot\mathbf{x}}.
\end{aligned}
$$

Substituting this into model 1 results in coupled ODEs for amplitudes B_1 and B_2:

$$
\begin{aligned}
\dot{B}_1 &= -Pr(c^2 + k^2 + l^2)B_1 - g_m\mathcal{F}_\gamma(\lambda_+A_1\bar{A}_0 - \lambda_-\bar{A}_{-1}A_0 + \eta_+\bar{A}_1A_2 - \eta_-A_{-1}\bar{A}_{-2}), \\
\dot{B}_2 &= -Pr(c^2 + 4(k^2 + l^2))B_2 - 8g_m\mathcal{F}_\gamma(\upsilon_+\bar{A}_0A_2 - \upsilon_-A_0A\bar{}_{-2} + k(1+q)\bar{A}_1A\bar{}_{-1}).
\end{aligned}
\tag{4.17}
$$

Therefore the reduced system for model 1 is given by the system of ODEs (4.16) and (4.17). On the other hand, model 2 gives an algebraic relations for eigenfunctions B_1 and B_2:

$$
\begin{aligned}
B_1 &= -g_m \mathcal{F}_\gamma(\lambda_+ A_1 \bar{A}_0 - \lambda_- \bar{A}_{-1} A_0 + \eta_+ \bar{A}_1 A_2 - \eta_- A_{-1} \bar{A}_{-2}) \\
B_2 &= -8 g_m \mathcal{F}_\gamma(\upsilon_+ \bar{A}_0 A_2 - \upsilon_- A_0 \bar{A}_{-2} + k(1+q) \bar{A}_1 \bar{A}_{-1}). \qquad (4.18)
\end{aligned}
$$

Therefore the reduced system for model 2 is the system of ODEs (4.16), with the algebraic relations (4.18).

4.3 Theoretical Analysis

We treat all the amplitudes to be real and to consider the real system; real system is an invariant subspace. Due to the translational invariance of the system (with X and Y translations), the amplitudes, A_0 and A_1 are real. Applying $\bar{A}_0 = A_0$ and $\bar{A}_1 = A_1$ to equations (4.8-4.10), we get $\bar{A}_{-1} = A_{-1}$ and hence real system is an invariant subspace.

This finally results in equations with four and three real variables in 3-mode truncation of model 1 and 2 respectively, whereas 5-mode truncation yields equations with seven and five real variables for model 1 and 2 respectively. The system of four ODEs (4.8)- (4.11) with real variables in the 3-mode truncation has the same structure as the Busse system. However, they restricted to 3 selected wave vectors, while, in our system, k and l can be varied in order to choose the most relevant wave vectors. Moreover, the coefficients in the Busse system are different from ours.

We restrict our theoretical analysis to model 2; model 1 is investigated numerically. We start our analysis with the system of 3 coupled ODEs (3-mode truncation of model 2) that describes the evolution in time of the amplitudes:

$$\begin{aligned}
\dot{A}_0 &= (r_0 - [3A_0^2 + (6-P)A_1^2 + (6-Q)A_{-1}^2])A_0 - RA_1A_{-1}A_0 \\
\dot{A}_1 &= (r_1 - [(6+P)A_0^2 + 6A_1^2 + 3A_{-1}^2])A_1 - (3-Q)A_0^2A_{-1} \\
\dot{A}_{-1} &= (r_{-1} - [(6+Q)A_0^2 + 3A_1^2 + 6A_{-1}^2])A_{-1} - (3-P)A_0^2A_1.
\end{aligned} \tag{4.19}$$

We also consider the system of 5 coupled ODEs (5-mode truncation of model 2):

$$\begin{aligned}
\dot{A}_0 &= (r_0 - 3D_0)A_0 - 6\left[A_0(A_{-1}A_1 + A_2A_{-2}) + A_{-1}A_1(A_{-2} + A_2)\right] - 3\left[A_1^2A_2 + A_{-1}^2A_{-2}\right] \\
&\quad + \frac{\delta}{2}\left[2B_1(A_{-1} - A_1) + B_2(A_{-2} - A_2)\right] \\
\dot{A}_1 &= (r_1 - 3D_1)A_1 - 6\left[A_0(A_1A_{-2} + A_2A_1) + A_2A_{-1}(A_0 + A_{-2})\right] - 3A_0^2A_{-1} \\
&\quad + \frac{\delta}{2}\left[2B_1(A_0 - A_2) + B_2A_{-1}\right] \\
\dot{A}_{-1} &= (r_{-1} - 3D_{-1})A_{-1} - 6\left[A_0(A_1A_2 + A_{-2}A_{-1}) + A_{-2}A_1(A_0 + A_2)\right] - 3A_0^2A_1 \\
&\quad - \frac{\delta}{2}\left[2B_1(A_0 - A_{-2}) + B_2A_1\right] \\
\dot{A}_2 &= (r_2 - 3D_2)A_2 - 6A_1A_{-1}(A_0 + A_{-2}) - 3A_0(A_0A_{-2} + A_1^2) + \frac{\delta}{2}\left[B_2A_0 + \nu_+B_1A_1\right] \\
\dot{A}_{-2} &= (r_{-2} - 3D_{-2})A_{-2} - 6A_{-1}A_1(A_0 + A_2) - 3A_0(A_0A_2 + A_{-1}^2) + \frac{\delta}{2}\left[B_2A_0 + \nu_-B_1A_{-1}\right] \\
B_1 &= -g_m\mathcal{F}_\gamma(A_0(\lambda_+A_1 - \lambda_-A_{-1}) + \eta_+A_1A_2 - \eta_-A_{-1}A_{-2}) \\
B_2 &= -8g_m\mathcal{F}_\gamma(A_0(\upsilon_+A_2 - \upsilon_-A_{-2}) + k(1+q)A_1A_{-1}).
\end{aligned} \tag{4.20}$$

Observe that in both truncations the origin is always an equilibrium, which is stable for μ sufficiently negative. We note that if we ignore nonlinear terms in our systems of ODEs (apart from $-A_0^3$ in the $\dot{A}_0$), the linearized equations are in agreement with the linear theory established in chapter 2 for the exact stripe solution. Pitchfork bifurcations lead first to equilibria corresponding to stripe patterns; secondary pitchfork bifurcations lead to equilibia corresponding to patterns with less symmetry: these secondary bifurcations correspond to the skew-varicose instability.

Our systems have two equilibia correspond to the stripe pattern on the A_0 axis with coordinate $A_0 = \pm\sqrt{\frac{r_0}{3}}$ (recall $r_0 = \mu - (1-(1+q)^2)^2$). In chapter 2, we performed the linear stability analysis of stripes and established the regime where stripes become unstable to the skew-varicose instability. The work following aims to find nearby nonlinear solutions at this transition. We present our results using bifurcation diagrams. The theoretical approach towards the understanding of this bifurcation is by centre Manifold Reduction (CMR).

4.3.1 Centre Manifold Reduction

It is important to note that the new branches of solutions emerge from the stripe equilibrium in a continuous fashion with μ. Close to the secondary bifurcation point, the distance from the original equilibrium to the new solution can be made arbitrarily small. Therefore these small amplitude solutions are contained in a centre manifold, which describes bifurcations at the equilibrium point.

Our analysis first follows for the system (4.19), where the Jacobian J_1 evaluated at the equilibrium point $(\sqrt{\frac{r_0}{3}}, 0, 0)$ takes the form

$$\left(\begin{array}{c:c} -2r_0 & \begin{matrix} 0 & \qquad 0 \end{matrix} \\ \hdashline \begin{matrix} 0 \\ 0 \end{matrix} & \left.\begin{matrix} r_1 - \frac{(6+P)r_0}{3} & -\frac{(3-Q)r_0}{3} \\ -\frac{(3-P)r_0}{3} & r_{-1} - \frac{(6+Q)r_0}{3} \end{matrix}\right\} A \end{array}\right)$$

Given the block structure of this matrix, we know that $-2r_0$ is an eigenvalue, which is always negative for the stripe solution. Hence the equilibrium is stable if the trace of A, $T(A)$, is negative and the determinant, $D(A)$, is positive. The other two eigenvalues are $\sigma_\pm = \frac{T(A)\pm\sqrt{T(A)^2-4D(A)}}{2}$. For real eigenvalues, σ_+ will be the first to cross through zero, resulting at the bifurcation point with a one-dimensional centre manifold which is tangential at the equilibrium point to the space spanned by the eigenvector corresponding to the zero eigenvalue. This eigenvector corresponding to σ_+ can be obtained with the zero determinant:

$$\begin{pmatrix} 0 \\ -a_1/a_2 \\ 1 \end{pmatrix}$$

where $a_1 = -\frac{(3-Q)r_0}{3}$ and $a_2 = r_1 - \frac{(6+P)r_0}{3}$. Hence a linear approximation of the centre manifold is ,

$$\begin{aligned} &A_1 = u_1 A_{-1} \text{ with } u_1 = -a_1/a_2 = \frac{(Q-3)r_0}{(P+6)r_0 - 3r_1} \\ &A_0 = \sqrt{r_0/3} \end{aligned} \tag{4.21}$$

It follows that the nonlinear centre manifold can be represented locally as a function of A_{-1}. We write,

$$A_1 = u_1 A_{-1} + u_2 A_{-1}^2 + u_3 A_{-1}^3 + \cdots = f_1(A_{-1})$$

and

$$A_0 = \sqrt{r_0/3} + w_2 A_{-1}^2 + w_3 A_{-1}^3 + \cdots = f_2(A_{-1}),$$

where $u_i, w_i \in \mathbb{R}$, $i = 2, 3, \cdots$ are to be determined. To identify these constants we perform a power series expansion in powers of A_{-1}. We write $\dot{A}_1 = \frac{df_1(A_{-1})}{dA_{-1}} \dot{A}_{-1}$ and $\dot{A}_0 = \frac{df_2(A_{-1})}{dA_{-1}} \dot{A}_{-1}$, and then substitute the values of $\dot{A}_{-1}$, $\dot{A}_0$ and $\dot{A}_1$ from (4.19) into these two equations. Finally, we consider coefficients of each power of A_{-1}. This procedure results in an approximation to the centre manifold which is valid close to the equilibrium point and close to the bifurcation point. We find fourth order approximations $A_1 = u_1 A_{-1} + u_3 A_{-1}^3 + ...$ and $A_0 = \sqrt{r_0/3} + w_2 A_{-1}^2 + w_4 A_{-1}^4 + \cdots$ which serve to determine $\dot{A}_{-1}$:

$$\dot{A}_{-1} = a_1 A_{-1} + a_3 A_{-1}^3 + \cdots, \tag{4.22}$$

where $a_1 = \sigma_+$.

This is the normal form of the pitchfork bifurcation and when $\sigma_+ < 0$, the equilibrium $(\sqrt{\frac{r_0}{3}}, 0, 0)$ is stable. When σ_+ is increases through zero, there is an unstable equilibrium at $A_{-1} = 0$, which is the equilibrium point $(A_0, A_1, A_{-1}) \equiv (\sqrt{\frac{r_0}{3}}, 0, 0)$ and two equilibria at $A_{-1} = \pm\sqrt{\frac{\sigma_+}{-a_3}}$. These equilibria are stable if $a_3 < 0$ (pitchfork bifurcation is supercritical), unstable otherwise. We illustrate this in section 5, where we present a case study. We investigate the value of a_3 later in this section.

Next, our analysis follows for the system (4.20), where the Jacobian (J_2) evaluated at the equilibrium point $(\sqrt{\frac{r_0}{3}}, 0, 0, 0, 0)$ takes the form

$$\left(\begin{array}{c|c|c}
-2r_0 & \begin{matrix} 0 & \quad 0 \end{matrix} & \begin{matrix} 0 & \quad 0 \end{matrix} \\ \hline
\begin{matrix} 0 \\ 0 \end{matrix} & \left.\begin{matrix} r_1 - \frac{(6+P)r_0}{3} & -\frac{(3-Q)r_0}{3} \\ -\frac{(3-P)r_0}{3} & r_{-1} - \frac{(6+Q)r_0}{3} \end{matrix}\right\} A & \begin{matrix} 0 & \quad 0 \\ 0 & \quad 0 \end{matrix} \\ \hline
\begin{matrix} 0 \\ 0 \end{matrix} & \begin{matrix} 0 & \quad 0 \\ 0 & \quad 0 \end{matrix} & \left.\begin{matrix} r_2 - \frac{(6+U)r_0}{3} & -\frac{(3-V)r_0}{3} \\ -\frac{(3-U)r_0}{3} & r_{-2} - \frac{(6+V)r_0}{3} \end{matrix}\right\} B
\end{array}\right)$$

Here $U = g\delta\upsilon_+ F_\gamma$ and $V = g\delta\upsilon_- F_\gamma$. Given the block structure of this matrix, we observe that three eigenvalues are $-2r_0$ and $\sigma_\pm$, which are the eigenvalues of J_1. The other two eigenvalues, are the eigenvalues of matrix B. Despite the two new eigenvalues, we focus on the case where σ_+ first becomes zero, resulting a one-dimensional centre manifold which is tangential at the equilibrium point to the space spanned by the eigenvector corresponding to the eigenvalue with zero real part, σ_+. Hence the centre manifold at the linear approximation is , $A_1 = u_1 A_{-1}$ with $A_0 = \sqrt{r_0/3}$ and $A_2 = A_{-2} = 0$, where u_1 is given by (4.21). Following the outlined procedure for centre manifold reduction in system (4.19), we find fourth order approximations, $A_1 = u_1 A_{-1} + u_3^{J_2} A_{-1}^3 + ...$, $A_0 = \sqrt{r_0/3} + w_2^{J_2} A_{-1}^2 + w_4^{J_2} A_{-1}^4 + ...$, $A_2 = v_2 A_{-1}^2 + v_4 A_{-1}^4 + ...$ and $A_{-2} = z_2 A_{-1}^2 + z_4 A_{-1}^4 + ...$, where all the coefficients are known at this point. These approximations serve to determine $\dot{A}_{-1}$ in 4.20:

$$\dot{A}_{-1} = b_1 A_{-1} + b_3 A_{-1}^3 + \cdots, \tag{4.23}$$

where $b_1 = \sigma_+$.

This is the normal form of the pitchfork bifurcation and when real part of $\sigma_+ < 0$, the equilibrium $(\sqrt{\frac{r_0}{3}}, 0, 0, 0, 0)$ is stable. When σ_+ is increases through zero, there is an unstable equilibrium at $A_{-1} = 0$, which is the equilibrium point $(A_{-2}, A_{-1}, A_0, A_1, A_2) = (0, 0, \sqrt{\frac{r_0}{3}}, 0, 0)$ and two equilibria at $A_{-1} = \pm\sqrt{\frac{-\sigma_+}{b_3}}$. These equilibria are unstable if $b_3 > 0$ (pitchfork bifurcation is subcritical), stable otherwise. We illustrate this in section 5, where we present a case study.

The expressions for a_3 and b_3 in terms of system parameters are enormous. Therefore the theoretical derivation of their signs and limiting values are not straightforward. Therefore we numerically determine how the signs of a_3 and b_3 change with system parameters. Figure 4.2 depicts the values of a_3 and b_3 on the SVI points for parameter $g = 20$ and $k = l = 2\pi/L = 0.05$, where the domain size $L = 40 \times 2\pi$. We first numerically compute the skew-varicose instability points, (q_{SV}, μ_{SV}), for $g = 20$ and $k = l = 0.05$ (the SVI boundary for these parameters is illustrated in figure 4.6). We then put these values into the derivations of CMR in order to obtain a_3 and b_3. Along the SVI bifurcation points, a_3 is negative (figure 4.2(a)) whereas b_3 is positive (figure 4.2(b)). When q is small b_3 tends to the value 3, while a_3 tends to zero.

Figure 4.3 illustrates how the values of a_3 and b_3 on the SVI points behave for different domain size, L, with $g = 20$ and $q = 0.1$. We first numerically compute the skew-varicose instability points, μ_{SV}, changing k (changing the domain size L) with $k = l$, for $g = 20$. This is illustrated in figure 4.3(a). We then put these values into the derivations of CMR in order to obtain a_3 and b_3. At the SV bifurcation points in large domains, a_3 is negative (figure 4.3(b)) and tends to -3 for infinite domain (both k and l tends to zero). However, b_3 tends to approximately zero in infinite domain as shown in figure 4.3(c).

Figure 4.4 illustrates how the values of a_3 and b_3 at the SVI bifurcation depend on g for $\mu = 0.1$. Figure 4.4(a) shows the numerically computed skew-varicose instability points, q_{SV}, for $\mu = 0.1$ with $k = l = 0.05$ (denoted in black dotted curve) and k and $l \to 0$ (denoted in red dotted curve). We put parameter values along these two curves into the derivations of CMR in order to obtain a_3 and b_3. When k and $l \to 0$, a_3 is approximately -3 (figure 4.4(b)) and b_3 is approximately 0. However, when $k = l = 0.05$, as g becomes large, a_3 changes the sign from negative to positive (figure 4.4(c)) whereas b_3 changes the sign from positive to negative (figure 4.4(d)). This strange behavior is due to the selection of k and l; by selecting $k = l = 0.05$, we have fix $\theta = \tan^{-1}(k/l) = \pi/4$. However SVI emerges with different angles and for large g, the maximum eigenvalue occurs with large angle $\theta \gg \pi/4$ and for small g , it occurs with small angle $\theta \ll \pi/4$. Moreover, θ of the maximum eigenvalue changes when instability grows and therefore figures in 4.4 are accurate only for parameters when g close to 20.

We note the unexpected behaviour of b_3; it does not seem to be in agreement with a_3 in any asymptotic limit and also its value tends to zero in infinite domain. This theoretical analysis does not leave us with a firm conclusion about the supercriticality of the SVI bifurcation: it is supercritical for the 3-mode truncation and subcritical for the 5-mode truncation. This suggests that the extension of the system by incorporating more modes

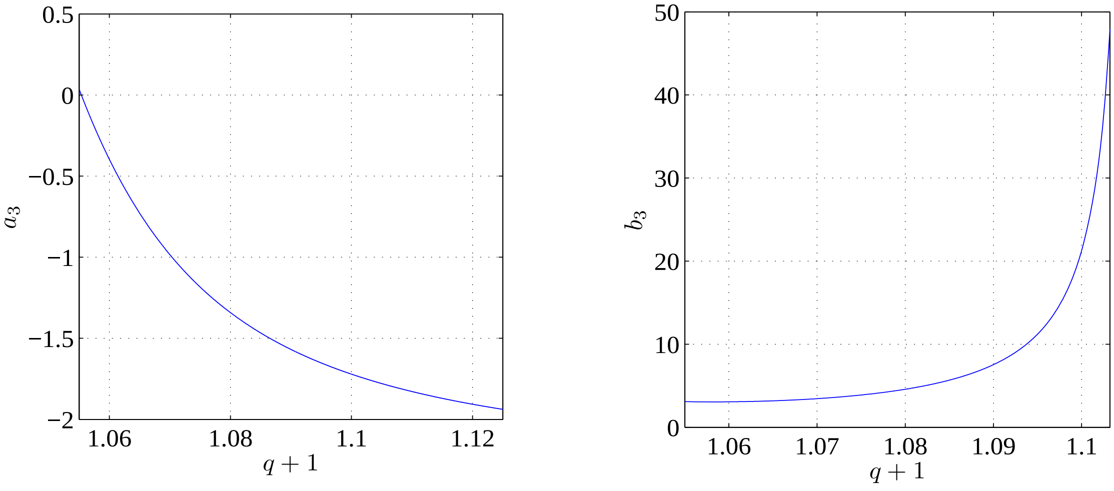

(a)

(b)

Figure 4.2: *Results of CMR along the SVI points calculated for* $g = 20$ *with* $k = l = 2\pi/L = 0.05$ *(SVI boundary for these parameters is indicated by red dotted curve in figure 4.6). (a)* a_3 *and (b)* b_3 *with respect to the wavenumber are shown for the parameter values along these SVI points.*

has changed the bifurcation scenario. We present a case study for both scenarios in the next section, where we also present numerically computed bifurcation diagrams to verify 5-mode truncation gives more insight into the character of the solution at the bifurcation.

4.4 Numerical Methods

In this section we describe the way the bifurcation curves and points in our systems were found and continued. Various software packages are available to assist in a numerical study of the differential equations. We used the software package MATCONT [92] for numerical path following of bifurcation curves and for identifying the various codimension-one bifurcations along them. Equipped with a collection of bordering methods and minimally extended systems, MATCONT can locate several local and global bifurcations and detect and continue bifurcations of equilibria (in our systems these are pitchfork bifurcations of equilibria). We obtain the data of starting points for the continuation by our analyti-

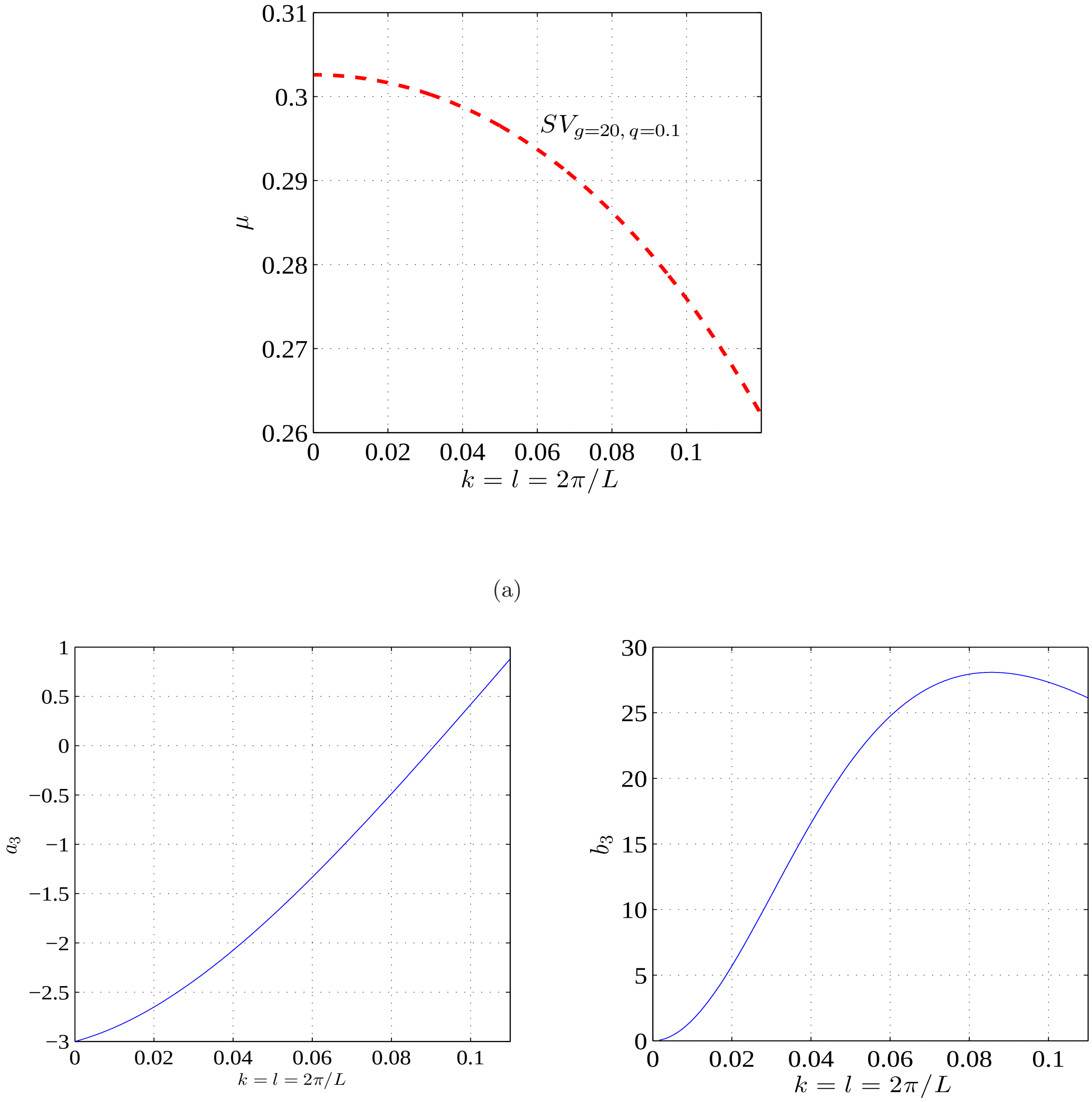

(a)

(b)

(c)

Figure 4.3: *Results of CMR along the SVI points calculated for* $g = 20$ *and* $q = 0.1$ *with different* $k = l$*. (a) Numerically computed points,* μ*, of the skew-varicose instability, varying the size of the domain,* L*. (b)* a_3 *and (c)* b_3 *with respect to* $k = l = 2\pi/L$ *are shown for the parameter values along the red curve in (a).*

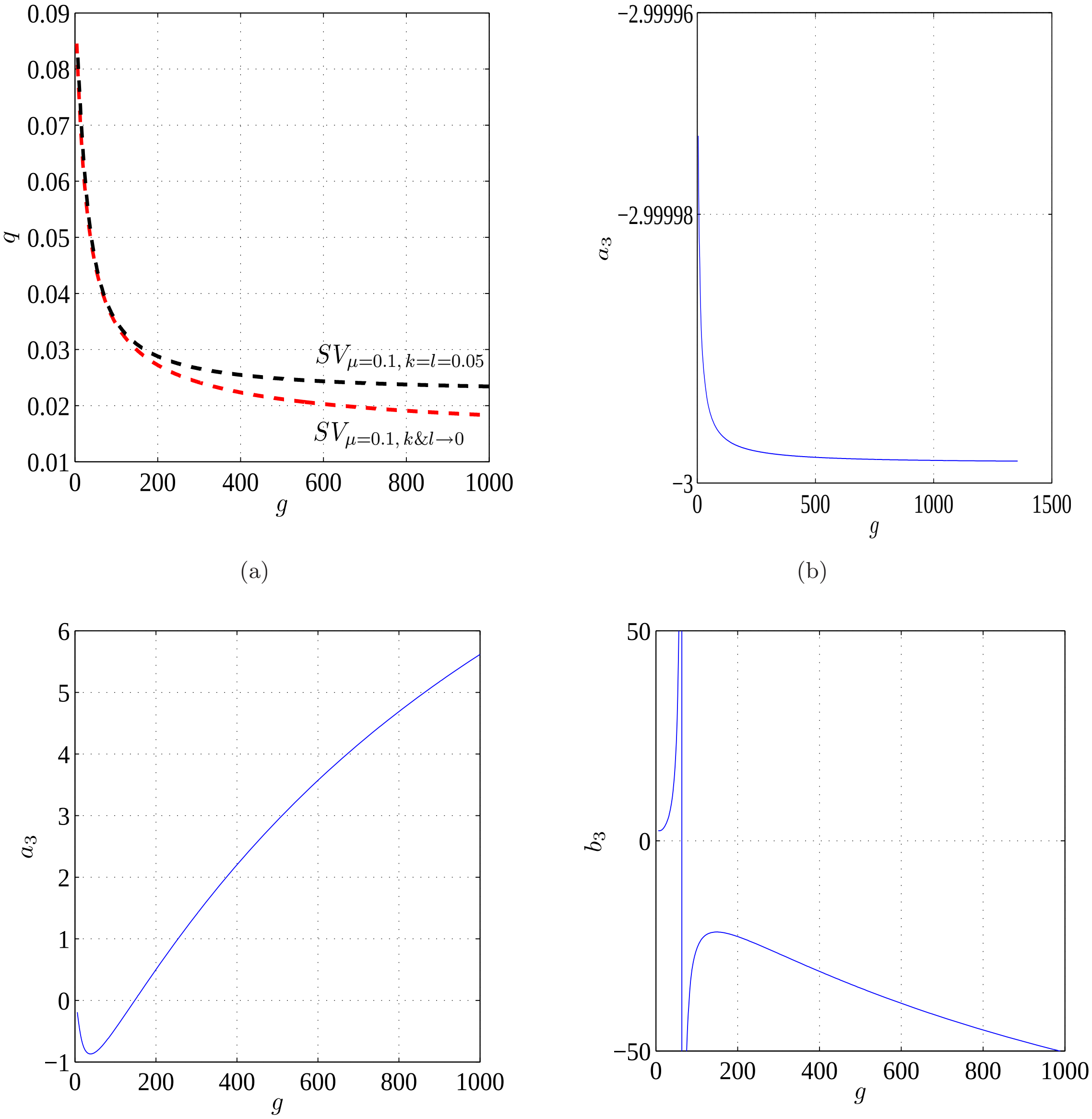

(a) (b)

(c) (d)

Figure 4.4: *Results of CMR along the SVI points calculated for $\mu = 0.1$.(a) Numerically computed points for the skew-varicose instability, in (q, g) plane for different size of the domain, L: $k = l = 2\pi/L = 0.05$ (denoted in black) and $k \,\&\, l \to 0$ $(L \to \infty)$ (denoted in red) (b) a_3 with respect to g is shown for the parameter values along the red curve in (a). (c) a_3 and (d) b_3 with respect to g is shown for the parameter values along the black curve in (a)*

cal investigations. We also examined our results using numerical integration, assisted by ODE45 package, MATLAB's standard solver for ODEs. This routine uses a variable step Runge-Kutta Method to solve differential equations numerically.

4.5 Case study

In this section, we show how the bifurcations organize the bifurcation diagram by combined numerical and theoretical analysis of a selected set of parameter values and modes. We fix $g = 20$. Following the linear investigation in chapter 2 we can find the skew-varicose boundary. Recall that the skew-varicose instability emerges from $(k,\, l) = (0,\, 0)$. However, in order to consider $(k,\, l) = (0, 0)$, we need to have an infinite domain. In a finite domain, for example a square domain with size $20 \times 2\pi$, $(k,\, l)$ in the lattice are integer multiples of 0.05. Stripes will be unstable until the maximum eigenvalue becomes zero on a point on the lattice. This is illustrated in figure 4.5, for the parameter values $(q, \mu) = (0.1,\, 0.29652)$. For this set of parameters, zero contour of the maximum eigenvalue touches a point in the lattice, in this case $(k, l) = (0.05,\, 0.05)$. Therefore, when $q = 0.1$, stripes are stable until $\mu = 0.29652$; we encounter that for the parameters $q = 0.1$ and $g = 20$, with $(k,\, l) = (0.05,\, 0.05)$, the bifurcation for the skew-varicose instability occurs at $\mu = 0.29652$. We fix $(k,\, l) = (0.05,\, 0.05)$ and when the maximum eigenvalue at this point becomes zero, we picked the parameter values $(q,\, \mu)$ and induced the skew-varicose boundary in $(q,\, \mu)$ parameter space, as depicted by the red dotted curve in 4.6. The SVI boundary with this selection of perturbation wave vector has a downward shift from the original SVI boundary as expected.

In the following we illustrate results of the nonlinear solutions at the point $(g,\, q,\, \mu) = (20,\, 0.1,\, 0.29652)$ with $(k, l) = (0.05,\, 0.05)$.

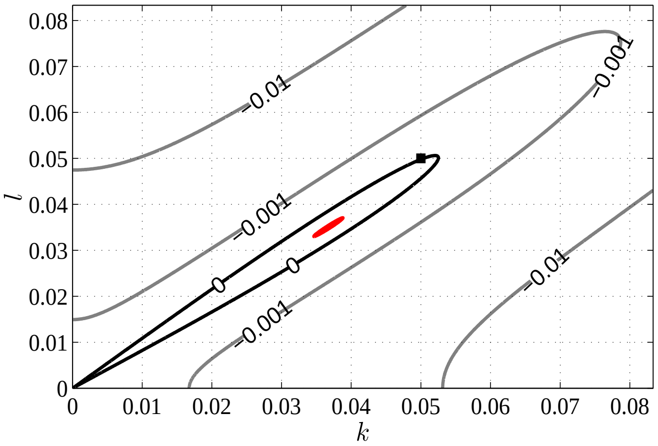

Figure 4.5: *Contour behavior of the the maximum eigenvalue in the (k, l) plane for the system parameters $q = 0.1$, $g = 20$ and $\mu = 0.29652$ (point (a) in figure 4.5). The maximum eigenvalue occurs with $(k,\ l) = (0.036,\ 0.033)$. The zero contour (denoted in black) extends through the point $(k,\ l) = (0.05,\ 0.05)$. A negative value of the maximum eigenvalue is indicated by gray contours while positive values of the maximum eigenvalues are in red.*

4.5.1 The 3-mode truncation

In this subsection we describe the analysis for the system parameter values $(g,\ q,\ \mu,\ k,\ l) = (20,\ 0.1,\ 0.29652,\ 0.05,\ 0.05)$, using the 3-mode truncation (4.19). The eigenmodes corresponding to A_0, A_1, A_{-1} are $e^{i(1.1,0)\cdot\mathbf{x}}$, $e^{i(1.15,0.05)\cdot\mathbf{x}}$ and $e^{i(1.05,-0.05)\cdot\mathbf{x}}$ respectively. Figure 4.7 shows how the values of σ_+ vary along the part of solid line indicated in figure 4.6, close to the bifurcation point $(q, \mu) = (0.1, 0.0296519)$. At the bifurcation point, $a_3 = -1.73$. Therefore the secondary bifurcation due to the skew-varicose is via a supercritical pitchfork bifurcation, stable equilibria at $A_{-1} = \pm\sqrt{\frac{\sigma_+}{-a_3}}$. When μ is decreasing, σ_+ becomes positive and the stripe solution becomes unstable. As a consequence, the bifurcating branches exist only for $\mu < \mu_{sv}$ and are necessarily stable.

We show in figure 4.8 how the computation of equilibria replicates the derivation using centre manifold reduction. As expected, they agree close to the bifurcation point. The illustration is for the nonlinear solutions that bifurcate from the primary single mode

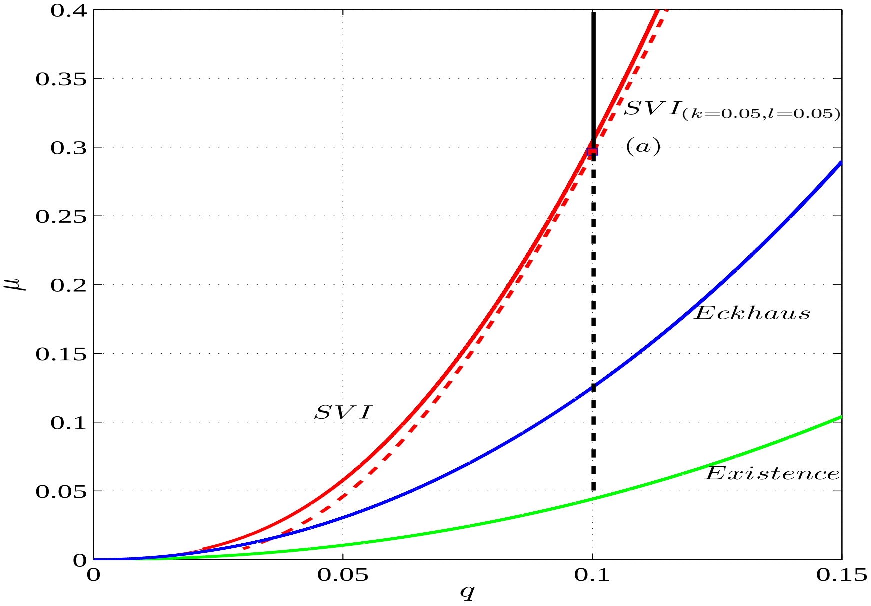

Figure 4.6: *Numerical computation (in model 2) of the SV stability boundary in the* (μ, q) *plane. For* $g = 20$*, the SVI pre-empts the Eckhaus instability for all* μ *and hence the region of stable stripes is bounded by the skew-varicose instability curve, SVI. However, if we fix* $k = l = 0.05$*, the new skew-varicose instability curve (red dotted),* $SVI_{(k=l=0.05)}$ *extends below the boundary of* SVI*. The point,* $(a) = (0.1, 0.29652)$ *on the* $SVI_{(k=l=0.05)}$ *is denoted as a red square and we present the eigenvalue behaviour of this point in figure 4.5. The blue curve is for the Eckhaus boundary whereas the green curve is the boundary of existence of stripes. A vertical line is added to indicate the parameter value* $q = 0.1$*. The dotted and solid portions represent unstable and stable stripe solutions to the skew-varicose instability, respectively.*

solution, A_0.

We are now in a position to illustrate the complete bifurcation diagram for the SVI in the context of this 3-mode truncation. Figure 4.9 shows the numerically computed bifurcation diagram using the software package, MATCONT. We illustrate the connection between the primary instability and the skew-varicose instability. The primary and secondary bifurcations are all supercritical pitchforks. As the primary solution family emerges from the base solution at $\mu_{Existence} = (1 - K^2)^2$, where $K = \sqrt{(1 + q + k)^2 + l^2}$, just after the primary bifurcation point, the states $\pm A_{-1}$, $\pm A_0$ and $\pm A_1$ bifurcating from

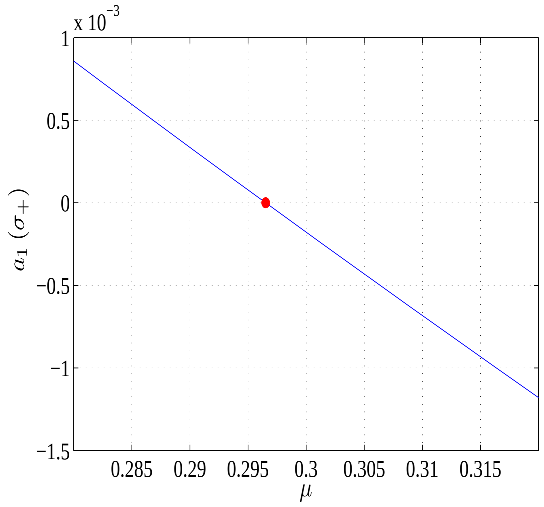

(a)

Figure 4.7: *Variation of a_1 close to μ_{sv} for $q = 0.1$, $g = 20$ and $k = l = 0.05$. The bifurcation is represented by red point.*

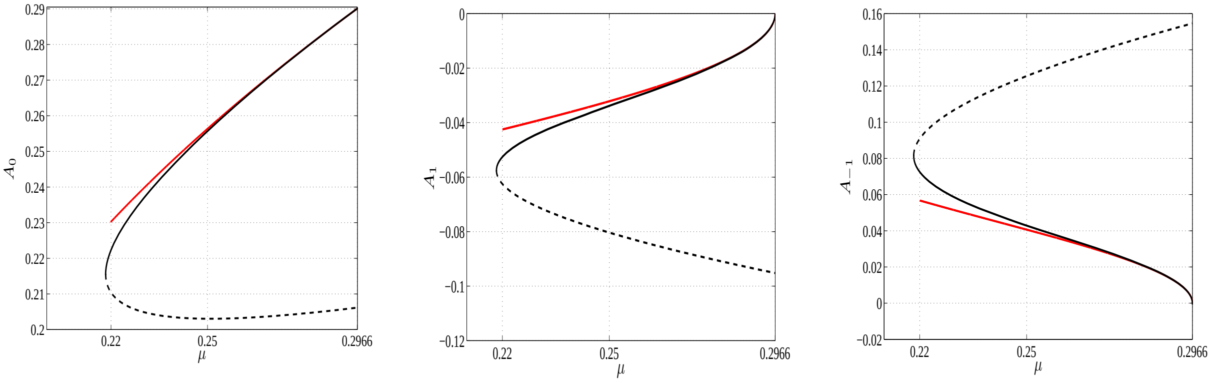

(a) (b) (c)

Figure 4.8: *Correspondence between numerical computation and derivations of the centre manifold reduction. Numerically computed mixed mode solution near the bifurcation point, $\mu = 0.296519$, of the SVI is illustrated in black while the derivation using centre manifold reduction is in red. Amplitudes of (a) A_0 (b) A_1 (c) A_{-1}, of the nonlinear solution after the secondary bifurcation, which is supercritical. The branch extends towards $\mu < 0.296519$ and is stable; it bends back and becomes unstable in a saddle-node bifurcation at $\mu = 0.217$.*

non-existence state at μ for which $r_{-1} = 0$, $r_0 = 0$ and $r_1 = 0$ respectively and these values are $(\mu_{r_{-1}=0}, \mu_{r_0=0}, \mu_{r_1=0}) = (0.011025, 0.0441, 0.105625)$. The members $\pm A_0$ and

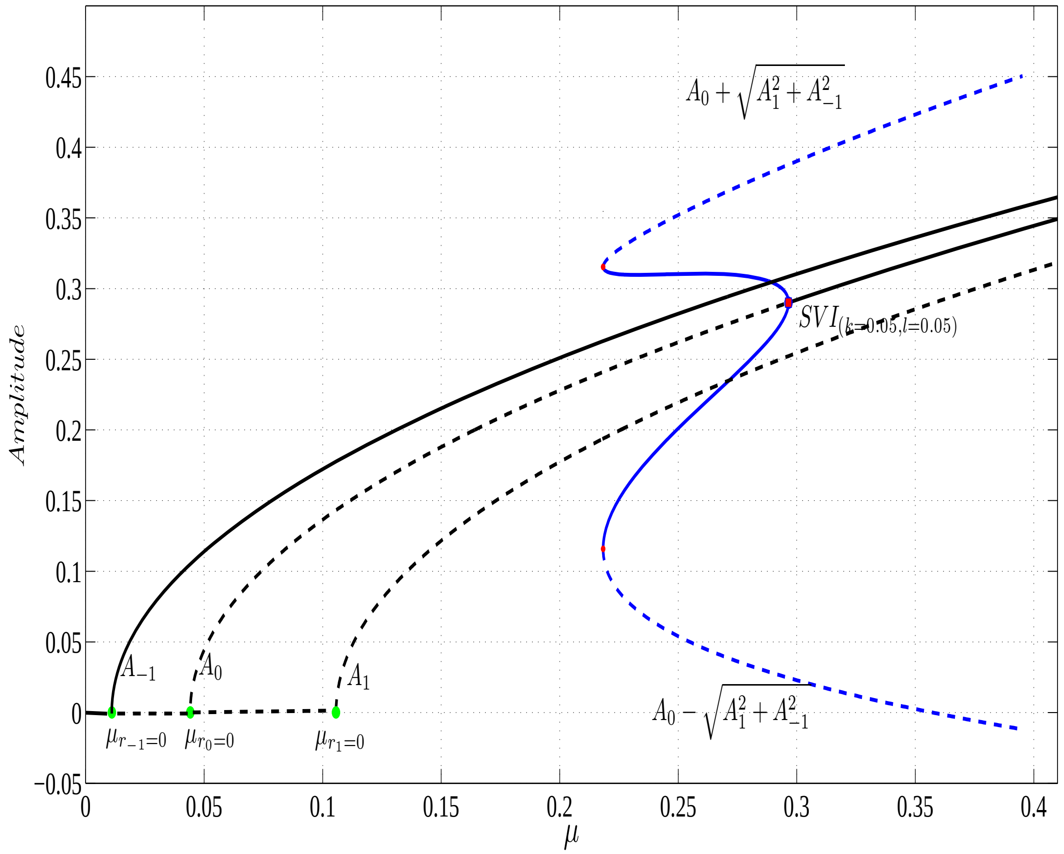

Figure 4.9: *Bifurcation diagram showing the connection between the primary and secondary instabilities and the nonlinear solutions of the 3-mode truncation in model 2. Primary bifurcations (supercritical pitchforks), occur at points* $(\mu_{r_{-1}=0}, \mu_{r_{-1}=0}, \mu_{r_{-1}=0}) = (0.011025, 0.0441, 0.105625)$ *indicated in green, from which primary single-mode solutions* $(\pm A_{-1}, \pm A_0, \pm A_1)$ *bifurcate with the stability properties inherited from the trivial solution. The wavenumber,* K*, of each branch is* $(1.0512, 1.1, 1.1510)$*. The square represents the secondary bifurcation point (the SVI at* $\mu = 0.296519$*) on the primary* A_0 *branch at which point the branch is restabilised. The stable mixed solution bifurcating at this point is denoted in blue, showing the amplitude variation of* $A_0 \pm \sqrt{A_1^2 + A_{-1}^2}$*. These stable branches bend back and become unstable at saddle-node bifurcation points indicated in red. Solid and dashed curves denote stable and unstable branches, respectively.*

$\pm A_1$ are unstable while $\pm A_{-1}$ is stable. The corresponding wavenumbers for A_{-1}, A_0 and A_1 are $K = 1.0512$, 1.1 and 1.1510 respectively. Secondary bifurcation points, due to the SVI, appear from the primary A_0 solution at the critical values are represented by a red square. At this secondary bifurcation the primary solutions regain stability; in other words, secondary bifurcations restabilize the parent branch. The locus of secondary bifurcation points is plotted as a red dotted curve (falling just below the original SVI boundary) in Fig. 4.6. Numerical computations show the bifurcation due to the SVI is supercritical (confirming the centre manifold calculations) and as a consequence, this mixed-mode branch exists for $\mu < \mu_{SVI_{k=l=0.05}}$ and is necessarily stable. The bending back of the unstable branch at a saddle-node bifurcation is also illustrated.

4.5.2 The 5-mode truncation

In this subsection we describe the analysis for the same parameter values ($g = 20$, $k = l = 0.05$ and $q = 0.1$), using the five-mode system 4.20. Reconsider the derivation using centre manifold reduction for this system, where the eigenmodes corresponding to A_0, A_1, A_{-1}, A_2 and A_{-2} are $e^{i(1.1,0)\cdot\mathbf{x}}$, $e^{i(1.15,0.05)\cdot\mathbf{x}}$, $e^{i(1.05,-0.05)\cdot\mathbf{x}}$, $e^{i(1.2,-0.1)\cdot\mathbf{x}}$ and $e^{i(1,-0.1)\cdot\mathbf{x}}$ respectively. We presented in figure 4.7 how the values of σ_+ vary along the part of solid line indicated in figure 4.6, close to the bifurcation point $(q, \mu) = (0.1, 0.0296519)$. At the bifurcation point, $b_3 \approx 21$. Therefore the secondary bifurcation due to the skew-varicose is via a subcritical pitchfork bifurcation, leading to unstable equilibria with $A_{-1} = \pm\sqrt{\frac{\sigma_+}{-b_3}}$.

When μ is decreasing, σ_+ becomes positive at the bifurcation point whereas b_3 is positive, verifying the subcriticality. As a consequence, the branch exists only for $\mu > \mu_{sv}$ and is necessarily unstable. We show in figure 4.10 how the computation of equilibrium points replicates the derivation using centre manifold reduction: these agree close enough to the bifurcation point as expected. The illustration is for the nonlinear solutions that bifurcate from the primary single mode solution, A_0, in subcritical manner. The illustration of amplitudes of A_0, A_1, A_{-1}, A_{-2} and A_2 is for the nonlinear solutions that bifurcate from

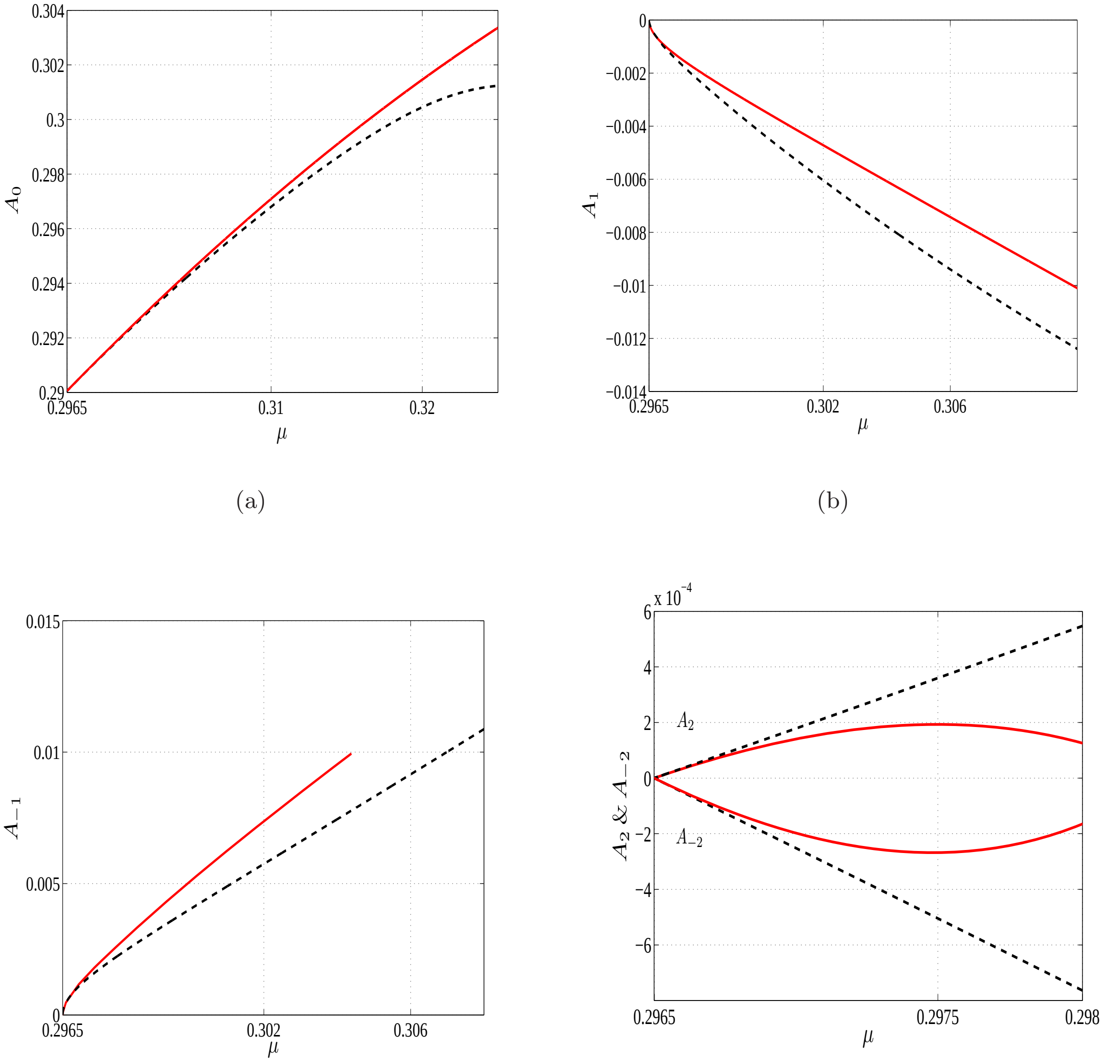

(a) (b)

(c) (d)

Figure 4.10: *Correspondence between numerically computated equilibrium point and the centre manifold reduction of the 5-mode truncation. The mixed mode solutions are illustrated in black while the derivation using centre manifold reduction is in red. Amplitudes are (a)* A_0 *(b)* A_1 *(c)* A_{-1} *(d)* A_{-2} *and* A_2*. The unstable branch exists for* $\mu > 0.296519$.

the primary single mode solution, A_0 at $\mu = 0.296519$.

We are now in a position to illustrate the complete bifurcation diagram for the SVI in the context of this 5-mode truncation. Figure 4.11 shows the numerically computed bifur-

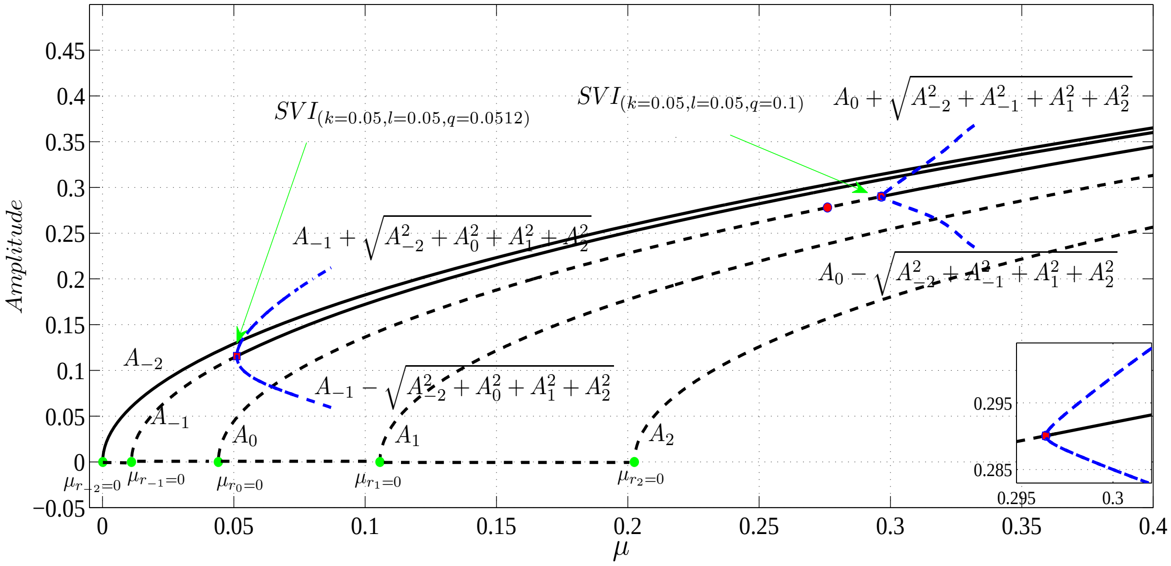

Figure 4.11: *Bifurcation diagram of model 2 with the five-mode truncation showing the connection between the primary and secondary instabilities. The primary bifurcations (supercritical pitchforks), occur at points points* $(\mu_{r_{-2}=0}, \mu_{r_{-1}=0}, \mu_{r_0=0}, \mu_{r_1=0}, \mu_{r_2=0}) = (0.0001, 0.011025,\ 0.0441,\ 0.105625,\ 0.2025)$ *indicated in green, from which primary single-mode solutions* $(\pm A_{-2}, \pm A_{-1}, \pm A_0, \pm A_1, \pm A_2)$ *bifurcate with the stability properties inherited from the trivial solution. The wavenumber,* K*, of each branch is* $(1.005, 1.0512,\ 1.1,\ 1.1510,\ 1.2)$*. The squares represent secondary bifurcation points on the primary branches, where the single mode solutions restabilize. We follow the branches* A_0 *and* A_{-1}*, where the secondary bifurcations (subcritical pitchforks) occur at* $\mu = 0.296519$ *and* $\mu = 0.051$ *respectively. As a consequence, the mixed-mode branches exist only for* $\mu > 0.296519$ *on* A_0 *and* $\mu > 0.051$ *on* A_{-1} *and these unstable solution, originating from the primary single-mode steady solutions, are denoted as a blue curves, showing the amplitude variation of* $A_0 \pm \sqrt{A_{-2}^2 + A_1^2 + A_{-1}^2 + A_2^2}$ *and* $A_{-1} \pm \sqrt{A_{-2}^2 + A_0^2 + A_{-1}^2 + A_2^2}$ *respectively. We also note another bifurcation point on* A_0 *(red circle) at* $\mu = 0.276$ *where* A_2 *and* A_{-2} *become non-zero. Solid and dashed curves denote stable and unstable branches, respectively*

cation diagram using the software package, MATCONT. We illustrate the connection between the primary instability and the skew-varicose instability. The primary and secondary bifurcations are all supercritical pitchforks. As the primary solution family emerges from the base solution at $\mu_{Existence} = (1 - K^2)^2$, where $K = \sqrt{(1 + q + k)^2 + l^2}$, just after the primary bifurcation point, the states $\pm A_{-2}$, $\pm A_{-1}$, $\pm A_0$, $\pm A_1$ and $\pm A_2$ bifurcating from non-existence state at μ for which $r_{-2} = 0$, $r_{-1} = 0$, $r_0 = 0$, $r_1 = 0$ and $r_2 = 0$ respectively $((\mu_{r_{-2}=0},\ \mu_{r_{-1}=0},\ \mu_{r_0=0},\ \mu_{r_1=0},\ \mu_{r_2=0}) = (0.0001, 0.011025,\ 0.0441,\ 0.105625,\ 0.2025)$). In the first branch, A_{-2}, the trivial solution is stable, but all subsequent solutions bifurcating from the trivial solution are unstable. The corresponding wavenumbers for A_{-2}, A_{-1}, A_0, A_1 and A_2 are 1.005, 1.0512, 1.1, 1.1510 and 1.2 respectively. Secondary bifurcation points, due to the SVI, appear from the primary A_{-1} and A_0 solutions at the critical values are represented by a red squares. At these secondary bifurcations the primary solutions regain stability; in other words, secondary bifurcations restabilize the parent branch. Numerical computations show the bifurcation due to the SVI is subcritical (confirming the centre manifold calculations) and as a consequence, those mixed-mode branches, which are originated at $\mu = \mu_{SVI_{k=l=0.05}}$, exist for $\mu > \mu_{SVI_{k=l=0.05}}$ are unstable. We note here that the secondary bifurcation due to the SVI of A_{-1} primary solution is subcritical, presumably due to the contributions from modes A_1 and A_2. We also show another bifurcation point on the A_0 solution. At this point the values of A_2 and A_{-2} become non-zero.

We continue with a brief study of the 5-mode truncation obtained from model 1, real system of equations (4.16 and 4.17). The results of a computation of its equilibrium points show that the secondary bifurcation is also a subcritical pitchfork. We established in chapter 2, using linear stability analysis, that models 1 and 2 had the same SVI boundary provided the relation $g = g_m/(Pr\, c^2)$ held; therefore, the SVI boundary for model 1 with $g_m = 40$, $Pr = 1$ and $c^2 = 2$ is same as in figure 4.6. The bifurcation point at the primary

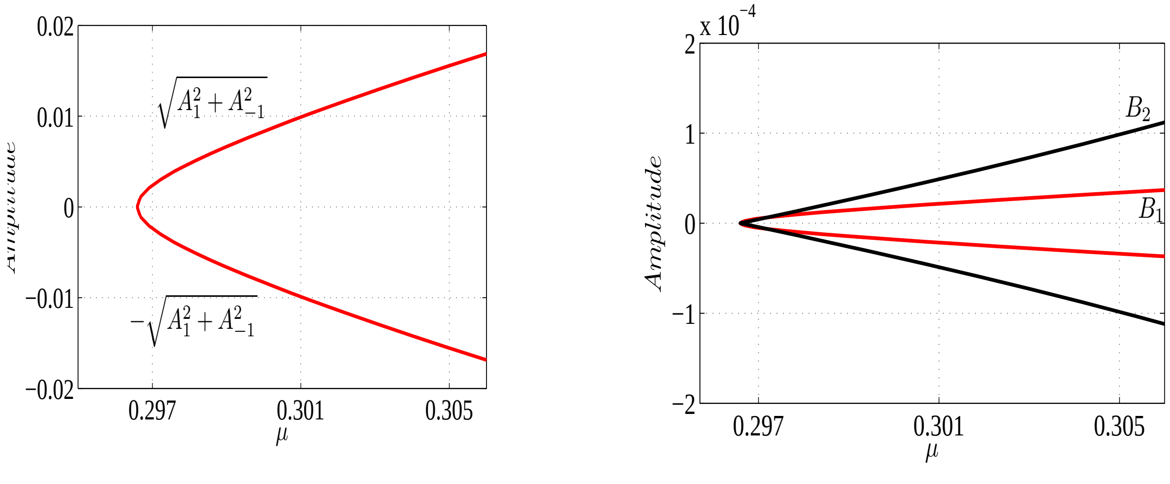

(a) (b)

Figure 4.12: *Numerically computed mixed mode equilibrium points close to the subcritical bifurcation point, $\mu = 0.296519$, of the SVI for the system (parameter values are $g_m = 40$, $Pr = 1$ and $c^2 = 2$). Amplitudes are (a) $\pm\sqrt{A_1^2 + A_{-1}^2}$ and (b) B_1 and B_2 representing the mean flow. The unstable branch exists for $\mu > 0.296519$ and is necessarily unstable.*

solution branch of A_0 is at $\mu = 0.296519$, at which nonlinear unstable solutions emerge. Numerically computed mixed-mode equilibrium points are presented in figure 4.12.

4.6 Agreement of results of direct simulations of the models and bifurcation analysis of systems of ODEs

In this section we show by an example that the results of systems of ODEs (4.19) and (4.20) are in remarkable agreement with studies of the truncated PDEs; only modes relavent to theoretical analysis are retained in PDE calculations. In order to compare the bifurcation analysis that we performed for the SVI, we find the solutions to the nonlinear system of PDEs (4.2-4.3 & 4.2-4.4). These PDEs are solved numerically using the numerical scheme described in detail in chapter 3.

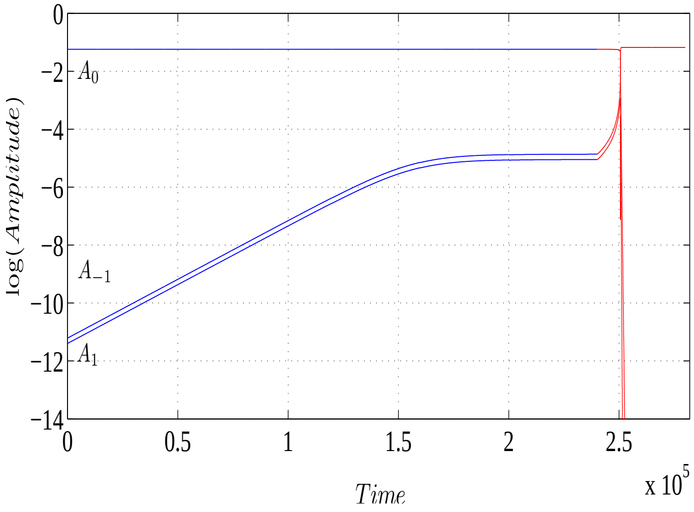

Figure 4.13: *Logarithmic plot of the amplitude of the modes A_0, A_1 and A_{-1} with respect to time. Here the wavevector component of the perturbed mode is $(1.15, 0.05)$. Parameter values are $\mu = 0.294$ and $g = 20$. Our initial simulation results (in Blue) includes only three modes corresponding to amplitudes A_0, A_1 and A_{-1} and after a long time the solution saturates to the nonlinear solution we obtained from the 3-mode truncation at $\mu = 0.294$, a mixed mode solution on the stable (supercritical) branch (see figure 4.9). We then introduce additional modes corresponding to the amplitudes A_2 and A_{-2} and the resulting behaviour is denoted in red. The solution switches onto the single mode branch with $A_{-1} \neq 0$, due to the fact that the skew-varicose instability occurs via a subcritical bifurcation, as illustrated in figure 4.11*

We solve the PDEs in an $L \times L$ square cell with, $L = 20 \times 2\pi$. This fixes a lattice in (k, l) space with lattice spacing $2\pi/L = 0.05$. A grid with N^2 Fourier modes has been used with $N = 256$ and we use periodic boundary conditions. We apply the projection and filtering operations in numerical simulations to keep the same conditions on the numerical solution and in the bifurcation analysis.

We present the results we obtained for the parameter values $g = 20$, $q = 0.1$ and $k = l = 0.05$. This selection of q, k and l is allowed by the size of the domain and in order to investigate details of stability for small (k, l), we need a large domain size and this is time consuming. We find nonlinear solutions for the truncated PDEs (keeping 3 modes and their complex conjugates) which agrees with the 3-mode truncation; we cut off the spectrum so as to include only eigenmodes corresponding to wavevectors $(1.05, -0.05)$, $(1.1, 0)$, $(1.15, 0.05)$ (accordingly to $(1 + q \pm k, \pm l)$, as in the 3-mode truncation) and their complex conjugates. We begin with the initial condition $\psi = 0.01 \sin((1.1)x)$ and $\omega = 0$ for $\mu = 0.298$ (stripes are stable at this point) and time stepping until the amplitude of $\sin((1.1)x)$ saturates. We then decrease μ to 0.294 and add perturbations to the stripe solution, $10^{-6} \sin((1.15)x, 0.05y)$, and time step for a further length of time. We are looking for exponential growth of the selected three modes followed by nonlinear saturation (the blue curves in figure 4.13). Note that we choose the initial amplitude of the perturbation and the time interval over which the calculation was done to ensure that the amplitudes of the modes saturate to a constant value, and we found this is same as the bifurcation analysis we carried out in previous sections. In order to find the behavior of non linear solutions for the truncated PDEs (keeping 5 modes and their complex conjugates) which agrees with the 5-mode truncation, we include the modes corresponding to wavevectors $(1, -0.1)$ and $(1.2, 0.1)$ (accordingly to $(1+q \pm 2k, \pm 2l)$, as in 5 mode truncation) and time step for further length of time. We then noted that the solution switches to the single mode stable solution A_{-1}, and this scenario is indicated in red curves. The behavior is due to the switch from a supercritical to subcritical bifurcation as we move from the 3-mode to 5-mode truncation, and is consistent with the behaviour that would be expected from figure 4.11.

4.7 Concluding remarks

The bifurcation analysis for the skew-varicose instability is presented for model 1 (4.2 and 4.3) and model 2 (4.2 and 4.4). We derived systems of ODEs selecting three relevant modes (3-mode truncation) and extending the selection to include 2 more relevant modes

(5-mode truncation). The 3-mode truncation was derived in order to gain insight into the skew-varicose instability in large domains that destroys roll patterns. However, the results of the 3-mode truncation showed that the secondary bifurcation is supercritical, which was inconsistent with our experience with solving the PDE numerically (in chapter 4). We therefore introduced the 5-mode truncation, which has the subcritical bifurcation as expected.

We performed a theoretical analysis with Centre Manifold Reduction in order to capture the supercriticality or subcriticality of the skew-varicose bifurcation. However, the expressions for a_3 and b_3 (of 3-mode and 5-mode truncations), which are incorporated in the normal form of pitchfork bifurcation are enormous. Therefore a theoretical analysis to determine the sign of a_3 and b_3 was not performed. However, we numerically calculated these values for selected parameters and found a_3 is negative for large domains. On the other hand, we note that b_3 is positive, but tends to zero when $L \to 0$. This curious behaviour was not expected.

The supercriticality or subcriticality of the skew-varicose bifurcation was also obtained by direct computation of equilibrium points of the ODEs. We illustrated this scenario using a case study with the parameters, $g = 20$, $q = 0.1$ and $k = l = 2\pi/L = 0.05$. Results of numerical computations agreed well with the results of Centre Manifold Reduction; in 3-mode truncation the secondary bifurcation due to the SVI is supercritical pitchfork whereas it is subcritical pitchfork in 5-mode truncation. In addition we established an agreement with results of systems of ODEs and numerical computations of truncated PDEs (including relevant 3 modes and 5 modes). Results of full PDEs are the same as the results of PDEs with 5-mode truncation.

The bifurcation structure presented by Nguyen *et al.* [97] is based on the Busse system, which is obtained as a truncation to just three modes with wave vectors $k_i = (\frac{\pi}{2} + \frac{\pi i}{4}, \frac{\pi}{2})$

for $i = -1, 0, 1$. This selection involves the specific domain size $L = 2 \times 2\pi$, in the fluid layer. They confined to brief discussion on the extension of Busse system including one more mode with wavevector $k_4 = (0, \frac{3\pi}{4})$. With this selection, they claimed that much of the bifurcation scenario of the Busse system remains same in the extension and noted some additional bifurcations. It should be emphasized that this selection of modes may not fully and accurately describe the structure of the bifurcation diagram. On the other hand, the bifurcation diagram for the Eckhaus instability was presented by Tuckerman and Barkley, based on Ginzburg-Landau equation for finite aspect ratio. With this 3 mode selection they claimed that the secondary bifurcations are all subcritical, as was expected.

We claim that the three mode truncation can not capture the correct nonlinear solutions at the bifurcation due to the skew-varicose instability and a truncated system of 5 modes may capture the correct behaviour. We suggest to consider truncations with more modes and systems with higher aspect ratio in order to get the accurate behaviour of nonlinear solutions.

Chapter 5

Solutions to the Generalized Swift–Hohenberg model: Spiral Defect Chaos and Defect Chaos

5.1 Introduction

In this chapter we perform a qualitative and quantitative analysis to improve the understanding of the full numerical solutions to the generalized Swift–Hohenberg model. We discuss how the model parameters produce different solutions: Spiral Defect Chaos (SDC), Defect Chaos (DC) and Target (T) states. We obtain these solutions by numerical integration of the model of interest (model 1 in chapter 2) for very long times. We perform simulations in large domains over a range of parameter values in order to discover how the parameter values alter the different solution states, particularly SDC. We show that the generalized Swift–Hohenberg model can produce SDC that resembles the SDC in convection if the mean flow is large, the Prandtl number is small, the domain is large and the parameter that accounts for the top and bottom boundary conditions is small. We also find that slowly moving target states dominate for large Prandtl numbers, weak values of the mean flow or large values of the parameter that accounts for the top and bottom boundary conditions.

Spiral Defect Chaos (SDC) and global spiral patterns were experimentally observed in low-viscosity convection nearly 20 years ago [38], and yet much of the detail of its origin remain unexplained. Spiral Defect Chaos is characterized by the dynamics of rotating spirals and defects and interestingly the state occurs for fluid parameters even where straight parallel convection rolls are linearly stable [20, 47]. So far, very limited theoretical insight has been obtained as to why the spiral chaotic state develops, or of the dynamic behaviour of spirals and defects within chaotic state and global spirals in Rayleigh–Bénard Convection and the understanding of these patterns.

After being discovered experimentally [38], SDC was first found numerically in solutions of the generalized Swift–Hohenberg (GSH) models [56, 69, 73], and of the Boussinesq approximation for the full hydrodynamic equations for convection [11, 44, 45, 46, 47]. Although significant progress has been made in the ability to simulate convection using the Boussinesq equations in large domains, the computational cost remains very high [86].

The GSH models are computationally less expensive to integrate than the Boussinesq equations and hence have the advantage of allowing longer runs and a more detailed exploration of parameter values, helping to understand features of SDC in RBC. As models of convection, the generalized Swift–Hohenberg models have been proven very successful in characterizing convective patterns, and numerical solutions of GSH models reproduce qualitative features of SDC, resembling experimental results reasonably well [69]. However, Schmitz *et al.* [76] suggest that making a direct comparison between the model and convection is not appropriate.

Spatially disordered patterns, such as SDC, have been described by several researchers using local pattern properties: Hu *et al.* [49] computed local wavenumbers and curvatures in experimental pictures and proposed order parameters to describe transitions in spatiotemporal chaos in Rayleigh–Bénard Convection: Cross and Tu [55] used a model of convection rotating about a vertical axis and characterized the domain structure. However the methods they used took large amounts of time to process each snapshot in systems exhibiting complicated time-dependent behaviour. Morris *et al.* [45] used experimentally obtained shadowgraph images of SDC to characterize the space-time behaviour by means of the structure-factor. More recently, Egolf *et al.* [52] described a fast method for calculating properties of locally striped pattern based on ratios of simple partial derivatives. We use this method to investigate the local properties of the solutions to the model of interest.

In this chapter, we base our numerical study on the GSH model,

$$\frac{\partial \psi}{\partial t} + (\mathbf{U} \cdot \nabla)\, \psi = \left[\mu - (1 + \nabla^2)^2\right] \psi - \mathcal{P}_\alpha \left(\psi^3\right), \tag{5.1}$$

$$\left[\frac{\partial}{\partial t} - Pr(\nabla^2 - c^2)\right] \omega = -g_m \mathcal{F}_\gamma \left[\nabla(\nabla^2 \psi) \times \nabla \psi\right] \cdot \widehat{\mathbf{z}}, \tag{5.2}$$

that has been developed to include the effects of mean flow [69, 87]. We present results of extensive numerical work, which provides a criterion for when Spiral Defect Chaos, defect chaos or target states may be expected, depending on the different parameters of the system, on the size of system and on different boundary conditions. This includes a study of transition between the different states for different parameters. We attempt to quantify several aspects of the different patterns and to understand the time dependence of these aspects. We also investigate the small scale features using the images of solution states of the model.

This chapter is constructed as follows. We present our numerical scheme in section 2. In section 3, the different possible solutions of the model are illustrated. We include a qualitative study of these solutions to show how they depend on different parameters of the model in section 4, where we present how the onset of the defect chaotic state depends on the Prandtl number and the size of the domain. In section 5, we discuss our attempts to differentiate the solutions of the model quantitatively using a count of Spirals and Defects, Kinetic Energy. We present our results of local wavenumber in section 6, where we illustrate SVI distortions in different solutions and the wave-vector orientation of different structures. We conclude in section 7.

5.2 Numerical Scheme

The numerical scheme we employ to solve these two-dimensional model equations is for periodic boundary conditions. This leads, conveniently, to the application of the Fourier pseudospectral approximation in space using a spectral method, which is an elegant technology for the numerical solution of PDEs [100]. This involves the use of the Fast Fourier Transform to discretize the PDEs into a coupled system of ordinary differential equations (ODEs) for the time-dependent coefficients of the complex exponentials; we then use a time-stepping method to solve those ODEs. The linear parts of this system, $L_1 = \mu - \left(1 - K^2\right)^2$ and $L_2 = -Pr\left(K^2 + c^2\right)$, where K is the wavenumber, are diagonal in spectral space. The nonlinearities are evaluated at grid points by transforming to physical space and then transforming back to the spectral space. In order to maintain the projection operator in the cubic nonlinearity, the contributions to the cubic nonlinearity are cutoff in the spectral space if wavenumber $|K| > 2.5$. The contributions of high wavenumber modes in the vorticity field that contributes to short-wavelength instabilities are reduced by filtering operator to the nonlinearity and that is performed in the Fourier space; amplitudes of higher wavenumbers are damped by $e^{-\gamma^2 K^2}$. Aliasing is a phenomenon that occurs when higher wavenumbers are folded back into the lower spectrum; nonlinearities generate high wavenumbers and aliasing is initiated when resolution cannot be increased to the extent that high wavenumbers are resolved. The higher wavenumbers that can be aliased are filtered out by the dealiasing.

In this work, time stepping, which is carried out in spectral space, is based on an exponential time differencing (ETD) scheme. The idea behind the ETD methods is to multiply the differential equation by an integrating factor that allows to solve the linear part by exact integration with an approximation of an integral involving the nonlinear components. Different ETD schemes have been introduced based on the approximation of this integral.

We employ an ETD method based on the Runge-Kutta scheme, the exponential time differencing fourth-order Runge-Kutta (ETDRK4) method, which was derived by Cox & Matthews in 2002 [101]. For all Fourier modes, L_1 and L_2 span a wide range of values and this method is well suited to handle this wide range.

However, a well-known difficulty associated with ETDRK4 is that its coefficients resemble the higher orders of the form, $(e^L - 1)/L$ (here L refers to a linear operator) and therefore suffer from cancellation errors when the linear operator has eigenvalues close or equal to zero. There is a chance of having small values in the discretized linear operators, L_1 and L_2 for some values of the wavenumbers, particularly for larger box sizes and hence special care is needed in calculating coefficients in order to avoid rounding errors. We handle this issue by introducing a cutoff for small values and using a Taylor series approximation to the coefficients for diagonal elements below the cutoff. We select this cutoff value ensuring that Taylor series representation and the direct computation of coefficients preserve the highest accuracy; our implementation approximates the explicit formula by a 9-term Taylor series when $|\Delta t\, L| < 0.04$, where Δt is the time step.

Our results are reported in a square domain that is discretized on a spatially uniform grid. Owing to the necessity of the large aspect ratios for the study of SDC, most of our simulations are for aspect ratios, $\Gamma = 40$ and 100 wavelengths. We extended our simulations in domains with aspect ratios, 10, 20 and 200 in order to check the state dependence with the domain size, L, where $L = 2\pi\Gamma$. We discretized the spatial domain using N Fourier modes in each horizontal direction so that $\Delta x = \Delta y = L/N$. The number of Fourier modes, N is chosen to satisfy the maximum allowed wavenumber, $K_{max} = N_d/(2\Gamma)$ where ($N_d = 2N/3$) (here 2/3 is the dealiasing power), to be greater than the required cutoff value of the wavenumber, which is 2.5 due to the projection cutoff describe above. The results presented in this chapter are mostly based on $k_{max} = 4.26$ (i.e., $N = 512$ for $L = 2\pi \times 40$ and $\Delta x = \Delta y = 5\pi/32$). We impose periodic lateral boundary conditions and each individual simulation is allowed to evolve for very long time for a time step of $\Delta t = 0.1$.

The numerical code was initially developed in MATLAB. However, due to the need to carry out long simulations over a range of parameter values, we translated the code into C. Both developments share a common phenomenon listed below. We recall PDE 1,

$$\frac{\partial \psi}{\partial t} + (\mathbf{U} \cdot \nabla)\, \psi = \left[\mu - (1 + \nabla^2)^2\right] \psi - \mathcal{P}_\alpha \left(\psi^3\right),$$

and PDE 2

$$\left[\frac{\partial}{\partial t} - Pr(\nabla^2 - c^2)\right] \omega = -g_m \mathcal{F}_\gamma \left[\nabla(\nabla^2 \psi) \times \nabla \psi\right] \cdot \widehat{\mathbf{z}},$$

of GSH model.

- We begin with introducing global variables (Pr-Prandtl number, μ-bifurcation parameter, g_m-coupling coefficient to the mean flow, c-parameter that models boundary conditions) and constants (time step, $\Delta t = 0.1$, $L = 40 \times 2\pi$, $N = 512$).
- We then set up spatial grid, $X = Y = (0 \cdots N-1)L/N$, wavenumbers, $K_x = K_y = 2\pi[0 \cdots N/2 \;\; -N/2+1 \cdots -1]/L$ and $K = \sqrt{K_x^2 + K_y^2}$, and linear operators,

$L_1 = (\mu - 1) + 2K^2 - K^4$ and $L_2 = -Pr(K^2 + c^2)$;

- The initial condition we used is a random number for ψ with random amplitude between 0.0001 and 0.001, scaled down by $1/(1 + K^6)$ to make it smooth and zero mean flow. We then define dealiasing keeping 2/3 of the spectrum. The projection operator is used to cut off the spectrum if $K > 2.6$ (this is applied only to the cubic nonlinearity of PDE 1).

- We then precompute various ETDRK4 scalar quantities. In evaluating coefficients of ETDRK4, we define a threshold for small eigenvalues, and Taylor series representation of the coefficients is used for diagonal elements below the threshold. If $|L_1 \Delta t| < 0.04$ and $|L_2 \Delta t| < 0.04$, coefficients are approximated using 9-term Taylor series expansion.

- The space transformations between the spectral and physical space are supported to compute all spatial derivatives in Fourier space, the nonlinearities in physical space. Temporal evolution for PDE 1 and PDE 2 is performed in Fourier space ETDRK4. Nonlinear terms, which are calculated by going back to physical space, are transformed into spectral space in order to compute ETDRK4 update of the solution.

- The nonlinear part of PDE 1 is $-\left(\mathbf{U} \cdot \nabla\right) \psi - \mathcal{P}_\alpha \left(\psi^3\right)$. For the illustration we use hat notation to denote in spectral space. In spectral space, $\hat{\nabla \psi} = (iK_x \hat{\psi}, iK_y \hat{\psi})$ and $\hat{\mathbf{U}} = (iK_y \hat{\zeta}, -iK_x \hat{\zeta})$. Using inverse Fourier transformation, these two expressions are converted into physical space, and compute $-\left(\mathbf{U} \cdot \nabla\right) \psi$. The nonlinear term $-\psi^3$ is also computed in physical space and then transfered into spectral space, where we apply the projection.

- The nonlinear part in PDE 2 is $\mathcal{F}_\gamma \left[\nabla(\nabla^2 \psi) \times \nabla \psi\right] \cdot \hat{\mathbf{z}}$. In spectral space, $\nabla(\hat{\nabla^2 \psi}) =$

$-(K_x^2+K_y^2)(iK_x\hat{\psi}, iK_y\hat{\psi})$ ($\hat{\nabla\psi}$ is same as above). Using inverse Fourier transformation, these two expressions are converted into physical space and compute the vector product $\left[\nabla(\nabla^2\psi)\times\nabla\psi\right]\cdot\widehat{\mathbf{z}}$ and convert back to spectral space, where we apply the filtering operator, $e^{-\gamma^2K^2}$.

In order to check the accuracy of the code, we tested code development for linear terms and nonlinear terms. For the linear problem, we measured the growth rates of the modes that are excited for the initial condition and compared with linear theory, which was performed in chapter 2. The nonlinear term in PDE 2 is tested with weakly nonlinear theory of the square solution. The mean flow term is tested with stability calculations, which we performed in chapter 2 and we illustrate our results in the same chapter. We also checked the relative error against step sizes, Δt = 0.1, 0.01, 0.001 and verified that ETDRK4 is fourth order with our development.

5.3 Solutions to the model: Spatial features of convection pattern, ψ and the mean flow field, ζ

In this section, the differences of spatial features between the patterns observed in the mean flow field are illustrated. We present our results in two fields: ψ, which describes the spatial and temporal variation of pattern and ζ, the stream function for the mean flow. The mean flow, which can be written in terms of stream function, tends to reach a local maximum at locations that contain defect structures and it remains large on a length scale of several roll wavelengths around the defect.

We also present the circularly averaged power spectrum of both fields, ψ and ζ. Through out this chapter in presenting the field ψ, we use colour red, $\psi > 0$, representing hot rising fluid and blue, $\psi < 0$, representing cold descending fluid. However, with

Boussinesq symmetry there is no real distinction; $\psi = -\psi$. In the vorticity field, patches indicate the regions of large mean flow; red colour corresponds to clockwise rotations and blue corresponds to counterclockwise rotations.

5.3.1 Stripe pattern

Figure 5.1(a) shows the regular spatial structure of perfect stripe pattern, the stable solution of the model that corresponds to convection rolls. This illustration is for the set of parameters, $Pr = 0.5$, $g_m = 50$ and $\mu = 0.1$. We start with random initial conditions to evolve with $\Delta t = 0.1$, and this shadowgraph is taken at time 4×10^4. The global wave-vector distribution of ψ is presented in figure 5.1(b); the distribution is peaked at $K = 0.93$ and is isotropic. For these parameters, the region of stable stripes is bounded by the Eckhaus instability boundary from below, $K \approx 0.908$ and by the SVI boundary $K \approx 1.045$ from above.

5.3.2 Defect Chaos state

These models exhibit defect chaos (DC), where the dynamics is apparently associated with defects and patches of curved stripes. Figure 5.2(a) denotes the DC phenomenon in the field ψ for parameter values $g_m = 50$, $c^2 = 2$, $Pr = 0.5$ and $\mu = 0.4$ at $t = 10^4$; the system organizes into a structure comprising moving defects, which is exhibited by large patches in corresponding ζ field, as denoted in 5.2(b). The wavenumber distribution is illustrated in figure 5.2(c) where the vertical dotted green and red lines we denote the stability boundaries of stable stripes. The lower tail of power spectrum belongs to the Eckhaus unstable region whereas a part of the upper tail belongs to the skew-varicose unstable regime. In the phenomenon of Defect Chaos, the persistent dynamics is apparently associated with easily identified defects or coherent structures and it exhibits transitions between bend-roll

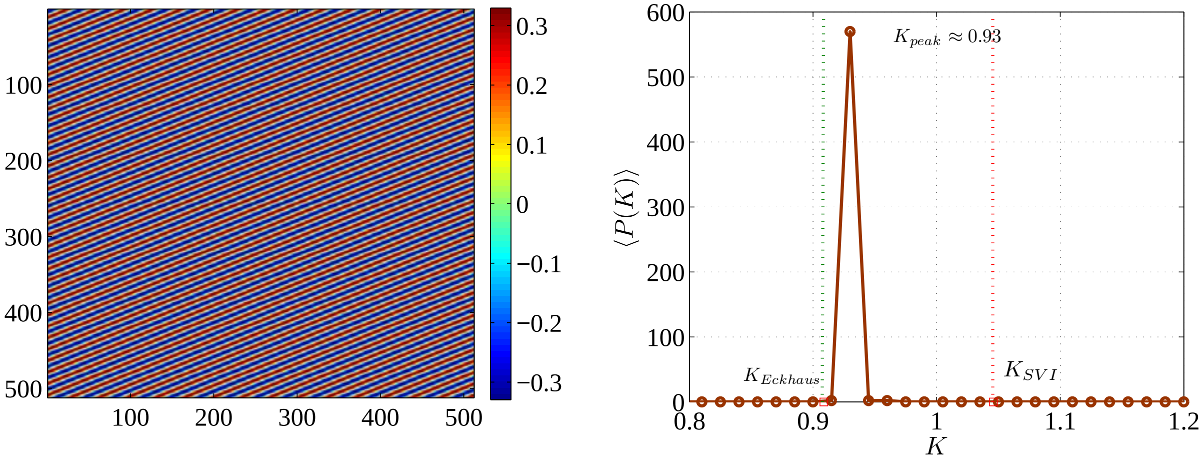

(a)

(b)

Figure 5.1: *A typical configuration of the perfect stripe pattern: (a) Field ψ (colour red correspond to $\psi > 0$, and blue for $\psi < 0$). The configuration shown is at $t = 4 \times 10^4$ for parameter values $g_m = 50$, $c^2 = 2$, $Pr = 0.5$, $L = 40 \times 2\pi$ and $\mu = 0.1$ (b) Circularly averaged power spectrum. The peak of the spectrum is at the wavenumber $K_{peak} \approx 0.93$, in units of the critical wavenumber, $K_c = 1$. For these parameters, the SVI occurs if $K \gtrsim 1.045$ (red dotted line is at $K_{SVI} \approx 1.045$) and the Eckhaus instability limit the stable stripes if $K \lesssim 0.908$ (green dotted line).*

states, curved roll states and patches of rolls that are time dependent. The mean flow at the locations that contain defect structures is spread.

5.3.3 Spiral Defect Chaos state

The Spiral Defect Chaos (SDC) pattern is a disordered state characterized by a collection of spirals and dynamical defects; this state provides an intriguing example of the Defect Chaotic state. This state is marked by the continuous creation and breaking of various sizes of the left and right handed spirals that can rotate in the counter-clockwise or clockwise senses. The background state contains many moving roll dislocations.

Figure 5.3(a) shows spatial variation of the convection field and the corresponding

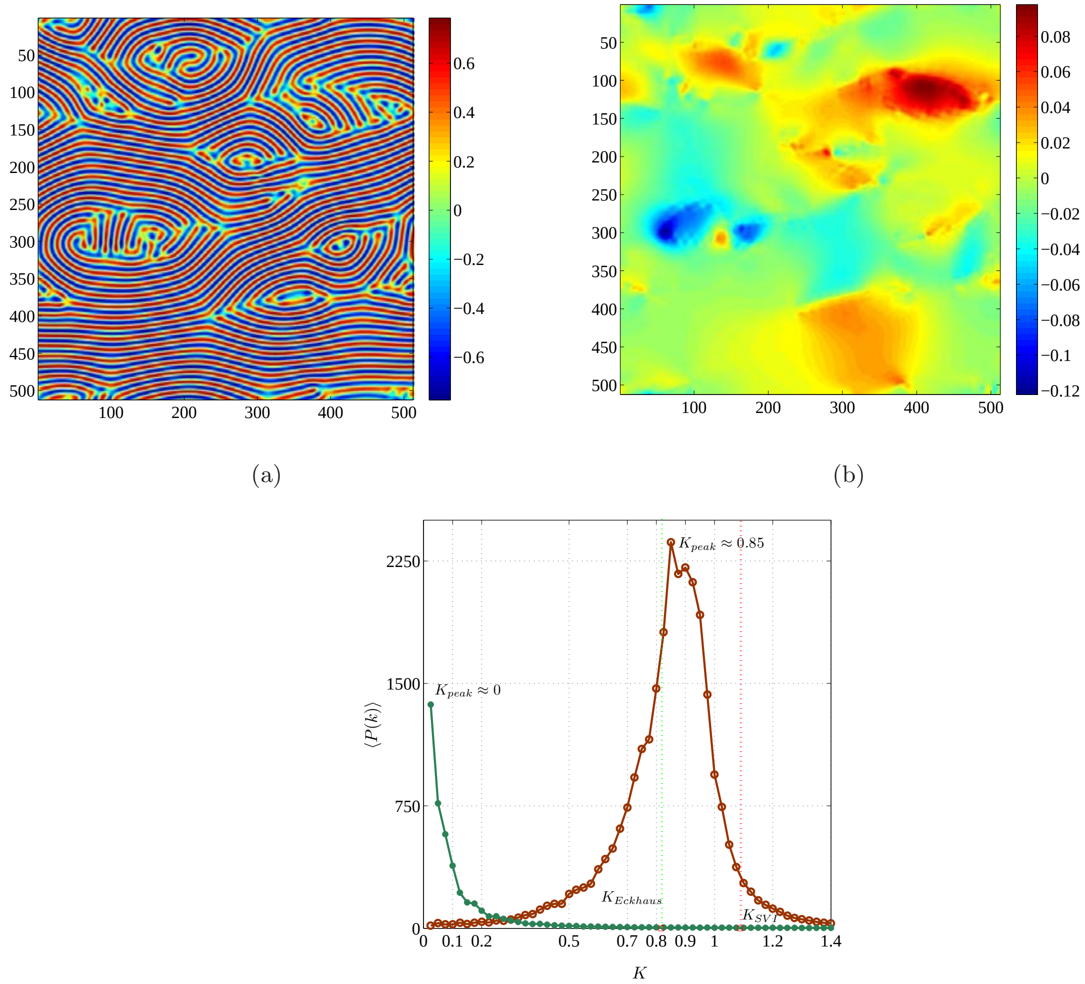

(a)

(b)

(c)

Figure 5.2: *Configuration of the defect chaos state for system parameter values* $g_m = 50$, $c^2 = 2$, $Pr = 0.5$ *and* $\mu = 0.4$ *at* $t = 10^4$*: (a) Field* ψ *(b) Field* ζ*, of which the patches indicate the large mean flow. (c) Circularly averaged power spectrum of the field* ψ *(in brown) and* ζ *(in green).* K_{peak} *of the amplitude of* ψ *is approximately at* 0.85 *whereas it is close to zero for* ζ*. For these parameters, the region of stable stripes is bounded by the Eckhaus instability from below,* $K \approx 0.817$ *(green dotted line) and by the SVI boundary* $K \approx 1.088$ *(red dotted line) from above.*

stream function, ζ, (figure 5.3(b)) for the parameters $Pr = 0.5$, $g_m = 50$, $c^2 = 2$ and $\mu = 0.7$, exhibiting chaotic pattern with many spiral defects. We show in figure 5.3(c) the circularly averaged power spectrum that correspond to configurations ψ and ζ. We see that the power spectrum of ψ is broad and peaked at a wavenumber, $k_{peak} < 1$. Power

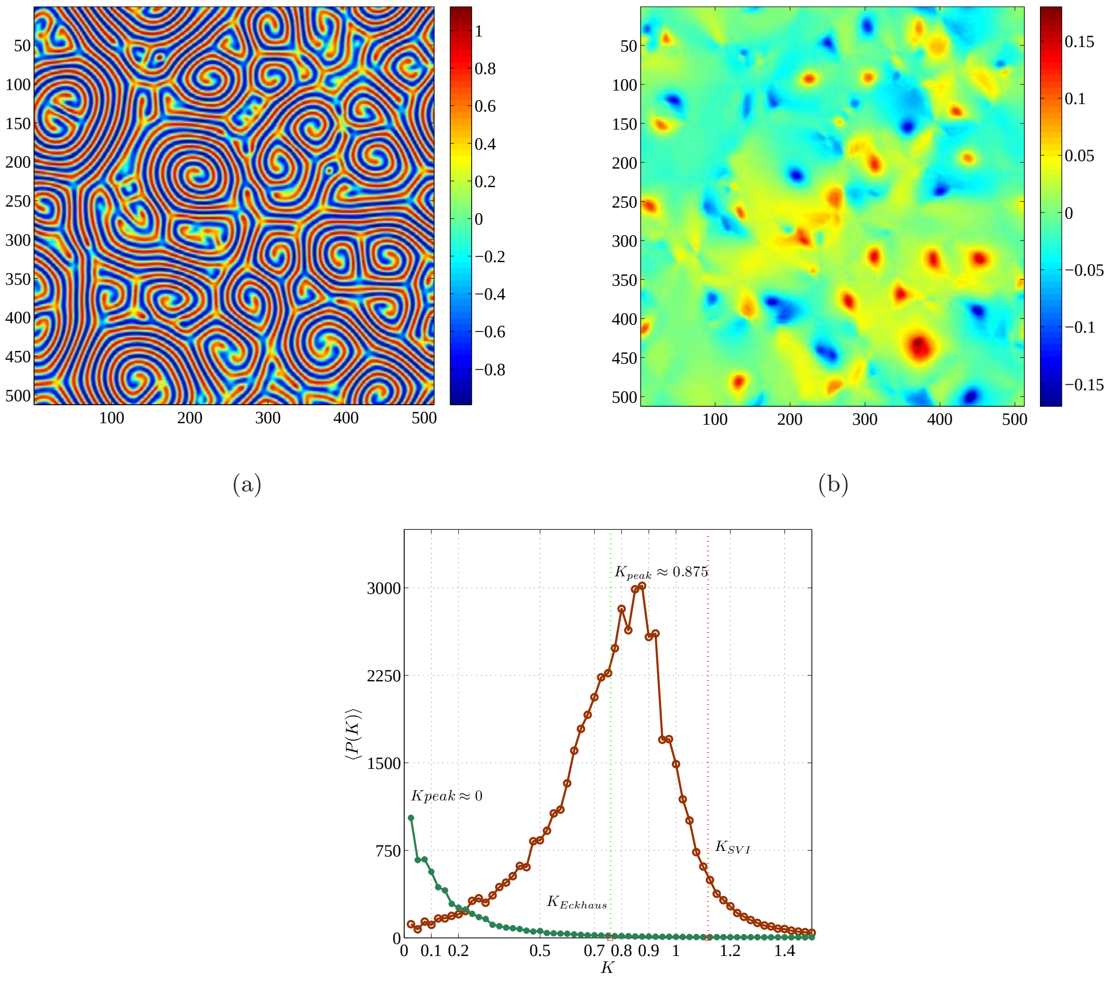

(a) (b)

(c)

Figure 5.3: *An example of Spiral Defect Chaos state observed at* $t = 10^4$ *in a numerical simulation for parameters* $Pr = 0.5$, $g_m = 50$, $c^2 = 2$ *and* $\mu = 0.7$ *(a) Field* ψ *(b) Field* ζ. *Red denotes the core of right handed spirals, while blue contours indicate the left handed spirals. (c) Circularly averaged power spectrum of the field* ψ *(in brown) and* ζ *(in green).* K_{peak} *of the amplitude of* ψ *is approximately at* 0.875 *whereas the peak close to zero for* ζ. *For these parameters, the region of stable stripes is bounded by the Eckhaus instability from below,* $K \approx 0.758$ *(green dotted line) and by the SVI boundary* $K \approx 1.1178$ *(red dotted line) from above.*

spectrum of ζ is peaked close to zero. The lower part of power spectrum belongs to the Eckhaus unstable region whereas a part of the upper tail belongs to the skew-varicose unstable regime.

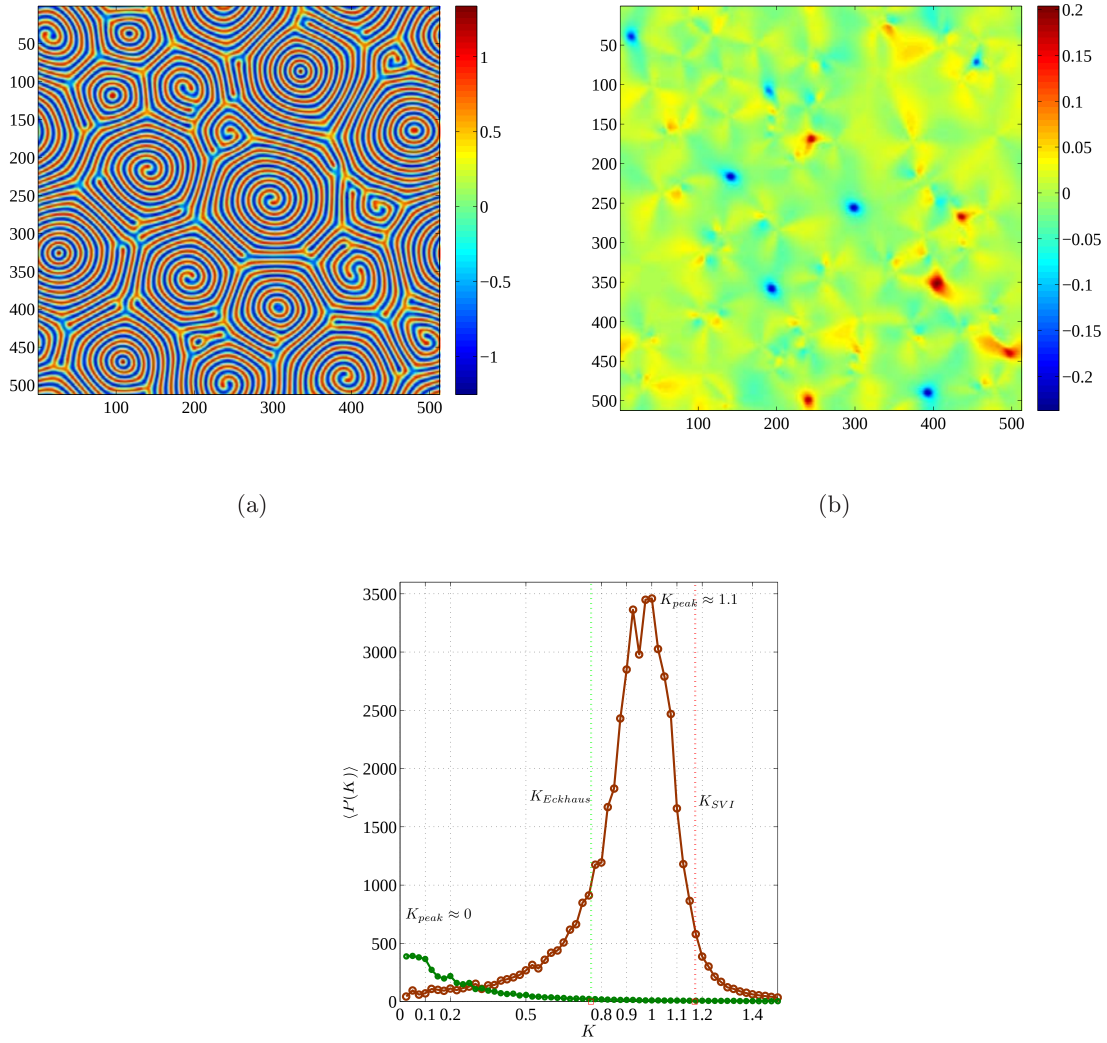

(a) (b)

(c)

Figure 5.4: *An example of target pattern (with many slowly moving spirals) observed at* $t = 10^4$ *in a numerical simulation for set of parameter values* $Pr = 0.5$, $g_m = 10$, $c^2 = 2$ *and* $\mu = 0.7$ *(a) Field* ψ *(b) Field* ζ*. Red denotes the core of right handed spirals, while blue contours indicate the left handed spirals. Note that* ζ *is zero at target core. (c) Circularly averaged power spectrum of the fields* ψ *and* ζ*.* $K_{peak} \approx 1.1$ *for the amplitude of* ψ *and* $K_{peak} \approx 0$ *for the field* ζ*. For these parameters, the region of stable stripes is bounded by the Eckhaus instability from below,* $K \approx 0.758$ *(green dotted line) and by the SVI boundary* $K \approx 1.17$ *(red dotted line) from above.*

5.3.4 Target pattern state

The Target pattern is a state comprising of concentric rolls and spirals, which move slowly in the evolution process. The background state contains some defects, and ill-formed

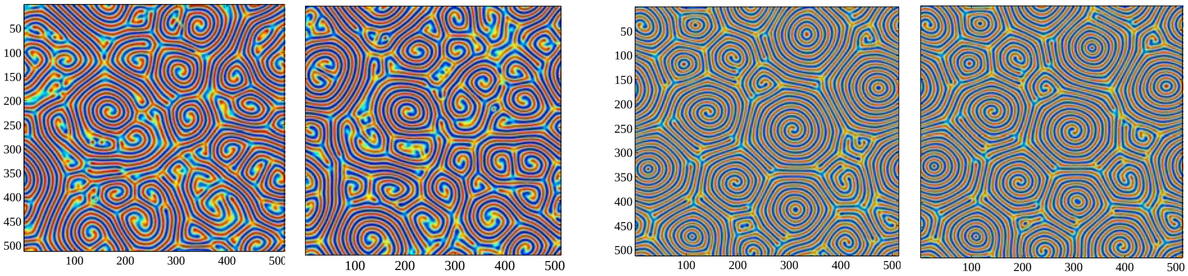

(a) (b) (c) (d)

Figure 5.5: *Instances of the evolution process of SDC state and target pattern. SDC pattern (a) at* $t = 9 \times 10^3$ *and (b) at* $t = 10^4$ *(similar to figure 5.3(a)) in a numerical simulation for set of parameter values* $pr = 0.5$, $g_m = 50$, $c^2 = 2$ *and* $\mu = 0.7$. *Target pattern (c) at* $t = 9 \times 10^3$ *and (d) at* $t = 10^4$ *(similar to figure 5.4(a)) in a numerical simulation for set of parameter values* $pr = 0.5$, $g_m = 10$, $c^2 = 2$ *and* $\mu = 0.7$. *The target pattern resembles stationary targets and spirals.*

spirals, which are less time dependent than SDC state and hence their impact on the well-formed spirals and targets is less. The scenario of the formation of targets is initiated by an instability of a core of dislocations or defects [9, 102]. Figure 5.4(a) illustrates a target state that coexist with spirals for the parameter values $Pr = 0.5$, $g_m = 10$, $c^2 = 2$ and $\mu = 0.7$. Figure 5.4(b) shows the relevant stream function, which is zero at target core in contrast, vorticity patches (these are are circular for well formed spirals) at spiral core. The corresponding global wavenumber distribution is shown in figure 5.4(c).

In the evolution process, the target pattern can be differentiated from the SDC state from its chaotic behaviour; the target pattern resembles slowly moving spirals whereas in SDC state, spirals and defects are chaotic. Figure 5.5 shows two snapshots at $t = 9 \times 10^3$ and $t = 10^4$ of SDC and target states.

5.4 Dependence of solutions of the model on Parameters

We intend, in this section, to illustrate the effect of parameters for the different solutions of the GSH model. We carry out this analysis based on a qualitative examination of different solution states. The choice of the parameters, Prandtl number, Pr, bifurcation parameter, μ, the strength of the mean flow effects, g_m, and boundary condition parameter, c, all have a strong influence on the dynamics of the model, generating different solution scenarios. It is important to determine the range of parameter values that yield dynamics that resemble stripes, Spiral Defect Chaos, Defect Chaos and Target state. Previous numerical work on the GSH model in searching for SDC has been carried out for system parameters $Pr = 1$, $\mu = 0.7$, $g_m = 50$ and $c^2 = 2$ [69, 76], although a justification for this particular choice is not given. Presumably the parameters were chosen to mimic experimental conditions; large aspect ratios and Pr around unity. We discussed this parameter selection in chapter 1.

Here we demonstrate numerical results for different parameter values and suggest most relevant parameters in order to obtain each solution state after transients have passed. We mostly base our study with varying the Prandtl number, Pr, the bifurcation parameter, μ, and the domain size, L. We also describe the effect of c and g_m in order to provide an insight into a sensible parameter range.

5.4.1 Prandtl number, Pr

The Prandtl number is a dimensionless number, the ratio of kinematic viscosity to thermal diffusivity. Experiments and numerical investigations have indicated that a low Pr is required to yield dynamics that generates spirals and defects [23, 49, 103]. We find SDC in the long-time dynamics of the GSH if the correct range of values of Pr is chosen. We

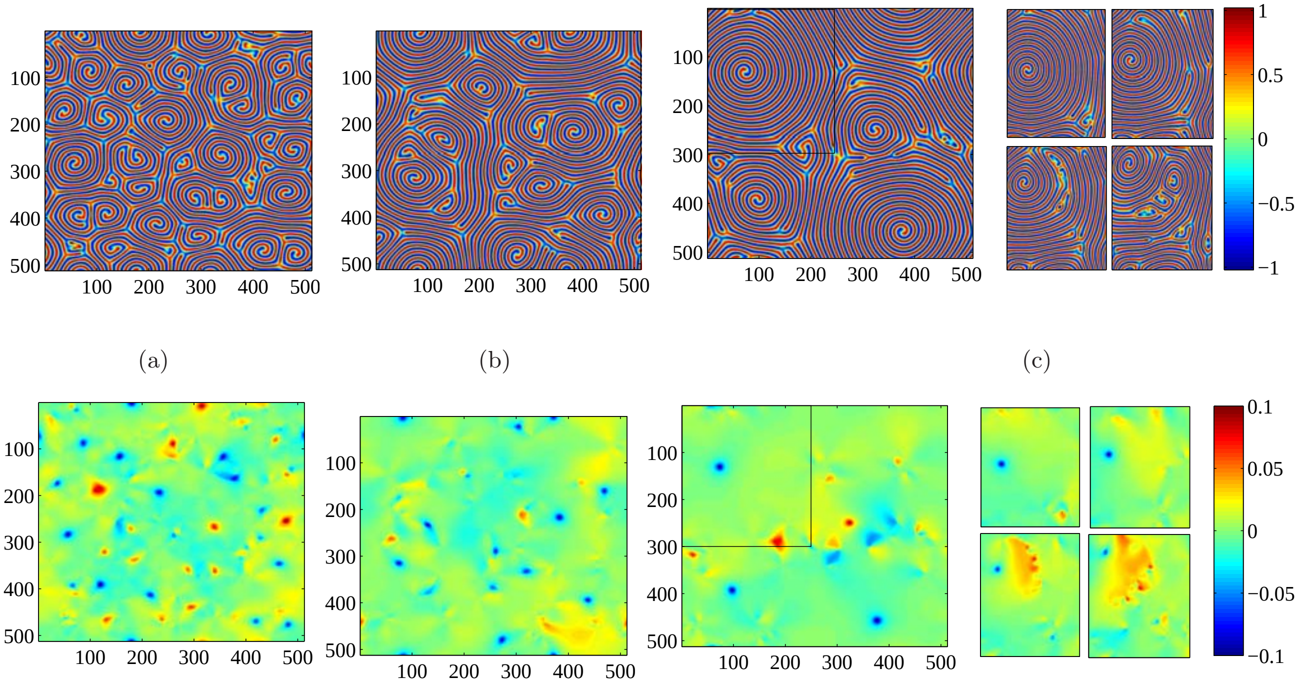

(a) (b) (c)

(d) (e) (f)

Figure 5.6: *Instances of the domain structure of the fields ψ and ζ in the evolution process for the system parameter values $Pr = 1$, $\mu = 0.7$, $g_m = 50$, and $c^2 = 2$. (a) At $t = 5 \times 10^3$; state dominated by small spirals and defects. (b) At $t = 2 \times 10^4$; adjacent spirals and defects combine to form bigger spirals. There are fewer spirals than in planform (a). (c) At $t = 6 \times 10^4$, showing how the pattern has evolved into a state with even bigger spirals. The panel of four plots shows the spiral breaking up (marked in black) in the evolution process. Four states are taken each with a time period of $t = 3000$. (d)-(f) Stream function to the mean flow corresponds to (a)-(c) respectively. Panel in (f) shows how the mean flow behaves in the breaking up process.*

explored the long time dynamics in the range $0.15 < Pr < 6$. Across this range, we found three major types of solutions: Target state, SDC state and complex chaotic state.

We first consider the parameter value used extensively in the literature, $Pr = 1$. Schmitz *et al.* [76] investigated the parameter set $Pr = 1$, $\mu = 0.7$, $g_m = 50$, and $c^2 = 2$ and claimed that Spiral Defect Chaos in the numerical simulations of the GSH disappears when the system evolves into a state dominated by bigger spirals, and therefore concluded that the SDC state is only a transient. Based on this result, they claimed that the use

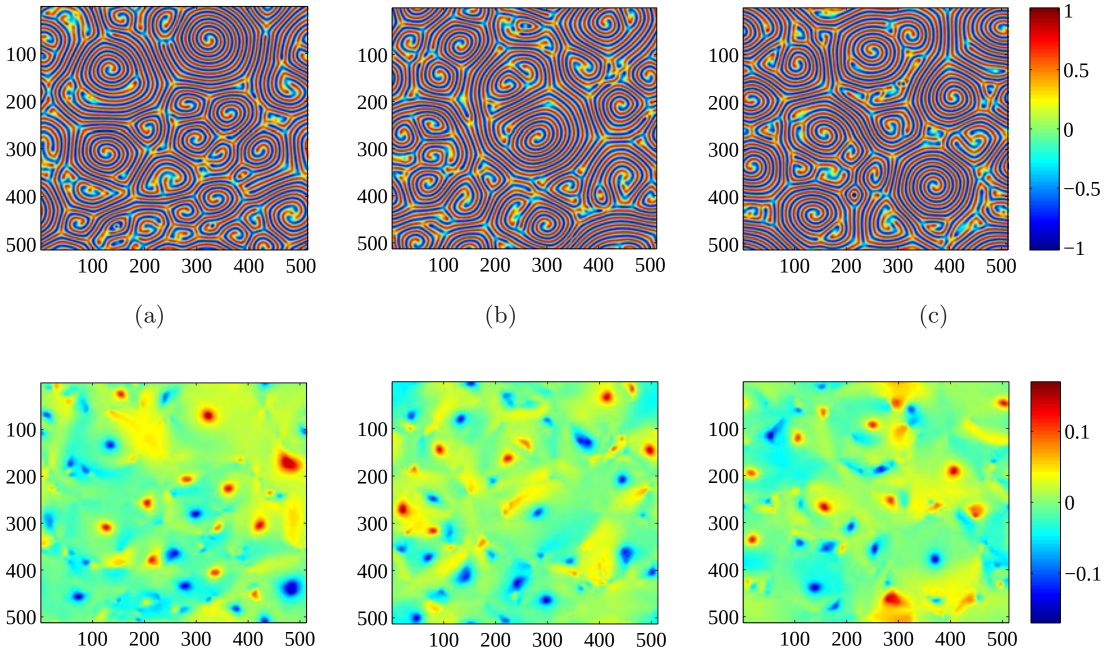

(a) (b) (c)

(d) (e) (f)

Figure 5.7: *Instances of the domain structure of the fields ψ and ζ in the evolution process for the system parameter values $Pr = 0.5$, $\mu = 0.7$, $g_m = 50$, and $c^2 = 2$. Spiral Defect Chaos state persists in long time in the evolution process. (a) At $t = 5 \times 10^3$; (b) At $t = 10^5$; (c) At $t = 2 \times 10^6$. (d)-(f) Stream function to the mean flow corresponds to (a)-(c) respectively. Note that the mean flow profile at the spiral core is wider than in figure 5.6 ($Pr = 1$).*

of the numerical simulations of the GSH model to study the SDC state is problematic. However, our new results, run over much longer times, suggest that these bigger spirals may eventually break into smaller spirals and defects, returning to the SDC state. We speculate that the system then cycles between SDC and a state dominated by bigger spirals.

Figure 5.6 shows instances of pattern evolution in ψ and ζ fields for system parameters as in [76], $\mu = 0.7$, $Pr = 1$, $g_m = 50$, and $c^2 = 2$. At small time, $t < 5 \times 10^3$ the pattern is chaotic and contains many dynamic spiral and defect structures as shown in figure 5.6(a). Planform 5.6(b) represents a snapshot at $t = 2 \times 10^4$, while the coarsening process to

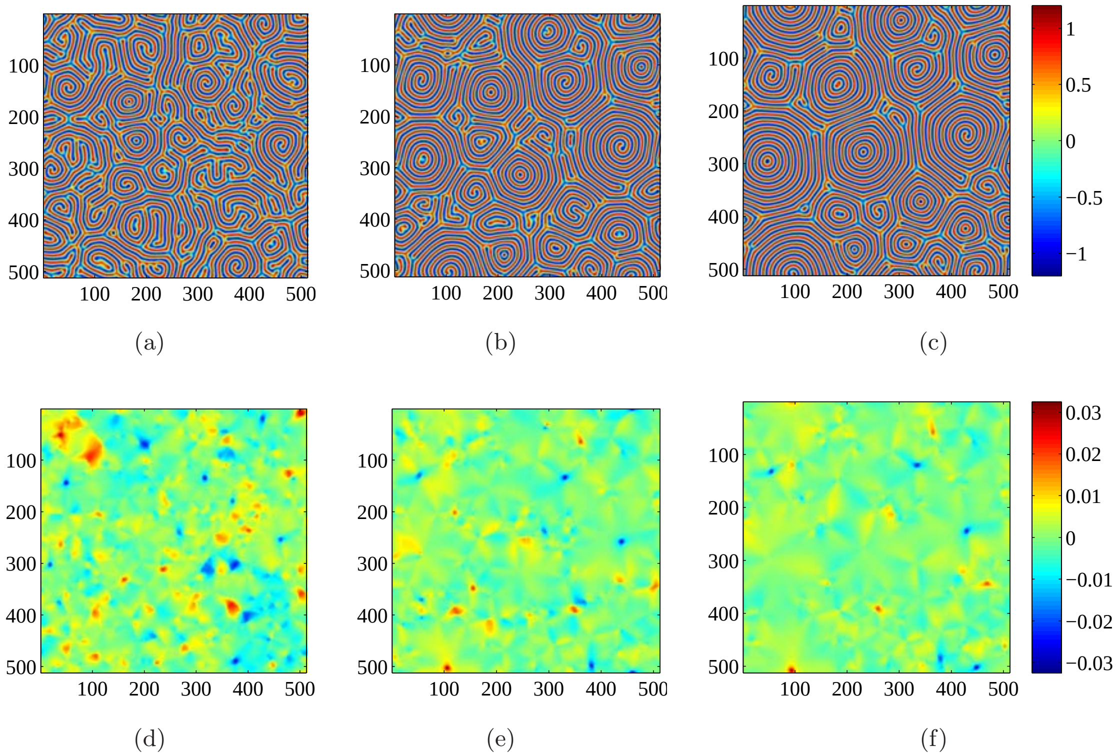

Figure 5.8: *Instances in the long time evolution of the field ψ and corresponding ζ for the system parameter values $Pr = 6$, $g_m = 50$, $c^2 = 2$ and $\mu = 0.7$. (a) At $t = 10^3$: Labyrinthine structure with small targets. (b) At $t = 10^4$: state dominated by targets, spirals and defects; (c) At $t = 10^6$: targets dominating state with few spirals. (d)-(f) Corresponding ζ field of (a)-(c) in order. Note that the mean flow is approximately zero at target core.*

bigger spirals is taking place; well formed spirals capture adjacent small spirals or defects to form bigger spirals. In figure 5.6(c), we show the planform at $t = 6 \times 10^4$, when the formation of bigger spirals has begun. The process of coarsening to bigger spirals is very slow and invasive spirals are evidenced by the pattern after $t = 3 \times 10^4$.

However, the defects that coexist with bigger spirals create instabilities, breaking up the bigger spirals to form small spirals and several defects. The combined motion of bigger spirals with defects can be understood by considering the situation shown in the panel in figure 5.6(c), where we show the evolution process of a bigger spiral that terminates with a dislocation. Note that during the time evolution, the dislocation climbs into the spiral, which breaks up, forming a few defects and a smaller spiral. The defects that are created in the breaking process will then interact with other spirals. We carried out this simulation for very long time $t = 2 \times 10^6$ and we could examine the process of breaking up tends to the Spiral Defect Chaos state invades the domain,similar to the behaviour shown in figure 5.6(a).

We speculate that in subsequent dynamics (time evolution for $t \gg 2 \times 10^6$), the domain structure of the pattern rests on two processes: coarsening to bigger spirals and breaking up into small spirals with defects (SDC state). Our numerical exploration indicates that this scenario occurs when $0.9 \lesssim Pr \lesssim 1.2$.

We attempt to check whether the spirals formed for $0.9 \lesssim Pr \lesssim 1.2$ are expected to capture the small scale features correctly by comparing the mean flow fields around a single spiral of two states: SDC state (for $0.25 \lesssim Pr \lesssim 0.8$) and pattern showing bigger spirals (this state can be seen in the evolution for $0.9 \lesssim Pr \lesssim 1.2$). Figure 5.9 shows the mean flow at core regions of left-handed spirals, which are taken from SDC evolution with $Pr = 0.5$ and bigger spiral evolution with $Pr = 1$. Each contour line shown is 0.02 distance apart.

If $0.25 \lesssim Pr \lesssim 0.8$, the pattern resembles the state of Spiral Defect Chaos even at long times. Figure 5.7 shows instances at $t = 10^4, 10^5$ and 10^6 during the time evolution process for $Pr = 0.5$, $g_m = 50$, $c^2 = 2$ and $\mu = 0.7$. Another interesting feature is that the behaviour, which is shown in figure 5.7(d), of the mean flow at spiral core is different than $Pr = 1$, shown in figure 5.6(d). The vorticity patches at the spiral core spread to couple of wavelengths for $Pr = 0.5$, whereas for $Pr = 1$, they appear to be limited to small scales at the spiral core. Therefore the claim of Schmitz *et al.* [76], that the mean flow in the GSH model is small and hence does not support the long time dynamics of SDC, may not true; for $Pr = 0.5$ (with $g_m = 50$, $c^2 = 2$ and $\mu = 0.7$), in fact, if $0.25 \lesssim Pr \lesssim 0.8$, the

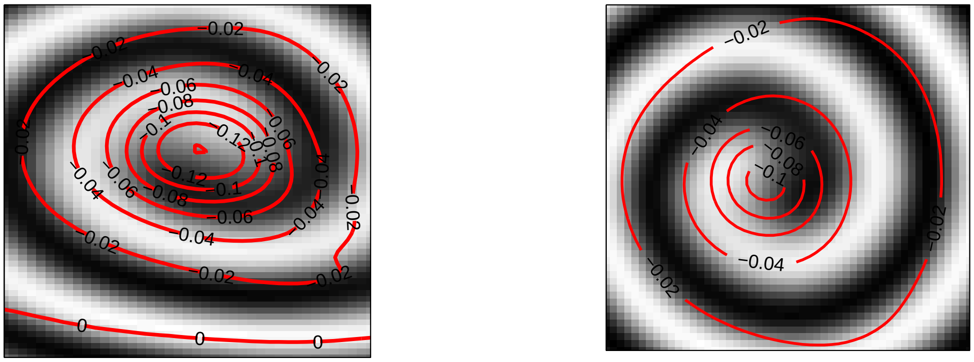

(a)

(b)

Figure 5.9: *Spatial variation of the mean flow at (a) a spiral core in SDC state* ($Pr = 0.5$) *and (b) a bigger spiral* ($Pr = 1$)*. The red contours represent the magnitude of the mean flow (each contour line is with* 0.02 *magnitude apart). The spiral is indicated in the black and white. Other parameters are* $g_m = 50$*,* $c^2 = 2$ *and* $L = 40 \times 2\pi$*.*

mean flow field at the spiral core is supported for persistent SDC and resembles qualitative features of rigorous solutions of the Boussinesq equations.

However, if $Pr \lesssim 0.2$, the behaviour is more chaotic and owing to the large mean flow at the spiral core, spirals break up; we can only notice fast moving patches of defects and parts of stripes. Figure 5.10 illustrates the solution state for $Pr = 0.1$. This shows a spatially complex structure with rapid dynamics. Although during the evolution process some small-scale spirals may be formed, they will soon breakup. The mean flow patches correspond to defects and are widely spread. This state is an example for $Pr \lesssim 0.2$. We therefore suggest the lower bound of Pr, that generates apparent SDC as $Pr \approx 0.25$.

On the other hand, if Pr is increased, the SDC state disappears and is replaced by a target pattern. Figure 5.8 illustrates the pattern evolution of the numerical simulations for $Pr = 6$ with $g_m = 50$, $\mu = 0.7$ and $c^2 = 2$. Xi *et al.* [69] used same parameters and they suggested the pattern is labyrinthine. However, their simulations were for short intervals of time $t \sim 900$, while our long time simulations reveal that this labyrinthine pattern (figure

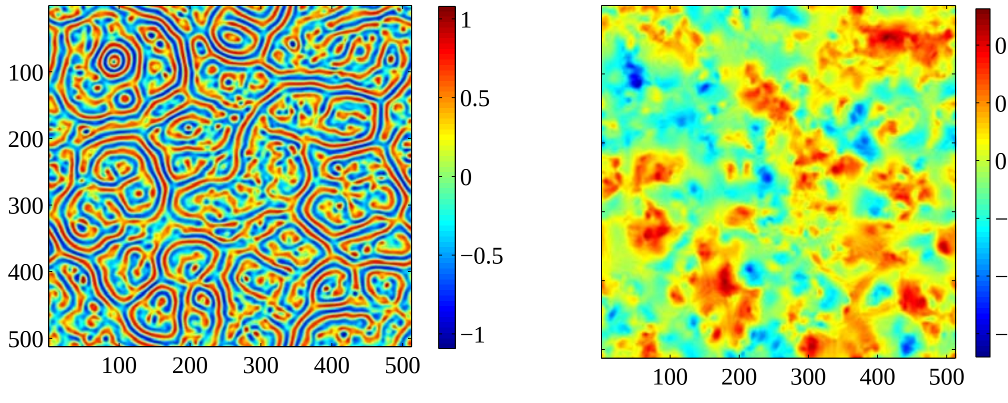

(a) (b)

Figure 5.10: *Instantaneous pattern in field* ψ *and corresponding* ζ *at* $t = 5 \times 10^5$ *for system parameters* $Pr = 0.1$, $g_m = 50$, $\mu = 0.7$, $L = 40 \times 2\pi$ *and* $c^2 = 2$. *Solution shows a domain structure, which is not well developed into SDC state, rather more defects state. Corresponding* ζ *field depicts the wide spreaded large mean flow at the defects. This solution state has the similar behaviour to pattern in figure 5.18.*

5.8(a)) evolves into dynamics that is dominated by small targets and defects (figure 5.8(b)) and then to a state with large and very slowly moving targets with a few spirals as shown in figure 5.8(c). The mean flow at the target core is approximately zero and hence not sufficient to turn the targets into spirals or defects. We find that if $Pr \gtrsim 2$, a labyrinthine structure is formed for a short time, but in the long term, the structure evolves into slowly moving target patterns. If Pr is high, the subsequent dynamics therefore has a labyrinthine structure followed by a target state. This labyrinthine structure may persist for long time before evolving into targets.

Therefore this analysis supports the prediction of when the SDC state should be expected if the other parameters are fixed as $g_m = 50$, $\mu = 0.7$, $c^2 = 2$ and $L = 40 \times 2\pi$; SDC state persists for long time if Pr is in the range $0.2 \lesssim Pr \lesssim 0.8$, while for $0.9 \lesssim Pr \lesssim 1.2$, SDC pattern can develop into a state dominated by bigger spirals and then back to SDC state (the solution may then cycle between SDC and a state dominated by bigger spirals).

We summarize our results of long time evolution ($t \approx 10^6$) for $g_m = 50$, $\mu = 0.7$, $c^2 = 2$

Pr range	Pr	Result and illustration
$Pr \lesssim 0.2$	0.1	Complex structures with rapid dynamics (Figure 5.10)
	0.15	Complex structure similar to figure 5.18
	0.2	Complex structure, but less chaotic than figure 5.18.
$0.25 \lesssim Pr \lesssim 0.8$	0.25	SDC (very chaotic).
	0.5	SDC state (Figure 5.7)
	0.8	SDC state similar to figure 5.7
$0.9 \lesssim Pr \lesssim 1.2$	0.9	In evolution, SDC→ bigger spirals→ SDC.
	1	In evolution, SDC→ bigger spirals→ SDC (Figure 5.6).
	1.2	SDC for short time → bigger spirals → SDC
$2 \lesssim Pr \lesssim 6$	2	Labyrinthine → target state similar to figure 5.8
	6	Labyrinthine → target state (Figure 5.8)

Table 5.1: *Summary of simulation results showing the dependence of Pr to different solution states. The other parameters are $g_m = 50$, $\mu = 0.7$, $c^2 = 2$ and $L = 40 \times 2\pi$.*

and $L = 40 \times 2\pi$, in the table. In the first column we illustrate the four different ranges of Pr that give different solution states. We then illustrate the values of Pr, for which we performed our simulations. Dynamics of the solution and its illustration are indicated in the last column.

5.4.2 The bifurcation parameter, μ

We also studied the role of the bifurcation parameter μ, which controls the amplitude of the stripe pattern. We find that for lower values of μ (e.g., for $\mu = 0.1$ with $Pr = 0.5$, $g_m = 50$, $c^2 = 2$ and $L = 40 \times 2\pi$), the system is dominated by stripes. When μ is increased, a defect state with curved stripes and patches of stripes is found; this does not settle into stripe state and further increase in μ generates Defect Chaos followed by Spiral Defect Chaos. This transition to different states depend on other system parameters. An example of this scenario in a large aspect ratio system, $L = 100 \times 2\pi$, is illustrated in figures 5.11 and 5.12 for parameter values $Pr = 0.25$, $g_m = 50$ and $c^2 = 2$. We use four different values of μ and each state is shown at $t = 10^5$. Figure 5.11(a) is for $\mu = 0.1$, which generates skewed stripes with moving defects; in subsequent dynamics (time evolution until $t = 5 \times 10^5$)

this state does not settle into a stripe solution. If μ is increased up to 0.3, stripes bend around defects and a defect dominated state as shown in figure 5.11(c) is found. Figure 5.12(a) shows the state when $\mu = 0.5$, in which spirals have begun to form. However, this planform is dominated more by patches of stripes and defects than by spirals. Figure 5.12(c) shows how the state evolves into SDC when $\mu = 0.7$. The mean flow is almost zero for $\mu = 0.1$ (figure 5.11(a)), while the corresponding field at $\mu = 0.7$ (figure 5.12(c)), has a much richer structure comprising of isolated bubbles of mean flow patches. The size of the mean flow patches decreases with μ. Our results suggest that the pattern evolves to a more chaotic state with higher μ.

We extend our analysis by investigating the onset of this chaotic state; the onset of the defect state is at a higher μ than the onset of stripes ($\mu = 0$), if the domain size is small ($L \lesssim 100 \times 2\pi$). The transition of stripe state to Defect Chaos state depends on other system parameters Pr, g_m and c for a particular L.

Transition to Chaotic state: dependence on the Domain size, L and the Prandtl number, Pr

In the following we investigate the transition of stripes to chaotic state. As the route to study the transition, we checked the long time behaviour, $t = 5 \times 10^5$ of each set of parameters starting with random initial conditions. For each set of parameters, we initially picked two values of μ, for which solution states are stripes at the smaller μ and defect chaos at the larger. Then we followed the bisection method to trace the onset of Defect Chaos. We remark that the DC to SDC transition scenario, however, is hard to identify since the DC to SDC developments is sequential: recall that the DC state is defect dominated and SDC state is spiral and defect dominated and in between, the scenario is apparently dominated by defects but few spirals exist with locally curved stripes (figure

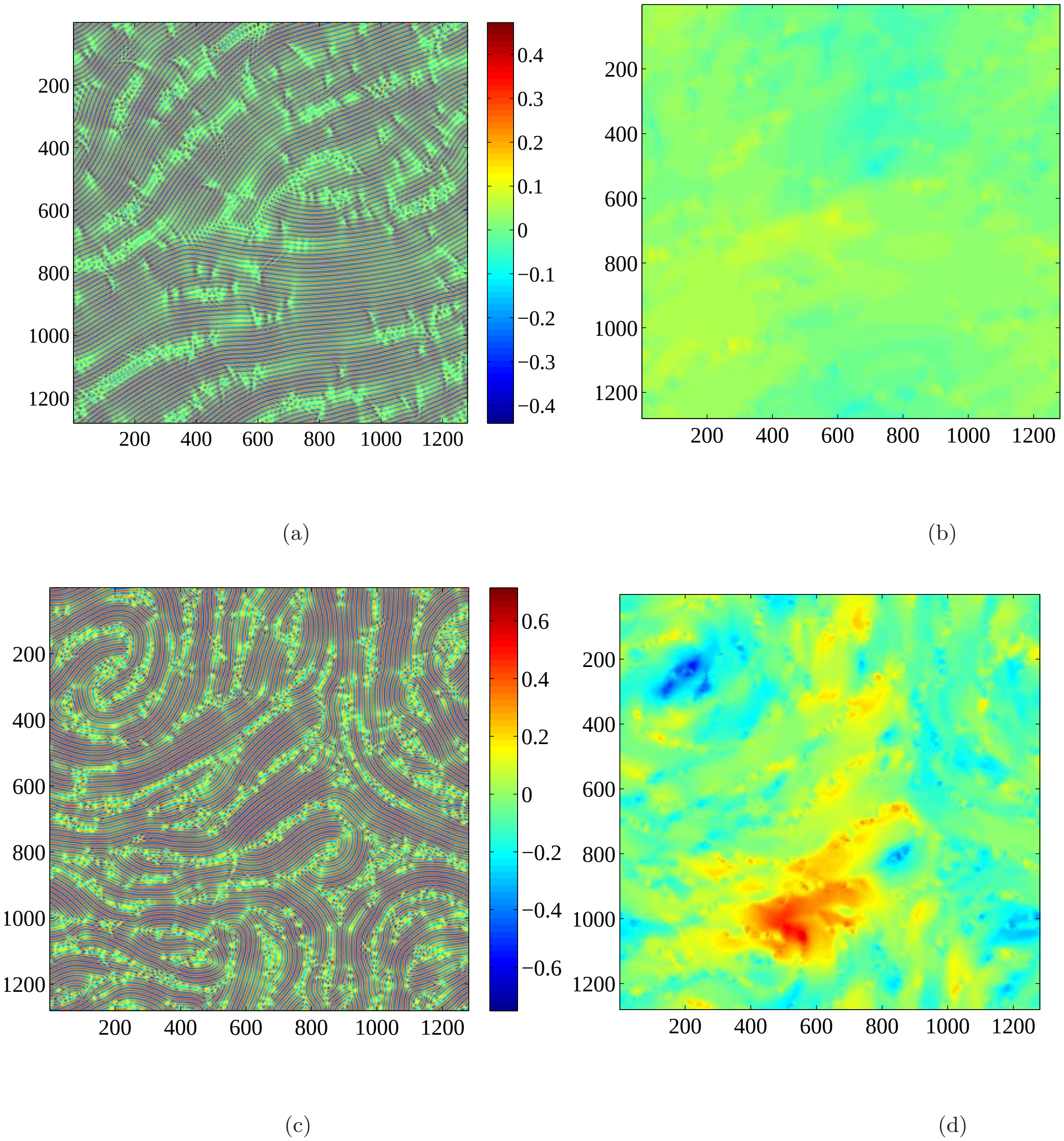

Figure 5.11: *Field ψ and corresponding ζ at $t = 10^5$ for the parameter values $Pr = 0.25$, $g_m = 50$, $c^2 = 2$ with $L = 100 \times 2\pi$. (a) $\mu = 0.1$: Skewed stripes with dislocations and defects. (c) $\mu = 0.3$: defects dominated sate. Defects are nucleated in curved stripes. (b) and (d) are corresponding ζ fields to a fixed colour scale.*

5.12(c)) or a state with defect and flattened spirals (an example is shown in figure 5.26). The solution exhibits a well developed SDC state if a higher μ ($\mu \gtrsim 0.6$) is considered. As

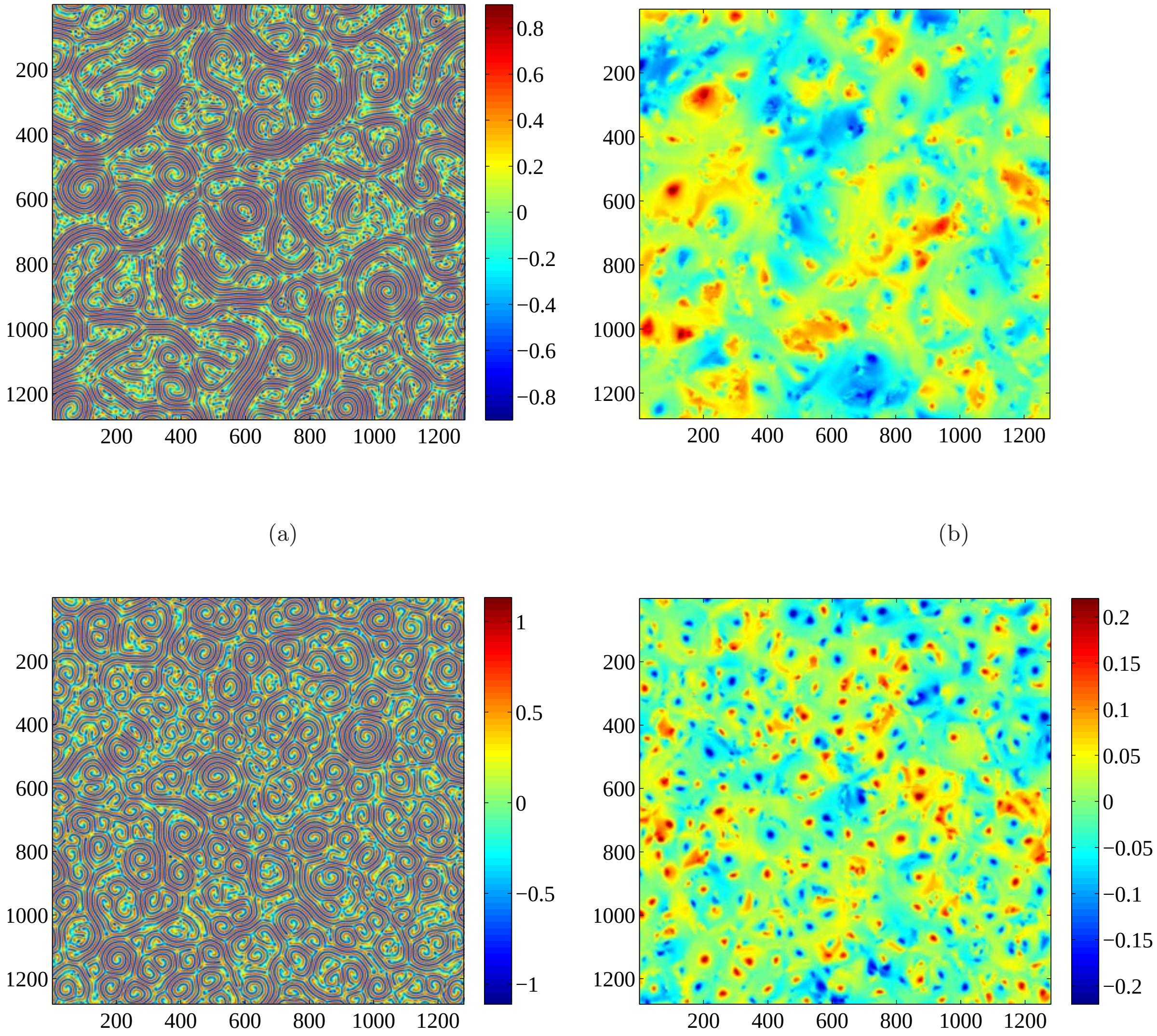

(a) (b)

(c) (d)

Figure 5.12: *Field ψ and corresponding ζ at $t = 10^5$ for the parameter values $Pr = 0.25$, $g_m = 50$, $c^2 = 2$ with $L = 100 \times 2\pi$. (a) $\mu = 0.5$: Defects dominated state with few spirals and locally curved stripes. (c) $\mu = 0.7$: SDC state. (b) and (d) are corresponding ζ fields to a fixed colour scale. Patches of vorticity decrease in size and appear as scattered patches with μ increasing.*

a consequence we only analyzed the stripes to DC transition.

We first demonstrate the transition from stripes to Defect Chaos as a function of the domain size, L to assess the driving parameter value at the onset of Defect Chaos in large

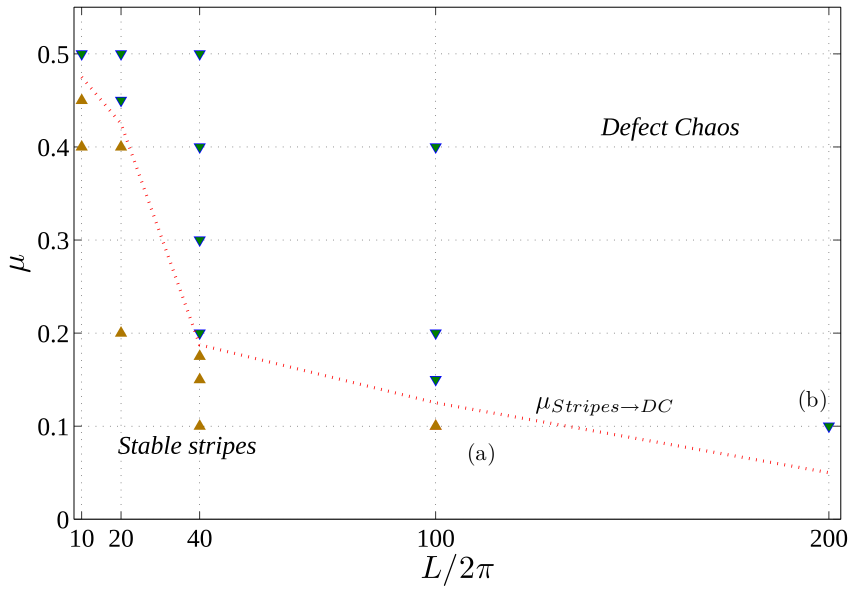

Figure 5.13: *Plot of $L/2\pi$ vs μ of the transition to DC state from stripes for the system parameters $g_m = 50$, $c^2 = 2$ and $Pr = 0.5$. The final solution state is presented in the figure: DC state (green triangles) and stripes state (brown triangles). We carried out numerical simulations for $t = 5\times10^5$, at each marked point except for the case $L = 200\times2\pi$, where we simulated the system only for $t = 10^5$. Dotted line indicates the approximate boundary to the stripe state and DC transition. We illustrate dynamics of points (a) and (b) in figure 5.14 and 5.15 respectively.*

aspect ratio systems. Figure 5.13 shows the L dependence of the transition (for system parameter values $g_m = 50$, $c^2 = 2$ and $Pr = 0.5$) of stripes to chaotic defect dynamics. We note that owing to the high computational cost only one data point is considered for $L = 200 \times 2\pi$ and simulated only for $t = 10^5$. We indicate the values of μ, that are used in deriving this boundary. Our results show that when L is large, the onset μ of the defect chaotic state decreases, and we speculate that it tends to zero in the limit of large L.

We note here that when $\mu > \mu_{transition}$, close to the boundary, DC structure is less chaotic. The structure contains curved stripes with defects and does not settle into a stripe state eventually. On the other hand, if μ is increased further, DC is chaotic and

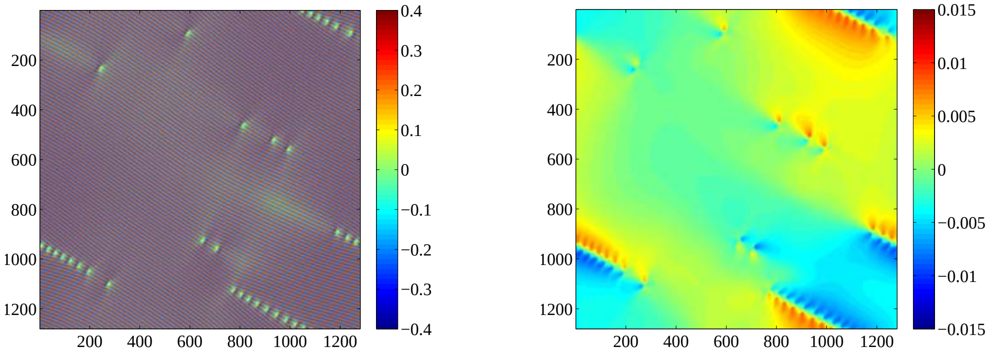

(a) (b)

Figure 5.14: *Fields ψ and corresponding ζ at $t = 10^5$ for the point (a) in figure 5.13, (parameter values $Pr = 0.5$, $g_m = 50$, $\mu = 0.1$ and $c^2 = 2$ with $L = 100 \times 2\pi$). Solution state is dominated by stripes with few defects. The stream function is approximately zero everywhere except at few dislocations. Evolution for long time ($t \approx 5 \times 10^5$) leaves a solution with perfect stripe state.*

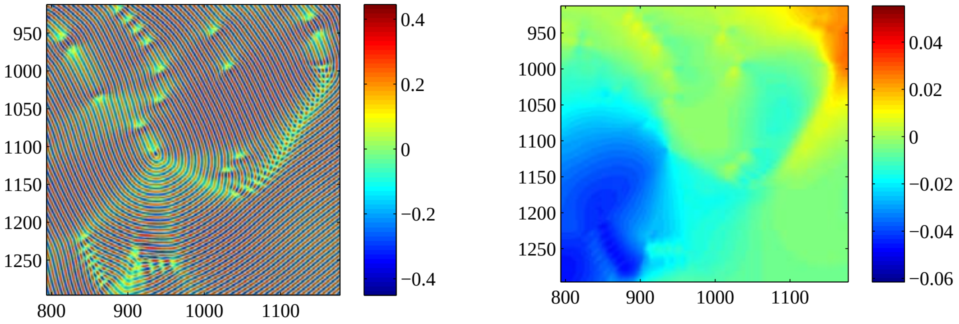

(a) (b)

Figure 5.15: *Domain structure of fields ψ and corresponding ζ at $t = 10^5$ for the point (b) in figure 5.13, (parameter values $Pr = 0.5$, $g_m = 50$, $\mu = 0.1$ and $c^2 = 2$ with $L = 200 \times 2\pi$), showing curved stripes with few defects. We speculate that the stream function is sufficiently large enough to support defects to persist for long time. Dynamics in the pattern come from the motion of defects and also by the motion of curved stripes.*

dominated by defects than curved stripes.

In figures 5.14 and 5.15 we illustrate the structure of the pattern for μ close to the boundary from above and below. We plot the instantaneous patterns of ψ and ζ at $t = 10^5$ for parameter values at points (a) and (b) in figure 5.13. In the first case ($\mu = 0.1$ with $L =$

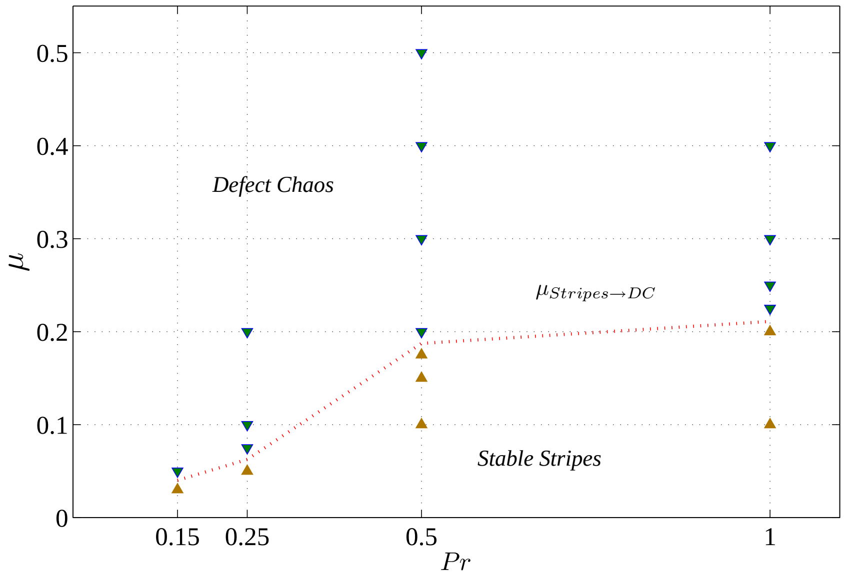

Figure 5.16: *Plot of Pr vs μ of the transition to DC state from stripes for the system parameters $g_m = 50$, $c^2 = 2$ and $L = 40 \times 2\pi$. The final solution state is presented in the figure: DC state (green triangles) and stripes state (brown triangles). We carried out numerical simulations for $t = 5 \times 10^5$, at each marked point. Dotted line indicates the approximate boundary to the stripe state and DC transition. We suggest that this boundary approaches to zero when Pr tends to zero.*

$100 \times 2\pi$), the planform shows few disclinations with straightened stripes. In the evolution process, straightened stripes become stationary so the dynamics in the pattern comes from the motion of disclinations. The disclinations glide opposite directions, eventually leading to perfect stripes (when $t \approx 5 \times 10^5$), whereas in the second case $\mu = 0.1$ with $L = 200 \times 2\pi$, defects coexist with curved stripes and we speculate that this disordered state persists in the long time limit.

Secondly, we illustrate the dependence of this transition from stripes to chaotic state with the parameter Pr in figure 5.16. We indicate the values of μ, that are used in deriving this boundary. Our results show that when Pr is small, the onset μ of the defect chaotic state decreases, and we speculate that it tends to zero in the limit of large L.

5.4.3 Coupling constant to the mean flow, g_m

The coefficient g_m represents the strength of the mean flow field. We have carried out simulations to study the effect of the magnitude of mean flow, which is inversely proportional to Pr, and increases with increasing values of the coupling strength g_m. If g_m is small, the slowly moving target state appears. An example of target state is illustrated in figure 5.4 for $g_m = 10$. This suggests that a higher parameter value of g_m is essential to develop the SDC state. Figure 5.17 shows an example of SDC state for $g_m = 100$ (for $Pr = 0.5$, $c^2 = 2$), and the domain structure is similar to the pattern which occurs for lower $Pr \approx 0.25$ with $g_m = 50$ and $c^2 = 2$. Note that the mean flow at the spiral core spreads to several wavelengths resulting in large patches in the field ζ at spiral cores. However, when $Pr = 0.5$, $c^2 = 2$, the solution state for very large g_m, $g_m \gtrsim 125$, is similar to that for smaller $Pr \lesssim 0.2$ with $g_m = 50$, $c^2 = 2$; a chaotic state where spirals become unstable breaking into circular patches of rolls with many defects. Our results show that the SDC state can be expected in the range $20 \lesssim g_m \lesssim 125$, when $Pr = 0.5$, $c^2 = 2$, $\mu = 0.7$, $L = 40 \times 2\pi$.

This leads us to an important result that the solution states preserve the ratio g_m/Pr for $c^2 = 2$ with $\mu = 0.7$.

5.4.4 Parameter c that models the boundary conditions

The parameter that models viscous damping of the horizontal flow component by the top and bottom cell walls is denoted by c, and it affects the magnitude of the mean flow. We used $c^2 = 2$ to simulate approximately no-slip boundary conditions whereas $c = 0$ approximates the stress-free boundary conditions. We discussed this selection of parameters in chapter 1. We observed a state with slowly moving targets for $c^2 \gtrsim 5$. This is similar to the structure illustrated in figure 5.4. On the other hand, smaller c leads the

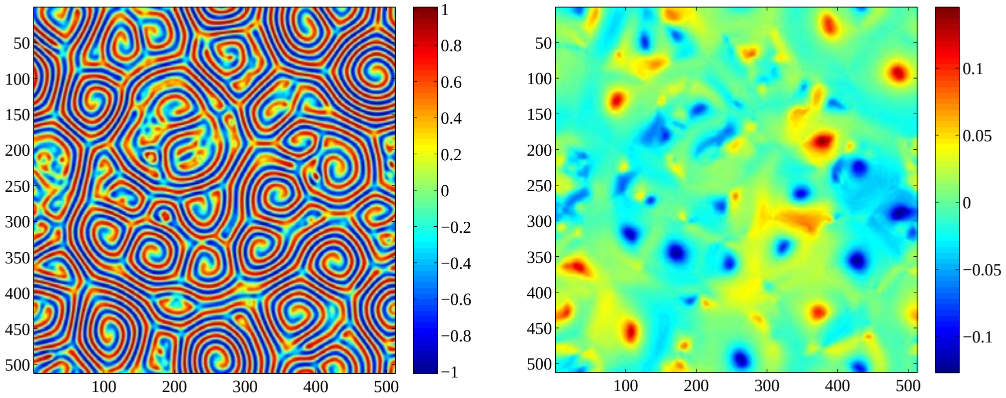

(a) (b)

Figure 5.17: *Instantaneous pattern in field ψ and corresponding ζ at $t = 5 \times 10^5$ for system parameters $g_m = 100$, $Pr = 0.5$, $\mu = 0.7$, $L = 40 \times 2\pi$ and $c^2 = 2$. Solution shows SDC state and corresponding ζ field depicts that the mean flow patches are large at spiral core.*

dynamics to be more chaotic and no SDC state is apparent. Figure 5.18 illustrates an example for smaller c, $c^2 = 0.8$ with the parameter values $\mu = 0.7$, $Pr = 0.5$, $g_m = 50$. This scenario is similar to the states at higher g_m ($g_m = 125$, $Pr = 0.5$) or lower Pr ($Pr = 0.2$, $g_m = 50$) with $c^2 = 2$. Our results suggest that the SDC state exists in the range $1 \lesssim c^2 \lesssim 5$ for $Pr = 0.5$, $g_m = 50$, $\mu = 0.7$, $L = 40 \times 2\pi$. We checked the solution state for series of values in different ranges. Combining these results, we suggest that the solution states depend on the parameter relation $g_m/Pr\,c^2$ as for the linear problem.

5.5 Quantitative analysis of different solution states

So far, we have defined qualitative features of the mean flow magnitude and order parameter in distinguishing different solution scenarios. In order to quantify different aspects of the solution states, we now define some important time averaged global quantities: spiral and defect count, Kinetic energy, root mean square of convection and mean flow fields.

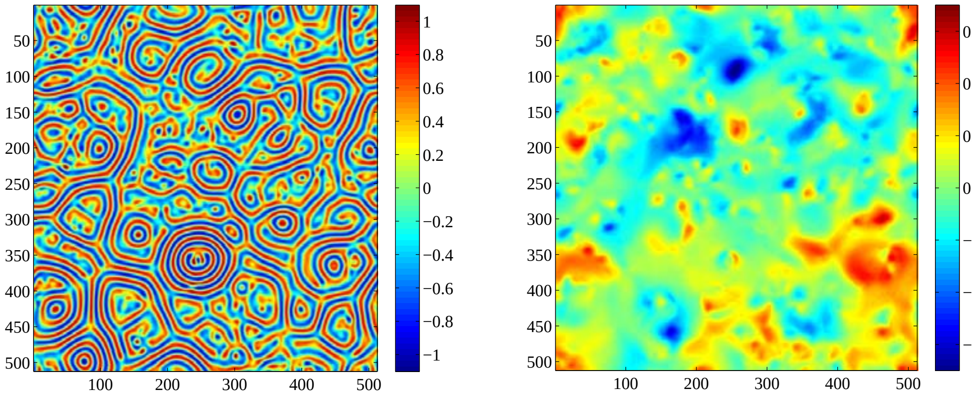

(a) (b)

Figure 5.18: *Instantaneous pattern in field ψ and corresponding ζ at $t = 5 \times 10^5$ for system parameters $c^2 = 0.8$, $g_m = 50$, $Pr = 0.5$ and $\mu = 0.7$. Solution shows a domain structure, which is not well developed into SDC state, rather more defects state. Corresponding ζ field depicts the wide spreaded large mean flow at the defects. This solution state has the similar behaviour to pattern in figure 5.10*

We note that these quantities are strongly fluctuating and the analysis of these data must be treated with caution. This fluctuation arises because of the chaotic behaviour of DC and SDC states. However the fluctuation of these quantities is around a well-defined average value. For our calculations, each simulation is performed for long time, $t = 10^5$. We calculated the average over the last 10^3 time periods. The horizontal diffusion time is $t_d = L^2/(2\pi\, Pr) = 1600/Pr$.

We include the maximum and minimum variations of the different measures, illustrated using error bars. We used the qualitative analysis, which we performed in previous sections, to describe different solutions and their dependence with system parameters. In the following, we attempt to get a demarcation between DC, SDC state. We also use these aspects to differentiate the long time persistent SDC state (illustrated in figure 5.7) and the bigger spiral formation during SDC evolution (illustrated in figure 5.6).

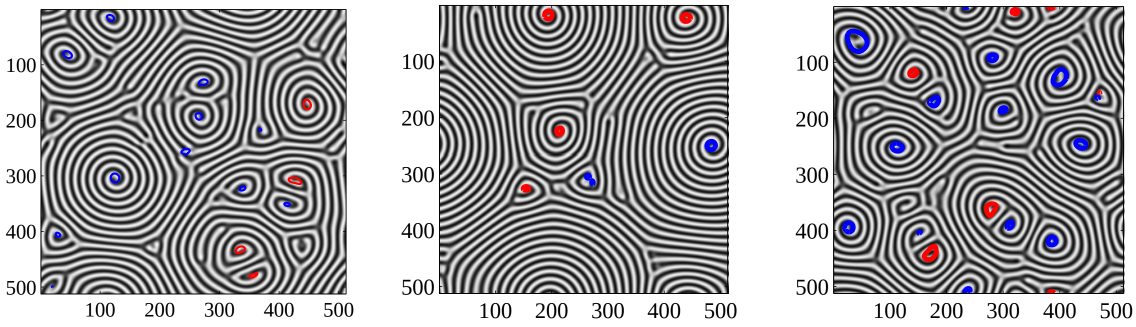

Figure 5.19: *The pattern observed for paramters* $Pr = 1$*,* $\mu = 0.7$*,* $c^2 = 2$*,* $g_m = 50$ *at* $t = 4.5 \times 10^4$*,* $t = 9 \times 10^4$ *and* 11×10^4 *(left to right). The contours indicates regions where* $|\zeta| = 0.06$*. Red denotes the core of right handed spirals, while blue contours indicate the left handed spirals.*

5.5.1 Spirals and Defects (SD) Count

The first measure we consider is the count of spirals and defects. We use the ζ field of the solution to capture the spiral core and regions of defects. However, the magnitude of the vorticity field at defects and spirals vary for different parameters and therefore in each set of parameters we define a threshold mean flow to differentiate spirals and well formed defects from other local patterns. We illustrate an example in figure 5.19 for parameter values $Pr = 1$, $\mu = 0.7$, $c^2 = 2$, $g_m = 50$ at $t = 4.5 \times 10^4$, $t = 9 \times 10^4$ and $t = 11 \times 10^4$. The coloured contour lines denote where the vorticity satisfies $|\zeta| = 0.06$; this particular value captures all spirals and well formed defects.

If the state is chaotic and contains many spirals and well formed defects, then the count of vorticity patches above this threshold is high. We therefore use a high value of a SD count as a characteristic of SDC.

Figure 5.20 shows the variation of SD count in the evolution process of the SDC state for the two cases discussed in section 4.1, $Pr = 1$ and $Pr = 0.5$ (the other system parameters are $g_m = 50$, $c^2 = 2$, $\mu = 0.7$, $L = 40 \times 2\pi$). We considered $|\zeta| = 0.075$ and 0.06 as the threshold mean flow of selecting spiral core and well formed defect patches for $Pr = 0.5$ and 1 respectively; vorticity is high for low Pr.

Recall that in section 4.1, we discussed the difference of SDC evolution for these two values of Pr; for $Pr = 0.5$, the SDC state persists for a long time, whereas for $Pr = 1$, the SDC state evolves into the spiral pattern state characterized by fewer, larger, slow-moving spirals and fewer defects and back to the SDC state. This scenario is verified in figure 5.20; for $Pr = 0.5$, the rapid fluctuations imply that the motion is more chaotic, and the SD count at any given time is between 35 and 55. On the other hand, for $Pr = 1$, spirals and defects move more slowly than in the previous case, and the SD count is approximately between 4 and 25. We define the solution states for $Pr = 1$, dividing the time evolution into three ranges. First, when $t \lesssim 3 \times 10^4$, the SDC state exits. The process of coarsening spirals in SDC state to bigger spirals is started when $t \approx 3 \times 10^4$. Second, in the time range, $3 \times 10^4 \lesssim t \lesssim 10.5 \times 10^4$, two states appear intermittently; many bigger spirals with fewer defects or fewer bigger spirals with many defects. Our SD count method counts both spirals and well formed defects. Therefore due to large number of defects in the bigger spiral state, in figure 5.20, we can see higher SD counts in the range $3 \times 10^4 \lesssim t \lesssim 10.5 \times 10^4$. We can observe the least SD counts, at $t \approx 4 \times 10^4, 6 \times 10^4$ (this state is shown in figure 5.6(c)) and 9×10^4 (this state is shown in the middle picture in figure 5.19) where the state with many bigger spirals and fewer defects exist. Third, when $t \gtrsim 10.5 \times 10^4$, each bigger spiral breaks into many smaller spirals and defects confirming the SDC state with many small spirals.

Owing to the behaviour in the range $3 \times 10^4 \lesssim t \lesssim 10.5 \times 10^4$ discussed above, we can not define a threshold of SD count for SDC state. However, we suggest that the state with many bigger spirals and fewer defects appear if SD count is approximately less than 5. We checked the spiral core distribution in different domain sizes, $L = 20$, 40 and $L = 100$ and

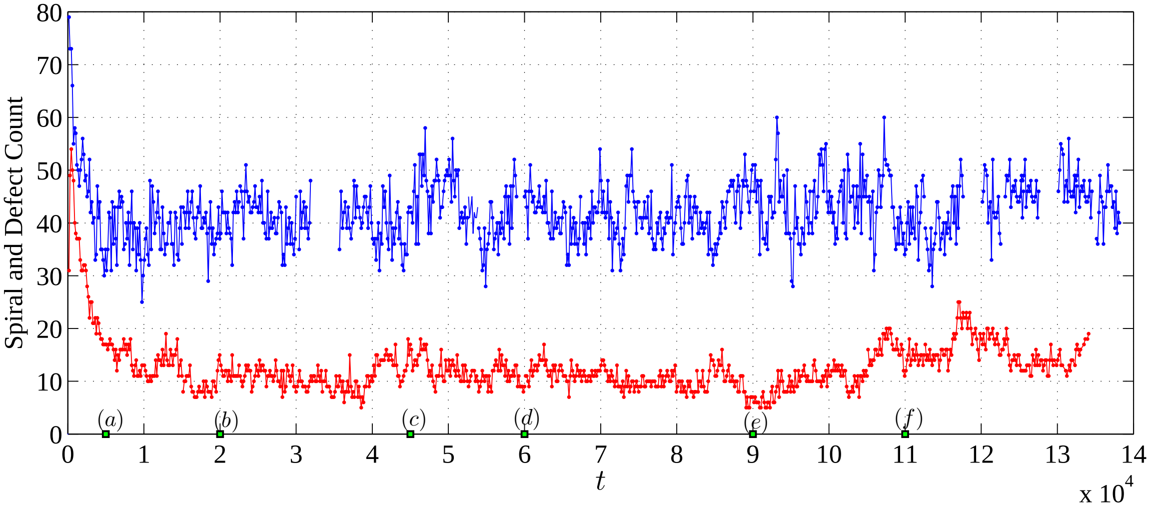

Figure 5.20: *Spirals and Defects count as a function of time for* $g_m = 50$, $c^2 = 2$ *and* $L = 40 \times 2\pi$ *with* $Pr = 0.5$ *(in blue) and* $Pr = 1$ *(in red). The SD count is lower for* $Pr = 1$ *than for* $Pr = 0.5$, *for which there is a recurrent transition between SDC and spiral pattern state. The domain structures of points (a), (b) and (d) are illustrated in figure 5.6 while (c), (e) and (f) are shown in 5.19.*

found that the spiral core density is a constant. We recall that the simulations of Schmitz *et al.* [76] are for $Pr = 1$ and only for time evolution up to $t = 64,000$.

Figure 5.21 shows how the SD count depends on the parameter Pr. The average SD count is taken after $t = 10^5$ together with the maximum and minimum count over the period $t = 10^3$ of time. Our results show that the solution is more chaotic for lower Pr, for which the SD count is high.

5.5.2 Kinetic Energy

The second property we investigate is the Kinetic Energy (KE) of the mean flow defined by $KE = \frac{1}{2}\left(\left(\frac{\partial\zeta}{\partial x}\right)^2 + \left(\frac{\partial\zeta}{\partial y}\right)^2\right)$. This quantity is zero for perfect parallel rolls, increases for the DC state and has the highest values in the SDC state. Therefore we postulate that

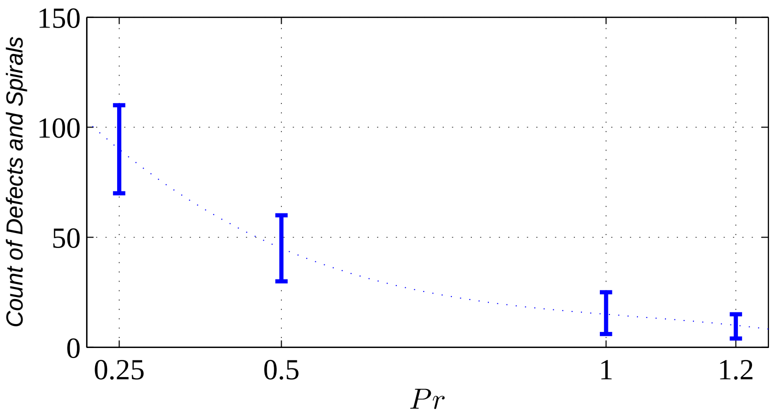

Figure 5.21: *Average count of spirals and Defects vs the parameter Pr* ($g_m = 50$, $c^2 = 2$ *and* $L = 40 \times 2\pi$)*. The maximum and minimum count for each Pr is shown in error bars. The count is averaged over a period* $t = 10^3$ *after evolving for* $t = 10^5$*. Long error bars indicate large fluctuations and the dotted line is a guide to eye.*

the mean flow Kinetic Energy can be used to characterize different solution states.

We illustrate in figure 5.22, the time variation of the space-averaged kinetic energy (this spatially averaged KE is then averaged over a short time periods of $t = 7500$), that corresponds to SD count shown in figure 5.20 for $Pr = 0.5$ (in blue) and $Pr = 1$ (in red). The triangular error bars indicate the maximum and minimum values of the KE in each profile. As with the SD count, the KE is high for $Pr = 0.5$ and it is reduced for $Pr = 1$, particularly when the simulation is dominated by bigger spirals.

Figure 5.23 shows the KE dependence on Pr for different values of μ, $\mu = 0.7$, 0.4 and 0.1. For each μ, the KE decreases when Pr is increased and for each Pr, the KE increases when μ is increased. Note that when $L = 40 \times 2\pi$, for $g_m = 50$ with $c^2 = 2$, the solution state depends on Pr and μ: at $\mu = 0.7$, the solution state is SDC if $0.25 \lesssim Pr \lesssim 1.2$ and targets if $Pr \gtrsim 2$. At $\mu = 0.4$, the solution state is defect, but the motion of dynamic is faster for lower Pr: At $\mu = 0.1$, the solution evolves into stable stripes if $Pr \gtrsim 0.5$ and defects otherwise. The KE is zero if the state is perfect stripes. We conclude that

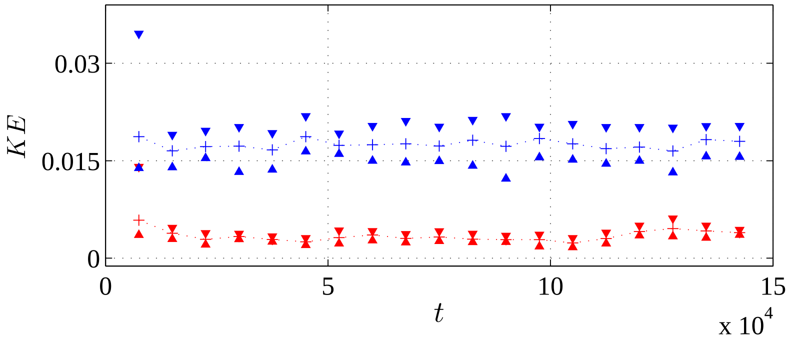

Figure 5.22: *Averaged KE, averaged over space and over small time periods $t = 7500$, as a function of time for $Pr = 0.5$ (in blue) and $Pr = 1$ (in red). The KE is lower for $Pr = 1$ than for $Pr = 0.5$, implying a smaller mean flow. The error bars show the maximum and minimum KE for each profile.*

the Kinetic Energy is high in the regime for which Spiral Defect Chaos arises. Note that the KE for $Pr = 1$ and $\mu = 0.7$ (SDC state) is smaller than the KE for $Pr = 0.25$ and $\mu = 0.4$ (DC state with few spirals), so the KE on its own is not enough to characterize the solution state.

5.6 Local pattern properties: local wave-vector

We further utilize instantaneous local pattern properties, the local wave-vector magnitude and local pattern orientation, to relate DC and SDC to the skew-varicose instability in our model, discussed in chapters 2 and 3. Using numerical estimates of these quantities, we provide evidence to demonstrate that defects are formed in regions of the pattern in which the local wavenumber exceeds the skew-varicose boundary. In addition, local properties can be used to characterize the domain structure of different patterns.

We followed the efficient method for calculating the local wave-vector of stripe patterns introduced by Egolf *et al.* [52]. The components of the wave-vector are approximated

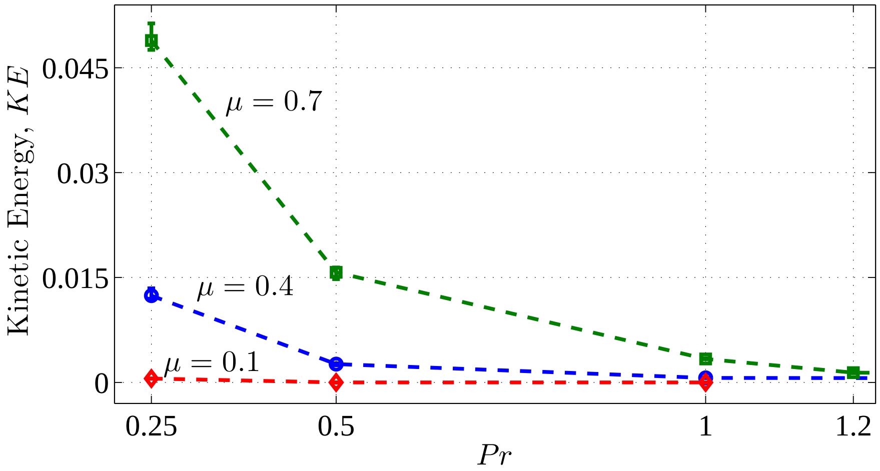

Figure 5.23: *The variation of the time averaged KE with Pr at $t = 10^5$ for $\mu = 0.7$ (in green), $\mu = 0.4$ (in blue) and $\mu = 0.1$ (in red). The other system parameter values are $g_m = 50$ and $c^2 = 2$ and $L = 40 \times 2\pi$. Time averaging is performed from the data for the final $t = 10^3$ period of the simulation. The error bars represent the maximum and minimum KE in this final period. The dotted lines are guides to the eye. Long error bars indicate large fluctuations which reflect the complex pattern contains many dynamic spirals and defect structures. The KE is approximately zero for $\mu = 0.1$, except at $Pr = 0.25$, for which the state evolves into DC state.*

using partial derivatives of order parameter, ψ. For patterns that are locally striped, we approximate $\psi(x)$ using, $\psi(x) = A(x)\cos(\phi(x))$ with local wave-vector $K_{local} \equiv \nabla\phi(x)$. Sufficiently far from defects, we expect that the variations in $A(x)$ are small compared to the variations in $\phi(x)$. Hence, the components of the wave-vector $\mathbf{K_{local}}$ are found using simple partial derivatives,

$$\left.\begin{aligned} \mathbf{K_{local}}.\hat{\mathbf{x}} &= \sqrt{-\psi_{xx}/\psi} \\ \mathbf{K_{local}}.\hat{\mathbf{y}} &= \sqrt{-\psi_{yy}/\psi} \end{aligned}\right\} \tag{5.3}$$

, where $\hat{\mathbf{x}}$ and $\hat{\mathbf{y}}$ are unit vectors. If ψ is close to zero then 5.3 will be very sensitive to small uncertainties in ψ. This problem is covered by taking the ratio of the third partial derivative to the first partial derivative for points where ψ is small. Relative signs of wave vectors are obtained by $K_{local}.\hat{y} = (\psi_{xy}/\psi_{xx})K_{local}.\hat{x}$. We calculated all the derivatives in Fourier space. Effects of noise can be reduced by smoothing the wave-vector over small regions; i.e., the wave-vector can be replaced by the average of it within a small square region. In our illustrations, we are only concerned with the areas corresponding to patches of compressed stripes and hence we have filtered out very high and very low wave-vector magnitudes. We note here that the local wavenumber is undefined at defects and grain boundaries due to the basic assumption we made in derivation.

We have also calculated the local stripe orientation, $\theta = tan^{-1}(K_{local}.\hat{x}/K_{local}.\hat{y})$ at each point of the pattern.

In this section, the corresponding local wave-vector magnitude of the patterns of large aspect ratio system $L = 100 \times 2\pi$, for the set of parameter values, $Pr = 0.5$, $g_m = 50$, $c^2 = 2$ with different bifurcation parameter values, $\mu = 0.1$, 0.3, 0.5 and 0.7 are illustrated. For this set of parameters, the skew-varicose instability boundary is shown in figure 5.24. Later in this section, we present the local stripe orientation for different patterns.

At $\mu = 0.1$, the pattern is dominated by stripes with few defects and the wavenumber is approximately constant across the pattern. Eventually the solution will get into a perfect stripe state with a wavenumber less than unity, which is in the stable region for the set of parameters of interest. Figure 5.25 shows the local wave-director magnitude at each point of the pattern shown for $\mu = 0.1$. The localized regions of wavenumber higher than that for the skew-varicose instability, K_{SV}, are indicated in white. A skew-varicose distortion for a selected region of high wavenumbers is marked in yellow and the magnified view is illustrated. Eventually, all such developed skew-varicose distortions propagate away leaving stable stripes of a smaller local wavenumber.

At $\mu = 0.3$, the pattern is dominated by curved stripes with few defects. Figure 5.26 shows the local wave-director magnitude at the each point of the pattern for $\mu = 0.3$,

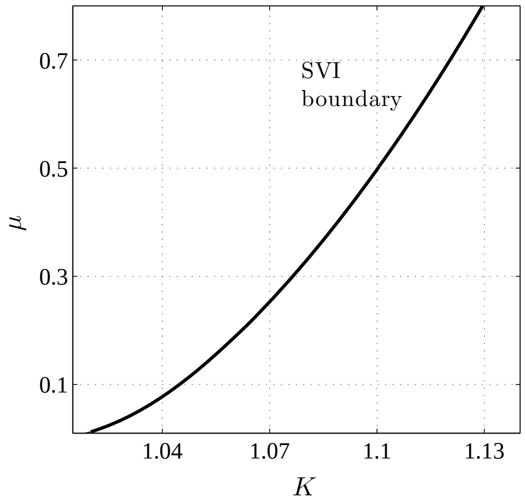

Figure 5.24: *SVI boundary for stripes, indicating wavenumber,* K_{SV} *for* $Pr = 0.5$, $g_m = 50$ *and* $c^2 = 2$.

for which we get a solution with largely curved stripes. We mark a region where the localized skew-varicose instability is observed where the local wavenumber of the pattern is larger than K_{SV}. We illustrate in figure 5.27 how this skew-varicose distortion evolves. In the evolution, defects are created. We speculate that for this bifurcation parameter, μ, skew-varicose distortions leave angled stripes in the solution state.

Figure 5.28 shows the local wave-director magnitude at each point of the pattern shown for $\mu = 0.5$. The localized regions of wavenumber higher than that for the skew-varicose instability, K_{SV}, are indicated in white. The corresponding skew-varicose distortions for some of selected regions of high wavenumbers are marked in yellow, some of which are inset to give magnified view.

At $\mu = 0.7$, the solution is a well developed SDC state. The stripes are squeezed largely between spirals and compressed stripes are then evolve into skew-varicose distortions.

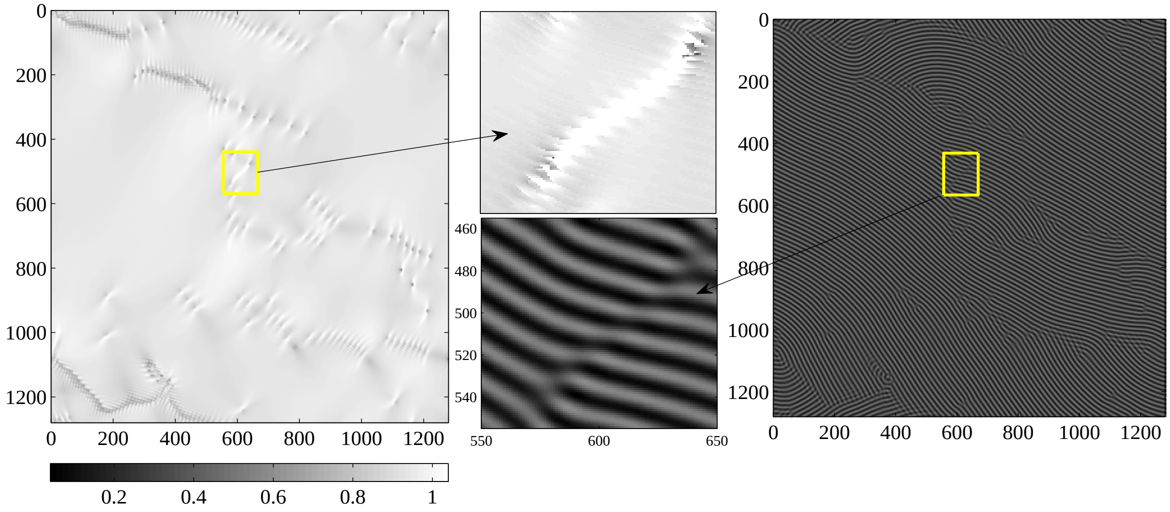

Figure 5.25: *Local wave-vector magnitude (left) and the corresponding the pattern (right) taken from simulations with* $Pr = 0.5$*,* $\mu = 0.1$*,* $L = 100 \times 2\pi$*,* $g_m = 50$ *and* $c^2 = 2$ *at* $t = 2 \times 10^4$*. In the plot of wave-vector magnitude, white indicates where the local wavenumber exceeds the wavenumber for SV instability (*$K_{SV} \approx 1.045$*). One of the SVI distortions (marked in yellow) is magnified in middle with the relevant local wavenumber.*

Figure 5.29 illustrates the magnitude of the local wave-vector over the SDC pattern at $\mu = 0.7$. The skew-varicose distortions, which are shown in small white patches in local wave-vector magnitude, appear largely in stripes between spirals. Some of these are indicated in yellow squares.

Besides checking the SV distortions, the local stripe orientation helps to characterize the variation of the domain structure of the patterns. The stripe orientation around a spiral, a defect state and a skew-varicose event are illustrated in figures 5.30, 5.31 and 5.32 respectively. Unlike defects, spirals can be clearly distinguishable as the switching phenomena in the pattern of local stripe orientation around the spiral core is unique to spirals and it is clearly apparent. At a defect, the local stripe orientation is not clear and the

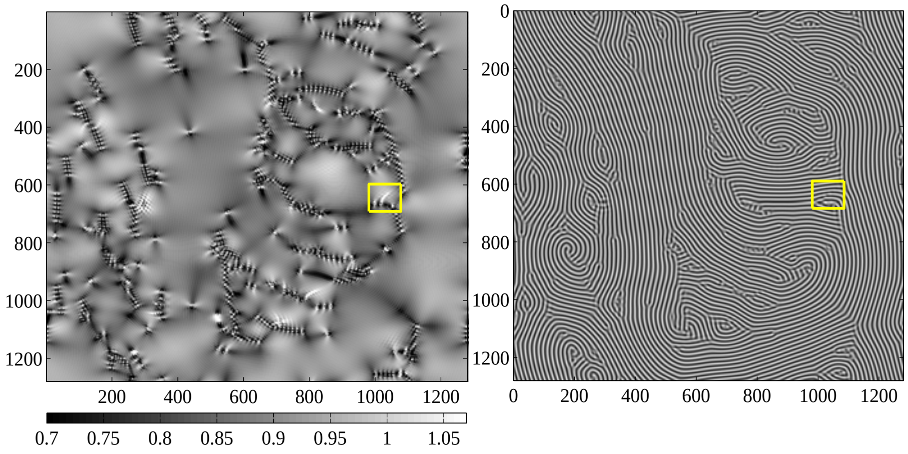

Figure 5.26: *Local wave-vector magnitude (left) and the corresponding pattern (right) of the simulations with* $Pr = 0.5$*,* $\mu = 0.3$*,* $L = 100 \times 2\pi$*,* $g_m = 50$ *and* $c^2 = 2$*. In the plot of wave-vector magnitude, white indicates the local wavenumber exceeds the wavenumber for the SV instability (*$K_{SV} \approx 1.075$*), while black signals lower wavenumbers. Pattern, taken at* $t = 2 \times 10^4$*, shows many curved stripes with a few defects. Marked region (in yellow) shows an example for compressed stripes due to skew-varicose event.*

boundary of different angles is non smooth. On the other hand, if the solution state is perfect a stripe state, the angle of stripes is constant globally.

5.7 Concluding remarks

We first explored the different solution states of numerical simulations: SDC, DC and target and large spiral pattern. The choice of the system parameters affects the dynamics and we have first presented numerical evidence to indicate the important role played by the parameters of the system, particularly Pr, μ and domain size L. Contrary to the results of Schmitz et. al. 2002 [76], we found that although some larger spirals may be formed for $Pr = 1$, (with $g_m = 50$, $c^2 = 2$ and $L = 40 \times 2\pi$) they will break up and eventually get to the SDC state. In the main analysis, we systematically varied Pr for

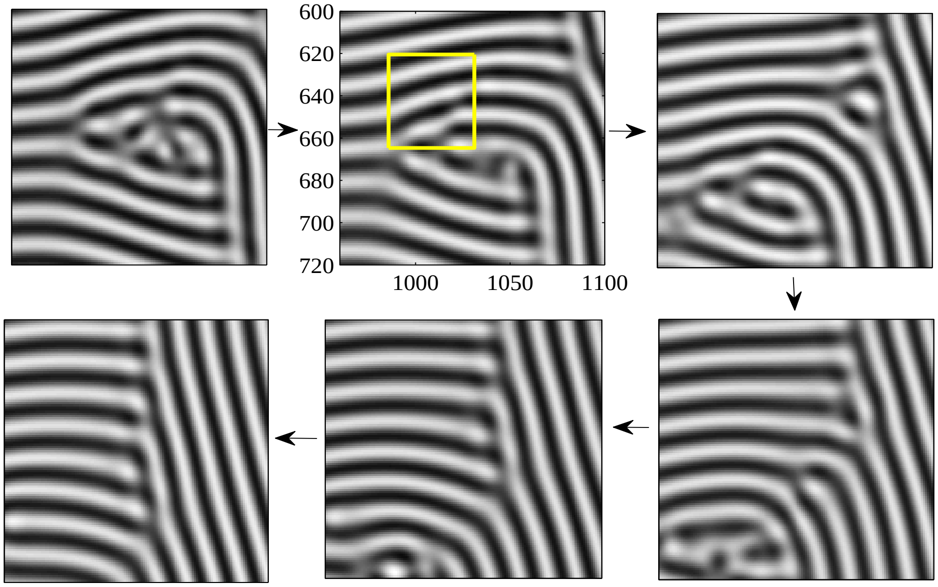

Figure 5.27: *Evolution of the skew-varicose distortion highlighted in figure 5.26 ($Pr = 0.5$, $\mu = 0.1$, $L = 100 \times 2\pi$, $g_m = 50$ and $c^2 = 2$). In the sequence (directed by arrows), the second plot is the skew-varicose distortion marked in yellow in figure 5.26 and each plot is 500 time units apart.*

$g_m = 50$, $c^2 = 2$ and $L = 40 \times 2\pi$ and we discovered four different ranges of the parameter Pr, for which the pattern structures are different and behave differently in the evolution. For $Pr \lesssim 0.2$, the solution has a complex structure which cannot be identified clearly. When $0.25 \lesssim Pr \lesssim 0.8$, the SDC state does not, at any time, evolve into global spirals and therefore the SDC state persists at all the times. However, when $0.9 \lesssim Pr \lesssim 1.2$, larger spirals are formed and they then breakup into small spirals forming SDC. We speculate that this transition between bigger spiral state and SDC occurs intermittently for long times ($t > 10^6$). On the other hand, for $2 \lesssim Pr \lesssim 6$, a solution has targets and spirals and they evolve slowly with time.

We note that the bifurcation parameter, μ should be greater than 0.6 (for $g_m = 50$,

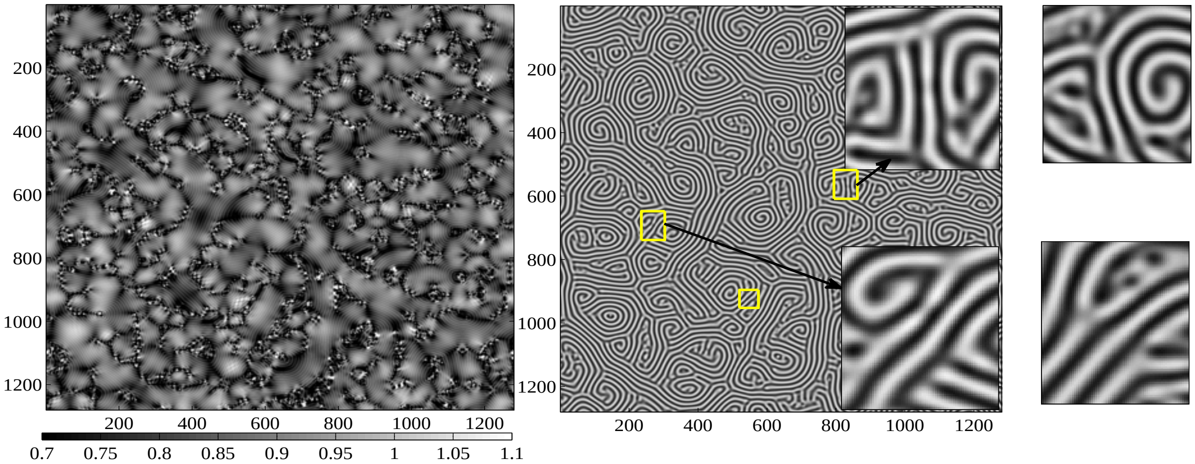

(a)

(b)

Figure 5.28: *(a) Local wave-vector magnitude (left) and the corresponding pattern (right) of the simulations with $Pr = 0.5$, $\mu = 0.5$, $L = 100\times 2\pi$, $g_m = 50$ and $c^2 = 2$. In the plot of wave-vector magnitude, white indicates the local wavenumber exceeds the wavenumber for SV instability ($K_{SV} = 1.1$), while black signals lower wavenumbers. Shadowgraph image is taken at $t = 2 \times 10^4$ and is largely dominated by defects and curved stripes with some few spirals. Marked regions show skewed stripes that correspond to selected white regions in the plot of wavevector magnitude. The insets show a magnified view of marked regions. (b) Panel shows the evolution of the selected magnified regions (at $t = 2.1 \times 10^4$).*

$c^2 = 2$ and $L = 40 \times 2\pi$) for the SDC state to occur. When μ is decreased, the domain structure of the solution shows a defect dominated state with fewer spirals followed by Defect Chaos with no spirals followed by a defect state with curved stripes. Further decrease in μ results in perfect stripe state. We suggested that the transition value of μ tends to zero in the limit of large L and in the limit of small Pr.

We also investigated the pattern structure varying g_m and c and we found the pattern structure and dynamics of the pattern preserve the ratio $g_m/Pr\, c^2$. We provided an analysis of quantitative aspects, Spirals and defects count and Kinetic energy to the mean flow of different solution states. We extended our analysis to estimate local properties, local wave-vector magnitude and wave-vector orientation of different patterns and illustrated

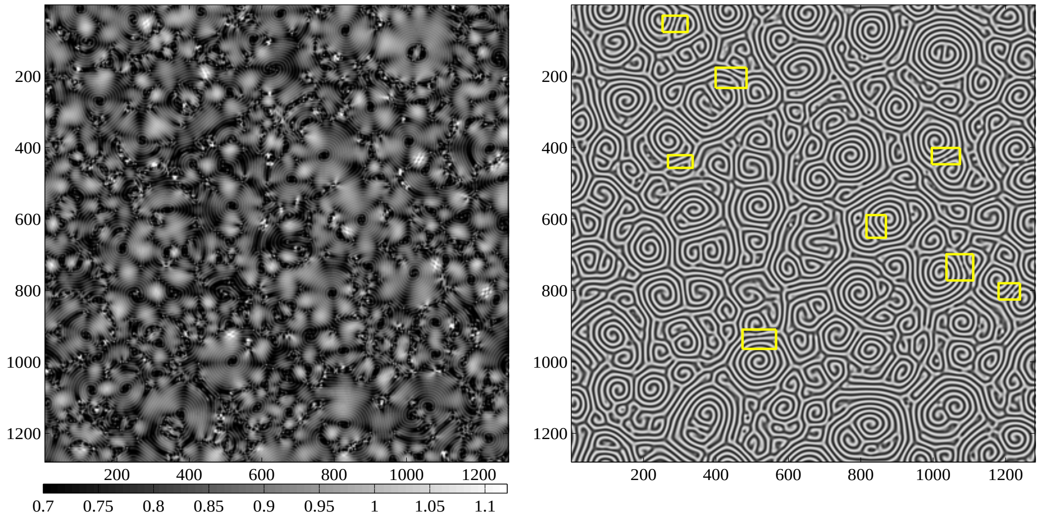

Figure 5.29: *Local wave-vector magnitude (left) and the corresponding pattern (right) of the simulations with $Pr = 0.5$, $\mu = 0.7$, $L = 100 \times 2\pi$, $g_m = 50$ and $c^2 = 2$. In the plot of wave-vector magnitude, white indicates the local wavenumber exceeds the wavenumber for the SVI ($K_{SVv} = 1.12$), while black signals lower wavenumbers. Shadowgraph image is taken at $t = 2 \times 10^4$ and largely dominated by spirals with defects. Marked regions show skew-varicose distortions.*

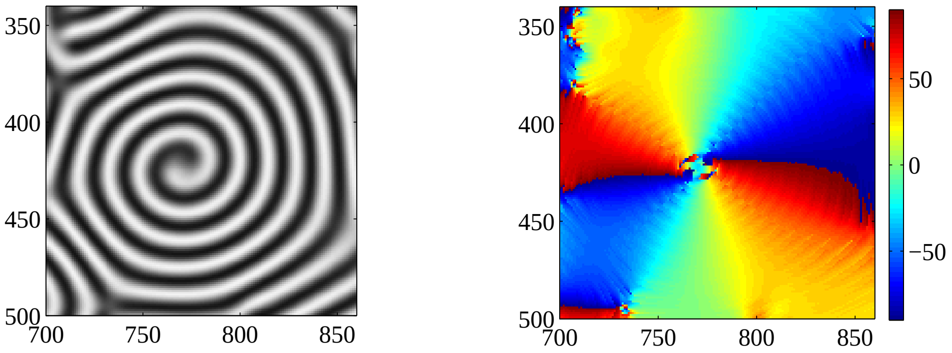

(a)

(b)

Figure 5.30: *(a) An image of spiral taken from the pattern in figure 5.29. (b) Local wave-vector direction, indicated in degrees with respect to the X direction. Red regions are for the stripes with 90° angle while blue denotes −90° angle.*

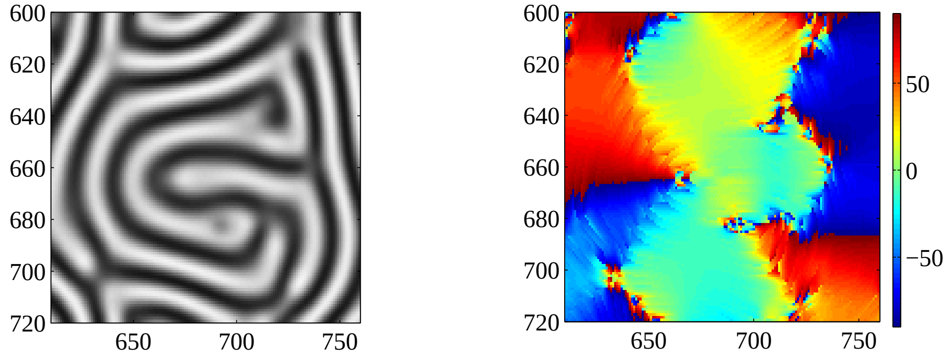

(a) (b)

Figure 5.31: *(a) Part of a defect taken from the pattern in figure 5.29 (b) Local wave-vector direction, indicated in degrees with respect to the X direction. Red regions are for the stripes with* 90° *angle while blue denotes* −90° *angle.*

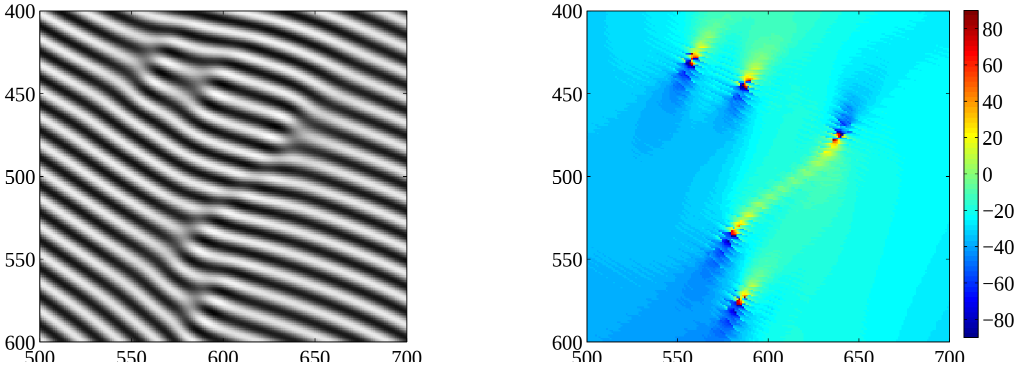

(a) (b)

Figure 5.32: *(a) The skew-varicose distortion shown in figure 5.25 (b) Local wave-vector direction, indicated in degrees with respect to the X direction. Red regions are for the stripes with* 90° *angle while blue denotes* −90° *angle.*

the SVI events in different patterns.

2

Chapter 6

Conclusions and Discussion

Motivated by the most striking signatures of the mean flow effects in Rayleigh–Bénard Convection, the Spiral Defect Chaos (SDC) state and the existence of the skew-varicose instability, we have investigated two generalized Swift–Hohenberg models of convection that include the mean-flow effects. The skew-varicose instability is known to play an important role in the formation of Spiral Defect Chaos [6, 47], a spatio-temporally complex pattern, that competes with stationary rolls near the onset of convection in medium to low Prandtl number convection.

The main difference between the two models we analyzed is that in the first model vorticity has its own independent dynamics [69], while in the second, vorticity is directly slaved to the order parameter [64]. In addition to the driving parameter μ, the dynamics of model 1 could be controlled using three parameters, Prandtl number, Pr, coupling coefficient to mean flow, g_m and a parameter c, which accounts the boundary conditions, stress-free ($c = 0$) and no-slip ($c^2 = 2$); in model 2, the coupling coefficient to mean flow, g, is the only extra parameter.

The skew-varicose instability in these models has been difficult to analyse owing to the absence of consistent scaling for the modulation wavenumber and the system parameters [90]. Therefore, previous work [90, 93, 94] has made varying assumptions on the relation between k, l (where (k, l) is the perturbation wavevector) and the amplitude of the basic stripe solution. The novelty of this work was that we used a projection operator, P_α, that applies to the cubic nonlinearity and acts as a filter in Fourier space, allowing the exact stripe solution of the PDEs to be written down explicitly [91]. We then carried out a complete linear stability analysis of the stripe solution. We expressed the relevant determinants as power series in k^2 and l^2 and hence derived explicit expressions for the largest growth rates; this has led to an improved understanding of the instabilities of stripes overcoming the main difficulty, the appearance of k^2+l^2 in the denominator of the determinant, by a careful consideration of appropriate limits. We theoretically derived the boundaries of Eckhaus, zigzag, skew-varicose and oscillatory skew-varicose instabilities with numerical verification, while cross-roll and oscillatory instabilities are investigated using numerical computations of the eigenvalues of the stability matrices. We established a relationship between two models through $g = g_m/(Pr\ c^2)$. Therefore the results we derived are in an agreement in both models with this relationship. However, the oscillatory instabilities do not exist in model 2, owing to the lack of intrinsic dynamics in the vorticity field.

We found two different behaviours of the skew-varicose instability: in the limit of μ going to zero, the SVI goes as $\mu \sim 12q^2$ ($q = K-1$, where K is the wavenumber), provided $g > 0.75$. The most unstable wave-vector satisfies $k^2/l^2 = \mathcal{O}(1)$. In this case, stripes are Eckhaus stable at the SVI. For $g < 0.75$, the SVI boundary crosses the Eckhaus curve, and in the limit of μ going to zero, it goes as $\mu \sim aq^2$ with $4 < a < 12$. In the large g limit (that is, for very low Pr, or for stress-free boundary conditions), there is a transition of the SVI boundary from $\mu \sim 12q^2$ to $\mu \sim 8q$ at a wavenumber satisfying $q \propto 1/g$. The oscillatory skew-varicose (OSV) instability occurs only with stress-free boundary conditions and is approximately $\mu = \left(\frac{-3+\sqrt{5}}{3}\right) qg_m$, for small μ. We presented results for both stress free and no-slip boundary conditions: stability diagrams in the (μ, q) plane, exploring the role of the mean flow and the effect of Prandtl number on the region of stable stripes. This region is eliminated for small μ if g is large enough or if Pr is small enough.

The use of the projection operator P_α, which is equivalent to a truncation to selected wavenumbers, made this analysis straightforward and allowed the complete understanding of the skew-varicose instability in our models. Numerical simulations of these projected models for small μ have qualitatively the same solutions as the unprojected PDEs; this is our justification for using these projected models in the stability analysis for small μ. The projected and unprojected models will of course differ for large μ.

We characterized the nonlinear evolution of the modes that are responsible for the skew-varicose instability in order to understand whether the bifurcation from stable stripes at the skew-varicose instability is supercritical or subcritical. We derived two systems of ODEs, first selecting three relevant modes (3-mode truncation), and then extending this to include 2 more relevant modes (5-mode truncation). We carried out a centre Manifold Reduction at the bifurcation point and showed that in the 3-mode truncation, the secondary bifurcation is supercritical. This was inconsistent with our experience with solving the PDE numerically. We therefore introduced the 5-mode truncation, in which the bifurcation is subcritical as expected. A bifurcation diagram illustrating this scenario is presented for the parameters, $g = 20$, $q = 0.1$ and $k = l = 2\pi/L = 0.05$.

Our results suggest that the three mode truncation does not capture the correct nonlinear solutions at the skew-varicose instability, and that a truncated system of 5 modes may capture the correct behaviour. We therefore claim that the bifurcation structure presented by Nguyen and Homburg [97] is unlikely to capture the correct nonlinear behaviour of the skew-varicose instability. Their work is based on the Busse system, which was derived by truncating to just three modes in the PDEs for Rayleigh–Bénard Convection assuming stress free boundary conditions and limiting to a small aspect ratio with domain size $L = 2 \times 2\pi$.

The improved understanding of the stability of stripes in this work provided the foundation for numerical simulations of the PDEs in large domains. We explored the Spiral Defect Chaos state using a generalized Swift–Hohenberg model (GSH model 1) and established numerically the role of the mean flow, the Prandtl number and the parameters c and μ in the transformation of different solutions (SDC, Defect Chaos and target states), in model 1.

Reasonable values of Pr and the coupling coefficient to the mean flow, g_m, that generate Spiral Defect Chaos have already been explored at some length in literature. However, Schmitz *et al.* [76] in 2002 claimed that the SDC in GSH models occurs only as a transient (in contrast to SDC found in experiments) and that the small-scale structure of the vorticity field at the spiral cores, which might be crucial for persistent SDC, may not captured in the GSH model. Their claim was based only on a simulation carried out for $t = 6 \times 10^4$ time units with the parameter values, $Pr = 1$, $g_m = 50$, $c^2 = 2$ and aspect ratio, $\Gamma = 32$. Our results for the same parameter values, run over much longer times, suggest that these bigger spirals may eventually break into smaller spirals and defects, returning to the SDC state. We speculate that the system then cycles between SDC and a state dominated by bigger spirals.

In our main analysis, we systematically varied Pr and μ keeping other parameter values fixed at $g_m = 50$, $c^2 = 2$, $L = 40 \times 2\pi$. Our results show that the SDC state occurs when $\mu \gtrsim 0.6$ and with suitably selected Pr, the GSH model generates SDC with persistent dynamics, resembling the spiral defect chaos of RBC. We found that for Pr in the range $0.25 \lesssim Pr \lesssim 0.8$, the SDC state persists for as long as we have simulated ($t = 2 \times 10^6$ time units) whereas in the range $0.9 \lesssim Pr \lesssim 1.2$, SDC pattern can develop into a state dominated by bigger spirals and then back to SDC state (the solution may then cycle between SDC and a state dominated by bigger spirals). We supported these conclusions by using time series evolution of the Kinetic Energy and by counting the number of spirals. The Spiral Defect Chaos state is replaced by a state with slowly moving targets if $Pr \gtrsim 2$, whereas if $Pr \lesssim 0.2$, the solution is more chaotic and spirals cannot be distinguished. By varying g_m and c^2, we found that which type of solution is present depends on the combination $g_m/Pr\, c^2$.

When μ is decreased, spirals break up into defects, giving a defect dominated state followed by perfect stripe pattern at even lower μ. We found that this transition of stripes to defect state, occurs at $\mu_{transition} > 0$ in finite domains, but in the limit of large L, $\mu_{transition}$ appears to go to zero, suggesting that the onset of stripes and onset of Defect Chaos are the same in an infinite domain. We also investigated the dependence of this transition on Pr, and $\mu_{transition}$ appears to go to zero, when Pr tends to zero.

With the support of the local wave vector in different patterns and the stability analysis for the skew-varicose instability we established that it is skew-varicose events that are responsible for maintaining Defect Chaos.

In the future it will be of interest to address the question whether a similar projection operator could be used in the analysis of the Navier–Stokes equations.

The Busse system, which is derived from the original fluid equations has the same structure as our 3-mode truncation of the GSH model and hence a relation to the coefficients could be found. We recommend the structure of our extended system of 5-mode truncation could be used to derive an extension to a Busse system and hence to follow the work carried out by Nguyen *et al.* [97] and Busse [95].

We anticipate that our results on SDC have brought a significant advantage that the GSH model, for some parameters, is capable of generating a Spiral Defect Chaos state that persists for long time, could be used to investigate several properties of dynamics of SDC in Rayleigh–Bénard convection. In addition, our investigation of the local wavenumber of the solution state combined with the stability diagram of the GSH model could be used to guide the development of a more accurate theoretical description of the connection between the skew-varicose instability and the SDC state and hence to get an improved understanding of why SDC occurs in convection.

Bibliography

[1] R. Joseph. Infinity patterned symmetry pythagoras and the black hole at the edge of the universe. *Journal of Cosmology*, 13, 2011. In press.

[2] N. Mui. `http://www.travelblog.org/Wallpaper/sand_dunes_mui_ne.html`, 2011. [Online; accessed 23-Oct-2011].

[3] P. Manneville. Rayleigh–Bénard Convection: Thirty years of experimental, theoretical, and modeling work. *Springer Tracts in Modern Physics*, 207:41–65, 2006.

[4] V. Croquette. Convective pattern dynamics at low Prandtl number: Part II. *Contemporary Physics*, 30:153–171, 1989.

[5] F. H. Busse and J. A. Whitehead. Instabilities of convection rolls in a high Prandtl number fluid. *J. Fluid Mech.*, 47:305–320, 1971.

[6] R. M. Clever and F. H. Busse. Large wavelength convection rolls in low Prandtl number fluids. *J. of App. Math. and Phys.*, 29:711–714, 1978.

[7] M. Lowe and J. P. Gollub. Pattern Selection near the Onset of Convection: The Eckhaus Instability. *Phys. Rev. Lett.*, 55:2575–2578, 1985.

[8] B. Plapp. *Spiral-pattern formation in Rayleigh–Bénard Convection.* PhD thesis, Cornell Univ., Ithaca, New York (Unpublished), 1997.

[9] M. Assenheimer and V. Steinberg. Rayleigh–Bénard convection near the gas-liquid critical point. *Phys. Rev. Lett.*, 70:3888–3891, 1993.

[10] H. Riecke and S. Madruga. Geometric diagnostics of complex patterns: Spiral defect chaos. *Chaos*, 16:013125, 2006.

[11] K. H. Chiam, M. R. Paul, M. C. Cross, and H. S. Greenside. Mean flow and spiral defect chaos in Rayleigh–Bénard convection. *Phys. Rev. E*, 67:056206, 2003.

[12] H. Bénard. Les tourbillons cellulaires dans une nappe liquide. *Rev. Gen. Sci. Pure Appl.*, 11:679–686, 1900.

[13] L. Rayleigh. On convection currents in a horizontal layer of fluid, when the higher temperature is on the under side. *Phil. Mag.*, 32:529546, 1916.

[14] G. Taylor. Stability of a Viscous Liquid Contained between Two Rotating Cylinders. *Phil. Trans. R. Soc. Lond. A*, 223:289–343, 1923.

[15] M. Faraday. On a peculiar class of acoustical figures; and on certain forms assumed by a group of particles upon vibrating elastic surfaces. *Phil. Trans. R. Soc. Lond.*, 121:299–318, 1831.

[16] M. Cross. *Pattern formation and dynamics in nonequilibrium systems*. Cambridge University Press, 2009.

[17] A. Schluter, D. Lortz, and F. Busse. On the stability of steady finite amplitude convection. *J. Fluid Mech.*, 23:129, 1965.

[18] C. Normand, Y. Pomeau, and M. G. Velarde. Convective instability: A physicists approach. *Rev. Mod. Phys*, 49:581–624, 1977.

[19] S. Chandrasekhar. *Hydrodynamic and hydromagnetic stability.* Oxford University Press, 1961.

[20] M. C. Cross and P. C. Hohenberg. Pattern formation outside of equilibrium. *Rev. of Mod. Phys.*, 65:851–1112, 1993.

[21] A. C. Newell, T. Passot, and J. Lega. Order parameter equations for patterns. *Ann. Rev. Fluid Mech.*, 25:399–453, 1993.

[22] M. Chen and J. Whitehead. Evolution of two-dimensional periodic Rayleigh–Bénard Convection cells of arbitrary wavenumbers. *J. Fluid Mech.*, 31:1–15, 1968.

[23] Y. Hu, R. Ecke, and G. Ahlers. Convection near threshold for Prandtl numbers near 1. *Phys. Rev. E*, 48:4399–4413, 1993.

[24] F. H. Busse. The oscillatory instability of convection rolls in a low Prandtl number fluid. *J. Fluid Mech.*, 52:97–112, 1972.

[25] F. H. Busse and R. M. Clever. Instabilities of convection rolls in a fluid of moderate Prandtl number. *J. Fluid Mech.*, 91:319–335, 1979.

[26] E. W. Bolton and F. H. Busse. Stability of convection rolls in a layer with stress-free boundaries. *J. Fluid Mech.*, 150:487–498, 1985.

[27] F. H. Busse. The stability of finite amplitude cellular convection and its relation to an extremum principle. *J. Fluid Mech.*, 30:625–649, 1967.

[28] F H Busse. *Fundamentals of Thermal Convection.* Mantle convection plate tectonics and global dynamics, Gordan and Breach Science publishers, New York, 1989.

[29] C. Newell and J. Whitehead. Finite bandwidth, finite amplitude convection. *J. Fluid Mech.*, 38:279303, 1969.

[30] W. Eckhaus. Studies in Nonlinear Stability Theory. *Berlin: Springer-Verlag*, 1965.

[31] J. Whitehead and M. Chen. Stability of Rayleigh–Bénard Convection rolls and bimodal flow at moderate Prandtl number. *Dynamics of Atmospheres and Oceans*, 1:33–59, 1976.

[32] T. Rossby. A study of Bénard convection with and without rotation. *J. Fluid Mech.*, 36:309, 1969.

[33] R. M. Clever and F. H. Busse. Large wavelength convection rolls in low Prandtl number fluids. *J. of App. Math. and Phys.*, 29:711–714, 1978.

[34] A. Zippelius and E. D. Siggia. Stability of finite-amplitude convection. *Phys. of Fluids*, 26:2905–2915, 1983.

[35] F. H. Busse and E. W. Bolton. Instability of convection rolls with stress-free boundaries near threshold. *J. Fluid Mech.*, 146:115–125, 1984.

[36] R. M. Clever and F. H. Busse. Transition to time-dependent convection. *J. Fluid Mech.*, 65:62545, 1974.

[37] R. M. Clever and F. H. Busse. Nonlinear properties of convection rolls in a horizontal layer rotating about a vertical axis. *J. Fluid Mech.*, 94:609–27, 1979.

[38] S. W. Morris, E. Bodenschatz, D. S. Cannell, and G. Ahlers. Spiral defect chaos in large aspect ratio Rayleigh–Bénard convection. *Phys. Rev. Lett.*, 71:2026–2029, 1993.

[39] G. Ahlers. Experiments on spatiotemporal chaos. *Physica A*, 249, 1998.

[40] M. Assenheimer and V. Steinberg. Transition between spiral and target states in Rayleigh–Bénard convection. *Nature*, 367:345 – 347, 1994.

[41] J. Liu and G. Alhers. Spiral-defect chaos in Rayleigh–Bénard Convection with small Prandtl numbers. *Phys. Rev. Lett.*, 77:312629, 1996.

[42] B. Plapp and E. Bodenschatz. Core dynamics of multi-armed spirals in Rayleigh–Bénard convection. *Phys. Scr.*, 67:111–116, 1996.

[43] M. J. Lees, M. S. Thurlow, J. R. Seddon, and P. G. Lucas. Convective Roll Dynamics in Liquid ^{4}He near the Onset of Convection. *Phys. Rev. Lett.*, 93(14):144502, 2004.

[44] W. Decker, W. Pesch, and A. Weber. Spiral defect chaos in Rayleigh–Bénard convection. *Phys. Rev. Lett.*, 73:648–651, 1994.

[45] S. W. Morris, E. Bodenschatz, D. S. Cannell, and G. Ahlers. The spatio-temporal structure of Spiral-Defect Chaos. *Physica D: Nonlinear Phenomena*, 97:164–179, 1996.

[46] W. Pesch. Complex spatiotemporal convection patterns. *Chaos*, 6:348–357, 1996.

[47] E. Bodenschatz, W. Pesch, and G. Ahlers. Recent Developments in Rayleigh–Bénard Convection. *Ann. Rev. Fluid Mech.*, 32:709–778, 2000.

[48] R. V. Cakmur, D. A. Egolf, B. Plapp, and E. Bodenschatz. Transition from Spatiotemporal Chaos to Ideal Straight Rolls in Rayleigh–Bénard Convection. In *eprint arXiv:patt-sol/9702003*, pages 2003–+, 1997.

[49] Y. Hu, R. Ecke, and G. Ahlers. Convection for Prandtl numbers near 1: Dynamics of textured patterns. *Phys. Rev. E*, 51:3263–3279, 1995.

[50] X. J. Li and J. D. Xi, H. W.and Gunton. Nature of roll to spiral-defect-chaos transition. *Phys. Rev. E*, 57:1705–1716, 1998.

[51] R. Ahlers G. Ecke, R. Mainieri. Excitation of spirals and chiral symmetry breaking in Rayleigh–Bénard Convection. *Science*, 269:1704–7, 1995.

[52] D. A. Egolf, I. V. Melnikov, and E Bodenschatz. Importance of Local Pattern Properties in Spiral Defect Chaos. *Phys. Rev. Lett.*, 80:3228–3231, 1998.

[53] D. A. Egolf, I. Melnikov, W. Pesch, and R. Ecke. Mechanisms of extensive spatiotemporal chaos in Rayleigh–Bénard Convection. *Nature*, 404:733736, 2000.

[54] M. Cross. Theoretical modelling of spiral chaos in Rayleigh–Bénard Convection. *Physica D*, 97:65–80, 1996.

[55] M. C. Tu, Y.and Cross. Chaotic domain structure in rotating convection. *Phys. Rev. Lett.*, 69:2515–2518, 1992.

[56] P. Manneville. A two-dimensional model for three-dimensional convective patterns. *Journal of Physics France*, 44:759–765, 1983.

[57] M. Cross. Phase dynamics of convective rolls. *Phys. Rev. A*, 27:490498, 1983.

[58] C. Newell, T. Passot, and M. Souli. The phase diffusion and mean drift equations for convection at finite Rayleigh numbers in large containers. *J. Fluid Mech.*, 220:187–252, 1990.

[59] M. C. Cross and A. C. Newell. Convection patterns in large aspect ratio systems. *Physica D: Nonlinear Phenomena*, 10(3):299–328, 1984.

[60] E. D. Siggia and A. Zippelius. Pattern Selection in Rayleigh–Bénard Convection near Threshold. *Phys. Rev. Lett.*, 47:835–838, 1981.

[61] Pocheau A. Daviaud F. Inhibition of phase turbulence close to onset of convection by

permeable lateral boundary condition for the mean flow. *Euro. phys. Lett.*, 9:67580, 1989.

[62] J. Swift and P. C. Hohenberg. Hydrodynamic fluctuations at the convective instability. *Phys. Rev. A*, 15:319–328, 1977.

[63] Y. Pomeau and P. Manneville. Stability and fluctuations of a spatially periodic convective flow. *J. Phys. France Lett.*, 40:L60912, 1979.

[64] H. S. Greenside and M. C. Cross. Stability analysis of two-dimensional models of three-dimensional convection. *Phys. Rev. A*, 31:2492–2501, 1985.

[65] M. Bestehorn and H. Haken. Traveling waves and pulses in a two-dimensional large-aspect-ratio system. *Phys. Rev. A*, 42:7195–7203, 1990.

[66] M. Bestehorn, M. Fantz, R. Friedrich, and H. Haken. Hexagonal and spiral patterns of thermal convection. *Phys. Lett. A*, 174:48–52, 1993.

[67] X.-J. Li, H.-W. Xi, and J. D. Gunton. Dynamical properties of multiarmed global spirals in Rayleigh–Bénard Convection. *Phys. Rev. E*, 54:R3105–8, 1996.

[68] V. Gertsberg and G Sivashinsky. Stability analysis of two-dimensional models of three-dimensional convection. *Prog. Theor. Phys.*, 66:1219, 1980.

[69] H. W. Xi, J. D. Gunton, and J. Viñals. Spiral defect chaos in a model of Rayleigh–Bénard convection. *Phys. Rev. Lett.*, 71:2030–2033, 1993.

[70] W. Decker and W. Pesch. Order parameter and amplitude equations for the Rayleigh-Bénard convection. *J. Phys. II France*, 4:419–438, 1994.

[71] H. W. Xi, J. D. Gunton, and J. Viñals. Spiral-pattern formation in Rayleigh–Bénard Convection. *Phys. Rev. E*, 47:R2987–R2990, 1993.

[72] M. Bestehorn, M. Neufeld, R. Friedrich, and H. Haken. Comment on Spiral-pattern formation in Rayleigh–Bénard convection. *Phys. Rev. E*, 50:625–626, 1994.

[73] M. C. Cross and Y. Tu. Defect Dynamics for Spiral Chaos in Rayleigh–Bénard Convection. *Phys. Rev. Lett.*, 75:834–837, 1995.

[74] H. W. Xi and J. D. Gunton. Spatiotemporal chaos in a model of Rayleigh–Bénard Convection. *Phys. Rev. E*, 52:4963–4975, 1995.

[75] L. S. Tsimring. Spiral dynamics in pattern-forming systems: mean-flow effects. *Physica A*, 249:125–133, 1998.

[76] R. Schmitz, W. Pesch, and W. Zimmermann. Spiral-Defect Chaos: Swift–Hohenberg model versus Boussinesq equations. *Phys. Rev. E*, 65:037302, 2002.

[77] J. R. de Bruyn, E. Bodenschatz, S. W. Morris, S. P. Trainoff, and Y. Hu. Apparatus for the study of Rayleigh–Bénard Convection in gases under pressure. *Rev. Sci. Inst.*, 67:2043–2067, 1996.

[78] J. Liu and G. Alhers. Rayleigh–Bénard Convection in Binary-Gas Mixtures: 1. Thermophysical Properties and the Onset of Convection. *Phys. Rev. E.*, 55:6950, 1997.

[79] P. Manneville. *in Cellular Structures in Instabilities(Springer-Verlag)*, 210:137–155, 1984.

[80] M. Bestehorn, M. Fantz, R. Friedrich, H. Haken, and C Pérez-Garcia. Spiral patterns in thermal convection. *Z. Phys. B - Condensed Matter*, 88:93–94, 1992.

[81] J. Manneville, P. Piquemal. Zigzag instability and axisymmetric rolls in Rayleigh–Bénard Convection, the effects of curvature. *Phys. Rev. A*, 28:1714, 1983.

[82] M. Cross. Derivation of the amplitude equation at the Rayleigh-Bénard instability. *Phys. of Fluids*, 23:1727, 1980.

[83] H. W. Xi, J. D. Gunton, and J. Viñals. Study of Spiral Pattern Formation in Rayleigh–Bénard Convection. In *arXiv:patt-sol/9706007v1*, 1992.

[84] J. Ahlers G. Cannell D. Bodenschatz, E. de Bruyn. Transitions between patterns in thermal-convection. *Phys. Rev. Lett*, 67:3078, 1991.

[85] X.-J. Li, H.-W. Xi, and J. D. Gunton. Phenomenological Theory for Spatiotemporal Chaos in Rayleigh–Bénard Convection. In *arXiv:patt-sol/9706007v1*, 1997.

[86] M. R. Paul, K. H. Chiam, M. C. Cross, P. F. Fischer, and H. S. Greenside. Pattern Formation and Dynamics in Rayleigh–Bénard Convection: Numerical Simulations of Experimentally Realistic Geometries. *Physica D*, 184:114–126, 2003.

[87] H. S. Greenside, M. C. Cross, and W. M. Coughran, Jr. Mean flows and the onset of chaos in large-cell convection. *Phys. Rev. Lett.*, 60:2269–2272, 1988.

[88] J. P. Gollub, A. R. McCarriar, and J. F. Steinman. Convective pattern evolution and secondary instabilities. *J. Fluid Mech.*, 125:259–281, 1982.

[89] Y. Hu, R. E. Ecke, and G. Ahlers. Transition to Spiral-Defect Chaos in Low Prandtl Number Convection. *Phys. Rev. Lett.*, 74:391–394, 1995.

[90] R. Hoyle. Pattern Formation: An Introduction to Methods. *Cambridge University Press*, 2006.

[91] I. Melbourne. Private Communication.

[92] A. Dhooge, W. Govaerts, and Y. A. Kuznetsov. Numerical Continuation of Branch

Points of Limit Cycles in MATCONT. *Lecture Notes in Computer Science*, 3037:42–49, 2004.

[93] A. J. Bernoff. Finite amplitude convection between stress-free boundaries; Ginzburg–Landau equations and modulation theory. *Euro. J. Appl. Math*, 5:267–282, 1994.

[94] Y. Ponty, T. Passot, and P. L. Sulem. A new instability for finite Prandtl number rotating convection with free-slip boundary conditions. *Phys. of Fluids*, 9:67–75, 1997.

[95] F. H. Busse, M. Kropp, and M. Zaks. Spatio-temporal structures in phase-turbulent convection. *Physica D*, 61:94–105, 1992.

[96] E. N. Lorenz. Deterministic nonperiodic flow. *J. Atmospheric Sci.*, 20:130–141, 1963.

[97] Nguyen, A. J. Homburg, and G. Ahlers. Global bifurcations to strange attractors in a model for skew varicose instability in thermal convection. *Physica D*, 211:235–262, 2005.

[98] K. Tsiveriotis and R. A. Brown. Bifurcation structure and the Eckhaus instability. *Phys. Rev. Lett.*, 63:2048–2051, 1989.

[99] L. S. Tuckerman and D. Barkley. Bifurcation analysis of the Eckhaus instability. *Phys. D*, 46:57–86, 1990.

[100] D. Gottlieb and S. Orszag. *Numerical analysis of spectral methods: theory and applications.* SIAM, Philadelphia, Pennsylvania, 1993.

[101] S. M. Cox and P. C. Matthews. Exponential Time Differencing for Stiff Systems. *Journal of Computational Physics*, 176:430–455, March 2002.

[102] J. H. Siggers. Dynamics of target patterns in low-Prandtl-number convection. *J. Fluid Mech.*, 475:357–375, 2003.

[103] J. Liu and G. Ahlers. Spiral-Defect Chaos in Rayleigh–Bénard Convection with Small Prandtl Numbers. *Phys. Rev. Lett.*, 77:3126–3129, 1996.